ČESKÉ VYSOKÉ UČENÍ TECHNICKÉ V PRAZE
Fakulta jaderná a fyzikálně inženýrská
Katedra inženýrství pevných látek

Pohyblivé mikrostruktury v monokrystalech termoelastických martenzitů

Mobile microstructures in single crystals of thermoelastic martensites

Ing. Hanuš Seiner, Ph.D.

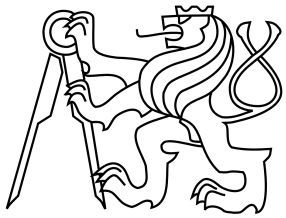

Praha, duben 2015

Poděkování

V této habilitační práci jsou shrnuty poznatky ze studia fázových transformací a deformačních mechanismů v monokrystalech termoelastických martenzitů, se zaměřením na vlastnosti uspořádaných mikrostruktur (tzn. martenzitických laminátů a feroických domén) v těchto materiálech. Časově práce zahrnuje výsledky získané v rámci řešení postdoktorského projektu GAČR *Elasticita martenzitických mikrostruktur* (2009–2010) a v následujících čtyřech letech, kdy jsem se problematikou termoelastických martenzitů zabýval především jako člen řešitelských týmů projektů *Feromagnetické slitiny s tvarovou pamětí na bázi kobaltu* (GAČR) a *Experimentální a teoretická analýza mikromechanických procesů v pokročilých funkčních materiálech* (AVČR) a později jako hlavní řešitel projektů *Experimentálně podložené multiškálové modelování slitin s tvarovou pamětí* (GAČR) a *Matematické modelování feromagnetických slitin s tvarovou pamětí* (DAAD).

Výsledků shrnutých v této práci by nebylo možno dosáhnout bez masivní a obětavé pomoci řady mých kolegů z vědeckých pracovišť v České republice i v zahraničí, kterým bych rád na tomto místě poděkoval. V první řadě to byli mí spolupracovníci a přátelé z Laboratoře ultrazvukových metod Ústavu termomechaniky AV ČR, zejména Michal Landa, Petr Sedlák, Jan Zídek a Lucie Bodnárová; značná část prezentovaných výsledků se rovněž opírá o práci bývalých studentů této laboratoře, konkrétně Ondřeje Glatze, Pavla Sedmáka a Michala Novotného. Dále můj vděk patří kolegům z Fyzikální ústavu AV ČR, zejména Olegu Heczkovi, Jaromíru Kopečkovi, Janu Drahokoupilovi a Vítu Kopeckému.

Z řady zahraničních kolegů, se kterými jsem měl tu čest spolupracovat, se na výsledcích uváděných v této práci nejvíce podíleli Ladislav Straka (Aalto University, Finsko), John M. Ball (Oxford University, Velká Británie), Sebastian Fähler (IFW Dresden, Německo), Konstantinos Koumatos (dříve Oxford University, Velká Británie, nyní GSSI L'Aquilla, Itálie) a Alexej Sozinov (dříve AdaptaMat Helsinki, nyní Aalto University, Finsko), mé poděkování patří i dalším spoluautorům uváděných publikací. Mimo ně mi připomínkami k práci a plodnou diskuzí velmi pomohli Petr Šittner (FzÚ AV ČR Praha), Robert Niemann (IFW Dresden, Německo), Richard D. James (University of Minnessota, USA), Doron Shilo a Eilon Faran (oba Technion, Haifa, Izrael), Felix Otto (MPI Leipzig, Německo), Christof Melcher (RWTH Aachen, Německo) a Barbora Benešová (Universität Würzburg, Německo).

Dále bych chtěl poděkovat Ladislavu Kalvodovi, vedoucímu Katedry inženýrství pevných látek FJFI ČVUT, a Jiřímu Kunzovi, vedoucímu Katedry materiálů FJFI ČVUT, že mi dali

možnost se současně s výzkumnou činností věnovat také pedagogické činnosti a vedení studentů na výše zmíněných katedrách.

Největší dík však patří mé rodině, především mé manželce a dcerám: za podporu v práci, za shovívavost vůči její časové náročnosti a za to nejpříjemnější možné rozptylování od ní.

Obsah

Úvod do tématu práce

Termoelastické martenzitické transformace [1–3] jsou základem řady unikátních termomechanických jevů v takzvaných inteligentních materiálech (smart materials), především jevu tvarové paměti [4, 5], superelasticity [6–8], hyperelastického chování [9] a magneticky indukovaného aktuátorového chování [10, 11]. Pro pochopení všech těchto efektů je nezbytné zkoumat termoelastické martenzitické transformace na nejzákladnější možné úrovni, tedy na úrovni atomární mříže a procesů v monokrystalech. Ukazuje se však, že tyto transformace mají výrazně multiškálový charakter [5, 12, 13] - pro popis makroskopického chování není popis na úrovni atomární mříže postačující, výraznou roli hrají také morfologie fázových a strukturních rozhraní na mikrometrické škále, tedy mikrostruktura jednotlivých fází.

Termoelastické martenzity, tedy materiály schopné plně reverzibilně přecházet mezi dvěma či více strukturními fázemi prostřednictvím martenzitických transformací pod vlivem teploty, napětí, či vnějšího magnetického pole, lze také charakterizovat termínem *feroelastika* [14, 15]. Tento termín dobře vystihuje ztrátu symetrie při přechodu z vysokoteplotní fáze (austenitu) do fáze nízkoteplotní (martenzitu). Stejně jako u jiných feroik (feromagnetika, feroelektrika) je i u feroelastik možno pozorovat tendence nízkoteplotních fází vytvářet doménové struktury, často výrazně geometricky uspořádané. U termoelastických martenzitů mají tyto mikrostruktury nejčastěji formu takzvaných laminátů prvního řádu [16], což jsou periodické struktury skládající se z tenkých vrstev jednotlivých variant martenzitů navzájem propojených dvojčatovými rozhraními. Geometrická uspořádanost struktur vyplývá z požadavků takzvané *geometrické kompatiblity* [17], tedy požadavku na spojitost pole posunutí popisující přechod z vysokoteplotní fáze do nízkoteplotní a zároveň z požadavku minimální uložené energie elastické napjatosti. V případě feromagnetických martenzitů nebo uspořádaných či slitin tyto pravidelné struktury mohou dále interagovat s mikrostrukturou magnetických domén [18], strukturou antifázových rozhraní [19] nebo fázovou strukturou [20].

Martenzitické transformace ve feroelastikách stejně jako reorientační procesy v nich probíhají mechanismem nukleace a růstu. Jsou-li pozorované mikrostruktury výsledkem požadavků na minimálně energeticky náročný průběh tohoto mechanismu, musí se transformace či reorientace projevit pohybem či růstem mikrostruktury v krystalové mříži. Ukazuje se, že takového pohybu jsou schopny jenom určité typy mikrostruktur [21–24], které zároveň s geometrickou kompatibilitou vykazují také specifické dynamické a disipační vlastnosti. Porozumění

těmto vlastnostem je jednou z esenciálních podmínek pro pochopení samotných mechanismů transformace a reorientace, pro jejich teoretický popis a matematické modelování, i pro vývoj nových feroelastických materiálů a jejich budoucí technologické aplikace.

Cíle a struktura práce

Cílem práce je poskytnout shrnutí výsledků týkajících se morfologie, mechanismů vzniku a pohybu, energetické bilance a makroskopických projevů pohyblivých mikrostruktur v termoelastických martenzitech. Po stručném teoretickém úvodu (Kapitola 1) je práce členěna do tří tématických částí. První se zaměřuje na rozhraňové mikrostruktury ve slitině Cu-Al-Ni a jejím cílem je ukázat, že tato rozhraní zaujímají specifickou morfologii ($X-$ a $\lambda-$ rozhraní), která nesplňuje kritérium minima energie, a diskutovat mechanismy jejich pohybu a nukleace. Druhá část je věnována pohyblivým makrodvojčatovým rozhraním ve slitině Ni-Mn-Ga a jejím cílem je ukázat relaci mezi krystalografickou orientací (a potažmo mikromorfologií) těchto rozhraní a jejich pohyblivostí, a to na základě jak experimentálních pozorování, tak teoretických modelů. Třetí část se pak zabývá pohyblivostí mikrostruktur ve vysokoteplotních fázích slitin Ni-Mn-Ga a Co-Ni-Al, tedy takzvanými prekurzorovými (nebo též premartenzitickými) efekty, předcházejícími vlastní transformaci do nízkoteplotní fáze. Cílem této části je ukázat, že elastická nestabilita vysokoteplotních fází, která na transformační teplotě inicializuje samotnou martenzitickou transformaci, je nad touto teplotou klíčová pro dynamiku magnetických a fázových mikrostruktur.

Habilitační práce je koncipována jako komentovaný výběr časopiseckých publikací z let 2009–2014. Kritéria pro výběr byla následující:

1. jedná se o článek z mezinárodně respektovaného časopisu s impaktfaktorem $\gtrsim 1$;
2. článek se bezprostředně týká mechaniky mikrostruktur v monokrystalech slitin vykazujících termoelastické martenzitické transformace;
3. podíl habilitanta na tvorbě článku byl výrazný a dobře definovaný.

Tato kritéria splnilo celkem jedenáct publikací. Ostatní publikace autora, tedy zejména články týkající se vývoje metodiky rezonanční ultrazvukové spektroskopie a jejích aplikací pro charakterizaci elastických vlastností materiálů, lze nalézt v Přehledu publikační činnosti (Příloha A).

Každá z vybraných publikací je uvedena krátkou informací o jejím obsahu a o specifickém podílu habilitanta na publikovaných výsledcích.

Kapitola 1

Základní poznatky z teorie termoelastických martenzitů

V této kapitole budou shrnuty základní teoretické pojmy používané při popisu termomechanického chování termoelastických martenzitů, a to zejména pojmy z teorie martenzitických mikrostruktur na úrovni mechaniky kontinua a z příslušných partií termodynamiky pevné fáze.

Poznámka k terminologii: V odborné literatuře a i v článcích komentovaných v této habilitační práci jsou většinou používány termíny *feroelastika*, *termoelastické martenzity* a *slitiny s tvarovou pamětí* jako zcela ekvivalentní a vzájemně zaměnitelné. V principu jsou však definovány mírně rozdílně. My se v této práci budeme držet druhého z termínů, protože nejlépe svojí definicí vyhovuje vlastnostem všech popisovaných materiálů.

Feroelastika (jak bylo už naznačeno v úvodu) jsou materiály schopné nabývat spontánních, symetrii porušujících deformačních stavů bez vnějšího napětí [14, 15]. *Termoelastické martenzity* [1–3] jsou taková feroelastika, ve kterých k nabývání těchto deformačních stavů dochází prostřednictvím specifické fázové transformace popsané v následující podkapitole. *Slitiny s tvarovou pamětí* [4, 5] jsou potom materiály vykazující makroskopicky jev tvarové paměti, nebo přesněji materiály, ve kterých je tento jev z technologického hlediska využitelný. Z termoelastických martenzitů popisovaných v této práci je klasickým reprezentantem slitin s tvarovou pamětí slitina Cu-Al-Ni [6, 25, 26]. U slitin Ni-Mn-Ga [27, 28] a Co-Ni-Al [29, 30], rovněž v této práci uváděných, je využíván a zkoumán především jev magneticky indukované reorientace [10, 11], samotná tvarová paměť je u těchto s litin z řady důvodů méně významná. Existují naopak paměťové slitiny, ve kterých martenzitickou transformaci nezle označit za čistě termoelastickou, protože je spojena s produkcí velkého množství defektů, zejména dislokací. Klasickým příkladem je slitina NiTi [31, 32], nejznámější a technologicky nejpoužívanější slitina s tvarovou pamětí, a dále pak paměťové slitiny na bázi železa [33, 34].

1.1 Vlastnosti termoelastické martenzitické transformace

Termoelastická martenzitická transformace [1–3] je fázová transformace prvního druhu (tedy transformace spojená s produkcí latentního tepla a s nespojitými skoky prvních derivací termodynamických potenciálů). Základní vlastnosti charakterizující tuto transformaci jsou:

1. Tato transformace je **bezdifúzní**, což znamená že jednotlivé atomy se při transformaci posouvají o menší relativní vzdálenosti, než je vzdálenost meziatomární.

2. Krystalové mřížky dceřiné a mateční fáze jsou provázány **koordinačními vztahy**. Tyto vztahy určují vzájemnou orientaci mezi mřížkovými vektory obou fází a většinou se vyjadřují pomocí matic přechodu v anglické literatuře označovaných jako *lattice correspondence matrices*.

3. Transformace je **obousměrná**, čili zpětná transformace z martenzitu do austenitu je opět bezdifúzní se zachováním stejných koordinačních vztahů mezi fázemi (platí pro ně invertované matice přechodu). Tato podmínka není splněna například v ocelích, kde přechod z austenitu do martenzitu přechází pomocí bezdifúzní transformace, ale zpětná transformace je difúzní.

4. Transformace je **plně reverzibilní**, čili fázová rozhraní při transformaci neindukují žádné poruchy (např. dislokace) v krystalové mříži. To znamená, že po transformačním cyklu z austenitu do martenzitu a zpět jsou výchozí a koncový stav materiálu zcela totožné.

5. Transformace probíhá geometricky **čistě smykovým mechanismem,** což znamená, že transformace není spojena s žádnou výraznou změnou objemu. Ve srovnání s martenzitickými transformacemi v ocelích, kde je objemová změna přibližně 3%, objemová změna v termoelastických martenzitech je zanedbatelná (0.32% ve slitině Cu–Al–Ni, [26]). Přímým důsledkem smykového charakteru transformace je možnost vzniku kompatibilních rozhraní mezi austenitem a martenzitem bez produkce dislokací nebo vrstevnatých poruch (stacking faults).

6. Transformace probíhá nukleací a růstem, čili heterogenně v čase i prostoru, a může vykazovat značnou teplotní hysterezi. To ukazuje, že fázová rozhraní mají svoji povrchovou energii a další energii disipují při svém pohybu.

Všechny tyto vlastnosti platí jak pro dopředné a zpětné transformace mezi austenitem a martenzitem, tak pro intermediální transformace například mezi různými typy martenzitu, či mezi austenitem a premartenzitem. Stejné vlastnosti (bezdifúznost, koordinační vztahy, symetrie, reverzibilita, smykový charakter a heterogenita v čase a prostoru) lze přisoudit také reorientaci

martenzitu pod vnějším napětím; v tomto případě však nelze mluvit o martenzitické transformaci, protože zde nedochází ke změně entropie a tím pádem ani ke generování latentního tepla.

Tyto podmínky také zcela určují, jaké typy rozhraní mohou v termoelastických martenzitech existovat. Jsou to taková rozhraní, která jsou jednak koherentní, tedy umožňují spojité navázání sousedících krystalových mřížek, ale zároveň také pohyblivá, tedy jejich pohyb krystalovou mříží je možný prostřednictvím smykového mechanismu. Na atomární úrovni však mezi těmi rozhraními, která jsou koherentní a nepohyblivá (jako jsou například růstová dvojčata), a těmi pohyblivými nelze jednoduše rozlišit. Proto je výhodné používat k popisu mechaniky termoelastických martenzitů mechaniku kontinua a rozhraní popsat pomocí tzv. podmínek kinematické kompatibility.

1.2 Popis na úrovni kontinua

V této části budou shrnuty základní pojmy z matematické teorie martenzitických mikrostruktur. Podrobněji je tato teorie popsána například v učebnicích [5] a [35], nebo v řadě dnes již klasických článků jako jsou [36–38].

V celé této části budeme používat kartézský souřadný systém $\mathbf{x}$ k označení referenční konfigurace materiálu zaujímajícího nějakou omezenou oblast Ω a jiný kartézský systém $\mathbf{y}(\mathbf{x})$ pro konfiguraci okamžitou (čili deformovanou). O zobrazení $y : \Omega \to \mathbb{R}$ budeme předpokládat, že patří do Sobolevova prostoru $W^{1,1}(\Omega; \mathbb{R})$, což znamená, že jak toto zobrazení $\mathbf{y}(\mathbf{x})$ a jeho slabá derivace $\mathbf{F} = \nabla \mathbf{y}(\mathbf{x})$ jsou integrálním smyslu omezené.

1.2.1 Charakterizace transformací pomocí deformačního gradientu

Slabou derivaci $\mathbf{F} = \nabla \mathbf{y}(\mathbf{x})$ lze chápat jako zobecněný ekvivalent *deformačního gradientu* v bodě $\mathbf{x}$. Pokud je celá oblast Ω v austenitické fázi nebo v jedné z martenzitických variant, derivace $\mathbf{y}$ existují ve všech bodech oblasti a $\mathbf{F}$ je přímo rovna deformačnímu gradientu ve všech bodech. Pokud uvnitř oblasti Ω existují rozhraní vytvářející mikrostrukturu, je nutno chápat $\mathbf{F}$ jako deformační gradient ve slabém smyslu.

Pomocí této veličiny pak lze snadno popsat jak jednotlivé strukturní fáze termoelastických martenzitů, tak bezdifúzní přechody mezi nimi:

- **Deformační gradienty popisující austenit -** v souladu s většinou odborné literatury budeme brát deformační gradienty popisující austenitckou fázi jako

$$\mathbf{F} = \mathbf{Q}\mathbf{E}, \tag{1.1}$$

kde $\mathbf{Q} \in SO(3)$ je matice ortogonální rotace, a $\mathbf{E}$ může být buď jednotková matice $\mathbb{I}$, pokud je austenitcká fáze v bodě $\mathbf{x}$ elasticky nedeformovaná, nebo je tato matice rovná odmocnině z *Greenova tenzoru*

$$\mathbf{E} = \sqrt{\mathbf{F}^T\mathbf{F}}, \tag{1.2}$$

pokud $\mathbf{y}(\mathbf{x})$ reprezentuje elasticky deformovaný stav. V takovém případě lze vztah (1.1) chápat jako *polární rozklad* deformačního gradientu $\mathbf{F}$ [5].

- **Deformační gradienty popisující martenzit -** martenzitické fáze budeme charakterizovat pomocí spontánního deformačního gradientu $\mathbf{F} = \nabla\mathbf{y}(\mathbf{x})$ v nulovém vnějším napětí, přičemž tento deformační gradient nepatří do grupy rotací $SO(3)$. Předpokládáme, že v závislosti na třídě symetrie může materiál v martenzitu příslušet k několika různým variantám, čili těchto spontánních gradientů je více.

  Opět s použitím polární dekompozice můžeme psát pro $I-$tou variantu martenzitu

$$\mathbf{F}_I = \mathbf{Q}_I\mathbf{U}_I, \tag{1.3}$$

kde $\mathbf{Q}_I$ je matice rotace a $\mathbf{U}_I = \sqrt{\mathbf{F}_I{}^T\mathbf{F}_I}$ (odmocnina z Greenova tenzoru) je *Bainův tenzor* (nebo *Bainova matice*) I-té varianty martenzitu. Je zřejmé, že

$$\mathbf{U}_I \neq \mathbf{U}_J \Rightarrow \mathbf{F}_I \neq \mathbf{F}_J \tag{1.4}$$

čili rozdílné varianty martenzitu lze charakterizovat rozdílnými Bainovými maticemi bez ohledu na přidruženou rotaci.

Oblast Ω se může transformovat v různých bodech $\mathbf{x}$ do různých variant martenzitu (**Obr.1.1**). Potom je deformační gradient na této oblasti po částech spojitý a na spojitých podoblastech existuje ve silném smyslu, zatímco přes rozhraní pouze ve slabém smyslu.

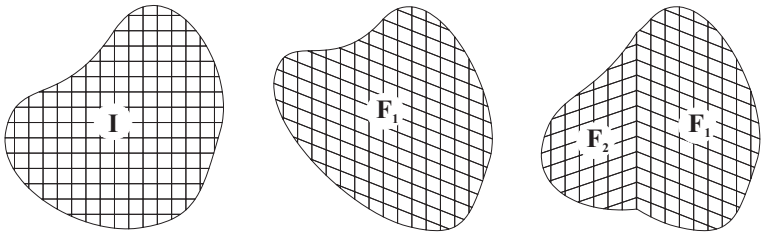

Obr. 1.1: Referneční konfigurace (a), transformující buďto do jedné varianty martenzitu (b), nebo do jejich směsi (c). Přejato z [39].

V případě, že martenzit je dále elasticky deformován, je třeba popis poněkud rozšířit. Deformační gradienty $\mathbf{F} = \nabla\mathbf{y}(\mathbf{x})$ v sobě kombinují transformační a elastické složky, které

je nutno odseparovat. Uvažujeme-li nejprve, že celá oblast Ω přechází do jediné varianty martenzitu, lze pro její deformovanou konfiguraci bez vnějšího napětí možno psát

$$\mathbf{y}_I(\mathbf{x}) = \mathbf{F}_I\mathbf{x} = \mathbf{Q}_I\mathbf{U}_I\mathbf{x}. \tag{1.5}$$

Po zahrnutí elastické deformace I-té varianty $\mathbf{z}(\mathbf{y}_I)$ je potom celkový deformační gradient roven

$$\nabla\mathbf{y}_I(\mathbf{x}) = \nabla\mathbf{z}(\mathbf{y}_I)\mathbf{Q}_I\mathbf{U}_I. \tag{1.6}$$

Vztah (1.6) lze aplikovat také na *reorientaci martenzitu*, tedy na napěťově indukovaný přechod mezi variantami. V takovém případě je

$$\nabla\mathbf{z}_{IJ}(\mathbf{y}_I) = \mathbf{F}_J\mathbf{F}_I^{-1}. \tag{1.7}$$

1.2.2 Relace grupa-podgrupa a efekt tvarové paměti

Spontánní narušení symetrie austenitcké fáze při přechodu do martenzitu může, za jistých předpokladů, vést ke vzniku takzvaného jevu tvarové paměti. Pro tento jev je nezbytné, aby grupa symetrie austenitu byla vždy podgrupou symetrie martenzitu. V takovém případě lze libovolné martenzitické variantě přiřadit zpětně právě jednu orientaci referenční konfigurace (tedy austenitu) a materiál vykazuje tvarovou paměť naznačenou na obrázku **Obr.1.2**:

- Nad kritickou teplotou je celá oblast v austenitu $\mathbf{F} = \mathbf{I}$.
- Po ochlazení přejde oblast do směsi martenzitických variant tak, že celková změna tvaru je minimální (to je tzv. akomodovaný martenzit, *self-accommodated martensite*). Každému bodu oblasti lze přisoudit konkrétní deformační gradient

  $$\mathbf{F}(\mathbf{x}) = \mathbf{F}_I. \tag{1.8}$$

  Při aplikaci vnějšího napětí dochází k reorientaci martenzitu

  $$\mathbf{F}(\mathbf{x}) = \mathbf{F}_J\mathbf{F}_I^{-1}\mathbf{F}_I, \tag{1.9}$$

  přičemž zanikají varianty nevýhodně orientované vzhledem k vnějšímu napětí. Protože martenzit nepatří ke stejné grupě symetrie jako austenit (ale k nadgrupě), mění se při takové reorientaci makroskopický tvar oblasti v deformované konfiguraci, zatímco v referenční konfiguraci zůstává nezměněn.
- Po ohřevu oblast transformuje zpět do austenitu

  $$\mathbf{F}(\mathbf{x}) = \mathbf{F}_J^{-1}\mathbf{F}_J\mathbf{F}_I^{-1}\mathbf{F}_I = \mathbf{I}. \tag{1.10}$$

  Přechodem zpět do referenční konfigurace získává vzorek svůj původní tvar, protože všechny operace související s reorientací martenzitu patří v referenční konfiguraci do grupy symetrie austenitické fáze.

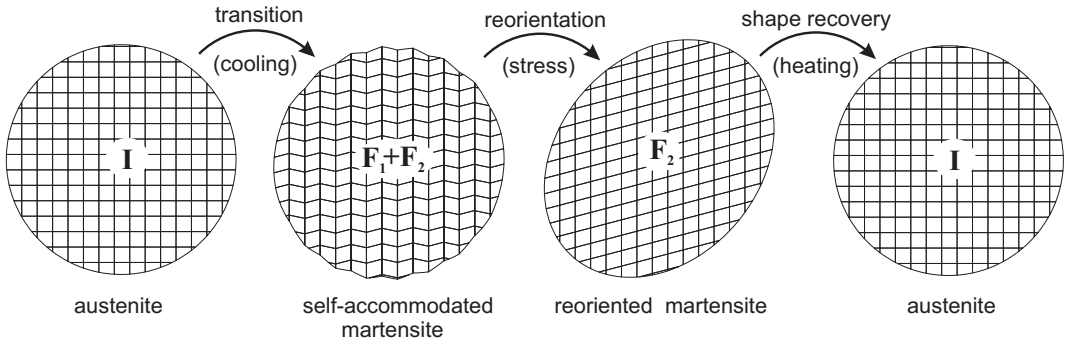

Obr. 1.2: Geometrická interpretace jevu tvarové paměti. Přejato z [39].

1.2.3 Cauchy–Bornova hypotéza

Aby bylo možno přiřadit jednotlivým strukturním fázím správné deformační gradienty, je potřeba provázat popis na úrovni kontinua s popisem na úrovni atomární mříže. Toto provázání zajišťuje takzvaná *Cauchy-Bornova hypotéza* [5]. Tato hypotéza říká, že poziční vektory generující atomární mříž dané fáze (označme je $\mathbf{i}_i$) se při přechodu do jiné fáze transformují podle tenzoru deformačního gradientu, tedy

$$\mathbf{i}_i^{\text{transformované}} = \mathbf{F}\mathbf{i}_i^{\text{referenční}}. \tag{1.11}$$

Cauchy-Bornovu hypotézu podporuje řada experimentálních pozorování (viz např. publikace uvedené v [40]). Pro termoelastické martenzitické transformace umožňuje tato hypotéza zkonstruovat Bainovy matice jednotlivých fází na základě měření atomárních pozic např. rentgenovou difrakcí. Díky tomu lze popis na úrovni kontinua získat, aniž by bylo nutné deformační gradienty pro danou slitinu skutečně makroskopicky měřit.

1.2.4 Podmínky kinematické kompatiblity

Na úrovni mechaniky kontinua je snadné formulovat podmínky, za kterých je rozhraní mezi dvěma oblastmi s homogenními deformačními gradienty koherentní a zároveň pohyblivé. Tyto podmínky se nazývají podmínkami *kinematické kompatibility* a matematicky je lze zapsat následovně [5]:

Nechť Ω_I a Ω_J jsou disjunktní podoblasti oblasti Ω takové, že Ω_I a Ω_J sousedí přes hladkou hranici s normálou $\mathbf{n}(\mathbf{x})$. Nechť $\mathbf{x}_0$ je pevný bod ležící v této hranici a $\mathbf{F}_I(\mathbf{x})$ a $\mathbf{F}_J(\mathbf{x})$ jsou deformační gradienty v infinitezimálních okolích tohoto bodu $\mathbf{x}_0$ označených $\omega_I(\mathbf{x}_0) \subset \Omega_I$ a $\omega_J(\mathbf{x}_0) \subset \Omega_J$. Hranici mezi Ω_I a Ω_J pak nazveme kinematicky kompatibilní, pokud

$$[\mathrm{cof}\mathbf{F}_I(\mathbf{x} \overrightarrow{x \in \omega_I^{\prime}} \mathbf{x}_0)]\mathbf{n}(\mathbf{x}_0) = [\mathrm{cof}\mathbf{F}_J(\mathbf{x} \overrightarrow{x \in \omega_J^{\prime}} \mathbf{x}_0)]\mathbf{n}(\mathbf{x}_0) \tag{1.12}$$

pro každé $\mathbf{x}_0 \in (\partial\overline{\Omega_I} \cap \partial\overline{\Omega_J})$, pro které tyto limity existují.

Jsou-li deformační gradienty v Ω_I a Ω_J homogenní, podmínka kinematické kompatibility se zjednodušší na

$$(\mathrm{cof}\mathbf{F}_I)\mathbf{n} = (\mathrm{cof}\mathbf{F}_J)\mathbf{n}. \tag{1.13}$$

Pro homogenní deformační gradienty má podmínka kompatiblity řadu možných jednodušších formulací, které nepožadují výpočet kofaktorů vstupujících tenzorů. Z nich jsou nejčastěji používané tyto tři:

1. **Rank-1 konektivita:** rozhraní mezi $\mathbf{F}_I$ a $\mathbf{F}_J$ je kinematicky kompatibilní pokud

$$\mathrm{rank}(\mathbf{F}_I - \mathbf{F}_J) = 1. \tag{1.14}$$

   Jádro operátoru $\ker(\mathbf{F}_I - \mathbf{F}_J)$ je potom rovno $\mathbf{n}^\perp$.

2. **Podmínka na smykový vektor:** hranice mezi $\mathbf{F}_I$ a $\mathbf{F}_J$ je kinematicky kompatibiliní přes rovinné rozhraní s normálou $\mathbf{n}$, pokud existuje takový vektor $\mathbf{a} \in \mathbb{R}^3$, že

$$\mathbf{F}_I - \mathbf{F}_J = \mathbf{a} \otimes \mathbf{n}. \tag{1.15}$$

   Tento vektor $\mathbf{a}$ je potom nazýván smykovým vektorem *smykovým vektorem*.

3. **Podmínka na invariantní rovinu :** hranice mezi $\mathbf{F}_I$ a $\mathbf{F}_J$ je kinematicky kompatibilní přes rovinné rozhraní s normálou $\mathbf{n}$, pokud

$$\mathbf{F}_I\mathbf{v} = \mathbf{F}_J\mathbf{v} \tag{1.16}$$

   pro každé $\mathbf{v} \perp \mathbf{n}$.

Tyto podmínky jsou navzájem zcela ekvivalentní a každou z nich lze snadno odvodit z (1.13). Nejčastěji je používána podmínka na smykový vektor (1.15). Ta se obvykle zapisuje ve tvaru nepoužívajícím přímo deformační gradienty $\mathbf{F}_I$, ale Bainovy matice $\mathbf{U}_I$ získané pomocí polární dekompozice:

$$\mathbf{Q}_I\mathbf{U}_I - \mathbf{Q}_J\mathbf{U}_J = \mathbf{a} \otimes \mathbf{n}. \tag{1.17}$$

Pokud tuto rovnici vynásobíme zleva $\mathbf{Q}_I^T$, dostáváme

$$\mathbf{U}_I - \mathbf{Q}'\mathbf{U}_J = \mathbf{a}' \otimes \mathbf{n}, \tag{1.18}$$

kde jsme zavedli "čárkované" veličiny jako $\mathbf{Q}' = \mathbf{Q}_I^T\mathbf{Q}_J$ a $\mathbf{a}' = \mathbf{Q}_I^T\mathbf{a}$. To nám umožňuje formulovat často používanou podmínku kinematické kompatibility pro Bainovy tenzory $\mathbf{U}_I$:

Oblasti s homogenními Bainovými tensory $\mathbf{U}_I$ a $\mathbf{U}_J$ mohou vytvářet kinematicky kompatibilní rozhraní přes rovinu s normálou $\mathbf{n}$, pokud existuje matice rotace $\mathbf{Q}'$ a nenulový vektor $\mathbf{a}'$ takový, že je splněna podmínka (1.18).

Poznamenjme ještě, že normála $\mathbf{n}$ v rovnicích (1.17) a (1.18) je stejná, protože násobení (1.17) zleva maticí $\mathbf{Q}_I^T$ ji nijak neovlivní.

Další zjednodušení podmínky kompatibility je možné vyloučením orientace rozhraní $\mathbf{n}$. Pokud Bainovy tenzory $\mathbf{U}_I$ a $\mathbf{U}_J$ reprezentují dvě různé varianty martenzitu, a tedy se navzájem liší pouze ortogonální rotací nebo jiným prvkem symetrie austenitické fáze, platí následující tvrzení [41]:

Martenzitické varianty popsané Bainovými maticemi $\mathbf{U}_I$ a $\mathbf{U}_J$ mohou vytvořit kinematicky kompatibilní rovinné rozhraní tehdy a jen tehdy, když

$$\det(\mathbf{U}_I - \mathbf{U}_J) = 0. \tag{1.19}$$

Pro Bainovy tensory, které nelze navzájem provázat takovým prvkem symetrie, tedy například pokud jeden z nich reprezentuje austenit a jeden nějakou z variant martenzitu, platí jiná, obecnější podmínka [41]:

Dvě oblasti s homogenními Bainovými tensory $\mathbf{U}_I$ a $\mathbf{U}_J$ mohou vytvořit kinematicky kompatibilní rovinné rozhraní tehdy a jen tehdy, když

$$\det({\mathbf{U}_I}^2 - {\mathbf{U}_J}^2) = 0. \tag{1.20}$$

Všehny tyto podmínky mají existenční charakter, tedy neposkytují žádný postup pro určení smykového vektoru a invariantní roviny ze vztahu (1.17). Jak ukázali Ball a James [36], smykový vektor a invariantní rovinu lze získat analýzou vlastních čísel matice

$$\mathbf{C} = {\mathbf{U}_I}^{-1}{\mathbf{U}_J}^2{\mathbf{U}_I}^{-1}. \tag{1.21}$$

Tento postup je relativně komplikovaný a jeho detaily spadají mimo rámec této práce. Nicméně jeden teoretický poznatek z [36] je natolik významný, že ho zde explicitně zmíníme:

Pokud $\mathbf{U}_I$ a $\mathbf{U}_J$ mohou vytvořit kinematicky kompatibilní rozhraní, pak existují právě dvě řešení $(\mathbf{Q'}_1, \mathbf{n}_1, \mathbf{a}'_1)$ a $(\mathbf{Q'}_2, \mathbf{n}_2, \mathbf{a}'_2)$ taková, že tuto kompatibilitu umožňují.

Tento poznatek platí pro libovolnou třídu symetrie a hraje významnou roli při klasifikaci martenzitických mikrostruktur.

1.2.5 Martenzitické mikrostruktury

Mohou-li dvě nebo více martenzitických variant vytvářet kompatibilní rozhraní, mohou vytvářet také geometricky pravidelná uspořádání, ve kterých se deformační gradient periodicky (přinejmenším ve statistickém smyslu) mění v prostoru. Taková uspořádání se nazývají *martenzitické mikrostruktury.*

Pro popis těchto mikrostruktur je viditelně nezbytné *multiškálové* rozšíření kontinuálního popisu termoelastických martenziťů, neboť zatímco na úrovni jednotlivých komponent mikrostruktury deformační gradient osciluje mezi dvěma fixními hodnotami, na hrubší prostorové škále lze materiál opět chápat jako homogenní, ovšem s efektivním deformačním gradientem $\mathbf{M}$. Je zřejmé, že tento deformační gradient lze zapsat jako

$$\mathbf{M} = \sum_{I=1}^{N} \lambda_I \mathbf{Q}_I \mathbf{U}_I, \tag{1.22}$$

kde λ_I jsou objemové zlomky jednotlivých variant v mikrostruktuře, $\mathbf{U}_I$ jsou jejich Bainovy matice a $\mathbf{Q}_I$ jsou matice rotací zajišťujících vzájemnou kinematickou kompatibilitu.

Otázkou zůstává, jestli takto zavedený deformační gradient může být chápán jako slabá derivace nějaké deformované konfigurace $\mathbf{y}$. Analýzou tohoto problému se zabývá matematická teorie martenzitických mikrostruktur založená na konceptu Youngových měr [5, 12, 37, 42, 43]. Pro účely této práce však budeme zjednodušeně chápat deformační gradient $\mathbf{M}$ jako efektivní (zprůměrovanou) slabou derivaci přes celou oblast zahrnující makroskopicky homogenní mikrostrukturu.

Sousedí-li dvě varianty martenzitu přes rovinné kinematicky kompatibilní rozhraní, označují se tyto varianty většinou termínem *dvojčata*, a rovinné rozhraní mezi nimi je potom nazýváno *rovinou dvojčatění* nebo *dvojčatovým rozhraním*.

Pro systémy dvojčatění je většinou používána následující kategorizace [44]:

- **Dvojčata typu Compound** jsou tvořena takovou dvojicí variant, že normála k rozhraní $\mathbf{n}$ stejně jako smykový vektor $\mathbf{a}$ jsou v referenční konfiguraci rovnoběžné s některým z mřížkových vektorů austenitu.

- **Dvojčata typu I** jsou tvořena takovou dvojicí variant, že pouze normála k rozhraní $\mathbf{n}$ je v referenční konfiguraci rovnoběžná s mřížkovým vektorem, zatímco smykový vektor $\mathbf{a}$ nikoliv.

- **Type-II twins** jsou tvořena takovou dvojicí variant, že pouze smykový vektor $\mathbf{a}$ je v referenční konfiguraci rovnoběžný s mřížkovým vektorem, zatímco normála k rozhraní $\mathbf{n}$ nikoliv.

- **Nekonvenční dvojčata** jsou tvořena takovou dvojicí variant, že ani normála k rozhraní $\mathbf{n}$ ani smykový vektor $\mathbf{a}$ nejsou v referenční konfiguraci rovnoběžné s žádným mřížkovým vektorem.

Každý z těchto dvojčatových systémů může být základní stavební jednotkou martenzitické mikrostruktury. Pokud jsou v mikrostruktuře obsaženy pouze dvě varianty, pak má mikrostruktura většinou formu *laminátu prvního řádu*, čili skládá se z navzájem rovnoběžných, periodicky se střídajících vrstev těchto dvou variant, navzájem propojených dvojčatovými rozhraními.

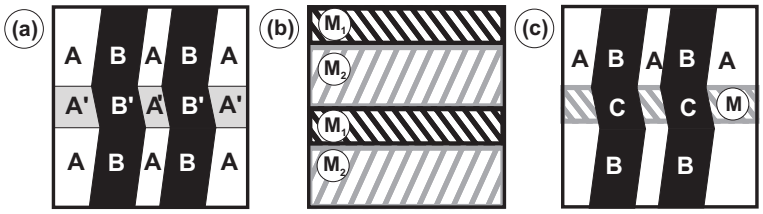

Obr. 1.3: Příklady uspořádaných martenzitických mikrostruktur vyšších řádů: (a) Dva kompatibilně se křížící lamináty prvního řádu ($A - A'$ a $A - B$). (b) Laminát druhého řádu. (c) Hierarchická struktura, skládající se z laminátu druhého řádu kompatibilně se křížícího s laminátem řádu prvního. Přejato z [39].

Takové mikrostruktury byly opakovaně experimentálně pozorovány prakticky ve všech známých termoelastických martenzitech.

Efektivní (makroskopický) deformační gradient laminátu prvního řádu složeného z vrstev variant I a J o střídajících se tloušťkách d_I a d_J lze zapsat jako

$$\mathbf{M} = \frac{d_I}{d_I + d_J}\mathbf{F}_I + \frac{d_J}{d_I + d_J}\mathbf{F}_J = \lambda\mathbf{F}_I + (1-\lambda)\mathbf{F}_J, \tag{1.23}$$

kde $\lambda = d_I/(d_I + d_J)$ je objemový zlomek varianty I v laminátu. Taková mikrostruktura je viditelně plně kinematicky kompatibilní pro libovolné λ.

Stejným algoritmem, jakým byl z jednotlivých martenzitických variant vytvořen laminát prvního řádu, lze z dvojice laminátů prvního řádu vytvořit laminát řádu druhého (**Obr.1.3**(b)) nebo mikrostrukturu složenou ze dvou vzájemně se kompatibilně křížících laminátů prvního řádu (**Obr.1.3**(a)). Opakováním této operace pak získáváme složité, hierarchicky uspořádané mikrostruktury **Obr.1.3**(c), jejichž popis pomocí klasické krystalografie by byl téměř nemožný – na úrovni mechaniky kontinua je však dále možno používat koncept deformačních gradientů a přenést výše uvedenou kategorizaci rovněž na makro-dvojčatová rozhraní a na rozhraní mezi lamináty vyšších řádů. To ukazuje, jak efektivní je využití Cauchy-Bornovy hypotézy pro teoretický popis termoelastických martenzitů.

1.3 Základy termodynamiky termoelastických martenzitů

Uvažujme nyní polymorfní materiál schopný existovat ve dvou různých strukturních fázích, přičemž za daných vnějších podmínek (teplota, mechanické napětí, magnetické pole) zaujímá tento materiál vždy tu konfiguraci, která je energeticky výhodnější. Za nulového vnějšího zatížení a bez vnějšího magnetického pole existuje teplota, při které jsou si energie (tj. vhodné termodynamické potenciály) obou fází rovny, tuto teplotu nazveme *transformační teplotou* nebo *kritickou teplotou*.

Při nulovém vnějším zatížení je vhodným termodynamickým potenciálem pro popis chování termoelastických martenzitů *hustota Helmholtzovy volná energie* $\mathcal{F}$. Pro tuto energii musí platit pro každou fázi stabilní za dané teploty T podmínky stablity

$$\mathrm{d}\mathcal{F}(T, e_{ij}) = 0 \qquad \text{a} \qquad \mathrm{d}^2\mathcal{F}(T, e_{ij}) > 0. \tag{1.24}$$

Z toho vyplývá, že v blízkosti transformační teploty musí volná energie mít více než jedno minimum. Jedno odpovídá austenitu ($e_{ij} = 0$), a další martenzitckým variantám ($e_{ij} = e^{\mathrm{tr}}_{ij}$, kde e^{tr}_{ij} značí takzvaný *transformační strain*[1]). Takto nekonvexní hustota energie se v anglické terminologii označuje termínem *multi-well*. V češtině ekvivalentní termín není, jako jeho náhradu lze používat např. termín *multikonvexní*, naznačující, že hustota energie má v jedné ze svých proměnných více navzájem disjunktních konvexních oblastí.

Na dané teplotě T_0 pak o transformaci bez vnějšího zatížení rozhoduje, zda

$$\mathcal{F}(T_0, 0) > \mathcal{F}(T_0, e^{\mathrm{tr}}_{ij}), \qquad \text{nebo} \qquad \mathcal{F}(T_0, 0) = \mathcal{F}(T_0, e^{\mathrm{tr}}_{ij}), \qquad \text{nebo} \qquad \mathcal{F}(T_0, 0) < \mathcal{F}(T_0, e^{\mathrm{tr}}_{ij}), \tag{1.25}$$

čili rozhoduje hloubka jednotlivých minim hustoty energie.

V případě napěťově indukovaných transformací v termoelastických martenzitech a slitinách s tvarovou pamětí [45–49] je často vhodnější použít hustotu Gibbsovy volné energie $\mathcal{G}$,

$$\mathcal{G}(T, \Sigma_{ij}) = \mathcal{F} - \sigma_{ij} e_{ij}, \tag{1.26}$$

což je Legendrova transformace $\mathcal{F}$. Poté lze psát obdobné podmínky pro kritickou vnucenou deformaci, například

$$\mathcal{G}(T_0, C^A_{ijkl} e_{kl}) > \mathcal{G}(T_0, C^M_{ijkl}(e_{kl} - e^{\mathrm{tr}}_{kl})), \qquad \text{nebo} \qquad \mathcal{G}(T_0, C^A_{ijkl} e_{kl}) = \mathcal{G}(T_0, C^M_{ijkl}(e_{kl} - e^{\mathrm{tr}}_{kl})),$$
$$\text{nebo} \qquad \mathcal{G}(T_0, C^A_{ijkl} e_{kl}) < \mathcal{G}(T_0, C^M_{ijkl}(e_{kl} - e^{\mathrm{tr}}_{kl})), \tag{1.27}$$

kde C^A_{ijkl} a C^M_{ijkl} jsou tenzory elastických konstant austenitu a martenzitu. V případě kombinovaného (teplotního i mechanického) namáhání, lze použít oba výše zmíněné potenciály; porovnání obou postupů leze nalézt např. v [13]. Ve většině prací týkajících se termoelastických martenzitů na úrovni monokrystalu však převažuje popis pomocí Helmoltzovy volné energie [36, 37, 43],

Jako transformace prvního druhu je termoelastická martenzitická transformace spojena se skokovou změnou entropie. Pomocí Helmoltzovy volné energie je entropie vyjádřitelná jako

$$S(T, e_{ij}) = -\left(\frac{\partial \mathcal{F}}{\partial T}\right)_{e_{ij}}. \tag{1.28}$$

[1] Bohužel zde neexistuje vhodný ekvivalent v české terminologii - správný překlad, *transformační přetvoření*, se v komunitě zabývající se funkčními materiály nepoužívá.

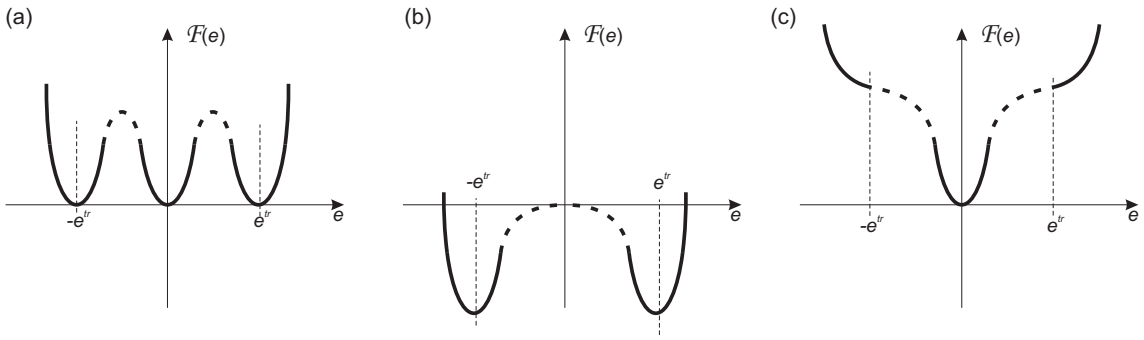

Obr. 1.4: Jednodimenzionální model chování termoelastických martenzitů: (a) na kritické teplotě, kde mají všechny potenciálové jámy stejnou hloubku, (b) pod teplotou T_M, (c) nad teplotou T_A. Přejato z [39].

Pokud tedy předpokládáme, že v blízkosti transformační teploty se s klesající teplotou začíná preferovat martenzit, tedy klesá energie příslušející martenzitickému minimu, dochází při transformaci k produkci entropie

$$S(T,0) - S(T, e_{ij}^{\mathrm{tr}}) > 0. \tag{1.29}$$

Koncept multikonvexní volné energie může být využit ke konstrukcím jednoduchých (většinou jednodimenzionálních) modelů chování termoelastických martenzitů. Takové modely jsou v literatuře často využívány k ilustraci základních vlastností těchto materiálů [5, 25, 40, 50, 51] nebo kinematiky fázových přechodů [52–57].

Všechny tyto modely vycházejí z předpokladu, že v jisté blízkosti transformační teploty jsou na křivce volné energie přítomna minima odpovídající oběma fázím, zatímco dále pod transformační teplotou se martenzitická minima stávají dominantními a austenitické minimum zcela zaniká, a obráceně, jak je naznačeno na obrázku **Obr.1.4**.

Takovéto jednoduché modely modou částenčně vysvětlit řadu experimentálně pozorovaných jevů, jako je například vznik jemných zdvojčatělých struktur při transformaci z austenitu do martenzitu, nebo teplotní hysterezi, jak je naznačeno na obrázku **1.5**: Předpokládejme, že na transformační teplotě, kde jsou minima příslušející oběma fázím stejně hluboká, nemůže k transformaci dojít, protože je mezi minimy příliš vysoká bariéra, kterou systém nedokáže překonat pomocí tepelných fluktuací [52, 53]. S dalším snižováním teploty minimum odpovídající austenitu zaniká a s tímto zánikem se snižují i bariéry. Na nějaké teplotě, označme ji T_M (**Obr.1.5**(a)), bariéra zaniká nebo ji již systém je schopen překonat a může přecházet do martenzitckých minim. Z důvodu symetrie však jednotlivé body materiálu přecházejí do různých martenzitických minim, čili vzniká jemná struktura s výsledným nulovým efektivním transformačním strainem. Tato mikrostruktura pak při ohřevu zůstává stabilní tak dlouho, dokud se dominantním minimem nestane minimum příslušející austenitu a bariéry bránící materiálu v návratu do tohoto minima nejsou překonatelné nebo nezaniknou. Takovou teplotu označíme T_A (**Obr.1.5**(b)). V důsledku toho

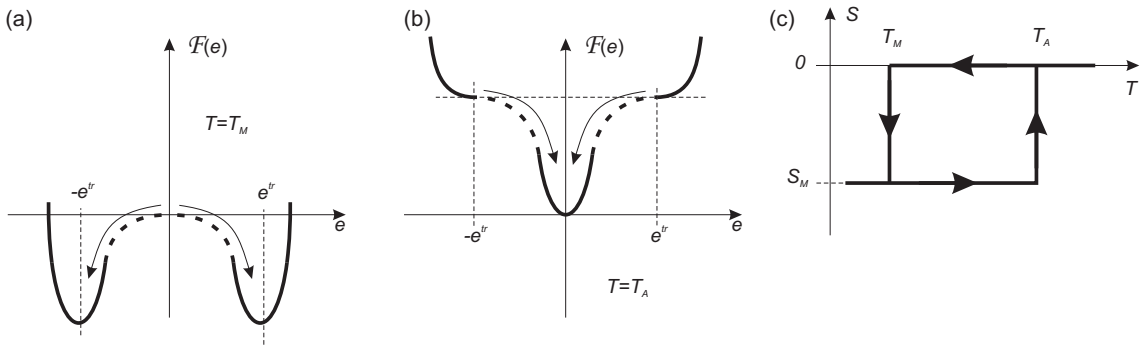

Obr. 1.5: Teplotní hystereze v jednodimenzionálním modelu. (a) Vznik zdvojčatělé struktury na teplotě T_M, (b) návrat do austenitu na teplotě T_A, (c) výsledná hysterezní smyčka. Přejato z [39].

se materiál chová hysterezně a vykazuje jistý rozsah teplot, při kterých může existovat v obou strukturních fázích.

Ve skutečných monokrystalech termoelastických martenzitů však transformace při teplotním cyklu probíhají podstatně složitějším způsobem, než jak naznačuje výše uvedený jednodimenzionální model. Především k transformaci nedochází na konkrétní teplotě, ale v celém teplotním intervalu. Díky formování mikrostruktur a jejich pohybu vzniká v materiálu nehomogenní pole elastických napjatostí a na nukleaci a růst nových fází jsou kladena další geometrická omezení. V důsledku toho a v důsledku přítomnosti defektů a jiných nehomogenit v krystalech lze každému materiálu přisoudit čtveřici transformačních teplot [4, 5]:

- **Martensite start** (M_s) - teplota, při které se při chlazení v austenitu objevují první zárodky martenzitu.
- **Martensite finish**(M_f) - teplota, při které při chlazení v martenzitu zanikají oblasti austenitické fáze.
- **Austenite start**(A_s) - teplota, při které se při ohřevu objevují první oblasti austenitické fáze.
- **Austenite finish**(A_f) - teplota, při které při ohřevu zanikají poslední částice martenzitu.

Vztáhenme-li tyto teploty k teplotám odpovídajícím zániku austenitických a martenzitických minim a bariér mezi nimi, musí zjevně platit

$$T_M \leq M_f \leq M_s \leq T_c \leq A_s \leq A_f \leq T_A, \tag{1.30}$$

kde T_c je kritická teplota, při které jsou hloubky minim navzájem rovné.

Samotná hystereze je pak u skutečných krystalů termoelastických martenzitů úzce spjata s disipací energie, formováním mikrostruktur a jejich pohybem. Aby bylo možno termodynamiku těchto materiálů rozšířit právě o tyto efekty, je potřeba studovat do detailů morfologii,

mechanismy růstu a pohybu a pohyblivost mikrostruktur. Příklady takových analýz jsou uvedeny v následujících třech kapitolách ve formách komentovaných souborů článků.

Kapitola 2

Rozhraňové mikrostruktury ve slitině CuAlNi

Slitina CuAlNi je slitinou s tvarovou pamětí vykazující čistě termoelastickou martenzitickou transformaci mezi kubickou austenitickou fází a ortorhombickou fází 2H martenzitu. (Označení 2H plyne z toho, že martenzitická struktura vykazuje pravidelnou modulaci na hexagonálních rovinách s periodou dvou meziatomárních vzdáleností. Díky symetričnosti této modulační sekvence je martenzit efektivně ortorhombický.)

Díky snadné přípravě a dobře definovaným vlastnostem je CuAlNi jednou z teoreticky nejstudovanějších slitin v literatuře. Díky tomu jsou podrobně známy Bainovy matice, dvojčatové systémy a související smykové vektory. V CuAlNi mohou existovat tři dvojčatové systémy: Compound, Typ 1 a Typ 2. Zatímco pro dvojčata Typu 1 a 2 mohou vytvořit jemné lamináty prvního řádu kinematicky kompatibilní s austenitem (tedy schopné vytvořit takzvanou *rovinu habitu*), žádný laminát dvojčat typu Compound toho schopen není, stejně jako toho není schopna monovarianta 2H martenzitu. Proto v této slitině musí každá fázová transformace probíhat mezi austenitem a jemným laminátem Typu 1 nebo 2.

Díky nemožnosti tvorby kinematicky kompatibilního rozhraní mezi austenitem a monovaraintou martenzitu dochází ve slitině CuAlNi snadno k takzvanému efektu *mechanické stabilizace*. Tento efekt je schématicky naznačen na obrázku **Obr.2.1**:

(a) Při čistě teplotně řízeném transformačním cyklu se austenit při ochlazení transformuje na zdvojčatělý martenzit, který je tvořen jemnými lamináty prvního řádu dvojčat Typu 1 nebo 2. Tento laminát je schopen vytvářet kompatibilní rozhraní s austenitem. Proto se při ohřevu mohou znovu vytvořit kompatibilní rozhraní a zdvojčatělý martenzit se transformuje do austenitu bez nutnosti změn v mikrostruktuře. Výsledkem je relativně malá teplotní hystereze.

(b) Pokud však je po transformaci martenzit reorientován vnějším mechanickým zatížením, takže vzniká monovariana, je martenzit mechanicky stabilizován - monovarianta nemůže vytvořit kinematicky kompatibilní rozhraní s austenitem, a proto musí vzniknout tzv. *rozhraňová mikrostruktura*, která umožňuje navázat monovaraintu martenzitu kinematicky kompatibilně na zárodky austenitu. Vznik této mikrostruktury i její následovný pohyb

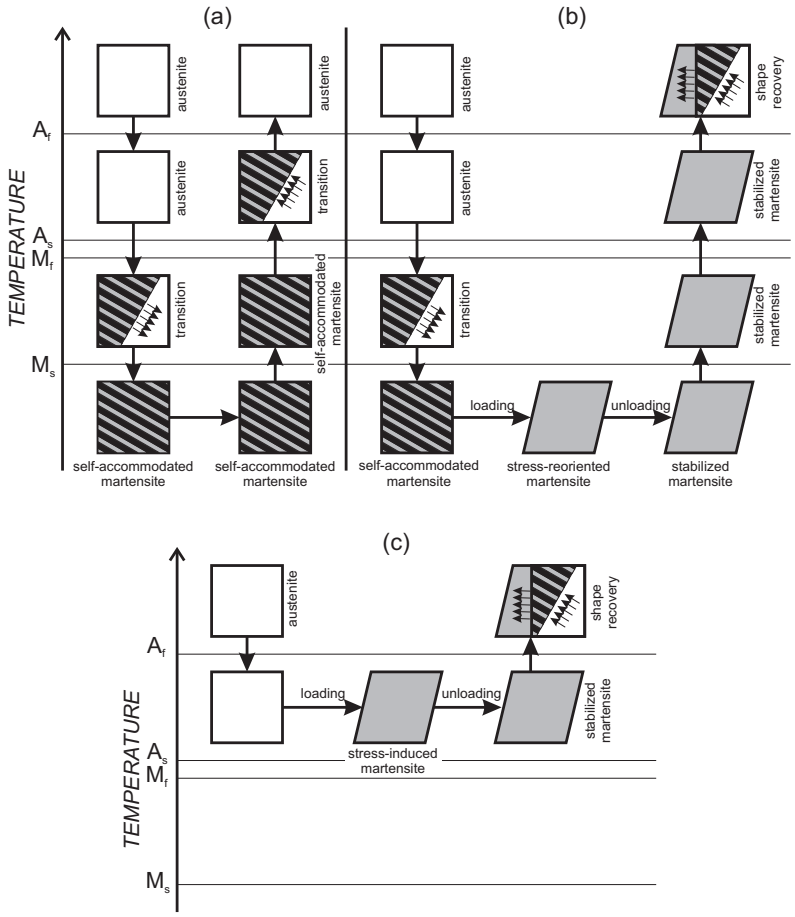

Obr. 2.1: Mechanická stabilizace martenzitu ve slitině CuAlNi: (a) čistě tepelný cyklus bez mechanické stabilizace; (b) mechanická stabilizace reorientací tepelně indukovaného martenzitu; (c) mechanická stabilizace napěťově indukovaného martenzitu. Přejato z [23].

krystalem jsou energeticky velmi náročné, to výrazně zvyšuje nukleační bariéru a posouvá transformační teploty vzhůru.

(b) Stejný efekt lze pozorovat i v případě, že monovarianta martenzitu byla vytvořena mechanickým zatížením austenitické fáze pod teplou A_f a zároveň proběhla transformace v celém objemu krystalu, tedy materiál po odlehčené neobsahuje zárodky austenitu. Opět dochází k posuvu transformačních teplot vzhůru v důsledku nezbytnosti vzniku rozhraňových mikrostruktur.

V následujících čtyřech publikacích jsou diskutovány různé aspekty rozhraňových mikrostruktur v monokrystalech CuAlNi. Nejprve je provedena analýza kinematické kompatibility dvou nejčastěji pozorovaných morfologií, konkrétně takzvaných rozhraní typu X a λ v podkapitolách 2.1 a 2.2, v každé z nich je navíc energie elastické napjatosti nezbytné pro vytvoření dané mikrostruktury vypočtena metodou konečných prvků. V podkapitole 2.3 je zdokumen-

továno experimentální pozorování složitějšího typu rozhraňové mikrostruktury zahrnujícího takzvaná neklasická rozhraní. V podkapitole 2.4 je potom řešena otázka nukleace martenzitu v mechanicky stabilizovaném martenzitu.

2.1 Publikace *Rozhraňové mikrostruktury v martenzitických transformacích: od optických pozorování k matematickému modelování.*

Bibliografická citace: Seiner, H., Glatz, O., Landa, M. Interfacial microstructures in martensitic transitions: From optical observations to mathematical modeling (2009) International Journal for Multiscale Computational Engineering, 7 (5), pp. 445-456.

Stručná anotace: V této publikaci je analyzována rozhraňová mikrostruktura typu X tvořená dvojicí rovin habitu a dvojicí dvojčatových rozhraní. Je popsána experimentální procedura přípravy těchto rozhraní a jejich pozorování optickou mikroskopií. Následně je konstruován konečněprvkový model mikrostruktury za účelem nalezení rozložení elastické napjatosti v mikrostruktuře a vyčíslení související hodnoty elastické energie. Je ukázáno, že mikrostruktura typu X není ani lokálním minimalizátorem energie ve smyslu klasické teorie martenzitických mikrostruktur [38] a její vznik tedy musí být řízen kinematikou a disipačními procesy.

Příspěvek habilitanta: Veškeré experimentální výsledky prezentované v publikaci byly získány habilitantem, který rovněž provedl analýzu kompatibility mikrostruktury a výpočet elasticity zdvojčatělé struktury pomocí homogenizačního schématu. Konečněprvkové výpočty byly provedeny studentem Ondřejem Glatzem v rámci jeho diplomové práce vedené habilitantem, použité elastické konstanty jednotlivých fází byly získány ve spolupráci s M. Landou.

International Journal for Multiscale Computational Engineering, 7(5)445–456(2009)

Interfacial Microstructures in Martensitic Transitions: From Optical Observations to Mathematical Modeling

Hanuš Seiner,[1,2]* *Ondřej Glatz,*[1,2] & *Michal Landa*[1]

[1]*Institute of Thermomechanics, Academy of Sciences of the Czech Republic, 18 200 Prague 8, Czech Republic*

[2]*Faculty of Nuclear Sciences and Physical Engineering, Czech Technical University in Prague, 120 00 Prague 2, Czech Republic*

ABSTRACT

We present a construction of a mathematical model of an interfacial microstructure (i.e., microstructure forming at the phase interface between austenite and martensite) in a single crystal of Cu-Al-Ni shape memory alloy. In the first part of the article, the experiment is briefly outlined and the compatibility of the experimentally observed microstructures is analyzed, showing that the observed X-interfaces cannot be compatible without the presence of elastic strains. Then, the elastic strains in the microstructure are evaluated by finite element method, whereby the elastic coefficients of finely microstructured regions are obtained by homogenization. The significant influence of the choice of the geometry on the numerical results is shown and discussed.

KEYWORDS

martensitic transition, shape memory alloys, X-interface, Cu-Al-Ni

*Address all correspondence to hseiner@it.cas.cz.

1543-1649/09/$35.00

1. INTRODUCTION

All the unique thermomechanical properties of shape memory alloys (SMAs), such as the shape memory effect, superelasticity, or pseudoplasticity, are commonly known to result from reversible martensitic transitions taking place in these materials under proper mechanical and/or thermal loading [1]. Similarly, most of these effects would be impossible without the ability of the low-temperature (martensitic) phases of SMAs to form geometrically ordered mixtures of different variants, i.e., of martensites rotated variously with respect to the parent (high-temperature, austenitic) crystal lattice. These mixtures are usually called *martensitic microstructures* [2], and their existence is enabled by reversible twinning of martensite (we will refer to them further in text as *twinned structures* or simply *twins*). According to the theory developed by Ball and James (see [3, 4]), the observed domain Ω of an SMA single crystal always forms such microstructure that the entire free energy

$$\Phi = \int_{\Omega} \varphi(\nabla \mathbf{y}(\mathbf{x}), T) \mathrm{d}V \tag{1}$$

is minimal for given boundary conditions at $\partial\Omega$. Here, $\mathbf{x}$ denotes the reference configuration (which is usually chosen identically with the unrotated austenite phase), $\mathbf{y}$ is the deformed configuration, T is temperature, and φ is the multiwell free-energy density. In a stress-free state, this energy density has equivalently deep minima in the deformation gradients $\nabla \mathbf{y}(\mathbf{x})$, corresponding to all particular variants of martensite, and one minimum in $\nabla \mathbf{y}(\mathbf{x}) \in \mathrm{SO}(3)$ (i.e., for austenite), which can be either deeper (at T higher than some critical temperature) or have the same or lower depth than the martensitic wells (at the critical temperature and below it). For most of the boundary conditions, the minimizer of (1) cannot be directly obtained, but the minimum (or infimum) can be approached by construction of minimizing sequences, which is an equivalent of fine microstructuring in the real material (for more details, see, e.g., [5]). The most usually observed homogeneous microstructure (the first-order laminate consisting of two variants of martensite forming parallel lamina of alternate thicknesses) corresponds to the simplest possible minimizing sequence for a wide range of boundary conditions [6].

The concept of microstructures as minimizing sequences of (1) has successfully explained many features observed in real single crystals of SMAs–above all, the formation of fine laminates at planar austenite-to-martensite interfaces, called *habit planes*. There are, however, few cases where this theory is not able to predict exactly what microstructure will form and how it will develop in time under given external mechanic and thermal loadings. Or, in other words, under some special mechanic and thermal loadings, microstructures can develop that do not minimize (1) for prescribed boundary conditions. An apparent example of such a case is the shape recovery process (i.e., the thermally induced transition from a mechanically stabilized martensite [7] to austenite) of Cu-Al-Ni single crystals, recently reported in [8]. In this case, the transition front has a form of the so-called X-interface (microstructure first documented in the In-Th alloy by Basinski and Christian [9]). As shown by Ruddock [10] for the In-Th system (and as it will be shown for Cu-Al-Ni in this article), this microstructure cannot achieve compatibility without elastic strains and thus cannot be an energy minimizer of (1) at the transition temperature for the free boundary conditions. However, the X-interfaces observed by the authors of [8] in Cu-Al-Ni were pretty stable in a whole range of temperatures and did not exhibit any tendency to get rebuilt into true energy minimizers. A similar situation appears for so-called wedge microstructures often observed during thermally induced transitions from austenite to self-accommodated martensite. In [11], the authors have given a detailed analysis of this microstructure, showing again that the compatibility can be attained only by the presence of elastic strains.

This article aims to discuss the X-interfaces in Cu-Al-Ni single crystals reported in [8], with a focus on determination of the elastic strain fields enabling such microstructure to achieve compatibility. This includes a detailed analysis of the experimentally observed microstructures, construction of a numerical model such that it copies the real geometry in an optimal way (although some simplifications are necessary), and solution of the resulting elasticity problem. In general, the mathematical modeling of martensitic microstructure is always a strongly multiscale problem [12], as the deformed configuration $\mathbf{y}$ can be always decomposed as follows:

$$\mathbf{y}(\mathbf{x}) = (\mathbf{y}_{\mathrm{elast}} \circ \mathbf{y}_{\mathrm{trans}})(\mathbf{x}) \tag{2}$$

where the elastic strains (given by mapping $\mathbf{y}_{\mathrm{elast}}$) are incomparably smaller than the transformation strains (mapping $\mathbf{y}_{\mathrm{trans}}$), i.e., strains given by the martensitic transition itself. In this article (analogously to [11]), we suppress the multiscale character of this problem by taking the mapping $\mathbf{y}_{\mathrm{trans}}$ directly from the experimental observations, instead of from the condition of minimality of (1). Then, the strain fields are determined as minimizers of (1) for given $\mathbf{y}_{\mathrm{trans}}$. Such an optimization problem is incomparably simpler than the solution of models capturing fully the constitutive behavior of the material [13–16]. On the other hand, the multiscale character cannot be fully avoided, as the analyzed microstructures include different length scales: They consist of finely twinned regions, which must be homogenized (both in their deformation gradients $\nabla\mathbf{y}_{\mathrm{trans}}$ and in their elastic properties) prior to their own numerical treatments.

2. EXPERIMENT

2.1 Examined Material

The Cu-Al-Ni alloy used in the experiments reported in [8] and in this article is a shape memory alloy undergoing a cubic-to-orthorhombic transition (for more details, see, e.g., [17], and the extensive list of references therein; for a comprehensice summary of microstructures forming in single crystals of this alloy, see [18]). For this kind of transition, the austenite phase can transform into six different variants of martensite. We will denote these variants in this article by arabic numbers 1 to 6, and use the same numbering as in [19], where, also, the Bain matrices $\mathbf{U}_{1,\ldots,6}$ for these variants can be found. As none of these variants can form a compatible interface with austenite (i.e., the compatibility equation [3, 4])

$$\mathrm{rank}\,(\mathbf{Q}\mathbf{U}_i - \mathbf{I}) = 1 \tag{3}$$

cannot be fulfilled for any i and any $\mathbf{Q} \in \mathrm{SO}(3)$), all the phase interfaces in this alloy can exist only between austenite and a twinned structure of martensite. According to [2], the martensitic phase of this alloy can form twins in three different twinning systems. These are the *compound twins*, where the twinning plane is a plane of mirror symmetry between the two involved variants, and *type I* and *type II twins*, where it is not. Another difference between these twinning systems is that whereas the fine laminates of type I and type II twins can form compatible interfaces with austenite (i.e., there exist matrices $\mathbf{Q}_A \in \mathrm{SO}(3)$ and $\mathbf{Q}_B \in \mathrm{SO}(3)$ and a scalar parameter λ such that

$$\mathrm{rank}\,(\lambda\mathbf{Q}_A\mathbf{U}_A + (1-\lambda)\mathbf{Q}_B\mathbf{U}_B - \mathbf{I}) = 1 \tag{4}$$

where A and B is a pair of variants able to form type I or type II twins), the laminates of compound twins cannot. For this reason, any transition from a single variant of martensite into austenite cannot proceed without formation of laminates of type I or type II twins at the transition front, i.e., without formation of the so-called *interfacial microstructures* (see [8] for a more exact definition).

For completeness, we will list here also the transition temperatures as determined for the examined material by DSC measurements: The martensite start temperature was $M_S = -5^\circ\mathrm{C}$, the martensite finish temperature was $M_F = -22^\circ\mathrm{C}$, the austenite start temperature was $A_S = 26^\circ\mathrm{C}$, and the austenite finish temperature was $A_F = 52^\circ\mathrm{C}$.

2.2 Experimental Procedure

The X-interfaces in Cu-Al-Ni single crystals were prepared by the following experimental procedure (for more details, see [8]). A specimen (15 mm long and 5×5 mm thick prismatic bar of single crystal of austenite oriented along the $[001]$ direction) was uniaxially compressed until it transformed into mechanically stabilized 2H martensite. Due to the mechanical stabilization (i.e., the inability of the obtained martensite to form directly compatible interfaces with austenite), the specimen did not return to austenite after the loading was removed, but remained in martensite even when it was heated over the A_S temperature. The obtained martensitic bar was a single variant of martensite including a negligible (less than 5%) volume fraction of another variant in the form of thin plates running through the specimen and forming compound twins with the major variant. In one corner of the specimen, a small nucleus of the austenite phase was induced by strong localized heating (using a gas lighter). Then, the whole specimen was heated by being immersed into a warm (60°C) water bath, which induced a growth of austenite from the nucleus. As soon as the transition front reached approximately the middle of the specimen, the specimen was removed from

the bath and cleaned and was cooled down by ethyl alcohol. The formed microstructure (stable at room temperature) was observed by optical microscopy.

Repeatedly, the transition front was arranged as shown in Fig. 1, forming the so-called X-interface, consisting of two mutually intersecting habit planes separating austenite from twinned regions of martensite and another pair of mutually intersecting interfaces separating these twinned regions from the original stabilized martensite. The interfaces between the twinned regions and the original stabilized martensite were parallel (or very close to parallel) to the twinning planes seen inside the twinned regions. The whole X-interface was mirror symmetric about the $(1\bar{1}0)$ plane in austenite.

2.3 Compatibility Analysis

Schematically, the geometry of the X-interface is sketched in Fig. 2. For simplicity, we will assume the stabilized martensite to be a single variant.[1] Under such an assumption, the microstructure consists of austenite and three variants of martensite only (denoted A, B, and C in Fig. 2). To analyze the compatibility, the particular variants of martensite and twinning systems appearing in the microstructure were identified. Optical micrographs of all faces of the specimen were taken, and the angles between the habit planes, twinning planes, and the edges of the specimen were measured. A script written in MATLAB was used to compute orientations of habit planes and twinning planes of all possible combinations of variants able to form X-interfaces, and to find which of these combinations fits the optical micrographs optimally. By this script, the twinning systems observed in the microstructure were identified as type II twinning planes of 2H martensite. The involved variants identified by this script were no. 4 and no. 6, forming one type II laminate, and no. 2 and no. 6, forming the second one. This induced that the stabilized martensite (i.e., the variant involved in both laminates) must be no. 6, which was verified by X-ray measurements (Laue method).

[1] As shown in [8] by a numerical example, the negligible amount of compound twins in the real specimen does not have any measurable effect on the orientation of the habit planes, etc.

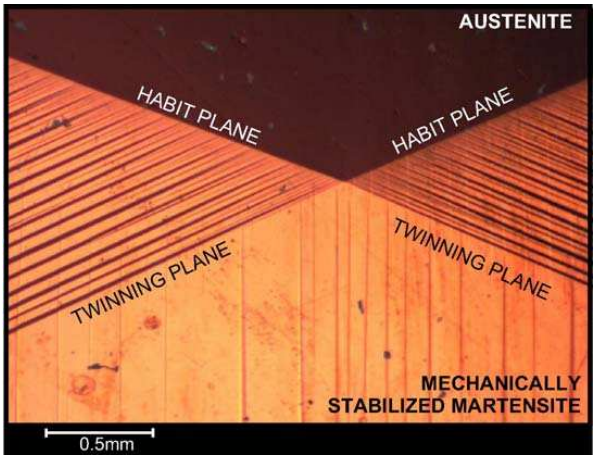

FIGURE 1. Optical micrograph of the X-interface in Cu-Al-Ni

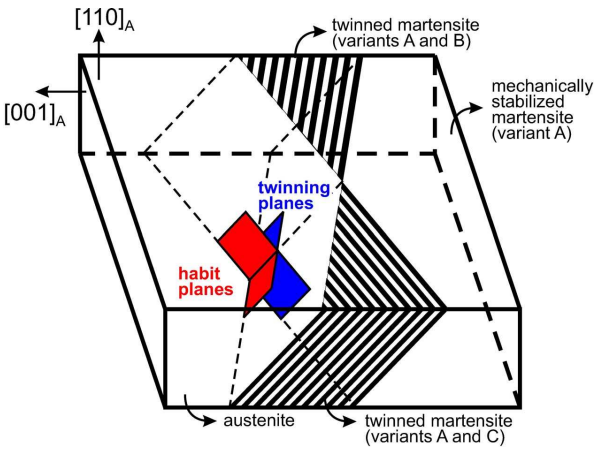

FIGURE 2. Geometry of the X-interfaces observed in Cu-Al-Ni single crystals

For general analysis of the compatibility of the microstructure, we will return to the notation introduced in Fig. 2 (now $A \sim$ no. 6, $B \sim$ no. 4, and $C \sim$ no. 2). The variants A and B form a laminate of type II twins, which borders on the austenite over a habit plane (let us denote a normal vector to this plane by $\mathbf{n}$) and pure variant A over the A-B type II twinning plane. Similarly, variant A forms a type II laminate with variant C, and this laminate borders over another habit plane (normal vector orientation $\hat{\mathbf{n}}$) on the austenite, and over the A-C type II twin-

ning plane on pure variant A. For $\mathbf{U}_A$, $\mathbf{U}_B$, and $\mathbf{U}_C$ being the Bain tensors of particular variants $\mathbf{b}$ and $\hat{\mathbf{b}}$ being the shearing vectors corresponding to transitions at habit planes with normals $\mathbf{n}$ and $\hat{\mathbf{n}}$, and λ and $\hat{\lambda}$ being the volume fractions of variant A in the two considered laminates, we can write the compatibility equations at both habit planes as

$$\mathbf{I} - (\lambda \mathbf{Q}_A \mathbf{U}_A + (1-\lambda)\mathbf{Q}_B \mathbf{U}_B) = \mathbf{b} \otimes \mathbf{n} \quad (5)$$

$$\mathbf{I} - \left(\hat{\lambda} \hat{\mathbf{Q}}_A \mathbf{U}_A + (1-\hat{\lambda})\mathbf{Q}_C \mathbf{U}_C\right) = \hat{\mathbf{b}} \otimes \hat{\mathbf{n}} \quad (6)$$

where $\mathbf{Q}_A$, $\mathbf{Q}_B$, $\hat{\mathbf{Q}}_A$, and $\mathbf{Q}_C$ are rotations between austenite and particular variants of martensite involved in the microstructure. Simultaneously, the compatibility conditions must be fulfilled at the type II twinning planes, i.e., there must exist such shearing vectors $\mathbf{a}$ and $\hat{\mathbf{a}}$ such that

$$\mathbf{Q}_A \mathbf{U}_A - \mathbf{Q}_B \mathbf{U}_B = \mathbf{a} \otimes \mathbf{m} \quad (7)$$

$$\hat{\mathbf{Q}}_A \mathbf{U}_A - \mathbf{Q}_C \mathbf{U}_C = \hat{\mathbf{a}} \otimes \hat{\mathbf{m}} \quad (8)$$

where $\mathbf{m}$ and $\hat{\mathbf{m}}$ are unit normals to the A–B and A–C twinning planes.

Two general conditions can be formulated, under which the whole microstructure is compatible without elastic strains. The first condition is that the pure variant A in the stabilized region must be rotated with respect to austenite equivalently as in the laminates since it borders an the variants B and C over the A–B and B–C twinning planes. This directly induces that $\hat{\mathbf{Q}}_A = \mathbf{Q}_A$. However, as it can be easily checked numerically, this condition is not satisfied for our material. For the lattice parameters taken from [18], we can calculate the difference between these two rotations $\hat{\mathbf{Q}}_A^{-1}\mathbf{Q}_A = \hat{\mathbf{Q}}_A^{\mathrm{T}}\mathbf{Q}_A$ (the all rotation matrices in (5) and (6) as well as the volume fractions can be obtained by algorithms described in [3, 4]). In a quaternion representation, the difference $\hat{\mathbf{Q}}_A^{\mathrm{T}}\mathbf{Q}_A$ equals a rotation by 6.6° around a direction close to $[77\bar{3}]$ in austenite.

The second condition is that the habit planes and the twinned-to-detwinned interfaces must intersect in the same line, i.e.,

$$(\mathbf{n} \times \hat{\mathbf{n}}) \| (\mathbf{m} \times \hat{\mathbf{m}}) \quad (9)$$

(providing that the twinned-to-detwinned interfaces are exactly equal to the twinning planes). Again, this condition cannot be fulfilled for the examined Cu-Al-Ni alloy. The difference between $\mathbf{n} \times \hat{\mathbf{n}}$ and $\mathbf{m} \times \hat{\mathbf{m}}$ determined numerically for the lattice parameters taken from [18] is 2.2°. The incompatibility of the X-interface can be also illustrated by the difference between vectors $\mathbf{m} \times \mathbf{n}$ and $\hat{\mathbf{m}} \times \hat{\mathbf{n}}$, which is, for the same lattice parameters, equal to 7.2°.

If the twinned-to-detwinned interfaces are declined from the orientation of the corresponding type II twinning planes, condition (9) can be fulfilled, but in such case, the presence of elastic strains is necessary to ensure compatibility along the twinned-to-detwinned interfaces.

3. MATHEMATICAL MODELING

The revealed difference from compatibility must be compensated by the presence of elastic strains. In this section, we will try to determine these strain fields by the finite element method (FEM). Unlike in most FEM models of SMAs [20, 21], the elements used in this case do not have to incorporate the constitutive behavior of the material, and thus common FEM solvers can be used.

3.1 Simplified Geometry Used in the Model

As mentioned in the introduction, the FEM model of the interfacial microstructure cannot be constructed for exactly the geometry obtained from the experiments, and some simplifications are necessary. The reason is that the difference between $\mathbf{n} \times \hat{\mathbf{n}}$ and $\mathbf{m} \times \hat{\mathbf{m}}$ (i.e., between the intersection of the habit planes and the type II twinning planes) is comparable to the accuracy with which the real angles from the optical micrographs are determined, so the exact orientation of the crossing line is unknown. Moreover, there is no physical justification for the assumption that the twinned-to-detwinned interfaces are exactly planar.

One possible way to solve this problem is to parametrize the orientations (and possibly also the shapes [22]) of all interfaces to find which geometry results in minimal energy (1). However, as the X-interface analyzed in this article is *a priori* not an energy minimizer of (1), such an approach would be completely unjustified. Instead, we decided to evaluate the elastic strain fields for four different simplified geometries (SG). These are ($\mathbf{c}$ is always a unit vector determining the direction of the crossing line) as follows:

- **SG 1:** where the crossing line lies in the intersection of the habit planes (i.e., $\mathbf{c} = \mathbf{n} \times \hat{\mathbf{n}}$), and the planar twinned-to-detwinned interfaces are chosen as such planes containing $\mathbf{c}$ that the declinations of the normal vectors to these planes from $\mathbf{m}$ and $\hat{\mathbf{m}}$ are minimal. In this case, the compatibility conditions at the habit planes (5) and (6) are fulfilled, but not at the twinned-to-detwinned interfaces, where the elastic strains must ensure the compatibility.

- **SG 2:** where the crossing line lies in the intersection of the type II twinning planes (i.e., $\mathbf{c} = \mathbf{m} \times \hat{\mathbf{m}}$), and the planar twinned-to-austenite interfaces are chosen as such planes containing $\mathbf{c}$ that the declinations of the normal vectors to these planes from $\mathbf{n}$ and $\hat{\mathbf{n}}$ are minimal. Here the compatibility conditions at the twinned-to-detwinned interfaces are identical to (7) and (8) and are fulfilled, whereas the compatibility at the twinned-to-austenite interfaces (which are slightly declined from the habit planes determined by conditions (5) and (6)) must be enabled by the presence of elastic strains.

- **SG 3:** where the crossing line lies in the intersection of one habit plane and one type II twinning plane (i.e., $\mathbf{c} = \mathbf{n} \times \mathbf{m}$), and the remaining twinned-to-austenite and twinned-to-detwinned interfaces are chosen as such planes containing $\mathbf{c}$ that the declinations of the normal vectors to these planes from $\hat{\mathbf{n}}$ and $\hat{\mathbf{m}}$ are minimal. In this case, only conditions (5) and (7) are fulfilled, so the region with the A–B laminate is compatibly connected to both austenite and the stabilized martensite.

- **SG 4:** is mirror symmetric to SG 3 (i.e., $\mathbf{c} = \hat{\mathbf{n}} \times \hat{\mathbf{m}}$) with the region with the A–C laminate compatibly connected to both austenite and the stabilized martensite.

The real geometry of the microstructure can be expected to be somewhere between the simplified geometries SG 1÷4.

The simplified geometries are shown in Fig. 3. For parametrization of the location of the crossing line in each geometry, the distance of the intersection of the crossing line with the chosen face from a

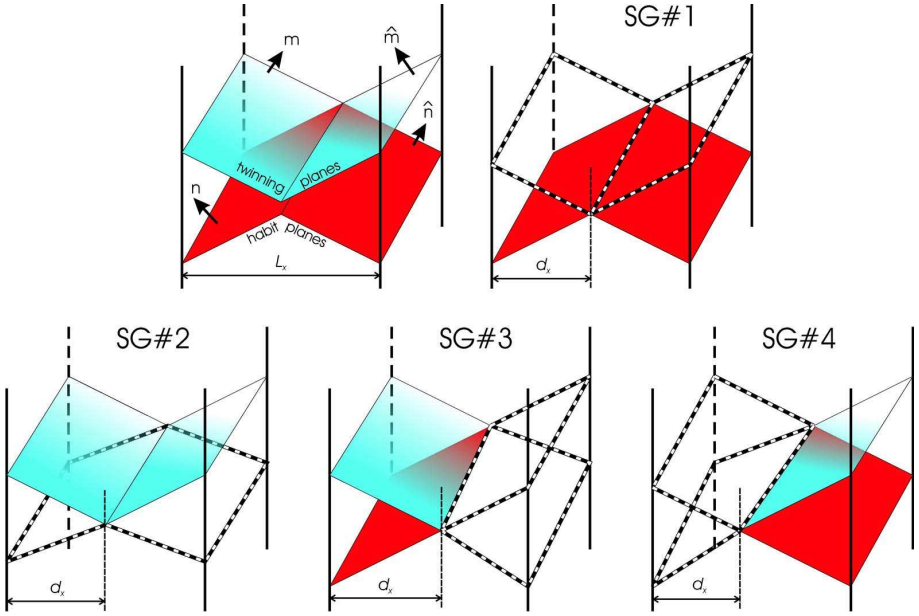

FIGURE 3. Simplified geometries SG 1 to SG 4. Filled (shaded) planes are always those compatible without elastic strains, planes outlined by the dashed lines are compatible only due to elastic strains. The first scheme shows the orientation of unit vectors $\mathbf{m}$, $\mathbf{n}$, $\hat{\mathbf{m}}$ and $\hat{\mathbf{n}}$, and the choice of L_x. Parametrization by d_x is shown for each geometry

chosen edge of the specimen was used. For this distance, denoted by d_x, the dimensionless ratio d_x/L_x (where L_x is the width of the chosen face in austenite; see Fig. 3) has the following sense: The geometries SG 1 and SG 2 are symmetric for $d_x/L_x = 1/2$, the geometry SG 3 is fully compatible for $d_x/L_x = 1$, and SG 4 is fully compatible for $d_x/L_x = 0$.

3.2 Elasticity of Pure and Twinned Regions

To evaluate the elastic stress and strain fields in the X-interface of known geometry, the elastic coefficients of all materials contained in the microstructure must be known. For austenite and stabilized martensite (single variant), the elastic coefficients can be found in [19], where the methodology of how these coefficients were determined from ultrasonic measurements is also described in details. Austenite exhibits cubic elastic anisotropy, which means that it can be fully described by three independent elastic coefficients. A single variant of martensite is orthorhombic; for this class of symmetry, the number of independent elastic coefficients is nine (e.g., [23]).

Theoretically, the coefficients for austenite and a single variant of martensite would be sufficient for evaluation of the stresses and strains in any microstructure. However, in our case of the X-interface, such an approach would require us to treat all the lamina within the twinned regions as individual components with prescribed geometries and elastic properties. This would turn the evaluation of the stress and strain fields into a strongly multiscale problem, as the thicknesses of individual layers are incomparably smaller than other dimensions of the microstructure. At the length scales comparable to the dimensions of the specimen, the twinned regions can be treated as homogeneous, with elastic properties obtained by some homogenization procedure.

The homogenization procedure used here for evaluation of all elastic coefficients (21 independent coefficients, as the resulting material is triclinic) of the type II twinned structures of CuAlNi was very similar to those used for evaluation of elastic coefficients of layered macroscopic composites (e.g., [24]). The details on the procedure can be found in [25] and in [26]. Here, thus, we restrict ourselves to a short outline of the algorithm and the obtained results only.

The procedure homogenizes a first-order laminate of two variants (denoted, again, A and B), which are connected by relation (7). In the natural coordinate system of variant A (i.e., the system aligned with the orthorhombic axes of this variant), the elastic coefficients of variant B can be obtained by rotating the tensor of elastic coefficients of variant A by two rotation matrices. The first is such a matrix $\mathbf{R}$ that

$$\mathbf{U}_A = \mathbf{R}\mathbf{U}_B\mathbf{R}^{\mathrm{T}} \tag{10}$$

The second matrix represents the mutual rotation of variants A and B within the laminate, i.e.,

$$\mathbf{Q} = \mathbf{Q}_A^{\mathrm{T}}\mathbf{Q}_B \tag{11}$$

where the matrices $\mathbf{Q}_A$ and $\mathbf{Q}_B$ are those appearing in (7). The homogenization procedure constructs a set of stress and strain fields homogeneous both in the lamina of variant A and the lamina of variant B. These fields are always chosen such that the compatibility and continuity conditions at the twinning plane are held. For these fields, the procedure evaluates the overall (averaged) elastic strain and the corresponding stored energy of the laminate. In the final step, the elastic coefficients of the laminate are obtained as (numerical) derivatives of the elastic energy function with respect to the averaged strains.

The way in which the twinning influences the symmetry and magnitude of the elastic anisotropy of martensite is shown in Fig. 4, where the Young moduli of austenite, martensite, and twinned martensite (a laminate of type II twins able to form a habit plane with austenite) are compared. The chosen graphical representation is as follows: The 3D surfaces are plots of the Young moduli for uniaxial tensions in directions given by unit vector $\mathbf{n}$, which runs through a unit sphere. The plotted vector quantity is thus $\mathbf{n}E(\mathbf{n})$. The moduli for austenite and a single variant of martensite are shown in the coordinate systems given by principal axes of austenite and martensite, respectively, whereas the moduli of the twinned martensite are plotted in the principal coordinate system of the major variant. Obviously, the difference between Young moduli of the single variant and the twinned martensite is mostly in the symmetry. Similar results can be obtained for shear moduli or for any other representation of the anisotropic elasticity (e.g., surfaces of phase or group velocity of ultrasonic waves, as used in [19]).

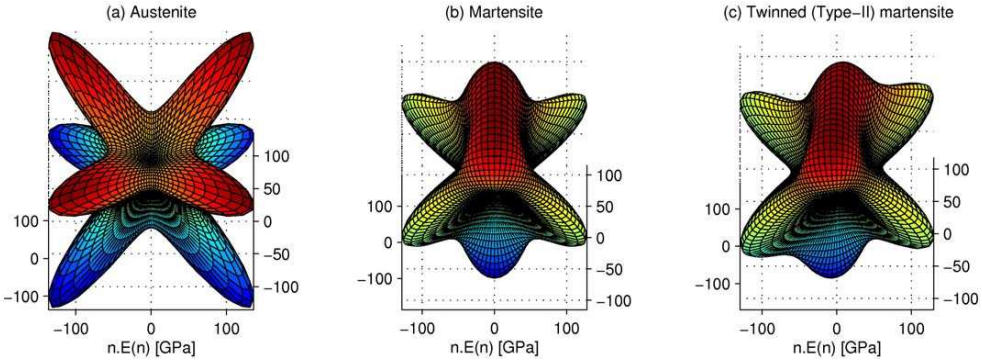

FIGURE 4. Surfaces of Young moduli $\mathbf{n}E(\mathbf{n})$ for all materials involved in the X-interface: **(a)** austenite phase; **(b)** single variant of martensite; **(c)** martensite in the twinned regions

3.3 Results of FEM Modeling

As mentioned in the introduction, to avoid problems with multiscale modeling, the displacement field was decomposed into two parts: transformation and elastic. The nature of the martensitic phase transition enables us to understand these two parts as two independent processes. The first is the deformation according to macroscopic gradients given by the transition, which leads to a discontinuous displacement field over the incompatible interfaces, and the second is the elastic deformation, which ensures the continuity of resulting displacements. Notice that both fields are discontinuous, but their composite is continuous. Whereas the first field is taken directly from the experimental observations, the second one is to be found using FEM.

In the following paragraphs, the whole procedure will be demonstrated for the case of simplified geometry SG 1. Let us denote the macroscopic deformation gradients for austenite, for the A–B laminate, for the A–C laminate, and for the pure variant A by

$$\mathbf{F}_I = \mathbf{I} \tag{12}$$

$$\mathbf{F}_{AB} = \lambda \mathbf{Q}_A \mathbf{U}_A + (1-\lambda)\mathbf{Q}_B \mathbf{U}_B \tag{13}$$

$$\mathbf{F}_{AC} = \lambda \widehat{\mathbf{Q}}_A \mathbf{U}_A + (1-\lambda)\mathbf{Q}_B \mathbf{U}_B \tag{14}$$

$$\mathbf{F}_A = \mathbf{Q}_A \mathbf{U}_A \tag{15}$$

Then, four affine transformations can be constructed:

$$\mathbf{y}_I : \mathbf{x} \to \mathbf{I}\mathbf{x} + \mathbf{b}_I \tag{16}$$

$$\mathbf{y}_{AB} : \mathbf{x} \to \mathbf{F}_{AB}\mathbf{x} + \mathbf{b}_{AB} \tag{17}$$

$$\mathbf{y}_{AC} : \mathbf{x} \to \mathbf{F}_{AC}\mathbf{x} + \mathbf{b}_{AC} \tag{18}$$

$$\mathbf{y}_A : \mathbf{x} \to \mathbf{F}_A\mathbf{x} + \mathbf{b}_A \tag{19}$$

The initial geometry for FEM modeling is obtained by applying these transformations to corresponding domains of the reference configuration. For SG 1, the vectors $\mathbf{b}_I$, $\mathbf{b}_{AB}$, $\mathbf{b}_{AC}$, and $\mathbf{b}_A$ are taken as follows: $\mathbf{b}_I = 0$, $\mathbf{b}_A$ is arbitrary, $\mathbf{b}_{AB}$ and $\mathbf{b}_{AC}$ are chosen so that the entire body remains unbroken over the habit planes (corresponding gradients are compatible, hence such vectors can be found). When the twinned-to-detwinned interfaces are not planes of compatibility, in general, the body splits into two parts. The first one comprises the region of austenite and both twinned regions; the second one contains only the stabilized (detwinned) martensite.

Now, the elasticity problem of putting those parts "back together" must be solved. Elastic moduli are known, so just boundary conditions are to be supplied. These conditions must ensure the uniqueness of the solution and the continuity of the overall displacement field, and thus the integrity of the resulting body. Consider (in the reference configuration) a point $\mathbf{x}_0$ lying in the twinned-to-detwinned interface between the A–B laminate and the pure variant A. In general, points $\mathbf{x}_A = \mathbf{y}_A(\mathbf{x}_0)$ and $\mathbf{x}_{AB} = \mathbf{y}_{AB}(\mathbf{x}_0)$ are different. Therefore the sought elastic displacement field $\mathbf{u}$ must meet the following condition:

$$\mathbf{x}_A + \mathbf{u}(\mathbf{x}_A) = \mathbf{x}_{AB} + \mathbf{u}(\mathbf{x}_{AB}) \tag{20}$$

It can be easily seen that $\mathbf{x}_{AB} = (\mathbf{y}_{AB} \circ \mathbf{y}_A^{-1})(\mathbf{x}_A)$, and the boundary condition in terms of $\mathbf{x}_A$ is

$$\begin{aligned}\mathbf{u}(\mathbf{x}_A) &= (\mathbf{y}_{AB} \circ \mathbf{y}_A^{-1})(\mathbf{x}_A) \\ &+\mathbf{u}((\mathbf{y}_{AB} \circ \mathbf{y}_A^{-1})(\mathbf{x}_A)) - \mathbf{x}_A\end{aligned} \tag{21}$$

This is exactly the boundary condition which was looked for. Similarly, such a condition can be found for the second twinned-to-detwinned interface. To achieve the uniqueness of the solution, the bottom face of the austenite domain was fixed. Hence the multiscale character was fully avoided in the problem formulation, but the non locality of the second term of the right-hand side of (21) is its consequence.

The problem was solved using FEM program COMSOL Multiphysics (formerly Femlab) in connection with the Matlab environment. In Matlab, the geometry was computed as prescribed by the macroscopic morphology. The following FEM computations were done in the COMSOL Structural Mechanics module (Solid, Stress-Strain application mode). For each part of the body in the initial configuration, an independent mesh was needed. To do this, the option *Use Assembly* was enabled. COMSOL was also able to deal with nonlocal couplings through *Extrusion Coupling Variables*. On boundary, where the "gluing" condition was prescribed, the *Boundary Extrusion Coupling Variable* was created according to the known mapping $y_{AB} \circ y_A^{-1}$. For the FEM discretization, the Lagrange cubic finite elements were used. The obtained linear system was solved by the memory-efficient SPOOLES direct solver implemented in COMSOL.

The elastic stress and strain fields were evaluated for all geometries SG 1÷4 and for ratios d_x/L_x running from 0 to 1. An example of the results is shown in Fig. 5. The plotted quantity here is the Von Mises stress (the square root of the second invariant of the stress tensor), evaluated on cuts of the specimen by planes as close as possible to the individ-

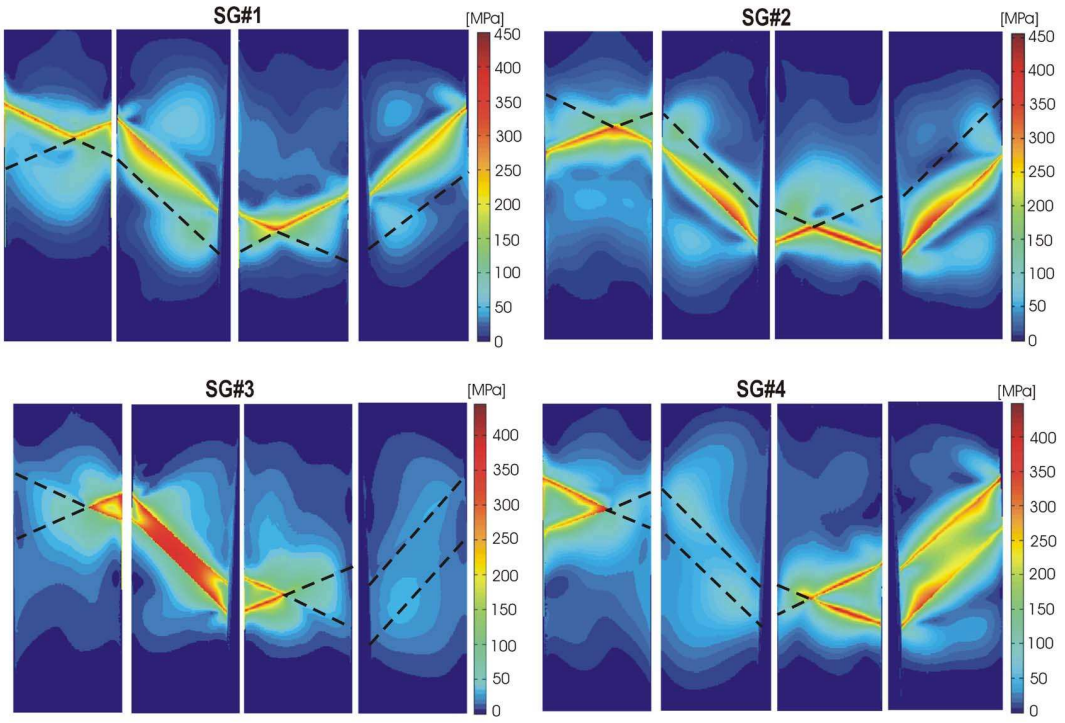

FIGURE 5. Maps of Von Mises stress evaluated on planar cuts closest to the faces of the specimen in simplified geometries SG 1÷4 for $d_x/L_x = 0.65$. The dashed lines denote the intersection of the cutting planes with planes of compatibility (habit planes for SG 1, twinning planes for SG 2, and combinations of habit and twinning planes for SG 3 and SG 4)

ual faces of the specimen.[2] In Fig. 5, the difference between those interfaces (habit planes, twinned-to-detwinned interfaces), which were chosen as planes of compatibility, and those at which the compatibility must be attained by elastic strains is obvious. For SG 1, the elastic strains are concentrated along the twinned-to-detwinned interfaces; for SG 2, a similar concentration is along the austenite-to-martensite interfaces. For SG 3 and SG 4, the maximum stress is localized within the regions surrounded by the interfaces not initially chosen as compatible (this is similiar to [11], where the stress concentration was revealed at the tip of the wedge microstructure). In other words, the obtained elastic fields are strongly influenced by our choice of the simplified geometry (see the last section for a more detailed discussion). In real microstructure (which can be expected to be somewhere between our SGs), both the habit planes and the twinned-to-detwinned interfaces could be elastically strained to achieve full compatibility.

The maximum of the Von Mises stress for all SGs shown in Fig. 5 is nearly the same (approximately 450 MPa). The difference between the geometries can be thus more clearly seen from Fig. 6, where the elastic energy stored in the specimen is plotted as a function of d_x/L_x for all SGs. As expected, the energies of specimens in SG 1 and SG 2 are symmetric about $d_x/L_x = 1/2$. For SG 3 and SG 4, the energy decreases towards the fully compatible configurations. Let us notice here that the crossing lines in the real X-interfaces reported in [8] were located close to the center of the specimen, i.e., close to maximal energies for SG 1 and SG 2.

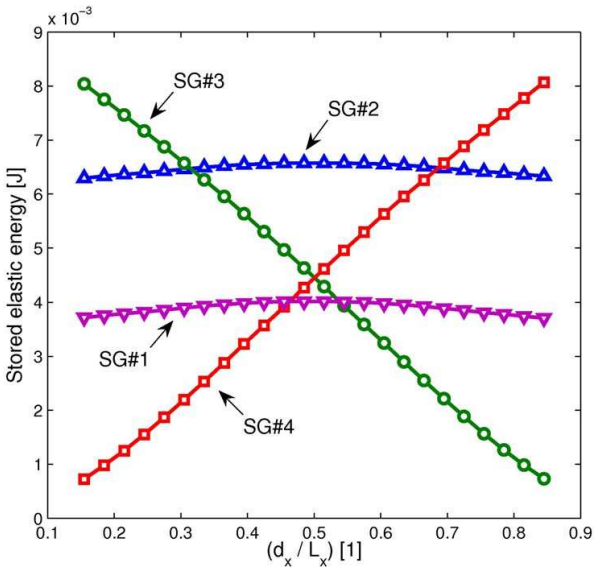

FIGURE 6. Dependence of the elastic energy stored in the specimen on the position of the crossing line for simplified geometries SG 1÷4

4. SUMMARY AND DISCUSSION

In this article, a procedure of construction of a mathematical model of an interfacial martensitic microstructure was presented. The examined material was the Cu-Al-Ni shape memory alloy, and the modeled interfacial microstructure was the X-interface appearing during the shape recovery process in single crystals of this material. From the analysis of the optical micrographs of the real microstructure, the individual twinning systems and variants of martensite forming the microstructure were identified. Based on this identification, the difference of the microstructure from compatibility was analyzed. The elastic strains necessary for the microstructure to achieve compatibility were evaluated by FEM, whereby the elastic coefficients of the twinned regions were evaluated by a homogenization procedure. Four different simplified geometries were used for the calculation. In each of these geometries, the calculation revealed strong concentrations of Von Mises stress along the interfaces not initially chosen as planes of compatibility. Although the simplified geometries are just rough approximations of the real X-interfaces, they enable us to estimate the dependence of the elastic energy stored in the specimen on a chosen geometric parameter (the distance d_x). The presented simulations show that the experimentally observed microstructures are not even local minimizers of the energy (their energy decreases with proper change of parameter

[2] The initial configuration for which the elasticity problem is solved is given by mapping $\mathbf{y}_{\mathrm{trans}}$, where the faces of the specimen are not planar and the specimen geometry is discontinuous. For this reason, the plotted Von Mises stress was evaluated on cuts of the specimen after the problem solution, i.e., after the "gluing" boundary condition (21) was fulfilled. As the cutting planes, planes as close as possible to the faces of the specimen were chosen. Thus the values of the Von Mises stress in Fig. 5 are very close approximations of the values at the surface

d_x), and thus there must be another explanation for their stability.

On the other hand, the results obtained for SG 1÷4 were strongly influenced by our (artificial) choice of at which planes the compatibility was achieved without elastic strains. Although the differences between the orientation of the habit and twinning planes and those planes that approximate them in our simplified geometries are minimal (less than 2° in the orientation of the normal vectors), the differences in the evaluated elastic fields are tremendous. The internal stress fields in real interfacial microstructures may thus significantly differ from those evaluated for SG 1÷4. However, construction of any more realistic geometry would be extremely complicated, at least for the following three reasons:

1. As the interfacial microstructure grows from the nucleus situated in the corner of the specimen (see [8] for more details), the laminates inside the twinned regions form under (varying) internal stress. For this reason, the laminates cannot be treated as fully homogeneous with the volume fractions given by relations (5) and (6). This may induce additional residual stresses both inside the twinned regions and at the habit plane. However, such variation of λ with the spatial coordinates cannot be evaluated without a complete knowledge of the microstructure's history.

2. As already mentioned, there is no justification for our assumption that the interfaces within the microstructure are exactly planar. Especially close to the crossing line, where all the compatibility conditions (5)–(8) are to be met and where the new martensitic needles nucleate (again, see [8] for more details), the shapes can be completely general. However, the real shapes of the interfaces can be determined neither experimentally (from optical micrographs, only the intersections of the interfaces with the surfaces of the specimen can be obtained; ultrasonic methods do not have sufficient resolution) nor theoretically (as the optimality criterion for the X-interfaces, which are *a priori* not minimizers of energy, is unknown).

3. The multiscale character cannot be fully avoided. Along the twinned-to-detwinned interfaces, the stress fields are not homogeneously distributed, but concentrated around the tips of individual martensitic needles nucleating at the crossing line and growing toward the lateral faces of the specimen. Moreover, the exact shapes of the needles are not known, and their determination is complicated for the same reasons as discussed in point 2.

Solution of the problems resulting from the preceding three points will be the subject of the authors' future work.

ACKNOWLEDGMENT

This work was supported by the project A200100627 of the Grant Agency of ASCR, the projects Nos. 101/06/0768 and 202/09/P164 of the Czech Science Foundation, by the institutional project of IT ASCR v.v.i. (CEZ:AV0Z20760514), and by the research center 1M06031 of the Ministry of Education of the Czech Republic. Authors would also like to acknowledge J. Kopeček, V. Novák and S. Ignácová (Institute of Physics ASCR) for specimen preparation and DSC measurements.

REFERENCES

1. Otsuka, K., and Wayman, C., Eds., *Shape Memory Materials*. Cambridge University Press, Cambridge, 1998.
2. Bhattacharya, K., *Microstructure of Martensite.* Oxford University Press, New York, 2003.
3. Ball, J. M., and James, R. D., Fine phase mixtures as minimizers of energy. *Arch. Rat. Mech. Anal.* **100**:13–52, 1987.
4. Ball, J. M., and James, R. D., Proposed experimental tests of theory of fine microstructure and the two-well problem. *Philos. Trans.* **338**:389–450, 1992.
5. Dolzmann, G., *Variational Methods for Crystalline Microstructure – Analysis and Computation.* Springer, Berlin, 2003.
6. Bhattacharya, K., Li, B., and Luskin, M., The simply laminated microstructure in martensitic crystals that undergo a cubic to orthorhombic phase trans formation. *Arch. Rat. Mech. Anal.* **149**:123–154, 1999.

7. Novák, V., Šittner, P., Ignacová, S., and Černoch, T., Transformation behavior of prism shaped shape memory alloy single crystals. *Mater. Sci. Eng. A.* **A438-440**:755–762, 2006.
8. Seiner, H., Sedlák, P., and Landa, M., Shape recovery mechanism observed in single crystals of Cu-Al-Ni shape memory alloy. *Phase Trans.* **81**:537–551, 2008.
9. Basinski, Z. S., and Christian, J. W., Experiments on the martensitic trasformation in single crystals of indium-thallium alloys. *Acta Metall.* **2**:148–166, 1954.
10. Ruddock, G., A Microstructure of martensite which is not a minimiser of energy: The X-interface, *Arch. Rat. Mech. Anal.* **127**:1–39, 1994.
11. Balandraud, X., and Zanzotto, G., Stressed microstructures in thermally induced M9R-M18R martensites. *J. Mech. Phys. Solids.* **55**:194–224, 2007.
12. Turteltaub, S., and Suiker, A. S. J., A multiscale thermomechanical model for cubic to tetragonal martensitic phase transformations. *Int. J. Solids Struct.* **43**:4509–4545, 2006.
13. Gao, X., Huang, H., and Brinson, L. C., A multivariant micromechanical model for SMAs, part 1. Crystallographic issues for single crystal model. *Int. J. Plasticity.* **16**:1345–1369, 2000.
14. Patoor, E., Lagoudas, D. C., Entchev, P. B., Brinson, L. C., and Gao, X., Shape memory alloys, part I: General properties and modeling of single crystals. *Mech. Mater.* **38**:391–429, 2006.
15. Lagoudas, D. C., Entchev, P. B., Popov, P., Patoor, E., Brinson, L. C., and Gao, X., Shape memory alloys, part II: Modeling of polycrystals. *Mech. Mater.* **38**:430–462, 2006.
16. Popov, P., and Lagoudas, D. C., A 3-D constitutive model for shape memory alloys incorporating pseudoelasticity and detwinning of self-accommodated martensite.*Int. J. Plasticity.* **23**:1679–1720, 2007.
17. Hane, K. F., Microstructures in Thermoelastic Martensites. Ph.D. Thesis, University of Minnesota, 1998.
18. Chu, C-H., and James, R. D., Analysis of microstructures in Cu-14.0%Al-3.9%Ni by energy minimization. *J De Phys. IV*. **JP5**:143–149, 1995.
19. Sedlák, P., Seiner, H., Landa, M., Novák, V., Šittner, P., and Manosa, L., Elastic constants of BCC austenite and 2H orthorombic martensite in CuAlNi shape memory alloy. *Acta Mater.* **53**:3643–3661, 2005.
20. Brinson, L. C., and Lammering, R., Finite element analysis of the behavior of shape memory alloys and their applications. *Int. J. Solids Struct.* **30**:3261–3280, 1993.
21. Auricchio, F., and Petrini, L., A three-dimensional model describing stress-temperature induced solid phase transformations: Solution algorithm and boundary value problem. *Int. J. Numer. Meth. Eng.* **61**:807–836, 2004.
22. Stupkiewicz, S., Maciewski, G., and Petryk, H., Low-energy morphology of the interface layer between austenite and twinned martensite. *Acta Mater.* **55**:6292–6306, 2007.
23. Musgrave, M. J. P., *Crystal Acoustics*. Holden-Day, San Francisco, 1970.
24. Nayfeh, A. H., *Wave Propagation in Layered Anisotropic Media.* North-Holland, Amsterdam, 1995.
25. Seiner, H., Dynamic and transient phenomena in single crystals of shape memory alloys, Ph.D. thesis, Czech Technical University in Prague, 2008.
26. Landa, M., Sedlák, P., Seiner, H., Heller, L., Bicanová, L., Šittner, P., and Novák, V., Modal resonant ultrasound spectroscopy for ferroelastics. *Appl. Phys. A*. **93**:557–567, 2009.

2.2 Publikace *Konečně-prvková studie morfologie rozhraní monovarianta-laminát pozorovaných ve slitině s tvarovou pamětí CuAlNi.*

Bibliografická citace: Seiner, H., Glatz, O., Landa, M. A finite element analysis of the morphology of the twinned-to-detwinned interface observed in microstructure of the Cu-Al-Ni shape memory alloy (2011) International Journal of Solids and Structures, 48 (13), pp. 2005-2014.

Stručná anotace: V této publikaci je analyzována rozhraňová mikrostruktura typu λ tvořená dvojicí rovin habitu, jedním dvojčatovým rozhraním a jedním rozhraním typu laminát-monovarainta. Právě toto rozhraní je zkoumáno podrobněji, a to jak experimentálně (interferometrií v bílém světle), tak konečněprvkovým modelováním. Je ukázáno, že tvar jehlic martenzitu na tomto druhu rozhraní neodpovídá minimu elastické energie.

Příspěvek habilitanta: Veškeré experimentální výsledky prezentované v publikaci včetně určení přesného tvaru jehlic pomocí interferometrie v bílém světle byly získány habilitantem. Konečněprvkové výpočty byly provedeny studentem Ondřejem Glatzem v rámci jeho postgraduálního studia pod vedením habilitanta.

International Journal of Solids and Structures 48 (2011) 2005–2014

Contents lists available at ScienceDirect

International Journal of Solids and Structures

journal homepage: www.elsevier.com/locate/ijsolstr

A finite element analysis of the morphology of the twinned-to-detwinned interface observed in microstructure of the Cu–Al–Ni shape memory alloy

Hanuš Seiner [a,*], Ondřej Glatz [b], Michal Landa [a]

[a] Institute of Thermomechanics, Academy of Sciences of the Czech Republic, Dolejškova 5, 18200 Prague, Czech Republic
[b] Faculty of Nuclear Sciences and Physical Engineering, Czech Technical University in Prague, Trojanova 13, 12000 Prague, Czech Republic

ARTICLE INFO

Article history:
Received 18 January 2011
Received in revised form 3 March 2011
Available online 12 March 2011

Keywords:
Shape-memory alloys
Finite element method
Energy minimization
Microstructure

ABSTRACT

A detailed morphology of the twinned-to-detwinned interface in microstructure of 2H-martensite phase of the Cu–Al–Ni shape memory alloy is observed by optical methods (optical microscopy, white-light interferometry). Based on these observations, a finite element model of the transition layer is constructed and applied to calculate the elastic stress distribution inside the observed microstructure. The results show that the real micromorphology does not correspond to the minimum of the sum of the elastic and surface energy, and that the maxima of the stress field necessary for the existence of this morphology are comparable to the elasticity limits of the 2H-martensite.

1. Introduction

The thermoelastic martensites, i.e. the low-temperature phases of shape memory alloys (SMAs), are known to be able to form fine, regular microstructures (Otsuka and Wayman, 1998; Bhattacharya, 2003). Among these microstructures, the geometrically simplest ones and also the most frequently observed ones are the 1st-order laminates (Bhattacharya et al., 1999), which are the microstructures consisting of parallel lamina of two variants of martensite with alternating thicknesses. Under some special conditions, the 1st-order laminates can form macroscopically planar interfaces with the high-temperature phase (these interfaces are called *the habit planes*), with single variants of martensite (so-called *twinned-to-detwinned interfaces*), or with other 1st-order laminates (e.g. the macrotwin boundaries in the laminates of higher orders). When the macroscopic compatibility over such interfaces is analyzed by a mathematical model, it is usually assumed that these macroscopic interfaces are exactly sharp. More precisely, these interfaces are typically modeled by approaching the infimum of the Helmoltz free energy of the material by some minimizing sequence of microstructures $\{\mathbf{M}_n\}_{n=1}^{\infty}$, whereby the thickness of the transition layer between the two homogeneous microstructures forming the interface is proportional to $1/n$ (see Ball and James, 1987, 1992 for more details). This does not, however, always exactly reflect the experimental observations. For example, Chu (1993) observed the interfaces between differently oriented laminates of compound twins of the Cu–Al–Ni alloy during a mechanically induced reorientation (see Abeyaratne et al., 1996; James et al., 1995; Li and Luskin, 1999) for a further discussion and analysis of these observations), and the widths of the transition layers (i.e. of the layers outside which the neighboring microstructures can be considered as homogeneous) in this case were up to few millimeters. In Chu (1993), the morphology of these transition layers is documented by detailed optical micrographs: when approaching the interface, the lamina of one of the variants involved in the laminate are narrowing and forming thin needles with sharp tips ending at the interface (Fig. 1a). Furthermore, the tips of the individual needles are slightly bended from the original orientation of the laminate, and there can be also some branching of the needles occurring within the transition region.

Similar morphology of the transition layer has been described in the literature repeatedly and for various SMAs: Basinski and Christian (1954a,b) have observed and discussed the tapering and bending needles at the twinned-to-detwinned interfaces (Fig. 1b) in the In-Tl alloy. Exactly the same phenomena (although at a completely different scale) were observed by Schryvers (1993), Schryvers et al. (2001, 2002), Boullay et al. (2001) at the macrotwin boundaries between two 1st-order laminates in the Ni–Al alloy.

There have been many attempts to analyze the micromorphology of the transition regions by means of geometrically non-linear elasticity. Besides the detailed discussions of this topic for the above mentioned macrotwin boundaries in Ni–Al given in Schryvers (1993), Boullay et al. (2001) and the finite-elements models of the macroscopic transition regions in Cu–Al–Ni described in James et al. (1995), Li and Luskin (1999), let us point

* Corresponding author.
E-mail address: hseiner@it.cas.cz (H. Seiner).

0020-7683/$ - see front matter © 2011 Elsevier Ltd. All rights reserved.
doi:10.1016/j.ijsolstr.2011.03.007

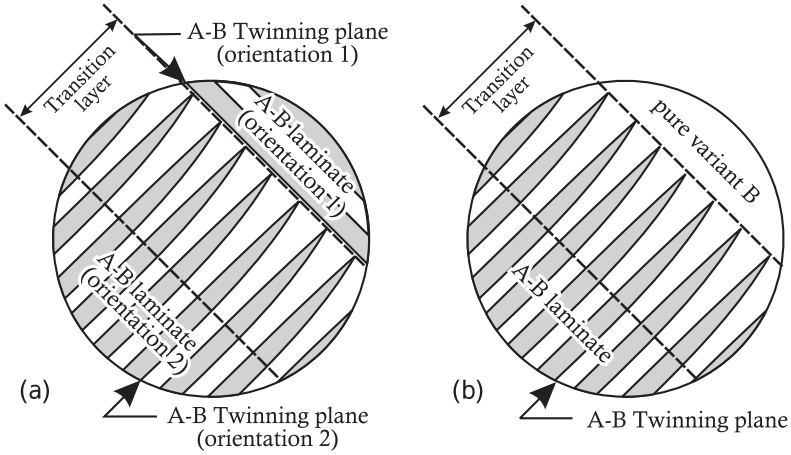

Fig. 1. Schematic sketches of the transition layers discussed in the introduction: (a) an interface between two differently oriented 1-st order laminates (Chu, 1993; James et al., 1995; Li and Luskin, 1999; Schryvers, 1993; Schryvers et al., 2001, 2002; Boullay et al., 2001; Finel et al., 2010); similar morphology can be observed also at the habit planes (Stupkiewicz et al., 2007); (b) a twinned-to-detwinned interface observed by Basinski and Christian (1954a) and analyzed in this paper.

out here the work of Stupkiewicz et al. (2007), who have used a finite-elements method to determine a low-energy micromorphology of the transition region at the habit plane for the Cu–Al–Ni alloy. Most recently, Finel et al. (2010) have obtained a realistic morphology of a Ni–Al macrotwin boundary as an output of a mathematical model based on the phase field method.

In this paper, we present a finite elements-based model of a twinned-to-detwinned interface in the Cu–Al–Ni alloy. The morphology of the transition layer used in this model is chosen to fit optimally the experimental observations (optical microscopy, white-light interferometry), and the elastic strain field within the transition layer is calculated for the elastic coefficients known quite accurately from the ultrasonic measurements (Landa et al., 2009). The main aim of this paper is to give a detailed quantitative comparison of the stress distribution inside the transition layer calculated for this experimentally obtained morphology and for the morphology obtainable by energy minimization. Such a comparison can answer the question whether the energy-minimization based approaches can reliably predict the main features of such microstructures.

2. Experimental observations

The analyzed interface was observed in a single crystal of the Cu–Al–Ni SMA prepared by the Bridgeman method at the Institute of Physics ASCR in Prague. The transition temperatures determined for this material by DSC were $M_S = -5\,^\circ\mathrm{C}$, $M_F = -22\,^\circ\mathrm{C}$, $A_S = 26\,^\circ\mathrm{C}$, and $A_F = 52\,^\circ\mathrm{C}$. The specimen used for the experiment was a prismatic $4.5 \times 4.5 \times 15.0\ \mathrm{mm}^3$ bar with the faces cut approximately along the $[1\ \ 1\ \ 0]$, $[1\ \ \bar{1}\ \ 0]$ and $[0\ \ 0\ \ 1]$ planes. This specimen was subjected to the following procedure (see Seiner et al., 2008 for more details):

1. By applying a uniaxial compression at the room temperature, the specimen was transformed from austenite into mechanically stabilized martensite (one variant of martensite with a negligible amount of compound twins). Due to the mechanical stabilization effect (Seiner et al., 2008; Novák et al., 2006), the specimen did not transform back into austenite when the loading was removed.
2. The specimen was locally heated up in one of the corners, which induced a nucleation of austenite in this corner and the subsequent formation and propagation of the interfacial microstructure (see Seiner et al., 2008; Seiner and Landa, 2009 for a definition of this term) through the specimen.
3. When the interfacial microstructure was approximately in the middle of the specimen, the heating was removed. The specimen with the 'frozen' microstructure was cooled down and cleaned by ethyl alcohol. The microstructure was then observed by optical methods.

The interfacial microstructure formed in this case was the so-called λ-interface (Basinski and Christian, 1954a; Seiner et al., 2008; Seiner, 2008), i.e. the microstructure with the macroscopic morphology sketched in Fig. 2a. This microstructure consists of two habit planes and two twinned-to-detwinned interfaces, all intersecting in one line. In this paper, we will focus on one of the twinned-to-detwinned interfaces, namely on the one being not parallel to the twinning planes inside the laminate. At this interface, a wide transition layer can be observed. In Fig. 2b–d, the optical micrographs of the λ-interface obtained by a Olympus SZ60 stereomicroscope (equipped by a CCD camera uEyE UI-2250-C used for recording) can be seen. Fig. 2b shows the entire morphology of the λ-interface, Fig. 2c shows the detailed morphology of the twinned-to-detwinned transition layer. It can be clearly observed that this transition layer consists of thin narrowing needles, i.e. that the volume fraction of the minor variant in the laminate decreases within the transition layer continuously from some starting value to zero. For comparison, the optical micrograph of the habit plane is shown in Fig. 2d. It can be clearly seen that although the twins are getting finer close to the interface, there is no well-defined, macroscopic transition region at the habit plane.

As seen in Fig. 2a, the width of the transition region is obviously dependent on the distance of the observation point from the crossing line of the λ-interface (seen in the middle of Fig. 2b). Close to the crossing line, the twins are much finer, and the transition region is significantly narrower. Starting from some distance (approx. 0.75 mm) from the crossing line, both the thickness of the needles and the width of the transition layer are approximately constant. It was checked by a comparison of detailed optical micrographs that the width of the transition layer and the thickness of the needles are approximately linearly proportional to each other; this means that the morphology of the transition region (the width/length ratio of the individual needles) is approximately scale-independent.

The optical micrograph in Fig. 2b and similar micrographs taken from all the faces of the specimen were used for the identification of the twinning systems and the martensitic variants involved in the microstructure. For this identification, the angles between the habit plane and the edges of the specimen and between the

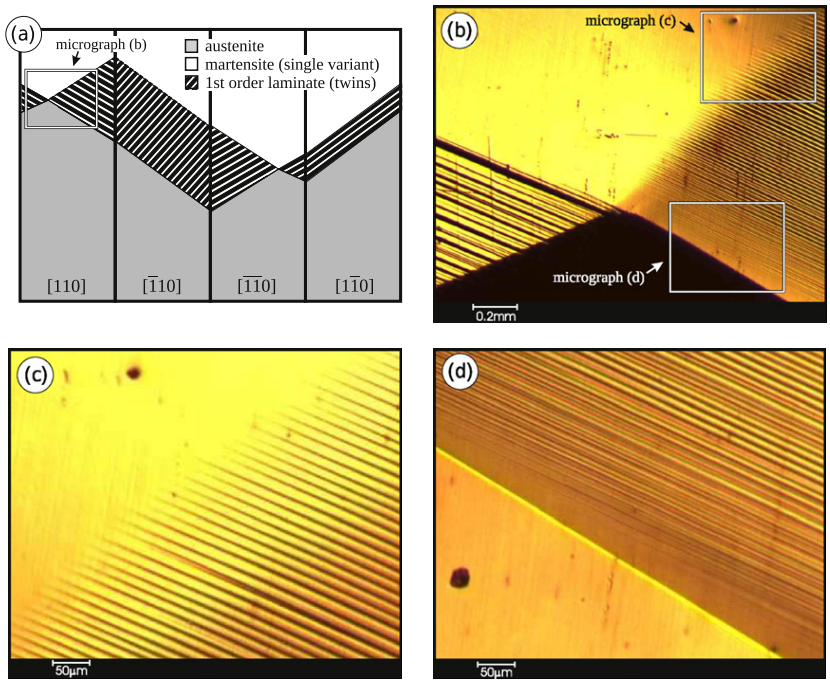

Fig. 2. (a) Macroscopic morphology of the λ-interface; (b–d) optical micrographs of the chosen segments of the microstructure.

habit plane and the twinning planes inside the laminate were used. The result was that the twinned-to-detwinned interface under study was formed between a laminate of Type-II twins of variants Nos. 3 and 6 (according to the notation of Sedlák et al. (2005)) and a single variant No. 6. From the micrographs, the exact volume fraction of the variant No. 3 in the laminate in the vicinity of the interface was determined as $\lambda = 0.319$, which is a slightly higher than the value which should be at the habit plane ($\lambda = 0.301$ (Bhattacharya, 2003)).

In order to obtain the exact morphology of the transition layer for the numerical model, a chosen segment of the twinned-to-detwinned interface was further analyzed by white-light interferometry using the topography module of the Polytec MSA-500 Micro System Analyzer. By this method, a 3D morphology of the transition layer was obtained with a nanometric vertical resolution. The mesoscopic 3D morphology of the interface (measured with horizontal pixel resolution 0.645 μm) is shown in Fig. 3. It is clearly seen that the analyzed interface has a 'smooth' character, as the continuous change of the volume fraction given by the continuous narrowing of the individual needles leads to a continuous change of the slope of the observed surface.

The shapes of the individual needles were determined from white-light interferometry measurements with horizontal pixel resolution equal to 0.129 μm. The obtained surface relief was numerically converted into a bitmap seen in Fig. 4a (and in Fig. 4b after disproportional rescaling), where the grayscale corresponds to the dz/dx gradient of the 3D surface in each point. By binarization of the bitmaps, the profile of the volume fraction inside the transition layer was determined (Fig. 4c). Close to the tips of the needles, this profile is approximately linear; at the opposite side of the transition layer, a smooth connection of the profile to the constant volume fraction of the minor variant in the laminate ($\lambda = 0.319$) can be seen.

All the geometric parameters of the morphology determined from the optical micrographs and from the interferometric measurements were used for the construction of the mathematical model of the interface.

3. Construction of a mathematical model

In this section, we will briefly summarize the mathematical theory of martensitic microstructures (Ball and James, 1987, 1992; Bhattacharya, 2003), apply this theory to analyze the compatibility at the twinned-to-detwinned interfaces in the Cu–Al–Ni alloy, and utilize the results of this analysis for a construction of a mathematical model.

3.1. Theoretical framework

In an SMA undergoing the cubic-to-orthorhombic transition (which is the case of Cu–Al–Ni alloy examined in this paper), the cubic lattice of austenite transforms, via a shearing mechanism, into the orthorhombic lattice of one of the six possible variants of martensite. At the continuum level, the cubic lattice of austenite is represented by deformation gradients from the $SO(3)$ group. After the transitions into martensite, the regions transformed into individual martensitic variants can be described by the *Bain tensors*, which are the symmetric components of the polar decompositions of the respective deformation gradients (see e.g. Bhattacharya, 2003 for more details). The Bain tensors $\mathbf{U}_{I=1,\dots,6}$ are sufficient for the analysis of the possible twinning systems and planar interfaces between homogeneous microstructures in the examined alloy. In particular, two variants of martensite ($\mathbf{U}_I$ and $\mathbf{U}_J$) can form a stress-free twin, whenever there exist vectors $\mathbf{a}$ and $\mathbf{n}$ (where $|\mathbf{a}| \neq 0$ and $|\mathbf{n}| = 1$) and rotations $\mathbf{R}_I \in SO(3)$ and $\mathbf{R}_J \in SO(3)$ such that

$$\mathbf{R}_I\mathbf{U}_I - \mathbf{R}_J\mathbf{U}_J = \mathbf{a} \otimes \mathbf{n}. \tag{1}$$

Then, the unit vector $\mathbf{n}$ is the normal to the twinning plane and the vector $\mathbf{a}$ represents the shear deformation between the two variants and is called *the shearing vector* (Bhattacharya, 2003).

Similarly, a stress-free planar (macroscopic) interface between two homogeneous microstructures $\mathbf{M_A}$ and $\mathbf{M_B}$ is possible if and only if there exist vectors $\mathbf{b}$ and $\mathbf{m}$ (where $|\mathbf{b}| \neq 0$ and $|\mathbf{m}| = 1$) and rotations $\mathbf{Q}_A \in SO(3)$ and $\mathbf{Q}_B \in SO(3)$ such that

$$\mathbf{Q}_A\mathbf{M}_A - \mathbf{Q}_B\mathbf{M}_B = \mathbf{b} \otimes \mathbf{m}. \tag{2}$$

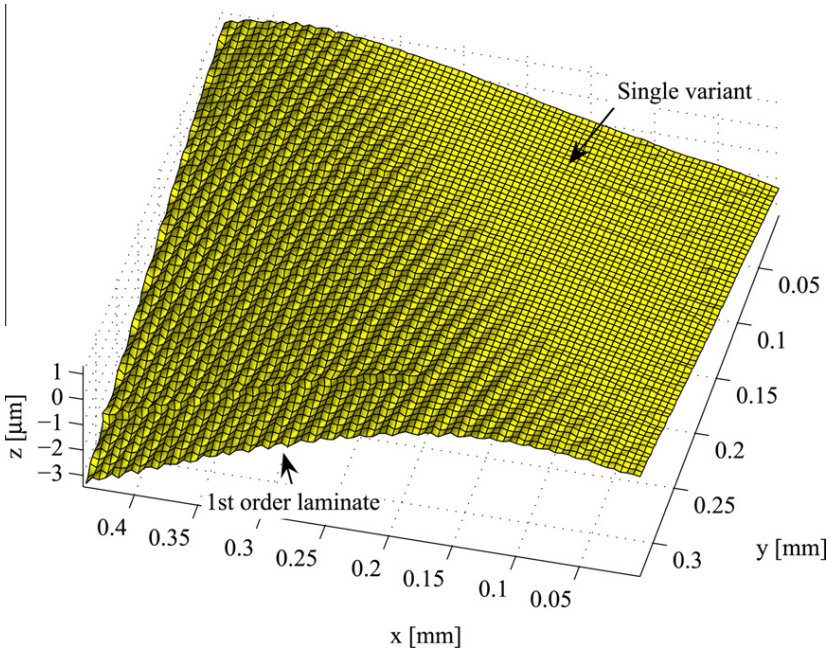

Fig. 3. 3D morphology of the twinned-to-detwinned interface obtained by white-light interferometry.

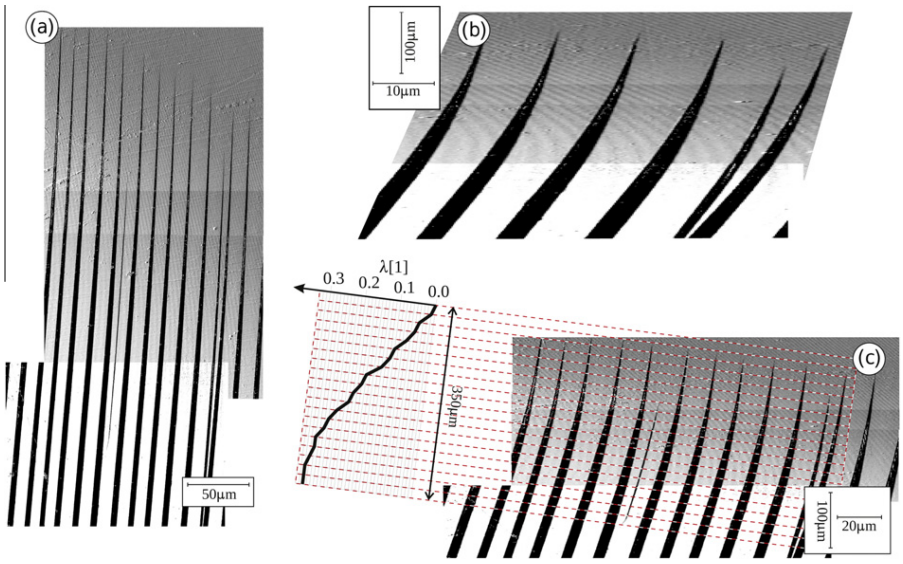

Fig. 4. Detailed morphologies of the transition layer determined from white-light interferometry measurements. The grayscale maps in sub-figures (b) and (c) are disproportionally rescaled to emphasize the bending and tapering of the needles. For the map in the sub-figure (c), the profile of the volume fraction of the minor variant across the transition layer is given.

The homogeneous microstructures can be the 1st-order laminates of two variants able to form a twin ($\mathbf{U}_I$ and $\mathbf{U}_J$ satisfy the condition (1))

$$\mathbf{M}_{A,B} = \lambda \mathbf{R}_J \mathbf{U}_I + (1-\lambda)\mathbf{R}_J \mathbf{U}_J, \tag{3}$$

where $\lambda \in \langle 0,1 \rangle$ is the volume fraction, or, in general, any members of the quasiconvex hull over the all possible components (see e.g. Dolzmann, 2003 for more details)

$$\mathbf{M}_{A,B} \in \mathcal{K}^{\mathrm{qc}}\left(\mathbf{I}, \bigcup_{I=1}^{6} \mathbf{U}_I\right). \tag{4}$$

In presence of the elastic strains, the compatibility conditions can be expressed in a similar way, both at the micro-scale (twinning plane under elastic loads) and at the macro-scale (marcoscopic compatibility between two elastically strained, homogeneous microstructures.) In this paper we adopt a slightly different approach to incorporate the elastic strains into the model. This approach has been successfully used by Balandraud and Zanzotto (2007) for the analysis of the elastic strains for the wedge microstructure in the Cu–Zn–Al alloy and for the X-interface microstructure in Cu–Al–Ni alloy by the current authors (Seiner et al., 2009; Glatz et al., 2009; Glatz et al., 2010). More details on this approach will be given within the description of the finite elements model.

3.2. Compatibility analysis at the twinned-to-detwinned interface and inside the transition layer

Let us first discuss the macroscopic compatibility between the 1st-order laminate and the single variant of martensite at the

twinned-to-detwinned interface. According to Ball and James (1987, 1992), Eq. (2) has either no solution or exactly two solutions (except for some extremely trivial cases, such as $\mathbf{M}_I = \mathbf{M}_J \in SO(3)$, where the number of solutions is infinite). In the case of the twinned-to-detwinned interface, for which $\mathbf{M}_A$ is a first order laminate given by Eq. (3) and $\mathbf{M}_B = \mathbf{U}_J$ is one of the variants involved in the laminate $\mathbf{M}_A$, the first solution of Eq. (2) is trivial: the laminate $\mathbf{M}_A$ can obviously border to the single variant $\mathbf{M}_B$ over a twinning plane between the variants $\mathbf{U}_I$ and $\mathbf{U}_J$. The second solution depends on the volume fraction λ and must be found numerically. For the volume fraction determined from the experiments ($\lambda = 0.319$), the corresponding calculated orientation of the twinned-to-detwinned interface is [0.02; 0.77; 0.64] in austenite (the reference configuration). Due to the macroscopic width of the transition layer and due to the fact that this width changes along the interface according to the changing fineness of the twins (see Fig. 2 and the discussion around it), it was not possible to determine the experimental orientation of this interface with accuracy higher than approximately 2°. If only those parts of the interface were taken into account where the width of the transition layer was approximately constant (sufficiently far away form the crossing line of the λ-interface as discussed above), the resulting orientation of this interface was about 0.5° declined from the numerically obtained value, which is an acceptable agreement. Let us mention here that the twinned-to-detwinned interface was considered as stress-free at the macroscale. This is not exactly correct, since the λ-interface itself cannot be compatible without elastic strains. However, it was checked by a direct FEM calculation (Glatz, 2010), that the macroscopic elastic loads acting particularly on the studied twinned-to-detwinned interface are negligible (especially compared with the elastic micro-stresses resulting from the morphology of the transition layer calculated in this paper).

The analysis of the microscale compatibility inside the transition layer is significantly more complicated. The fact that the needles are tapering and bending indicates that there must be non-negligible elastic strains accommodated inside the layer. In this paragraph, we will make a brief theoretical prediction of what the morphology of the layer could be (see the more detailed discussions on this topic by James et al. (1995), Schryvers et al. (2001), Boullay et al. (2001) for a comparison); the exact way how the elastic strains are treated in the model will be described in the next subsection.

Let us consider a twinned-to-detwinned interface between a single variant $\mathbf{U}_6$ and the laminate $\mathbf{M}_A$ given by (3) with $I = 3$ and $J = 6$. By putting (2) and (3) together and by denoting $\mathbf{Q}_3 = \mathbf{Q}_B^{\mathrm{T}}\mathbf{Q}_A\mathbf{R}_3$ and $\mathbf{Q}_6 = \mathbf{Q}_B^{\mathrm{T}}\mathbf{Q}_A\mathbf{R}_6$, the compatibility condition becomes

$$[\lambda\mathbf{Q}_3\mathbf{U}_3 + (1-\lambda)\mathbf{Q}_6\mathbf{U}_6] - \mathbf{U}_6 = \hat{\mathbf{b}} \otimes \mathbf{m}. \tag{5}$$

It can be clearly seen that the variant No. 6 appearing in the laminate is rotated with respect to the single variant by the matrix $\mathbf{Q}_6$. For the Bain tensors of the variants Nos. 3 and 6 taken from (Sedlák et al., 2005), it was calculated that the matrix $\mathbf{Q}_6$ represents a rotation by 4.6° around the direction [−0.98; 0.14; −0.14] (i.e. approximately $[\bar{7}\quad 1\quad \bar{1}]$) in the reference configuration. This direction is very close to the direction along the tips of the needles (i.e. the direction of the line at which the curved surfaces forming the individual needles intersect; the difference is approximately 2.5° only), so the matrix $\mathbf{Q}_6$ corresponds approximately to a rotation in the plane normal both to the twinning planes in the laminate and to the macroscopic twinned-to-detwinned interface. Let us, thus, consider a cut of the transition layer by this plane (Fig. 5): As the volume fraction λ continuously decreases from $\lambda = 0.319$ to zero across the layer, the rotation of the variant No. 6 continuously changes from $\mathbf{Q}_6$ to $\mathbf{I}$. The rotation $\mathbf{Q}_3$ and the orientation of the twinning planes $\mathbf{n}$ tend to follow this continual change to ensure the compatibility of the microstructure, which cannot be, however, fully achieved without elastic strains.[1] As the orientation of the faces of the needle tends to be as close to the twinning plane as possible (to minimize the elastic strains), the whole needle is continuously bended. The bending angle in a given point inside the layer should be approximately equal to the angle of the rotation of variant No. 6 in this point (cf. (Boullay et al., 2001; James et al., 1995)). The exact shapes of the needles (the evolution of the volume fraction, the bending angles) cannot be, however, theoretically predicted without the elastic strains taken into account.

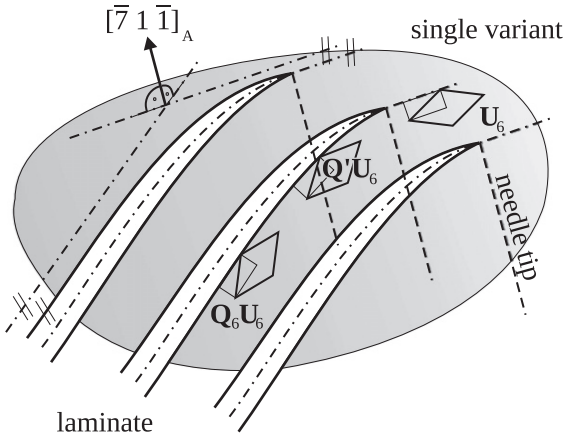

Fig. 5. The cut of the transition layer by the plane $(\bar{7}\ \ 1\ \ \bar{1})$ in the reference configuration. The rotation of the variant $\mathbf{U}_6$ is continuously changing from zero (in the single variant) to $\mathbf{Q}_6$ (inside the laminate). In any point inside the transition layer, this variant is rotated by some matrix $\mathbf{Q}'$ which lies between $\mathbf{I}$ and $\mathbf{Q}_6$. See the text for more details.

3.3. Finite element model

Our aim is now to construct a mathematical model able to treat elastically strained martensitic microstructures. On this purpose, we can understand the martensitic phase transition as two independent processes. The first is the inelastic deformation which represents the transition of the individual parts of the microstructure into different variants of martensite, and the second is the elastic deformation which ensures the continuity of the resulting displacement field.

Consider a simply connected volume Ω representing a periodically repeating segment of the twinned-to-detwinned interface in the reference configuration (i.e. in austenite). As outlined in Fig. 6, this volume consists of parts $\mathcal{G}_1$ and $\mathcal{G}_2$ representing the needle and the surrounding material, respectively. The transition of this volume into two different variants of martensite can be represented by affine transformations $\mathbf{y}_m(\mathbf{x}) = \mathbf{F}_m\mathbf{x} + \mathbf{b}_m$ $(m = 1, 2)$, each acting on the respective part $\mathcal{G}_m$. The deformation gradients $\mathbf{F}_m = \mathbf{R}_m\mathbf{U}_{N(m)}$ are the Bain tensors of the respective variants (see Section 3.2, $N(1) = 3, N(2) = 6$) rotated such that the compatibility condition (1) is satisfied inside the laminate. Without a loss of generality, we can take $\mathbf{b}_2 = \mathbf{0}$. The choice of the vector $\mathbf{b}_1$ will be discussed later.

[1] To prove this, it sufficient to notice that the needles must have the needle-like shapes even in the reference configuration, where the rotations do not apply. In other words, the interfaces between the homogeneously transformed regions (variant No. 3 inside the needle and variant No. 6 outside the needle) must be curved in this configuration, which contradicts the assumptions of the stress-free compatibility. For a more detailed explanation why the interfaces between homogeneously transformed regions cannot be curved we refer the reader to Bhattacharya (2003).

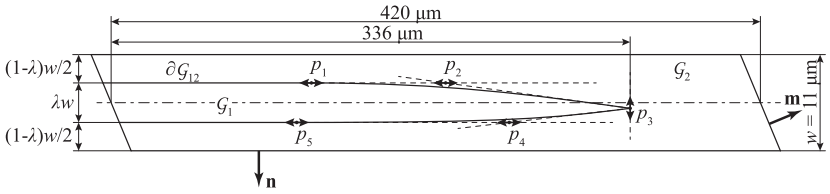

Fig. 6. Geometry of the modeled region in the reference configuration. The view is perpendicular to the $\mathbf{n}_{\text{base}}$ direction (see the text).

Inside the transition layer (i.e. outside the homogeneous laminate), the inelastic displacement field given by the transformations $\mathbf{y}_m(\mathbf{x})$ defined above is, in principle, discontinuous: we obtain two separated parts $\mathcal{V}_m = \mathbf{y}_m(\mathcal{G}_m)$ and we try to find an elastic strain field which puts these parts back together. More precisely, we are looking for the displacement fields $\widetilde{\mathbf{u}}_m(\mathbf{x})$ defined on $\mathcal{V}_m$ such that the composition $\widetilde{\mathbf{y}}$ defined by

$$\widetilde{\mathbf{y}}_{|\mathcal{G}_m} = \mathbf{y}_m + \widetilde{\mathbf{u}}_m \circ \mathbf{y}_m \tag{6}$$

represents a continuous deformation on the whole region Ω. These elastic strains can be determined by conventional finite elements (FEM) model with appropriately chosen geometry and boundary conditions.

Fig. 6 shows the detailed geometry of the used model in the reference configuration. The region Ω was a parallelepiped with lateral face normals $\mathbf{n}$ (perpendicular to the twinning planes in the homogeneous laminate) and $\mathbf{m}$ (perpendicular to the macroscopic twinned-to-detwinned interface). The base face normal was chosen as

$$\mathbf{n}_{\text{base}} = \frac{\mathbf{U}_6^2(\mathbf{n}\times\mathbf{m})}{\left\|\mathbf{U}_6^2(\mathbf{n}\times\mathbf{m})\right\|}. \tag{7}$$

This choice ensured that after the given affine transformations the lateral faces of the needle were perpendicular to the base faces, which is necessary for further proper formulation of periodic boundary conditions on the base faces. To enable a simple parametrization of the shape of the needle, the boundary of the region $\mathcal{G}_1$ was defined by two straight segments and two quadratic Bézier curves (each having three control points). For the distance between the left edge of the region Ω and the tip of the needle fixed, the control points p_1, p_2, p_3, p_4, and p_5 were allowed to move as indicated by the arrows – the actual positions of these points were, then, the parameters controlling the exact micromorphology of the transition layer, i.e. the profile of the volume fraction and the curvatures of the individual faces of the needle. The width of the needle at the interface between the modeled region and the laminate was fixed to the value given by the volume fraction λ taken from the experimental observations. The in-plane dimensions of the modeled region (also given in Fig. 6) were taken in a rough agreement with the experimental observations as well. However, the change of the exact width of the transition layer (i.e. the layer where the faces of the needles are not straight) was enabled by moving the control points p_1 and p_5 along the respective twinning planes. The out-of-plane dimension of the modeled region (i.e. the dimension along the direction $\mathbf{n}_{\text{base}}$) was chosen to be equal to 3 μm. Let us point out here that although the shape of the needle is fully described by 2D curves lying in one plane in the reference configuration, and although the final elastic fields must satisfy the conditions of plane strain (under the assumption that the twinned-to-detwinned interface is unbounded as discussed later), the whole problem must be solved in 3D. The reason is that both the deformation gradients $\mathbf{F}_m$ and the additional elastic displacements $\widetilde{\mathbf{u}}_m$ are fully three-dimensional. Consequently, the plane in which the plane-strain condition is hold for the elasticity problem does not correspond to any plane in the reference configuration, where the geometry is defined.

Let us now discuss the boundary conditions (Fig. 7). These conditions apply for the elasticity problem, so they must be formulated for the geometry after the affine transformations $\mathbf{y}_m(\mathbf{x})$ were applied. Consider the volumes $\mathcal{G}_1$ and $\mathcal{G}_2$ in the reference configuration, and denote their common boundary as $\partial\mathcal{G}_{12} = \overline{\mathcal{G}}_1 \cap \overline{\mathcal{G}}_2$. Let $\mathbf{x}$ be a point of $\partial\mathcal{G}_{12}$. Then, this point transforms into two different points $\widetilde{\mathbf{x}}_1 = \mathbf{y}_1(\mathbf{x})$ and $\widetilde{\mathbf{x}}_2 = \mathbf{y}_2(\mathbf{x})$ after the application of the affine transformations. The requirement on the sought displacement field is that these two points become identical after the elastic deformation,

$$\widetilde{\mathbf{x}}_1 + \widetilde{\mathbf{u}}_1(\widetilde{\mathbf{x}}_1) = \widetilde{\mathbf{x}}_2 + \widetilde{\mathbf{u}}_2(\widetilde{\mathbf{x}}_2). \tag{8}$$

The relation between the points $\widetilde{\mathbf{x}}_1$ and $\widetilde{\mathbf{x}}_2$ is clear:

$$\widetilde{\mathbf{x}}_2 = (\mathbf{y}_2 \circ \mathbf{y}_1^{-1})(\widetilde{\mathbf{x}}_1) = \mathbf{F}_2\mathbf{F}_1^{-1}(\widetilde{\mathbf{x}}_1 - \mathbf{b}_1) + \mathbf{b}_2. \tag{9}$$

On substituting this relation into (8) we get

$$\begin{aligned}\widetilde{\mathbf{x}}_1 + \widetilde{\mathbf{u}}_1(\widetilde{\mathbf{x}}_1) = {}& \mathbf{F}_2\mathbf{F}_1^{-1}(\widetilde{\mathbf{x}}_1 - \mathbf{b}_1) + \mathbf{b}_2 \\ & + \widetilde{\mathbf{u}}_2\Big(\mathbf{F}_2\mathbf{F}_1^{-1}(\widetilde{\mathbf{x}}_1 - \mathbf{b}_1) + \mathbf{b}_2\Big).\end{aligned} \tag{10}$$

This relation holds for an arbitrary point $\widetilde{\mathbf{x}}_1 \in \partial\mathcal{V}_{12}$. Thus, we obtain a boundary condition for the field $\widetilde{\mathbf{u}}_1$ on the boundary $\partial\mathcal{V}_{12} = \mathbf{y}_1(\partial\mathcal{G}_{12})$. This condition can be written in the following form

$$\begin{aligned}&\widetilde{\mathbf{u}}_1(\widetilde{\mathbf{x}}) = \mathbf{F}_2\mathbf{F}_1^{-1}(\widetilde{\mathbf{x}} - \mathbf{b}_1) + \mathbf{b}_2 + \widetilde{\mathbf{u}}_2\Big(\mathbf{F}_2\mathbf{F}_1^{-1}(\widetilde{\mathbf{x}} - \mathbf{b}_1) + \mathbf{b}_2\Big) - \widetilde{\mathbf{x}}, \\ &\forall\widetilde{\mathbf{x}} \in \partial\mathcal{V}_{12},\end{aligned} \tag{11}$$

which obviously couples the field $\widetilde{\mathbf{u}}_1$ to the displacement field in the major variant ($\widetilde{\mathbf{u}}_2$). In other words, the elastic displacement fields in the transformed regions $\mathcal{V}_1$ and $\mathcal{V}_2$ are coupled through the requirement of the continuity of the resulting (inelastic + elastic) displacement field over the interface between the needle and the major variant. At the points where the boundary $\partial\mathcal{V}_{12}$ reaches the interface between the modeled region and the laminate, the elastic strains are expected to be zero (the all elastic stored energy is localized solely inside the transition layer). Then, the condition (11) can be used for the determination of the vector $\mathbf{b}_1$.

Further boundary conditions follow from the symmetries of the system. The twinned-to-detwinned interface at the macroscale is assumed to be an unbounded plane separating two homogeneous half-spaces. Thus, at the microscale, the interface is supposed to consists of an infinite number of needles of infinite height. The effect of the infinite height is simply modeled by periodic boundary conditions imposing equal displacement fields on the upper and lower base faces. At the lateral faces, the conditions are the following: at the face separating the modeled region from the twinned martensite, the displacements simulating an elastically unstrained laminate are prescribed; the opposite lateral face is considered to be far enough from the tip of the needle, and the material at this face is assumed to be stress-free. The second set of the periodic boundary conditions imitates the infinite number of adjacent

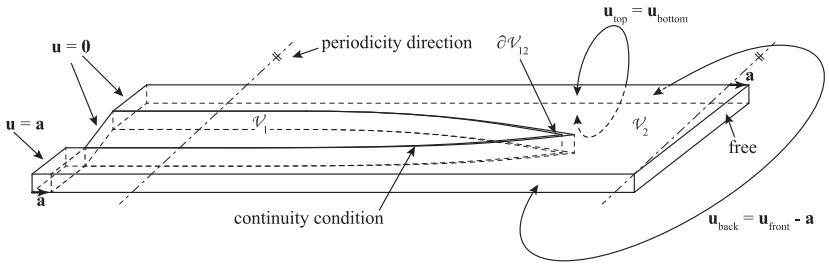

Fig. 7. Initial configuration for the FEM computation and the boundary conditions.

needles, and is put on the long lateral faces (whereto, however, the constant shift **a** resulting from the macroscopic shear of the laminate must be taken into account, see Fig. 6 for an outline).

The finite element model used for the solution of the final elasticity problem with boundary conditions described above was implemented in COMSOL MULTIPHYSICS computational environment, the initial geometry for this model was computed in MATLAB. Since the involved deformations were beyond the limits of linear elasticity, the finite strain framework had to be used. Both domains $\mathcal{V}_1$ and $\mathcal{V}_2$ were meshed independently by one layer of prismatic Lagrange cubic elements, with the mesh near the tip of the needle refined. The total number of elements was approximately 580 (approx. 52,000 DOFs). As material parameters, full orthorhombic elasticity tensors of 2H-martensite were taken from Landa et al. (2009) and rotated according to the actual orientation of the individual variants.

4. Results and discussion

The above described model was used to calculate the elastic field inside the transition layer. It was assumed that the energy of the microstructure consists of two parts ($E = E_{\text{elast.}} + E_S$), where the first is the energy of the elastic strains induced by the compatibility conditions and the second is the *surface energy* of the interfaces between the individual variants. The elastic energy tends to elongate the needles (i.e. to make the individual interfaces closer to the stress-free twinning planes), the surface energy tends to minimize the surface of the needles, so the resulting width of the transition layer can be assumed to be a result of a balance between $E_{\text{elast.}}$ and E_S. Under this assumption, two different optimizing procedures were solved:

1. The elastic energy $E_{\text{elast.}}$ was minimized by optimizing the positions of the control points $p_1 \div p_5$ (i.e. optimizing the shape of the needle). Only such positions of these points were allowed that the entire width of the transition region (i.e. the distance between the control point p_3 and the edge of the homogeneous laminate) remained unchanged. This width was taken from the experimental observations.
2. The misfit between the experimentally obtained morphology (taken from the optical micrographs and the white-light interferometric profiles) and the morphology resulting from the FEM calculations was minimized by optimizing the positions of the control points $p_1 \div p_5$ at the input of the FEM model.[2] The shape of the first of the four non-branching needles in Fig. 4b was taken as the 'optimal' shape (i.e. the shape fitted by the model); this shape is, nevertheless, in a satisfying visual agreement with the shapes of all the needles in Fig. 4a (except of the branched ones), and the results (the distribution of the elastic stresses inside the modeled region) are both qualitatively and quantitatively very similar when any other of these needles is used. For the resulting morphology, the elastic energy $E_{\text{elast.}}$ was calculated and compared to the minimal value obtained by the first procedure.

In addition, it was checked that without the surface energy taken into account, the minimum of the energy of the transition layer (which is equal to $E_{\text{elast.}}$ in this case) corresponds to a more then five times wider transition layer (more than five times longer needles) than what was observed. If we assume that the E_S term is linearly proportional to the area of the faces of the needles per unit volume, it can be written that $E_S \approx \gamma L$, where L is the width of the transition region and γ is a constant. The parameter γ can be tuned such that the minimum of the entire energy E corresponds to the experimentally observed width, which gives a rough estimate of the surface energy of the Type-II twins. The value of the surface energy obtained by this approach was 530 mJ m^{-2} which is considerably higher than the values found in the literature for similar materials (Shilo et al., 2007; Waitz et al., 2005). The reason for this discrepancy will be discussed later.

Finally, the fact that the surface energy term (E_S) is dominantly responsible for the width of the transition layer, not for the exact shapes of the needles, was proved by the following simulation: The changes of $E_{\text{elast.}}$ and E_S induced by small variation of the positions of the control points $p_2 \div p_4$ (i.e. by small changes of the shape of the needle without altering the width of the transition layer) were calculated. The result was that the changes of E_S (under the above made assumption that $E_S \approx \gamma L$) were by more than two orders of magnitude lower than the corresponding changes of $E_{\text{elast.}}$.

The results of the two optimizing procedures described above are seen in Fig. 8, which shows both the resulting morphology in the reference configuration and the deformed morphology with a map of the Von Mises stress (a square root of the second invariant of the stress tensor). Obviously, there is a significant difference between the morphology obtained by energy minimization and the morphology taken from the experiments.

The minimal elastic energy (Fig. 8a) corresponds a to a perfectly symmetric needle in the reference configuration (the control points p_1, p_2, p_4 and p_5 are arranged mirror-symmetrically around the midrib plane, the control point p_3 lies in this plane). In the deformed configuration, the needle is bended and the bending angle of the axis of the needle is fully given by the angle of rotation represented by the matrix $\mathbf{Q}_6$ (as it follows from the symmetry of the needle in the reference configuration); the same bending angle can be observed at the lateral faces of the modeled region. According to the plot of the Von Mises stress, the most of the stored elastic energy is concentrated in a banana-shaped region surrounding the tip of the needle. In Fig. 9, the dependence of the elastic energy density stored in the transition layer on the position along the needle can

[2] Let us mention here that the plane perpendicular to $\mathbf{n}_{\text{base}}$ in the model is completely different from the plane of the free surface on which the micrographs were taken and the profiles measured. Thus, the geometric misfit was, more precisely, minimized between the experimental observations and the cuts of the morphology resulting from the FEM calculation by proper planes.

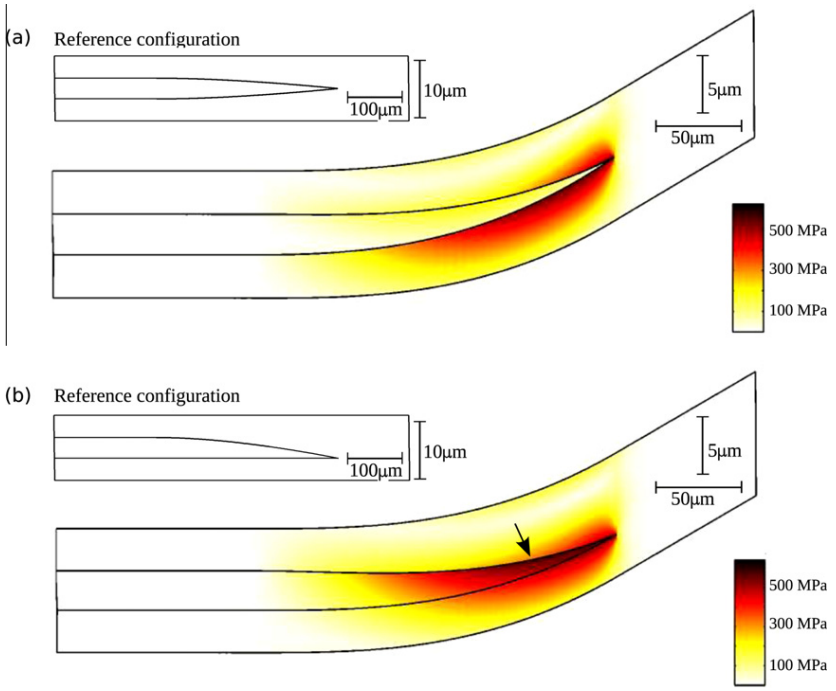

Fig. 8. Results of the FEM calculations in the form of the geometries in the reference configuration and the plots of the Von Mises stress in the deformed configuration: (a) the morphology corresponding to the minimal elastic energy; (b) the morphology corresponding to the experimental observations (the arrow marks the stress concentration along the curved interface.) Notice the slightly different orientation of the needle tip in the deformed configurations in (a) and in (b).

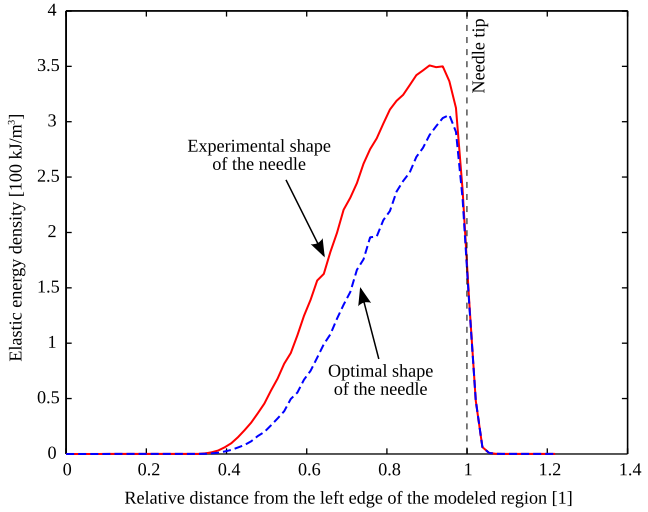

Fig. 9. Distribution of the elastic energy density along the longest dimension of the modeled region (i.e. along the needle). Each point corresponds to a mean value of this density at a planar cut of the deformed geometry at a given distance form the left edge of the modeled region. The dimensionless parameter on the horizontal axis is equal to the ratio between this distance and the length of the needle.

be seen: Along the curved part of the needle, this density smoothly increases up to some maximal value located close to the tip of the needle. The entire stored elastic energy in the modeled region is 97.10^{-8} mJ, which corresponds to the macroscopic energy per unit area of the twinned-to-detwinned interface equal to 29 J m^{-2}.

A completely different situation appears for the experimentally obtained shape of the needle (Fig. 8b). First of all, let us mention the reference configuration. In this case, the symmetry is completely lost. Quite on the contrary, one of the faces of the needle is completely flat, and the control point p_3 lies at one of the twinning planes. Consequently, the bending angle of the axis of the needle is slightly different from the bending angle of the lateral faces of the modeled region (let us mention here that a slight systematic declination of the bended tips of the needles from the direction predicted by the theory was observed also by Boullay et al. (2001), Schryvers et al. (2002), Finel et al. (2010). The asymmetric shape of the needle enables us to imagine clearly of the growth mechanism of the twinned-to-detwinned interface. The individual needles grow each along one twinning plane and are thickening inside the layer until the volume fraction of the homogeneous laminate is reached. Let us mention that we assume that the shapes of the needles are the same inside the material and on a cut of the material by the free surface of the examined specimen (i.e. we take the morphology observed at the free surface and use it for the model of the whole interface). Strictly speaking, this might not be exactly true. Inside the material, the plane-strain conditions apply, whereas the free surface imposes the plane-stress conditions. However, the fact that one of the faces of the needle is exactly equal to the twinning plane seems to be rather a fundamental finding related e.g. to the growth mechanism than just a result of the plane-stress conditions on the surface.

The distribution of the Von Mises stress around the needle with the shape taken from the experiments is also considerably different from the previous case. As indicated in Fig. 8b by the arrow, there is a significant stress concentration along that interface which is curved in the reference configuration, but no concentration at the second interface (at which the compatibility conditions for the elastically unstrained material are satisfied). According to the plot of the stored elastic energy density distribution along the direction of the needle seen in Fig. 9, the stress concentrated along the curved interface increases with the narrowing of the needle and reaches its maximum close to the tip of the needle. The entire stored elastic energy in the modeled region is 132.10^{-8} mJ (the corresponding energy per unit area of the twinned-to-detwinned interface is 40 mJ m^{-2}), which is about 1.4 times higher than for the optimal shape.

The maximal values of the Von Mises stress calculated for the optimal shape and for the experimental shape of the needle are similar and both are slightly higher than 600 MPa. In the points where these maxima are reached, the strain fields can be well approximated by pure shear strains of magnitudes nearly 0.5%; the corresponding maximal shear stresses are approximately equal to 350 MPa. The question is whether such high shear stresses do not exceed the stability limits of the 2H-martensite. As described e.g. by Otsuka et al. (1979), the 2H-martensite tends to undergo further stress-induced martensite-to-martensite transitions (to the β_1'' or β_1' and α_1 phases) at much lower stresses than this maximal value. At the room temperature, Otsuka et al., 1979 observed the $2H \rightarrow \beta_1''$ transition at approximately 320 GPa of unidirectional tensile load (i.e. at 160 GPa of maximal shear stress) and the $\beta_1'' \rightarrow \alpha_1$ transition at 500 GPa of tensile load (250 MPa shear stress). On the other hand, Novák et al. (1999) proved that these stress-induced transitions cannot be observed in compression or in tension along directions not close to [001] in the reference configuration. However, as mentioned also in Novák et al. (1999), a plastic deformation of the 2H-martensite can be observed under unidirectional compressive loads higher than 600 MPa (300 MPa of shear stress). In other words, the material in the points corresponding to the maximal value of the Von Mises stress is subjected to shear loadings which are significantly higher than the limit for the stress-induced $2H \rightarrow \beta_1''$ transition and comparable to the critical stresses for the plastic deformation. Together with the fact that these maxima of the Von Mises stress are (in the both cases) concentrated along the interfaces, this finding may indicate that a part of the elastic energy stored in the microstructure could be relaxed by a presence of additional inelastic strains at these interfaces. These inelastic strains could be provided either by small regions of the stress-induced phases of martensite, or, more probably, by defects such as kinks or twinning dislocations on the twinning plane. (A discussion of the twinning dislocation as a possible source of bending of the twinning plane can be found in Basinski and Christian (1954b) for the compound twinning in the In-Tl system. This discussion is, nevertheless, carried out rather at the atomistic level and within a crystallographic framework, so the question how do these defects affect the compatibility at the continuum level remains open.) However, since the Type-II twinning planes tend to have a rather complicated internal structure (Ostapovets, 2010), the determination of the nature of these defects would require a more detailed analysis of the behavior of the Cu–Al–Ni alloy at the atomistic scale.

Let us now return to the surface energy of the Type-II twins determined from the width of the transition layer at the beginning of this section. If we accept the assumption that the elastic energy of the system is non-negligibly lowered by the defects at the curved interface, the corresponding surface energy responsible for the finite width of the transition layer should be proportionally lower as well. However, since the energies of the defects appearing at the curved interface are not known, no quantitative estimates of the real surface energy can be done.

5. Conclusions

In this paper, detailed experimental observations of the twinned-to-detwinned interface in the microstructure of 2H-martensite of the Cu–Al–Ni shape memory alloy were used for a construction of a FEM model of the transition layer. By this model, the distribution of elastic stress within the observed microstructure was calculated, and the results were compared to the predictions of the theory based on the minimization of the elastic and surface energy.

The most important conclusion to be drawn from this analysis is that the elastic stresses obtained by the FEM calculation seem to be comparable to the stability limits of the 2H-martensite. This finding is, in some sense, in an agreement with the results reported elsewhere in the literature. By using a similar FEM model, Balandraud and Zanzotto (2007) predicted a plastic deformation to appear at the tip of the wedge-microstructure in the Cu–Zn–Al alloy. Ostapovets et al. (2009a,b) analyzed the compatibility at the faceted austenite-to-martensite interface in a thin film of the Cu–Al–Ni alloy (TEM observations) and concluded that the existence of such interface could be enabled by an inelastic slip. Stupkiewicz et al. (2007) do not provide any details on the maxima of the shear stresses calculated for the austenite-to-martensite interface under study, but the elastic energy densities given in this reference (at least 3 MJ m^{-3}, which is about 10 times higher than the average density on cuts of our transition layer close to the tips of the needles; see Fig. 9) indicate that the stability limits for the 2H-martensite can be exceeded as well. From this point of view, it seems that there are indeed some additional inelastic shearing mechanisms taking place in the copper-based alloys and lowering the energy of the close-to-compatible microstructures.

In addition, the analysis presented in this paper indicates that the models based on the minimization of the sum of the elastic and the surface energy can lead to incorrect predictions. Not only that the exact morphology of the transition layer predicted by such a model is slightly different from the experimental observations, but, more importantly, such model does not give even rough estimates of entire energy of the microstructure (if only the elastic strains are taken into account, the energy of the real microstructure is 1.4 times higher than what corresponds to the minimum; if some additional inelastic mechanism is considered, the energy is lowered by relaxation in an unknown way.)

Acknowledgements

This work has been supported by the Czech Science Foundation (Project No. 202/09/P164), by the institutional project of IT ASCR v.v.i. (CEZ:AV0Z20760514), and by the research center 1M06031 of the Ministry of Education of the Czech Republic.

References

Abeyaratne, R., Chu, C., James, R.D., 1996. Kinetics of materials with wiggly energies: theory and application to the evolution of twinning microstructures in Cu–Al–Ni shape memory alloy. Philos. Mag. A 73, 1017–1032.
Balandraud, X., Zanzotto, G., 2007. Stressed microstructures in thermally induced M9R–M18R martensites. J. Mech. Phys. Solids 55, 194–224.
Ball, J.M., James, R.D., 1987. Fine phase mixtures as minimizers of energy. Arch. Rat. Mech. Anal. 100, 13–52.
Ball, J.M., James, R.D., 1992. Proposed experimental tests of theory of fine microstructure and the two-well problem. Philos. Trans.: Phys. Sci. Eng. 338, 389–450.
Basinski, Z.S., Christian, J.W., 1954a. Experiments on the martensitic trasformation in single crystals of indium–thallium alloys. Acta Metall. 2, 148–166.
Basinski, Z.S., Christian, J.W., 1954b. Crystallography of deformation by twin boundary movements in indium–thallium alloys. Acta Metall. 2, 101–116.
Bhattacharya, K., 2003. Microstructure of Martensite: Why it Forms and How it Gives Rise to the Shape-Memory Effect, first ed. Oxford University Press (Oxford Series on Materials Modelling), New York.
Bhattacharya, K., Li, B., Luskin, M., 1999. The simply laminated microstructure in martensitic crystals that undergo a cubic to orthorhombic phase transformation. Arch. Rat. Mech. Anal. 149, 123–154.
Boullay, Ph., Schryvers, D., Kohn, R.V., 2001. Bending martensite needles in Ni65Al35 investigated by two-dimensional elasticity and high-resolution transmission electron microscopy. Phys. Rev. B 64, 144105-1–144105-8.
Chu, C., 1993. Hysteresis and Microstructure: A Study of Biaxial Loading on Compound Twins of Copper–Aluminum–Nickel Single Crystals. Ph.D. Thesis, University of Minnesota.
Dolzmann, G., 2003. Variational Methods for Crystalline Microstructure-Analysis and Computation. Springer-Verlag, Berlin, Heidelberg.
Finel, A., Le Bouar, Y., Gaubert, A., Salman, U., 2010. Phase field methods: microstructures mechanical properties and complexity. C.R. Physique 11, 245–256.

Glatz, O., Seiner, H., Landa, M., 2009. FEM modelling of elastically strained interfacial microstructures in Cu–Al–Ni single crystals. In: Šittner, P. et al. (Eds.): Proceedings of ESOMAT 2009 – The 8th European Symposium on Martensitic Transformations, Prague, Czech Republic, pp. 3006-p.1–3006-p.6. EDP Sciences (Available Online at www.esomat.org).

Glatz, O., 2010. Mathematical Modelling of Mobility of Martensitic Microstructures. M.Sc. Thesis, Czech Technical University in Prague.

Glatz, O., Seiner, H., Landa, M., 2010. Rate-dependent model of mobility of interfacial microstructures in shape memory alloys. In: Gumbsch, P., Van der Giessen, E. (Eds.), Proceedings of the Fifth International Conference on Multiscale Materials Modelling MMM2010, Freiburg, Germany. Fraunhofer Verlag, Freiburg, pp. 58–61.

James, R.D., Kohn, R.V., Shield, T.W., 1995. Modelling of branched needle microstructures at the edge of a martensite laminate. J. de Physique III 5. pp. C8-235–C8-259.

Landa, M., Sedlák, P., Seiner, H., Heller, L., Bicanová, L., Šittner, P., Novák, V., 2009. Modal resonant ultrasound spectroscopy for ferroelastics. Appl. Phys. A. 93, 557–567.

Li, B., Luskin, M., 1999. Theory and computation for the microstructure near the interface between twinned layers and a pure variant of martensite. Mater. Sci. Eng. A, 237–540.

Novák, V., Šittner, P., Vokoun, D., Zárubová, N., 1999. On the anisotropy of martensitic transformations in Cu-based alloys. Mater. Sci. Eng. A, 280–285.

Novák, V., Šittner, P., Ignacová, S., Černoch, T., 2006. Transformation behavior of prism shaped shape memory alloy single crystals. Mater. Sci. Eng. A, 755–762.

Ostapovets, A., 2010. Atomistic model of type-II twin boundary. Comput. Mater. Sci. 49, 882–887.

Ostapovets, A., Paidar, V., Zárubova, N., 2009a. Austenite–martensite interfaces in strained foils of CuAlNi alloy. Int. J. Mater. Res. 100, 342–344.

Ostapovets, A., Paidar, V., Zárubova, N., 2009b. Cu–Al–Ni microstructure in the phenomenological theory of martensite with lattice invariant deformation. In: Šittner, P. et al. (Eds.): Proceedings of ESOMAT 2009-The 8th European Symposium on Martensitic Transformations, Prague, Czech Republic, pp. 03010-p.1–03010-p.4. EDP Sciences (Available Online at www.esomat.org).

Otsuka, K., Sakamoto, H., Shimizu, K., 1979. Successive stress-induced martensitic transformations and associated transformation pseudoplasticity in Cu–Al–Ni. Acta Metall. 27, 585–601.

Otsuka, K., Wayman, C. (Eds.), 1998. Shape Memory Materials. Cambridge University Press, Cambridge.

Schryvers, D., 1993. Microtwin sequences in thermoelastic Ni_xAl_{100-x} martensite studied by conventional and high resolution transmission electron microscopy. Philos. Mag. A 68, 1017–1032.

Schryvers, D., Boullay, Ph., Kohn, R.V., Ball, J.M., 2001. Lattice deformations at martensite-martensite interfaces in Ni–Al. J. de Physique IV 11. Pr8-23–Pr8-30.

Schryvers, D., Boullay, Ph., Potapov, L.P., Kohn, R.V., Ball, J.M., 2002. Microstructures and interfaces in Ni–Al martensite: comparing HRTEM observations with continuum theories. Int. J. Solid Struct. 39, 3543–3554.

Sedlák, P., Seiner, H., Landa, M., Novák, V., Šittner, P., Manosa, L., 2005. Elastic constants of bcc austenite and 2H orthorombic martensite in CuAlNi shape memory alloy. Acta Mater. 53, 3643–3661.

Seiner, H., 2008. Dynamic and Transient Phenomena in Single Crystals of Shape Memory Alloys. Ph.D. Thesis, Czech Technical University in Prague.

Seiner, H., Landa, M., Sedlák, P., 2008. Shape recovery mechanism observed in single crystals of Cu–Al–Ni shape memory alloy. Phase Trans. 81, 537–551.

Seiner, H., Landa, M., 2009. Non-classical austenite–martensite interfaces observed in single crystals of Cu–Al–Ni. Phase Trans. 82, 793–807.

Seiner, H., Glatz, O., Landa, M., 2009. Interfacial microstructures in martensitictransitions: from optical observations to mathematical modeling. Int. J. Multiscale Comput. Eng. 7, 445–456.

Shilo, D., Medelovich, A., Novák, V., 2007. Investigation of twin boundary thickness and energy in CuAlNi shape memory alloy. Appl. Phys. Lett. 90, 193113-1–193113-4.

Stupkiewicz, S., Maciewski, G., Petryk, H., 2007. Low-energy morphology of the interface layer between austenite and twinned martensite. Acta Mater. 55, 6292–6306.

Waitz, T., Spišák, D., Hafner, J., Karnthaler, H.P., 2005. Size-dependent martensitic transformation path causing atomic-scale twinning of nanocrystalline NiTi shape memory alloys. Europhys. Lett. 71, 98–103.

2.3 Publikace *Neklasická rozhraní austenit-martenzit pozorovaná v monokrystalech slitiny Cu-Al-Ni.*

Bibliografická citace: Seiner, H., Landa, M. Non-classical austenite-martensite interfaces observed in single crystals of Cu-Al-Ni (2009) Phase Transitions, 82 (11), pp. 793-807.

Stručná anotace: Tato publikace se zabývá komplexními rozhraňovými mikrostrukturami vznikajícími při zpětné transformaci, pokud mechanicky stabilizovaným martenzitem není monovarianta (jako v případech předchozích dvou publikaci) ale laminát dvojčat typu Compound. V takovém případě vznikají takzvaná neklasická rozhraní, tvořená kompatibilní hranicí mezi austenitem a dvěma navzájem se křížícími systémy martenzitických dvojčat. V publikaci je kromě popisu experimentální přípravy takovýchto rozhraní a jejich pozorování optickou mikroskopií provedena také analýza kompatibility pozorovaných rozhraní a diskutována možnost vzniku obecně tvarovaných (zakřivených) ploch habitu mezi heterogenní mikrostrukturou a austenitem.

Příspěvek habilitanta: Veškeré experimentální výsledky prezentované v publikaci a veškerá teoretická analýza (kromě algebraických podmínek kompatibility v příloze článku, které byly převzaty ze spolupráce s J. M. Ballem) jsou prací habilitanta. Metodologie přípravy laminátu typu Compound byla vyvinuta ve spolupráci habilitanta a M. Landy.

Phase Transitions
Vol. 82, No. 11, November 2009, 793–807

Non-classical austenite-martensite interfaces observed in single crystals of Cu–Al–Ni

H. Seiner[ab]* and M. Landa[a]

[a]*Institute of Thermomechanics ASCR, Dolejškova 5, 182 00 Prague 8, Czech Republic;*
[b]*Faculty of Nuclear Sciences and Physical Engineering, Czech Technical University in Prague, Trojanova 13, 120 00 Prague 2, Czech Republic*

(*Received 2 July 2009; final version received 26 September 2009*)

Interfaces between austenite and a crossing-twins microstructure consisting of four variants of 2H-martensite are optically observed in a single crystal of Cu–Al–Ni shape memory alloy. It is shown that these non-classical interfaces form during thermally induced transitions from compound twinned 2H-martensite into austenite, which is in agreement with theoretical predictions. Individual twinning systems and martensitic variants involved in the observed microstructure are identified. The corresponding volume fractions are estimated based on the compatibility conditions at the habit plane and the macroscopic geometry of the interface. Miscellaneous topics related to the observed microstructures (formation mechanism and planeness of the interface) are briefly discussed.

Keywords: shape memory alloys; martensitic microstructure; non-classical interfaces; crossing twins

1. Introduction

The shape memory alloys (SMAs) exhibit several unique thermomechanical properties resulting from the ability of these materials to undergo reversible martensitic transitions between the high-temperature phase called austenite and the low-temperature phase called martensite. The martensitic phase may appear in a given number of different crystallographic orientations to the parent austenitic lattice (the so-called variants of martensite), which enables the martensites to form fine, geometrically ordered mixtures called martensitic microstructures. In single crystals of most of the known SMAs, such fine microstructure must form at the transition front during every phase transition (in both directions) to enable the compatibility conditions to be fulfilled at the habit plane [1]. In other words, as the single variants of martensite of these SMAs cannot form any compatible (i.e., geometrically admissible) macroscopic interface with austenite, the transitions occur solely between austenite and those martensitic microstructures which are able to form compatible interfaces with austenite.

A well-known example of an SMA unable to form any austenite-to-single variant interfaces is Cu–Al–Ni (namely the austenite-to-2H martensite transition in this alloy,

*Corresponding author. Email: hseiner@it.cas.cz

ISSN 0141–1594 print/ISSN 1029–0338 online

DOI: 10.1080/01411590903366160
http://www.informaworld.com

see, e.g., [1–3] and the references therein). In this material, three different twinning systems are possible. These are the *Compound system*, where the two variants involved are mirror symmetric, and the *Type-I* and *Type-II* systems, where the relations between the involved variants are more general. The mathematical theory of martensitic microstructures (see the pioneering works by Ball and James [4] or the comprehensive book by Bhattacharya [1] for more details) predicts that the compatibility at the transition front for this material can be achieved by fine lamination *via* either Type-I or Type-II twinning systems with specific volume fractions. On the contrary, for the lattice parameters of the austenite and the 2H martensite of this alloy, lamination *via* the compound system does not fulfill the compatibility conditions with austenite for any volume fraction. Planar interfaces between austenite and a simple laminate (mostly the Type-II system) of martensite in Cu–Al–Ni have been experimentally observed several times (see the list of experimental literature in [2]), whereto habit plane orientations and volume fractions within the laminates determined from the experiments always agreed excellently with the theoretical predictions (a comparison is given in [1]). However, the theory also admits more general microstructures to form compatible interfaces with austenite. In the late 1990s, Ball and Carstensen [5] have published a theoretical analysis of the so-called *non-classical interfaces* (i.e., interfaces between austenite and any other microstructure than the first-order laminate) for a cubic-to-tetragonal transition. Although Ball and Carstensen have shown that such interfaces are possible for a wide range of lattice parameters, their results did not meet an adequate attention in the SMA community, since not supported by any experimental evidence of the existence of such microstructures. In 2005, Waitz [6] observed unique self-accommodated crossing-twins microstructure in bulk nanocrystalline Ni–Ti alloy, and has shown by a theoretical analysis that these nanoscopic checkerboard-like patterns of four variants of martensite could be able to form compatible planar interfaces with austenite. More recently, Seiner et al. [7] reported the microstructural mechanisms of the shape recovery process observed optically in Cu–Al–Ni single crystals. In a later, more detailed paper [8], the same authors have brought an analysis of the interfacial microstructures (X and λ interfaces) formed during this process. In one of the examined specimens, planar interfaces were observed between austenite and a Type-II laminate crossed by less than 5% volume fraction of thin needles of compound twins (microstructure termed *weakly non-classical interface* in [8]).

This article presents a continuation of the experimental research of the shape recovery processes in Cu–Al–Ni single crystals summarized in [8]. The experimental procedure has been modified in order to increase the volume fraction of the compound twins within the interfacial microstructure, i.e., to prepare macroscopic, fully non-classical interfaces instead of weakly non-classical only. The theoretical analysis of such interfaces was presented by Ball et al. in [9], where the first optical micrographs of the non-classical interfaces in Cu–Al–Ni were also shown. This article does not report any further development in the theoretical description of the non-classical interfaces, but employs the findings of [9] for the interpretation of observations.

2. Formation of non-classical interfaces

Before the description of the own experimental procedure and the obtained results, we will briefly summarize the terminology used throughout this article and make some preliminary theoretical discussion of what microstructures can be expected to appear.

2.1. *Notes on terminology*

Throughout this article, we will use the same terminology as in [8,9]. Namely, the following terms will be essential.

We will use the term *mechanically stabilized martensite* for any martensitic microstructure which cannot directly form a compatible interface with austenite. It can be either a single variant, or, for example, a laminate of compound twins, or Type-I or Type-II laminates with other volume fraction than those enabling compatible connection to austenite. The reason why such microstructures are called *mechanically stabilized* is clearly explained in [10,11] and discussed in [8]. The inability of such microstructure to transform directly into martensite shifts the A_s temperature (austenite start, i.e., the temperature at which the material starts transforming back to austenite) significantly upwards.

We will use the term *shape recovery process* for thermally induced return of the mechanically stabilized martensite into austenite. As this term indicates, this return is always accompanied by the change of the macroscopic shape of the specimen. Indeed, according to this definition, the thermally induced return from a self-accommodated microstructure (the only martensite-to-austenite transition not accompanied by any shape change) cannot be called the shape recovery process, as the self-accommodated microstructure is composed of twinned regions able to form compatible interfaces with austenite, and thus, is not mechanically stabilized.

We will use the term *interfacial microstructure* for any microstructure formed between austenite and mechanically stabilized martensite during the shape recovery process. The interfacial microstructure borders compatibly to austenite on one side and to the stabilized martensite on the other. The propagation of this interfacial microstructure enables the growth of austenitic region and simultaneous disappearance of the stabilized martensite. More about this process can be found again in [7,8].

We will use the term *X-interface* for a special kind of interfacial microstructure, characterized by two intersecting habit planes (interfaces between this microstructure and austenite) and two intersecting planar interfaces between this microstructure and the mechanically stabilized martensite. In the *X*-interface, the habit planes and the interfaces with the mechanically stabilized martensite intersect in the same line, so the whole interfacial microstructure looks like capital X. This interfacial microstructure was theoretically analyzed by Ruddock [12], who has shown that the *X*-interface cannot be fully compatible for the Indium–Thallium alloy. Similar analysis was done for the Cu–Al–Ni alloy in [13], showing again that the *X*-interface in this alloy requires elastic strains to achieve compatibility. In [8,14] (the first paper documenting this kind of microstructures), it is distinguished between the *X*-interface and λ-interface, depending on how the twins inside the microstructure are oriented. As the difference between these two interfacial microstructures does not play any role in this article, we will simply use the term *X*-interface for both the *X* and the λ interfacial microstrucutres.

2.2. *Theoretical predictions for the shape recovery process from compound twinned structures*

In this section, we will use the findings from Seiner et al. [8] to predict how the interfacial microstructures should look if the shape is not recovered from a single variant of martensite, but from a laminate of compound twins. Let us consider a specimen of a SMA. In the beginning, the specimen is in austenite. Let consider that it is

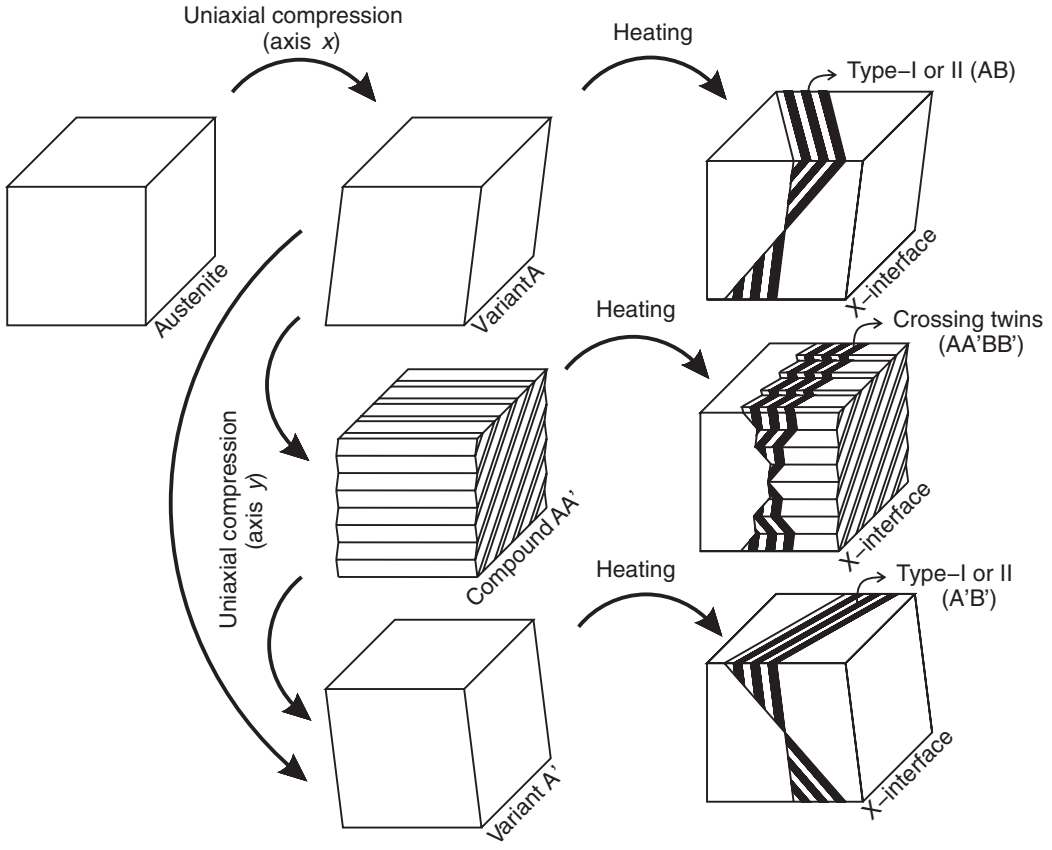

Figure 1. Scheme of the proposed experimental procedure.

subjected to the following sequence of mechanical and thermal loadings (see Figure 1 for an outline):

(i) **Stress-induced transition:** The specimen is, by applying uniaxial compression, transformed from austenite into a single variant of martensite (let us denote this variant as variant A and the axis along which the compression is applied as x).

(ii) **Mechanical stabilization:** Once the specimen is fully transformed into martensite, the loading is removed. However, the specimen does not return back to austenite, as the obtained single variant is mechanically stabilized, i.e., the A_s temperature is shifted upwards.

(iii) **Reorientation:** The specimen is uniaxially compressed again, but in another direction (perpendicular to the previous one, let it be denoted by y). Under loading in this direction, the specimen starts reorienting *via* the compound twinning system into another variant of martensite (denoted as A'). A fine laminar structure of compound twins appears in the specimen, whereto the volume fraction of A' in A increases continuously until the transition is completed. In every point of the transition, the loading can be interrupted and removed, which means we can obtain finely compound-twinned specimens with arbitrary volume fractions of variant A' in variant A. Let it be pointed out that such compound laminates are mechanically stabilized as well.

(iv) **Shape recovery *via* interfacial microstructures:** After the loading is removed, the specimen is heated up. This induces the shape recovery process. As mentioned

above, such transition is always provided by the formation and propagation of interfacial microstructures. The last column of Figure 1 shows the three possibilities how this transition could look like:

- A-to-austenite (the first row in Figure 1): If the specimen is in single variant A (i.e., no compression along the y axis was applied), a classical X-interface forms and propagates, so the specimen exhibits exactly the same behavior as those examined in [8]. Within this preliminary discussion, we will focus on one of the two twinned regions in the X-interface only. One of the variants included in this twinned region must be A (as this twinned region borders to this variant by a twinning plane). The second variant is some variant B able to form Type-I/II twins with variant A.
- A'-to-austenite (the third row in Figure 1): If the specimen is in single variant A' (the reorientation by the compression along the y axis was completed), the behavior is very similar to the previous case, with the only difference being that the observed twinned region of the X-interface is composed of variant A' and variant B' (where B' is able to form Type-I/II twins with variant A'). As the variants A and A' are mirror symmetric (the mirror plane is their compound twinning plane), the X-interfaces formed during the A-to-austenite transition and the A'-to-austenite transition possess this mirror symmetry as well, which means that the variants B and B' are also able to form compound twins with the same twinning plane as A and A'.
- AA'-to-austenite (the second row in Figure 1): The most interesting situation occurs when the shape recovery process is starting from the compound-twinned structure AA' (i.e. the reorientation by the compression along the y axis was interrupted somewhere in the middle). The X-interface (or some similar interfacial microstructure) forms again *via* Type-I/II twinning, since the already present compound twins cannot form any compatible interface with austenite. However, this Type-I/II twinning does not cause any disappearance of the compound twins. Instead, the Type-I/II twins penetrate the compound system and form a checkerboard-like microstructure with it. In the observed twinned region of the X-interface, the included variants are now A, A', B and B', where the compound systems AA' and BB' cross compatibly the Type-I/II systems AB and $A'B'$. The fact that in the Cu–Al–Ni alloy the compound and Type-I/II twins can cross compatibly was first mentioned in [3], and further discussed in [8,9]. Here, let us mention only that the variants A, A', B, B' can form the crossing-twins microstructure (a checkerboard-like pattern given by compound twinning planes AA' and BB' and Type-I/II twinning planes AB and $A'B'$) only if the compound twinning planes AA' and BB' are the same. Then, the resulting pattern indeed looks like the sketch in Figure 1: the compound twinning planes are straight and induce kinks on the Type-I/II twinning planes which change their orientation depending on whether they run between variants A and B or between variants A' and B'.

2.3. *Experimental procedure and observed microstructures*

The formation of non-classical interfaces, namely interfaces between austenite and two mutually crossing systems of martensitic twins, was observed in a single crystal of the

Cu–Al–Ni alloy. The examined specimen was a $3.9 \times 3.8 \times 4.2\,\mathrm{mm}^3$ rectangular prism of the austenitic phase of Cu–Al–Ni, cut from a larger single crystal such that the normals to the specimen's faces had approximately the principal crystallographic directions $\langle 100 \rangle$. The original single crystal was grown by a Bridgman method at the Institute of Physics, ASCR in Prague, the exact orientations were determined by Laue method as ([0.988; −0.122; 0.087], [0.140; 0.980; 0.070], [−0.105; −0.052; 0.993]), which differs from the principal orientations by less than 10°. (Further in the text we will denote individual faces of this specimen by their approximate outer normals in austenite, e.g. $[100]_A$ or $[\bar{1}00]_A$.) The transition temperatures of the specimen were determined by DSC as follows: the martensite start temperature was $M_S = -5°\mathrm{C}$, the martensite finish temperature was $M_F = -22°\mathrm{C}$, austenite start temperature was $A_S = 26°\mathrm{C}$, and the austenite finish temperature was $A_F = 52°\mathrm{C}$.

By uniaxial compression in a bench wise, this specimen was transformed into a single variant of martensite. As the austenitic specimen was cut along principal (e.g., $\langle 100 \rangle_A$) faces, the faces of resultant martensitic parallelepiped obtained after compression were approximately equal to $(010)_\mathrm{M}$, $(101)_\mathrm{M}$, and $(10\bar{1})_\mathrm{M}$ planes in martensite (in the crystallographic system for variant No.1 using the notation summarized in the Appendix). According to [11], we can predict which twinning systems will be activated by uniaxial compression in directions perpendicular to these planes. As far as the $[010]_\mathrm{M}$ direction is concerned (i.e. the direction in which was the specimen compressed during the stress-induced transition from austenite), further compression in this direction does not induce any reorientation, the specimen becomes only elastically deformed. Compression in two perpendicular directions induces reorientation into another variant of martensite. The compressions in directions close to $[101]_\mathrm{M}$ and $[10\bar{1}]_\mathrm{M}$ can initiate twinning both in Type-II and compound systems, depending on the exact orientations. The specimen used enabled the compound reorientation under compression in the $[101]_\mathrm{M}$ direction and the reorientation *via* the Type-II system under compression in the $[10\bar{1}]_\mathrm{M}$ direction. For this reason, this specimen was suitable for the proposed experiments.

Prior to the own experiments, the specimen was mechanically polished and cleaned by ethyl alcohol. The formed microstructures were observed by an OLYMPUS SZ60 stereomicroscope, and recorded by an uEye UI-2250-C camera (chip size 1/1.800″) with full 1600×1200 pts resolution. The obtained micrographs were converted into a 16-bit grayscale with proper intensity rescaling such that the microstructures were clearly visible. Let it be pointed out here that, due to compressions of the specimen in two different direction (one inducing the stress induced transition, the second the formation of compound twins), most of the optical micrographs presented in this article were taken from the faces on which the loading was previously applied. For this reasons, the observed surfaces are significantly rough and damaged and the resulting micrographs are significantly less distinct than those in [8] (or in most of the literature on SMA single crystals, e.g., [3]). This effect was even amplified by several repetitions of the experiments.

In Figure 2(a), an optical micrograph of the specimen after the steps (i), (ii), and (iii) of the above-proposed experimental procedure is shown, i.e., after the stress-induced transition, the mechanical stabilization and the partial reorientation *via* the compound twinning from variant A into variant A'. As clearly seen from this micrograph, the real microstructure obtained by this sequence of mechanical loads slightly differed from what predicted in the previous section: The compound laminate obtained was heterogeneous and, in the upper right corner, it was also intersected by few needles of another twinning system. However, after short localized heating (from the lower right corner), the material indeed formed a fully non-classical interface between austenite and the two crossing

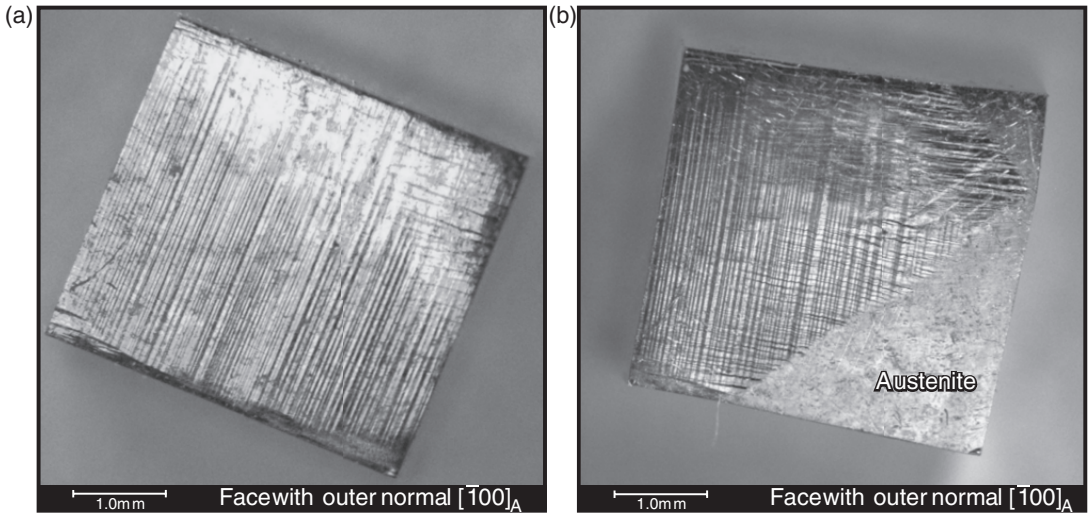

Figure 2. Compound-twinned structure (initial compound laminate, on the left) gets crossed by a Type-II twinning system during the shape recovery process (on the right). Optical microscopy.

systems of martensitic twins (optical micrograph on the right of Figure 2). On the other hand, the whole interfacial microstructure formed in the specimen was significantly more complicated than the *X*-interface sketched in Figure 1. At the boundary between the two crossing twinning systems and the initial compound laminate, a rather unordered mixture of various variants appeared. This effect was observed during most of the repetitions of the experimental procedure; simple *X*-interfaces were observed only in the cases when the compound volume fraction (A in A' or vice-versa) was close to zero, i.e., when the weakly non-classical interfaces formed, similar to those obtained in [8].

A typical example of the observed microstructures is given in Figure 3. It shows an *X*-interaface separating the austenite from the initial compound-twinned martensite. The global shape of this interface can be seen in Figure 3(a). At faces with outer normals $[100]_A$, $[010]_A$, and $[\bar{1}00]_A$, this interfacial microstructure forms a non-classical interface with austenite, as clearly seen in the zoomed areas in Figure 3(c–e). The zoomed area in Figure 3(f) reveals that only the Type-I/II twins can be observed at the face with outer normal $[001]_A$, i.e., the compound twinning planes are approximately parallel to this face.

At the face of the outer normal $[00\bar{1}]_A$, the martensitic microstructure at the interface with austenite can be again expected to be a pattern of two crossing twinning systems. However, in the particular run of the experiment for which the optical micrograph in Figure 3 were taken, the microstructure in this region was extremely fine and its reliable observation was, thus, impossible due to the roughness of the surface (see the comment on the quality of the surfaces above in this section). Similar effects were observed repeatedly: one part of the *X*-interface always formed a clearly visible non-classical interface with austenite, whereas the second part was extremely finely twinned. For the same reasons, it was impossible to observe the actual microstructure near the crossing line of the *X*-interface. The microstructure there (not only inside the crossing-twins regions but also in the initial compound laminate) was extremely fine and rather chaotic. Figure 4 shows two optical micrographs taken in the same run of the experiment as those in Figure 3. The difference between the fineness of the twins in the two regions of the *X*-interface

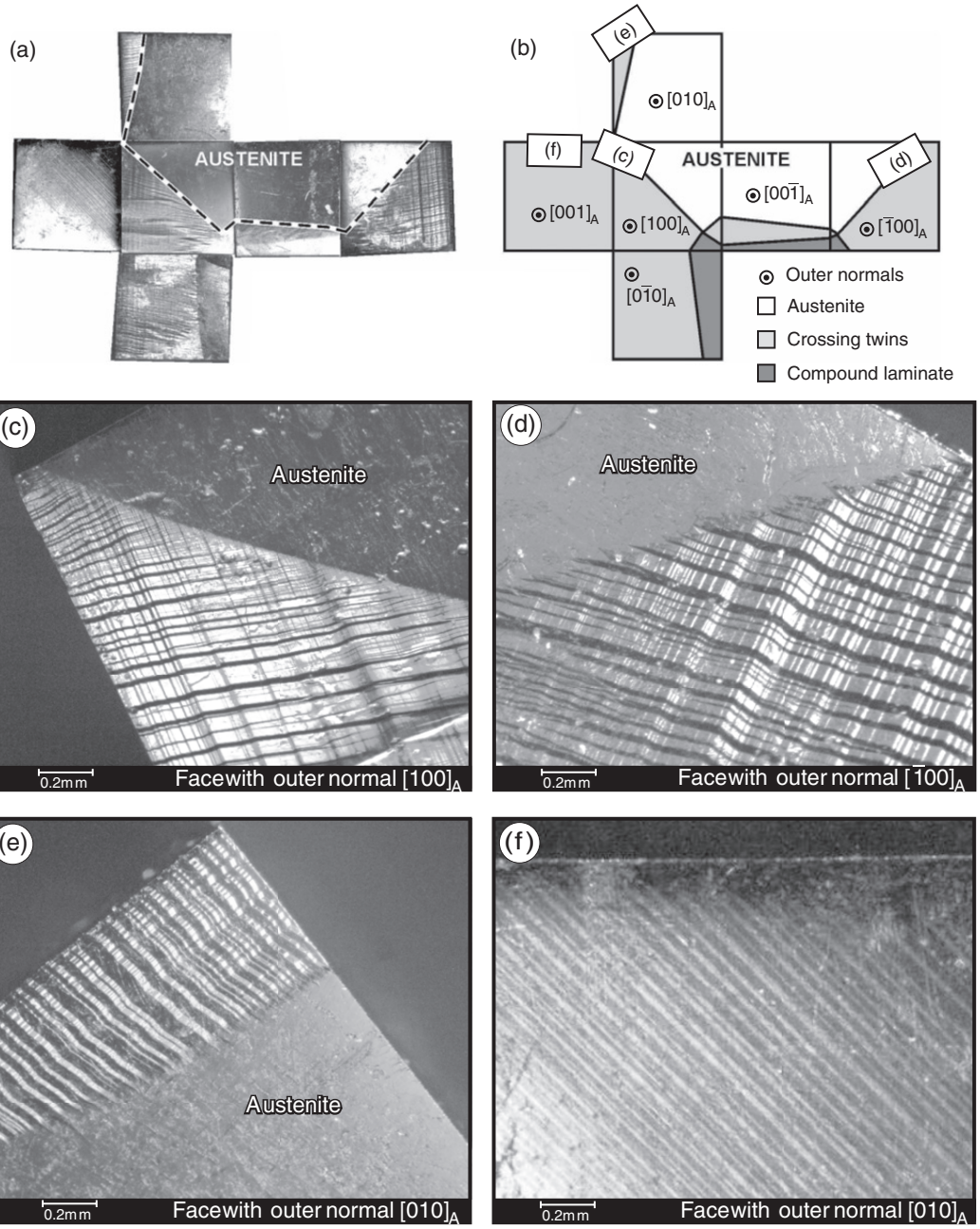

Figure 3. The interfacial microstructure formed during the shape recovery process from a compound twinned structure: (a) global view composed of optical micrographs of individual faces of the specimens, the dashed line follows the habit planes; (b) scheme showing the placement of zoomed areas (c–f).

is clearly seen in Figure 4(a), showing the crossing point of the X-interface at the face with outer normal $[100]_A$. The chaotic character and fineness of the microstructure in the region spanning over faces with outer normals $[100]_A$, $[00\bar{1}]_A$, and $[\bar{1}00]_A$ is illustrated by Figure 4(b). These observations reveal that the real interfacial microstructures formed during the shape recovery process from the compound laminate are significantly more complicated that those predicted by the preliminary theoretical analysis (Figure 1).

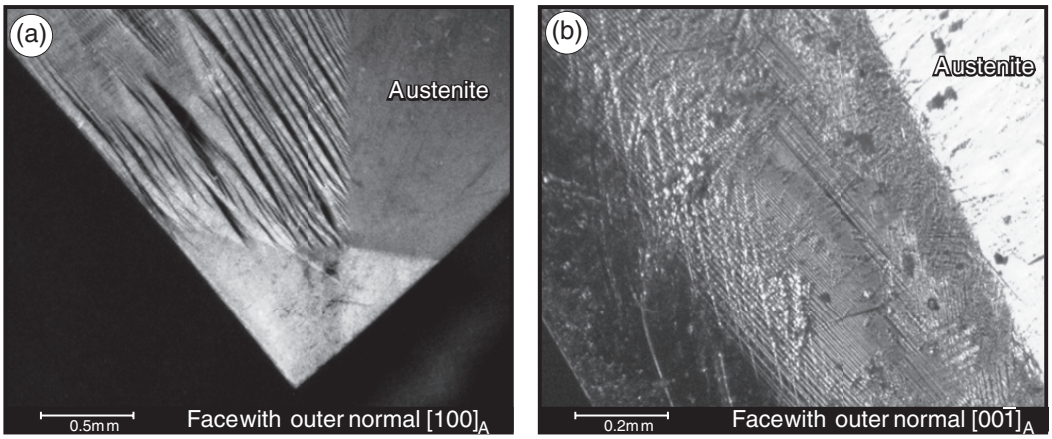

Figure 4. Optical micrographs illustrating the difference between the two regions of the observed interfacial micorstructure. (a) The X-interface at the face with outer normal $[100]_A$; (b) complicated, finely twinned interfacial region at the face with outer normal $[00\bar{1}]_A$.

3. Discussion and miscellaneous comments

3.1. *Identification of variants, twinning systems and volume fractions*

Within the theoretical discussion of the observed interfaces, it is necessary to identify which variants of martensite and which twinning systems are involved. This will be done in this section for the microstructure shown in Figure 3 (namely for the region where the existence of non-classical interfaces between austenite and martensite is indubitable, i.e., the region spanning over faces with outer normals $[100]_A$, $[010]_A$, $[001]_A$, and $[\bar{1}00]_A$), using consistently the notation of variants from [15], which can be also found in the Appendix.

As clearly seen in Figure 3, the twinning plane of the initial compound twinning system is perpendicular to the $[001]_A$ direction. This compound twinning plane appears also in the crossing-twins microstructure at the non-classical interfaces and must be, consequently, equal to the compound twinning planes of both systems AA' and BB', as mentioned in Section 2.2. The pairs of variants enabling such compound-twinning planes are No.1–No.2 and No.3–No.4 only. We can directly conclude that these four variants are involved in the observed crossing-twins microstructure. Similarly, the identification of the Type-I/II twinning systems is also simple. At the face with an outer normal $[001]_A$ (i.e. the face parallel to the compound twinning planes), the Type-I/II twinning planes are clearly visible (Figure 3(f)). The intersection of these planes with the face contains approximately a 45° angle with the edges of the specimen. There are four possible combinations of variants and twinning system:

(i) Type-I twins of variants No.1 and No.4 ($\boldsymbol{n}_{14} = (\sqrt{2}/2; \sqrt{2}/2; 0)$).
(ii) Type-I twins of variants No.2 and No.3 ($\boldsymbol{n}_{23} = (\sqrt{2}/2; \sqrt{2}/2; 0)$).
(iii) Type-II twins of variants No.1 and No.3 ($\boldsymbol{n}_{13} = (0.688; 0.688; 0.228)$).
(iv) Type-II twins of variants No.2 and No.4 ($\boldsymbol{n}_{24} = (0.688; 0.688; -0.228)$).

In other words, the variants involved in the observed microstructure can either be $A \sim$ No.1, $A' \sim$ No.2, $B \sim$ No.4, and $B' \sim$ No.3 with Type-I twinning, or $A \sim$ No.1, $A' \sim$ No.2, $B \sim$ No.3, and $B' \sim$ No.4 with Type-II twinning. However, as seen on the faces with outer normals $[100]_A$, $[\bar{1}00]_A$, and $[010]_A$, respectively (Figure 3(c–e)), the compound

twinning planes induce clearly visible kinks at the Type-I/II twinning planes, which is not possible for Type-I twins since $\boldsymbol{n}_{23}=\boldsymbol{n}_{14}$ for this twinning system. Thus, the twinning system crossing the compound twins in the analyzed microstructure must be Type-II and the individual variants are $A\sim$No.1, $A'\sim$No.2, $B\sim$No.3, and $B'\sim$No.4.

Unfortunately, the volume fractions of the variants involved cannot be determined using any similar manner. The fineness and heterogeneity makes the direct estimation of averaged volume fractions impossible. However, some rough estimates can be done based on the condition of the geometric compatibility at the observed non-classical interface. In [9], it was shown that a crossing-twins microstructure of variants A, A', B, and B' including AA' and BB' compound twins and AB and $A'B'$ Type-II twins can form a compatible planar interface with austenite if (and only if)

$$\lambda^2-\lambda=-\frac{a_0+a_2(\Lambda^2-\Lambda)}{a_1+a_3(\Lambda^2-\Lambda)}, \tag{1}$$

where λ is the volume fraction of variant B in the AB Type-II laminate (and simultaneously of variant B' in the $A'B'$ laminate), Λ is the volume fraction of variant A' in the AA' compound laminate (and simultaneously of variant B' in the BB' laminate), and a_0, a_1, a_2, and a_3 are the coefficients given by the lattice parameters of the examined material. Explicit formulas for these coefficients can be found in the Appendix. The relation (1) provides for each Λ between 0 and 1 such volume fraction λ (more precisely two volume fractions $\lambda_1<1/2$ and $\lambda_2=1-\lambda_1>1/2$) that the resulting crossing-twins microstructure is rank-one connectible to austenite. Furthermore, numerical simulations presented in [9] show that for Λ varying between 0 and 1, the orientation of the habit plane varies significantly as well. This enables us now to determine the volume fraction Λ inversely, i.e., to tune it such that the orientation of the habit plane evaluated for it using the numerical procedures described in [9] is in optimal agreement with the optical micrographs in Figure 3. Using such approach, it was shown that the averaged habit plane orientation seen in this figure is well approximated for $\Lambda\approx 1/3$ and for the smaller of the two possible solutions of (1) (The calculation was done for the normals of the observed faces taken as exactly equal to $[100]_A$ and $[010]_A$. However, as the initial compound laminate is significantly heterogeneous and as the observed habit interfaces are not exactly planar (Section 3.2.3), the obtained estimate of the volume fraction Λ is quite rough, and thus, also acceptable for the exact orientations of the individual faces as obtained by the Laue method.) The geometry of the crossing-twins microstructure constructed for these volume fractions and of the corresponding non-classical interface is sketched in Figure 5, where the shown areas (including the edges of the specimen, etc.) mimic the zoomed areas (c) and (e) of Figure 3. In Figure 5, the parameters used for the optimization of Λ are also shown. These were the angles between the habit plane and the edge of the specimen visible on the face with outer normal $[100]_A$ (approximately 46°) and a similar angle visible on the face with outer normal $[010]_A$ (approximately 100°). Both these angles were approximated by $\Lambda=1/3$ with accuracy better than 1°. Also the averaged orientation of the Type-II twinning planes sketched in Figure 5 is in good visual agreement with what is seen in the corresponding optical micrograph. As the Type-II volume fraction determined for $\Lambda\approx 1/3$ *via* Equation (1) is as well $\lambda\approx 1/3$, we can summarize that the crossing-twins microstructure forming a non-classical interface shown in Figure 3 consists of approximately 1/9 of variant No.4, 2/9 of variant No.3, 2/9 of variant No.2, and 4/9 of variant No.1.

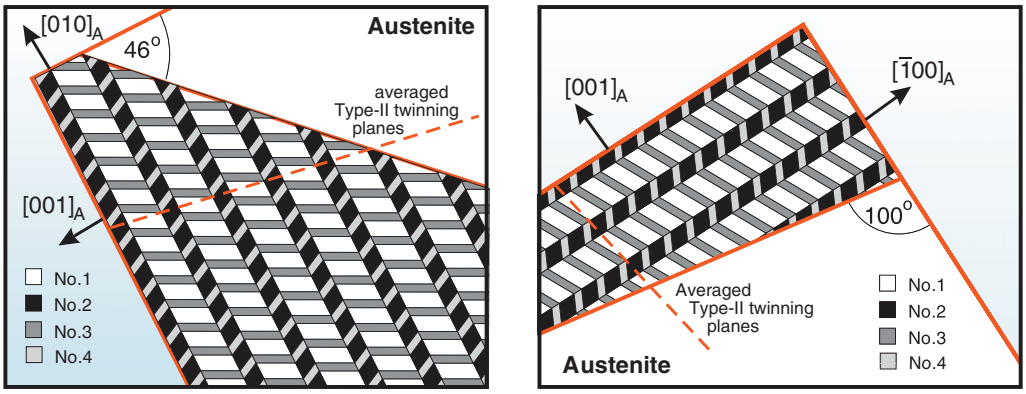

Figure 5. The geometry of the non-classical interfaces evaluated for volume fractions $\Lambda \approx \lambda \approx 1/3$. The shown areas mimic the optical micrographs in Figure 3(c and e).

Note here that the above analysis is valid only for one particular run of the experiment captured by the optical micrographs in Figure 3. The observed microstructures obtained by other repetitions of the experimental procedure differed by the initial volume fraction of the compound twins, and thus, also by the average orientations of the habit plane. However, in most of the runs of the experiment, two main features were observed: First, the Type-I/II twinning planes observed at the face with outer normal $[001]_A$ contained the angle approximately 45° with the edges of the specimen; second, the kinks induced at these planes by the compound twinning planes on faces with outer normals $[100]_A$ and $[010]_A$ were clearly visible. This means that the involved variants were always No.1, No.2, No.3, and No.4 and that the two mutually crossing twinning systems were always compound and Type-II.

3.2. *Miscellaneous comments on the experiments*

The following short comments address diverse topics related either to the experimental procedure or to the observed microstructure.

3.2.1. *Optical microscopy in polarized light*

It is relatively common to use polarized light for optical observations of martensitic microstructures. The advantage is that the use of a polarizing filter enables a selective display of individual martensitic variants or of austenite due to the differences in the slopes of the surface relief. This is optimal for the observation of the first-order laminates; the selective display of one of the variants enables the binarization of the obtained images and consequent automatized determination of volume fractions, twinning plane orientations, etc. [16]. However, this advantage becomes questionable for complex microstructures such as the crossing-twins microstructure reported in this article, where four different martensitic variants are observed. On the other hand, the selective display of one or two variants enables a more detailed analysis of the microstructure close to the interface with austenite. The optical micrographs of this region taken in polarized light (Figure 6) prove that the observed interfaces are really non-classical, i.e., none of the four variants (and none of the two twinning systems) disappear in the vicinity of the interface to austenite. These micrographs (namely the micrograph on the left of Figure 6) also clearly

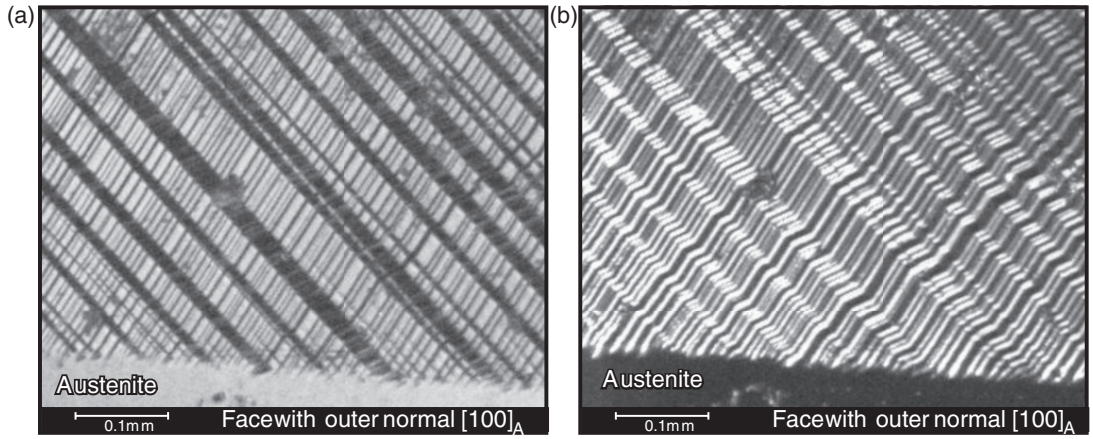

Figure 6. The same area of the non-classical interface (face with outer normal $[100]_A$) observed through a polarizing filter at two different rotation angles. On the left, variant No.1 and austenite are selectively displayed, on the right, martensitic variants Nos. 3 and 4 are selectively displayed.

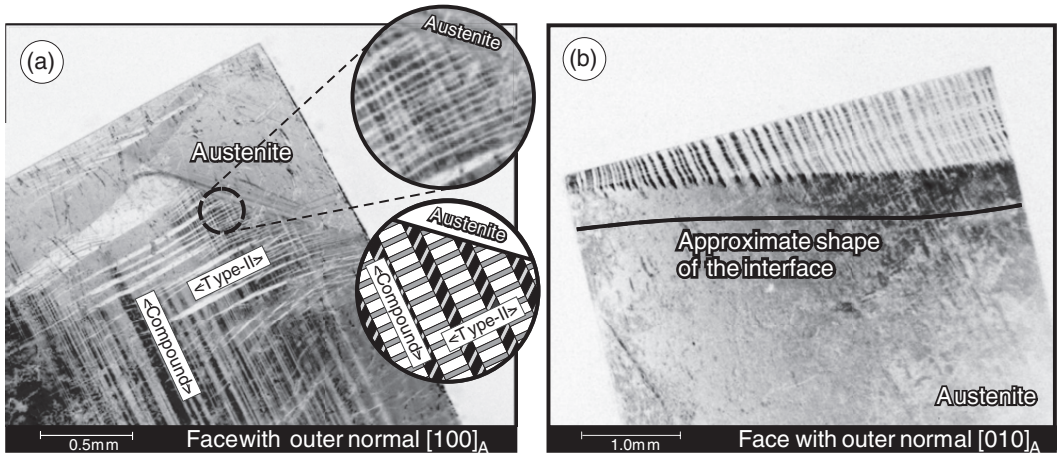

Figure 7. (a) Nucleation of austenite into the initial compound-twinned structure (optical microscopy, inverted grayscale). The zoomed area (with the illustrative scheme) shows the region where the non-classical interface forms. (b) Clearly visible curvature of the phase interface at the face with outer normal $[010]_A$ (optical microscopy, inverted grayscale; the micrograph was taken during the same run of the experiment as those in Figure 3).

illustrate the morphology of the crossing-twins microstructure, especially the kinks induced on the compound twinning planes by the intersection of Type-II twins.

3.2.2. *Nucleation of austenite*

The shape recovery process described in this article starts from the nucleation of austenite in the compound-twinned (i.e., mechanically stabilized) martensite. This nucleation is an extremely complicated microstructural process, as the martensite around the nucleus must locally rearrange to ensure the compatibility (i.e., the interfacial microstructure nucleates together with austenite). The question is whether the microstructure surrounding the nucleus already contains some non-classical interfaces, or whether these form later during the shape recovery process. In Figure 7(a), a nucleus of austenite in a corner of the examined specimen is shown. Similarly, as for the nucleation of austenite from a single

variant of martensite mentioned in [8], the nucleus is surrounded by a complicated twinned structure ensuring the compatibility. However, it is clearly seen that in the area where the compound twinning planes touch the nucleus, thin needles of Type-II twins appear and form locally a non-classical interface (see the zoomed area in Figure 7(a) and the corresponding scheme).

3.2.3. *Curved interfaces*

As clearly seen in the optical micrographs in Figures 2 and 3, the real interfaces between austenite and the crossing twins is approximately planar. On the other hand, especially the micrographs in Figure 3(c and e) reveal some slight deviations of the habit planes (habit interfaces) from exact planeness (in Figure 7(b), the approximate shape of this slightly curved interface is sketched in the optical micrograph of the face with outer normal $[010]_A$ taken during the same run of the experiment as Figure 3). This is natural due to the fact that the initial compound-twinned laminate is never exactly homogeneous and, consequently, the resulting crossing-twins microstructure cannot be compatibly connected to austenite over one planar habit plane. This fact requires a deeper discussion: although the results of [9] show that the orientation of the habit plane varies with the volume fraction λ, it is not clear whether these variations enable a compatible connection to austenite, or whether the curved interface can be obtained with the presence of elastic strains only. The problem is actually being solved by Ball et al. [9] (according to [17]).

4. Summary

In this article, the optical observations of interfaces between austenite and a crossing-twins microstructure of 2H martensite of the Cu–Al–Ni SMA were presented. In agreement with the theoretical predictions and with the results of [8], such non-classical interfaces formed during the shape recovery process from a compound-twinned single crystal of this alloy. The optical micrographs were used for the identification of twinning systems and variants of martensite involved in the microstructure, as well as for the estimation of volume fractions, for which the theoretical results of [9] were used.

Acknowledgements

This work was supported by the project A200100627 of the Grant Agency of ASCR, the project No. 202/09/P164 of the Czech Science Foundation, and by the institutional project of IT ASCR v.v.i. (CEZ:AV0Z20760514).

References

[1] K. Bhattacharya, *Microstructure of Martensite*, Oxford University Press, New York, 2003.
[2] K.F. Hane, *Microstructures in thermoelastic martensites*, *Ph.D. thesis*, University of Minnesota, 1998.
[3] C. Chu and R.D. James, *Analysis of microstructures in Cu-14.0%Al-3.9%Ni by energy minimization*, J. de Phys IV 5 (1995), pp. 143–149.
[4] J.M. Ball and R.D. James, *Fine phase mixtures as minimizers of energy*, Arch. Rat. Mech. Anal. 100 (1987), pp. 13–52.
[5] J.M. Ball and C. Carstensen, *Nonclassical Austenite-Martensite interfaces*, J. de Phys. IV 7 (1997), pp. 35–40.

[6] T. Waitz, *The self-accommodated morphology of martensite in nanocrystalline NiTi shape memory alloys*, Acta Mater. 53 (2005), pp. 2273–2283.
[7] H. Seiner, M. Landa, and P. Sedlák, *Propagation of an austenite-martensite interface in a thermal gradient*, Proc. Estonian Acad. Sci. 56 (2007), pp. 218–225.
[8] H. Seiner, P. Sedlák, and M. Landa, *Shape recovery mechanism observed in single crystals of Cu–Al–Ni shape memory alloy*, Phase Transitions 81 (2008), pp. 537–551.
[9] J.M Ball, K. Koumatos, and H. Seiner, Lecture at Icomat 2008, Santa Fe (US) 2008 (to appear in: *Proceedings of Icomat 2008*, The Minerals, Metals & Materials Society (TMS), 2009.
[10] C. Picornell, V.A. L'vov, J. Pons, and E. Cesari, *Experimental and theoretical study of mechanical stabilization of martensite in Cu–Al–Ni single crystal*, Mat. Sci. Eng. A 438 (2006), pp. 755–762.
[11] V. Novák, P. Šittner, S. Ignácová, and T. Černoch, *Transformation behavior of prism shaped shape memory alloy single crystals*, Mat. Sci. Eng A 438–440 (2006), pp. 755–762.
[12] G. Ruddock, *A microstructure of martensite which is not a minimiser of energy: the X-interface*, Arch. Rat. Mech. Anal. 127 (1994), pp. 1–39.
[13] H. Seiner, O. Glatz, and M. Landa, *Interfacial microstructures in martensitic transitions: From optical observations to mathematical modeling*, Int. J. Multiscale Com. 7 (2009), pp. 445–456.
[14] Z.S. Basinski and J.W. Christian, *Experiments on the martensitic transformation in single crystals of indium-thallium alloys*, Acta Metall. 2 (1954), pp. 148–166.
[15] P. Sedlák, H. Seiner, M. Landa, V. Novák, P. Šittner, and Ll. Mañosa, *Elastic constants of bcc austenite and 2H orthorhombic martensite in CuAlNi shape memory alloy*, Acta Mater. 53 (2005), pp. 3643–3661.
[16] C. Chu, *Hysteresis and microstructures: A study of biaxial loading in compound twins of copper-aluminum-nickel single crystals*, *Ph.D. thesis*, University of Minnesota, 1993.
[17] J.M. Ball and K. Koumatos, personal communication.

Appendix: Lattice correspondence, Bain tensors, and compatibility parameters

In this Appendix, the notation of the variants used throughout this article is summarized and the explicit formulas for the parameters appearing on the right-hand side of Equation (1) are given.

The individual variants of martensite are represented here as follows. For each variant, the lattice correspondence matrix **P** is given, which is the matrix relating the crystallographic planes in parent single crystal of austenite $(k;\ l;\ m)_A^{\mathrm{T}}$ to the corresponding planes in martensite $(k;\ l;\ m)_M^{\mathrm{T}}$,

$$(k;\ l;\ m)_M^{\mathrm{T}} = \mathbf{P}(k;\ l;\ m)_A^{\mathrm{T}}. \tag{A1}$$

These matrices unambiguously relate the individual variants to the parent lattice of austenite. Moreover, these matrices enable us to evaluate the *Bain tensors* (symmetric parts of polar decomposition of the deformation gradients, see [1] for more details) from the lattice parameters. For each variant, the resulting Bain tensor is also given.

For the variants Nos 1–6, the lattice correspondence matrices and the Bain tensors are:

$$\mathbf{P}_{\mathrm{No.1}} = \begin{pmatrix} 0 & -\frac{1}{2} & \frac{1}{2} \\ 1 & 0 & 0 \\ 0 & \frac{1}{2} & \frac{1}{2} \end{pmatrix}, \quad \mathbf{U}_{\mathrm{No.1}} = \begin{pmatrix} e_b & 0 & 0 \\ 0 & e_d & -e_s \\ 0 & -e_s & e_d \end{pmatrix}, \tag{A2}$$

$$\mathbf{P}_{\mathrm{No.2}} = \begin{pmatrix} 0 & \frac{1}{2} & \frac{1}{2} \\ 1 & 0 & 0 \\ 0 & \frac{1}{2} & -\frac{1}{2} \end{pmatrix}, \quad \mathbf{U}_{\mathrm{No.2}} = \begin{pmatrix} e_b & 0 & 0 \\ 0 & e_d & e_s \\ 0 & e_s & e_d \end{pmatrix}, \tag{A3}$$

$$\mathbf{P}_{\text{No.3}} = \begin{pmatrix} \frac{1}{2} & 0 & -\frac{1}{2} \\ 0 & 1 & 0 \\ \frac{1}{2} & 0 & \frac{1}{2} \end{pmatrix}, \quad \mathbf{U}_{\text{No.3}} = \begin{pmatrix} e_d & 0 & -e_s \\ 0 & e_b & 0 \\ -e_s & 0 & e_d \end{pmatrix}, \tag{A4}$$

$$\mathbf{P}_{\text{No.4}} = \begin{pmatrix} \frac{1}{2} & 0 & \frac{1}{2} \\ 0 & 1 & 0 \\ -\frac{1}{2} & 0 & \frac{1}{2} \end{pmatrix}, \quad \mathbf{U}_{\text{No.4}} = \begin{pmatrix} e_d & 0 & e_s \\ 0 & e_b & 0 \\ e_s & 0 & e_d \end{pmatrix}, \tag{A5}$$

$$\mathbf{P}_{\text{No.5}} = \begin{pmatrix} -\frac{1}{2} & \frac{1}{2} & 0 \\ 0 & 0 & 1 \\ \frac{1}{2} & \frac{1}{2} & 0 \end{pmatrix}, \quad \mathbf{U}_{\text{No.5}} = \begin{pmatrix} e_d & -e_s & 0 \\ -e_s & e_d & 0 \\ 0 & 0 & e_b \end{pmatrix}, \tag{A6}$$

$$\mathbf{P}_{\text{No.6}} = \begin{pmatrix} \frac{1}{2} & \frac{1}{2} & 0 \\ 0 & 0 & 1 \\ \frac{1}{2} & -\frac{1}{2} & 0 \end{pmatrix}, \qquad \mathbf{U}_{\text{No.6}} = \begin{pmatrix} e_d & e_s & 0 \\ e_s & e_d & 0 \\ 0 & 0 & e_b \end{pmatrix}, \tag{A7}$$

where the transformation strains are $e_b = 0.9154$, $e_s = 0.0200$, and $e_d = 1.043$. This notation is the same as used in [8] and defined in [15].

In Section 3.1, Equation (1) was used for approximate estimation of the volume fractions in the crossing-twins microstructure consisting of variants A, A', B, and B'. The parameters $a_0, \ldots, a_3$ are related to the Bain tensors $\mathbf{U}_I$, the shearing vectors $\boldsymbol{b}_{IJ}$ and the twinning plane normals $\boldsymbol{n}_{IJ}$ (where $I, J = A, A', B, B'$, see [8] for exact definition of these vectors), according to the relations derived by Ball and Koumatos in [9]. Here, only the results are listed:

$$a_0 = \det(\mathbf{U}_A^2 - \mathbf{1}), \tag{A8}$$

$$a_1 = -2\boldsymbol{b}_{AB} \cdot \mathbf{U}_A \text{cof}(\mathbf{U}_A^2 - \mathbf{1})\boldsymbol{n}_{AB}, \tag{A9}$$

$$a_2 = -2\boldsymbol{b}_{AA'} \cdot \mathbf{U}_A \text{cof}(\mathbf{U}_A^2 - \mathbf{1})\boldsymbol{n}_{AA'}, \tag{A10}$$

$$a_3 = 4\text{cof}\left(\mathbf{A}_0 + \frac{1}{2}\mathbf{A}_2\right) : \left(\mathbf{A}_1 + \frac{1}{2}\mathbf{A}_3\right) + 4a_1, \tag{A11}$$

where the matrices $\mathbf{A}_0, \ldots, \mathbf{A}_3$ are

$$\mathbf{A}_0 = \mathbf{U}_A^2 - \mathbf{1}, \tag{A12}$$

$$\mathbf{A}_1 = \mathbf{U}_A \boldsymbol{b}_{AB} \otimes \boldsymbol{n}_{AB} + \boldsymbol{n}_{AB} \otimes \mathbf{U}_A^{-1} \boldsymbol{b}_{AB}, \tag{A13}$$

$$\mathbf{A}_2 = \mathbf{U}_A \boldsymbol{b}_{AA'} \otimes \boldsymbol{n}_{AA'} + \boldsymbol{n}_{AA'} \otimes \mathbf{U}_A^{-1} \boldsymbol{b}_{AA'}, \tag{A14}$$

and

$$\mathbf{A}_3 = -(\mathbf{U}_A^{-1}\boldsymbol{n}_{AB} \cdot \boldsymbol{b}_{AA'} + \frac{2\boldsymbol{b}_{AA'} \cdot \boldsymbol{b}_{AB}}{|\boldsymbol{b}_{AB}|^2})\boldsymbol{n}_{AA'} \otimes \mathbf{U}_A^{-1}\boldsymbol{b}_{AB} - \frac{2\boldsymbol{b}_{AA'} \cdot \boldsymbol{b}_{AB}}{|\boldsymbol{b}_{AB}|^2}\mathbf{U}_A \boldsymbol{b}_{AB} \otimes \boldsymbol{n}_{AA'}. \tag{A15}$$

The algebraic operations used in these formulas are the *dot-product* of two vectors $\boldsymbol{a} \cdot \boldsymbol{b} = \sum_j a_j b_j$, the *dyadic product* of two vectors $(\boldsymbol{a} \otimes \boldsymbol{b})_{ij} = a_i b_j$, and the *double-dot product* of two matrices $\mathbf{A} : \mathbf{B} = \sum_i \sum_j A_{ij} B_{ij}$. The symbol cof($\mathbf{A}$) denotes the *cofactor matrix* to the matrix $\mathbf{A}$.

2.4 Publikace *Nukleace austenitu v mechanicky stabilizovaném martenzitu lokalizovaným ohřevem.*

Bibliografická citace: Ball, J.M., Koumatos, K., Seiner, H. Nucleation of austenite in mechanically stabilized martensite by localized heating (2013) Journal of Alloys and Compounds, 577 (SUPPL. 1), pp. S37-S42.

Stručná anotace: V této publikaci je popsána, experimentálně zdokumentována a pomocí metod variačního počtu teoreticky analyzována nukleace austenitu v mechanicky stabilizovaném martenzitu doprovázená vznikem rozhraňové mikrostruktury. Je pozorováno, že k nukleaci vždy dochází v rozích vzorku, bez ohledu na to, kde je aplikován lokalizovaný ohřev. Pomocí zjednodušeného, nelineárně-elastického modelu je pak ukázáno, že k efektivnímu snížení energie může dojít právě jenom ve volném rohu vzorku.

Příspěvek habilitanta: Veškerá prezentovaná experimentální pozorování jsou prací habilitanta. Dále se pak habilitant podílel na formulaci teoretického modelu a diskuzi jeho predikcí ve vztahu k experimentu.

Journal of Alloys and Compounds 577S (2013) S37–S42

Contents lists available at ScienceDirect

Journal of Alloys and Compounds

journal homepage: www.elsevier.com/locate/jallcom

Nucleation of austenite in mechanically stabilized martensite by localized heating

J.M. Ball [a,*], K. Koumatos [a], H. Seiner [b]

[a] Oxford Centre for Nonlinear PDE, Mathematical Instiute, 24-29 St. Giles', Oxford, OX1 3LB, United Kingdom
[b] Institute of Thermomechanics ASCR, Dolejškova 5, 182 00 Prague 8, Czech Republic

ARTICLE INFO

Article history:
Received 15 September 2011
Accepted 14 November 2011
Available online 23 November 2011

Keywords:
Phase transitions
Shape memory
Microstructure
Young measures
Quasiconvexity

ABSTRACT

The nucleation of bcc austenite in a single crystal of a mechanically stabilized 2H-martensite of Cu–Al–Ni shape-memory alloy is studied. The nucleation process is induced by localized heating and observed by optical microscopy. It is observed that nucleation occurs after a time delay and that the nucleation points are always located at one of the corners of the sample (a rectangular bar in the austenite), regardless of where the localized heating is applied.

Using a simplified nonlinear elasticity model, we propose an explanation for the location of the nucleation points, by showing that the martensite is a local minimizer of the energy with respect to localized variations in the interior, on faces and edges of the sample, but not at corners, where a localized microstructure can lower the energy.

1. Introduction

The shape-recovery process, i.e. the thermally driven transition from the low temperature phase (martensite) into the high-temperature phase (austenite), is a fundamental part of the shape-memory effect. For many shape-memory alloys, the critical temperature for initiation of the shape-recovery process is strongly dependent on the microstructure of martensite entering the transition. When the heating is applied on a thermally induced martensitic microstructure obtained by the stress-free cooling of the austenitic phase, the transition starts at a certain temperature, usually denoted as A_S (austenite start). However, if the material in the martensitic phase is, prior to the heating, deformed (i.e. if the microstructure is reoriented by application of external mechanical loads), this critical temperature can be shifted significantly upwards. This effect is called the mechanical stabilization of martensite and has been documented for both single crystals and polycrystalline shape-memory alloys (SMAs) [1,2].

The difference between the shape-recovery process from the mechanically stabilized martensite and from the thermally induced martensitic microstructure was clearly illustrated by acoustic emission (AE) measurements by Landa et al. [3]. The AE method is based on detecting and counting the number of acoustic signals emitted by the material during the course of the transition (see Refs. [4,5] for an example of the use of AE for characterization of the martensitic transitions in SMAs). Fig. 1 (taken from Ref. [3] with courtesy of M. Landa) gives an illustrative example of the comparison of AE records obtained for the same single crystal of the Cu–Al–Ni alloy undergoing the transition in these two different regimes. For the thermally induced microstructure, more than 90% of AE events occur in a temperature range between the austenite start temperature A_S and the austenite finish temperature A_F, which is in agreement with DSC measurements for the same material.[1] The transition in this temperature interval is preceded by a small number of events (less than 10%) appearing below A_S. These events can be ascribed to the formation of nuclei of austenite in the thermally induced martensitic microstructure. Above A_S, these nuclei grow successively through the material and provide the transition. For the stabilized martensite, more than 90% of the events are recorded within a very narrow temperature interval. As observed by Seiner et al. [6], the transition from the mechanically stabilized martensite is provided by the formation and propagation of special interfacial microstructures, which interpolate between austenite and mechanically stabilized martensite ensuring the kinematically compatible connection between them. These microstructures are able to exist and propagate in a wide range of temperatures and thermal gradients [7]. Thus, the AE record for the stabilized martensite can be interpreted as follows: the small number of AE events detected below the narrow interval corresponds to the nucleation of austenite. As soon as the nucleation barrier is overcome, the interfacial microstructure propagates abruptly through the

* Corresponding author. Tel.: +44 1865 615110; fax: +44 1865 615101.
E-mail addresses: ball@maths.ox.ac.uk (J.M. Ball), koumatos@maths.ox.ac.uk (K. Koumatos), hseiner@it.cas.cz (H. Seiner).

[1] These temperatures, however, differ from the transition temperatures of the material used in Section 2 of this paper, since the heat treatment of the material used by Landa et al. [3] was slightly different.

0925-8388/$ – see front matter © 2011 Elsevier B.V. All rights reserved.
doi:10.1016/j.jallcom.2011.11.070

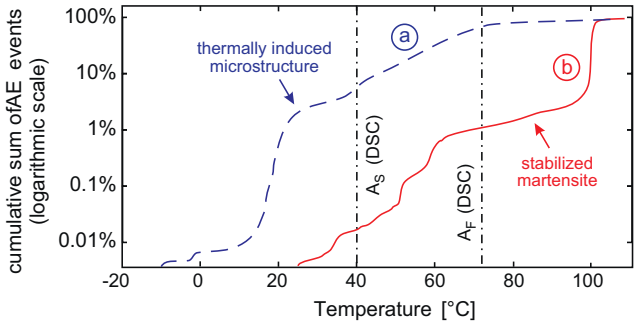

Fig. 1. Illustrative comparison of AE records for the transitions of Cu–Al–Ni single crystal from the thermally induced and mechanically stabilized states. (a) gradual increase of the number of events between A_S and A_F for the thermally induced microstructure; (b) abrupt transition of the stabilized martensite within a narrow temperature interval. The 100% corresponds to $\sim 10^7$ events.

specimen and no further increase of the temperature is necessary. This shows how essential the nucleation process is for the effect of mechanical stabilization and the shape-recovery process in general.

This mechanical stabilization effect resulted in a rather surprising nucleation mechanism of austenite in a Cu–Al–Ni single crystal. In a simplified setting, we provide a mathematical explanation for this mechanism, based on ideas of the modern calculus of variations.

2. Experimental observations

The observations that follow were made on a single crystal of Cu–Al–Ni, prepared by the Bridgman method at the Institute of Physics, ASCR. The specimen was a prismatic bar of dimensions 12 mm×3 mm×3 mm in the austenite with edges approximately along the principal directions of the austenitic phase (see Ref. [6] for a detailed description). The martensite-to-austenite transition temperatures determined by DSC were $A_S = -6\,^\circ$C and $A_F = 22\,^\circ$C. The critical temperature T_C for the transition from the stabilized martensite induced by homogeneous heating for this specimen was $\sim$60 °C. This was estimated from optical observations of the transition in this specimen with one of its faces laid on and thermally contacted with a gradually heated Peltier cell, using a heat conducting gel.

The specimen was subjected to the following experimental procedure:

a) by unidirectional compression along its longest edge, the specimen was transformed into a single variant of mechanically stabilized 2H martensite. Due to the mechanical stabilization effect the reverse transition did not occur during unloading.
b) the specimen was then freely laid on a slightly pre-stressed, free-standing polyethylene (PE) foil (thickness 10 μm, temperature resistance up to 140 °C). This ensured that there were minimal mechanical constraints to the specimen during the observations.
c) the specimen was locally heated by touching its surface with an ohmically heated tip of the Solomon SL-30 (Digital) soldering iron with temperature electronically controlled to be 200 °C (control accuracy $\sim \pm 5\,^\circ$C), i.e. significantly above the A_S and T_C temperatures. The nucleation of austenite was optically observed and recorded by a conventional CCD camera (7× optical zoom, 25 frames/s, PAL resolution with `mpeg` compression).

The localized heating was applied in three different ways: (i) with the tip touching one of the corners surrounding the upper face; (ii) with the tip touching one of the edges, approximately in the middle between two corners; (iii) with the tip touching approximately at the centre of the upper face. These experiments were repeated for various orientations of the specimens, i.e. with various faces chosen to be the upper (observed) ones.

When heating was applied at a corner, the nucleation was always induced exactly at that corner and occurred nearly immediately after touching the specimen with the tip. When heating either an edge or the centre of the upper face, the nucleation occurred at one of the corners as well, i.e. the localized heating did not result in formation of the nucleus under the tip. Moreover, the nucleus was only observable after 30–60 s, which was enough time for the corner to reach the T_C temperature. In different tests the nuclei were observed at different corners (including those lying on the PE foil) and the exact choice was probably governed by imperfections of the stabilized martensite. After the nucleation, the transition front formed and propagated through the specimen. The velocity of the transition front probably depended on the actual overheating of the specimen. For some runs of the experiment, it propagated at a few millimetres per second (comparable to the transition front propagating in a thermal gradient [7]); for other runs, the whole specimen transformed fully within less than 1 s. This also supports the conjecture that the nucleation is affected by the local microstructure in the corners: if the nucleation barrier in one of the corners is lowered e.g. by imperfections in the stabilized martensite, the nucleation occurs earlier (i.e. at a lower temperature) and the transition front, which lowers the temperature of the material by the latent heat [7], propagates more slowly.

In Fig. 2, snapshots from the observations are seen (video). The transition fronts have morphologies of the interfacial microstructures described in [6] (*X*- and λ-interfaces), in which the mechanically stabilized martensite is separated from austenite by a twinned region ensuring kinematical compatibility.

3. Nonlinear elasticity model: general and simplified

3.1. General model

The general nonlinear elasticity model [8,9], which neglects interfacial energy, leads to the prediction of infinitely fine microstructures which are identified with limits of infimizing sequences y^k, $k = 1, 2, \ldots$, for a total free energy

$$E_\theta(y) = \int_\Omega \varphi(\nabla y(x), \theta)\, dx.$$

Here, Ω represents the reference configuration of undistorted austenite at the critical temperature θ_c and $y(x)$ denotes the deformed position of the particle $x \in \Omega$. The free-energy function $\varphi(F, \theta)$ depends on the deformation gradient $F \in M^{3\times 3}$ and the temperature θ where $M^{3\times 3}$ denotes the space of 3×3 matrices. By frame indifference, $\varphi(RF, \theta) = \varphi(F, \theta)$ for all F, θ and for all rotations R; that is for all matrices in $SO(3) = \{R : R^T R = 1, \det R = 1\}$. Let

$$K_\theta = \{F : \varphi(G, \theta) \geq \varphi(F, \theta) \text{ for all matrices } G\}$$

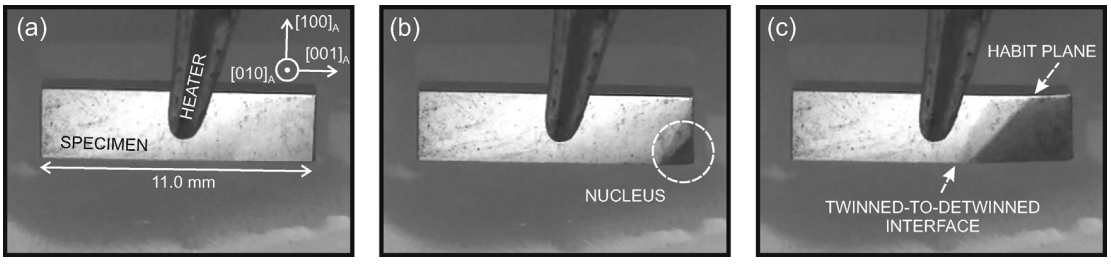

Fig. 2. Snapshots of the recorded video taken during the optical observations of the nucleation process. (a) The initial state with the length and crystallographic orientation of the specimen given in the coordinate system of the austenitic lattice (indicated by the subscript A); (b) formation of the nucleus at a corner (the first frame of the recorded video in which the nucleus was clearly visible); (c) the fully formed transition front propagating through the specimen. The morphology of the interfacial microstructure is outlined by the arrows indicating the austenite-to-twinned martensite interface (the habit plane) and the twinned-to-detwinned interface between the laminate and the stabilized martensite.

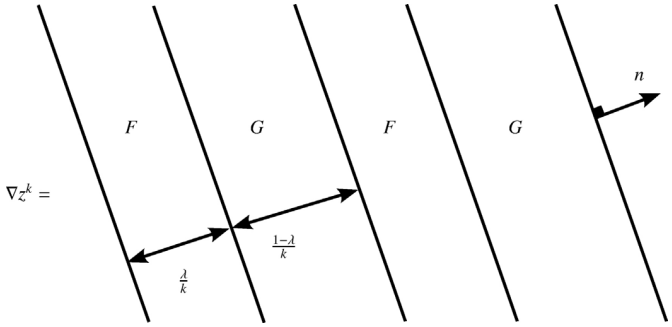

Fig. 3. Sequence of gradients ∇z^k generating the x-independent Young measure $\nu_x = \lambda\delta_F + (1-\lambda)\delta_G$.

denote the set of energy-minimizing deformation gradients. Then we assume that

$$K_\theta = \begin{cases} \alpha\left(\theta\right) SO(3) - \text{austenite} & \theta > \theta_c \\ SO(3) \cup \bigcup_{i=1}^{N} SO(3)\, U_i\left(\theta_c\right) & \theta = \theta_c \\ \bigcup_{i=1}^{N} SO(3)\, U_i\left(\theta\right) - \text{martensite} & \theta < \theta_c, \end{cases}$$

where the positive definite, symmetric matrices $U_i\left(\theta\right)$ correspond to the N distinct variants of martensite and $\alpha(\theta)$ is the thermal expansion coefficient of the austenite with $\alpha(\theta_c) = 1$.

However, information about the gradients of minimizing sequences y^k for E_θ is lost in the limit $k \to \infty$ and a more convenient way to describe microstructure is via the use of gradient Young measures, which are families of probability measures $\nu = (\nu_x)_{x\in\Omega}$ generated by sequences of gradients ∇z^k. Then we seek to minimize

$$I_\theta(\nu) = \int_\Omega \langle \nu_x, \varphi\rangle\, dx = \int_\Omega \int_{M^{3\times 3}} \varphi(A)\, d\nu_x(A)$$

over the space of gradient Young measures. In this case, the underlying (macroscopic) deformation gradient $\nabla z(x)$ corresponds to the centre of mass of ν, $\nabla z(x) = \overline{\nu}_x = \langle \nu_x, \mathrm{id}\rangle = \int_{M^{3\times 3}} A\, d\nu_x(A)$ (see Ref. [9]).

As an example of the use of Young measures, consider the x-independent measure $\nu_x = \lambda\delta_F + (1-\lambda)\delta_G$, for some $\lambda \in (0,1)$, supported on two rank-one connected matrices F and $G = F + a\otimes n$ where a, n are vectors and $\delta_\cdot$ denotes a Dirac mass. This Young measure is generated by gradients ∇z^k consisting of simple laminates formed from alternating layers with normal n of width λk^{-1} and $(1-\lambda)k^{-1}$ in which ∇z^k takes the respective values F and G (see Fig. 3). At each x, ν_x gives the limiting probabilities λ, $1-\lambda$ as $k \to \infty$ of finding the matrices F and G, respectively, in an infinitesimal neighbourhood of x. In this case, the macroscopic gradient is $\nabla z(x) = \overline{\nu}_x = \lambda F + (1-\lambda)G$.

3.2. Simplified model

For our simplified model, we assume that $\theta > \theta_c$ and drop the explicit dependence on the temperature. Let Ω denote the Cu–Al–Ni bar in the austenite at $\theta = \theta_c$ and $\varphi : M^{3\times 3}_+ \longrightarrow \mathbb{R}\cup\{+\infty\}$[2] be the free-energy function for the material. Since $\theta > \theta_c$, we may assume that φ is bounded below by some $-\delta < 0$ and that

$$\varphi(F) = \begin{cases} -\delta & F \in SO(3) \\ 0 & F \in \bigcup_{i=1}^{6} SO(3)\, U_i, \end{cases} \tag{1}$$

[2] $M^{3\times 3}_+$ denotes the space of 3 by 3 matrices with positive determinant.

where the matrices U_i correspond to the six martensitic variants for the cubic-to-orthorhombic transition of Cu–Al–Ni given by

$$U_1 = \begin{pmatrix} \beta & 0 & 0 \\ 0 & \frac{\alpha+\gamma}{2} & \frac{\alpha-\gamma}{2} \\ 0 & \frac{\alpha-\gamma}{2} & \frac{\alpha+\gamma}{2} \end{pmatrix} \quad U_2 = \begin{pmatrix} \beta & 0 & 0 \\ 0 & \frac{\alpha+\gamma}{2} & \frac{\gamma-\alpha}{2} \\ 0 & \frac{\gamma-\alpha}{2} & \frac{\alpha+\gamma}{2} \end{pmatrix}$$

$$U_3 = \begin{pmatrix} \frac{\alpha+\gamma}{2} & 0 & \frac{\alpha-\gamma}{2} \\ 0 & \beta & 0 \\ \frac{\alpha-\gamma}{2} & 0 & \frac{\alpha+\gamma}{2} \end{pmatrix} \quad U_4 = \begin{pmatrix} \frac{\alpha+\gamma}{2} & 0 & \frac{\gamma-\alpha}{2} \\ 0 & \beta & 0 \\ \frac{\gamma-\alpha}{2} & 0 & \frac{\alpha+\gamma}{2} \end{pmatrix}$$

$$U_5 = \begin{pmatrix} \frac{\alpha+\gamma}{2} & \frac{\alpha-\gamma}{2} & 0 \\ \frac{\alpha-\gamma}{2} & \frac{\alpha+\gamma}{2} & 0 \\ 0 & 0 & \beta \end{pmatrix} \quad U_6 = \begin{pmatrix} \frac{\alpha+\gamma}{2} & \frac{\gamma-\alpha}{2} & 0 \\ \frac{\gamma-\alpha}{2} & \frac{\alpha+\gamma}{2} & 0 \\ 0 & 0 & \beta \end{pmatrix}.$$

In order to make the problem more tractable we work with an energy functional that captures the essential behaviour of φ but becomes infinite off the energy wells

$$K := SO(3) \cup \bigcup_{i=1}^{6} SO(3)\, U_i.$$

In particular, we employ Γ-convergence to rigorously derive this functional (see Ref. [10] for details). For $k = 1, 2, \ldots$, let $\varphi^k = k\psi + \varphi$ where $\psi : M^{3\times 3} \longrightarrow \mathbb{R}$ is a map such that $\psi \geq 0$ and $\psi(A) = 0$ if and only if $A \in K$. For a Young measure $\nu = (\nu_x)_{x\in\Omega}$ and each $k = 1, 2, \ldots$, define the energies $I^k(\nu) = \int_\Omega \langle \nu_x, \varphi^k\rangle\, dx$.

The idea behind Γ-convergence is to precisely introduce a suitable notion of 'variational convergence' for which whenever I^k Γ-converges to I then $\min I = \lim_{k\to\infty} \inf I^k$ and if ν^k is a converging sequence such that $\lim_k I^k\left(\nu^k\right) = \lim_k \inf I^k$, then its limit is a minimum point for I; here, infima and minima are taken over the space of Young measures. In our case, one expects that as $k \to \infty$ the increasing term $k\psi$ will force the limiting energy to blow up everywhere outside K. Indeed, one can show that I^k Γ-converges to

$$I(\nu) = \int_\Omega \langle \nu_x, W\rangle\, dx = \int_\Omega \int_{M^{3\times 3}} W(A)\, d\nu_x(A)\, dx, \tag{2}$$

where $W(A) = \varphi(A)$ for all $A \in K$ and $W(A) = +\infty$ otherwise. Note that this energy forces minimizers to be supported entirely within the set K.

4. Why nucleation can only occur at a corner.

Let U_s be the stabilized variant of martensite so that δ_{U_s} is the Young measure corresponding to a pure phase of that variant. In our minimization problem, we consider variations of δ_{U_s} which are localized in the interior, on faces, edges and at corners. More precisely, letting B_i, B_f, B_e, B_c be as in Fig. 4, we say that a measure $\nu = (\nu_x)_{x\in\Omega}$ is *admissible* for the interior (resp. for a face, an edge, a corner) if $\nu_x = \delta_{U_s}$ outside B_i (resp. B_f, B_e, B_c) and $\overline{\nu}_x = \nabla y(x)$ almost everywhere in Ω for some y with $y(x) = U_s x$ on the boundary ∂B_i of B_i (resp. $\partial B_f \cap \Omega$, $\partial B_e \cap \Omega$, $\partial B_c \cap \Omega$).[3] For faces, edges and corners $\partial B_f \cap \partial\Omega$, $\partial B_e \cap \partial\Omega$ and $\partial B_c \cap \partial\Omega$ act as free boundaries.

We also assume that $\det U_s \leq 1$ and that

$$\int_\Omega \det \nabla y(x)\, dx \leq \mathrm{vol}\left(y\left(\Omega\right)\right) \tag{3}$$

[3] Technically, ν is required to be a $W^{1,\infty}$ gradient Young measure meaning that it is generated by a sequence of gradients ∇z^k such that for some M, $|\nabla z^k(x)| \leq M < \infty$ for all k and a.e. x; then the corresponding 'weak limit' z of z^k also satisfies $|\nabla z(x)| \leq M$.

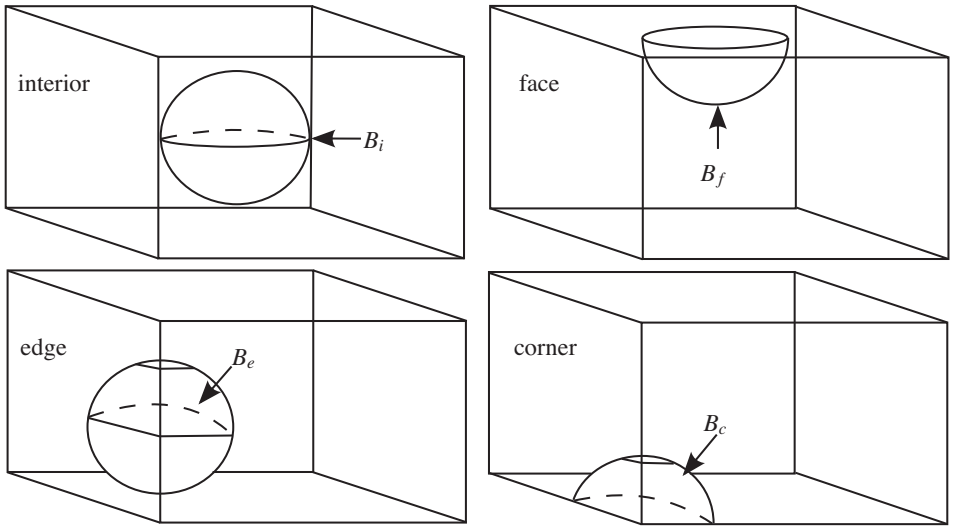

Fig. 4. Subsets of Ω used for testing whether nucleation of austenite can occur in the interior, on a face, an edge and at a corner; these are given respectively by the intersection of Ω with a small ball centred at a point in the interior, on a face, an edge or a corner.

for any map y underlying an admissible measure ν, i.e. $\nabla y(x) = \overline{\nu}_x$. Condition (3) was introduced by Ciarlet and Nečas [11] as a way to describe non-interpenetration of matter. We denote the sets of admissible measures $\nu = (\nu_x)_{x\in\Omega}$ for the interior, faces, edges and corners by $\mathcal{A}_i$, $\mathcal{A}_f$, $\mathcal{A}_e$ and $\mathcal{A}_c$, respectively.

For $s = 1, \ldots, 6$ and $S^2 = \{e \in \mathbb{R}^3 : |e| = 1\}$, the unit sphere, let

$$\mathcal{M}_s = \{e \in S^2 : |U_s e| = \max_i\{|U_i e|, 1\}\} \quad \text{and}$$
$$\mathcal{M}_s^{-1} = \{e \in S^2 : |\operatorname{cof} U_s e| = \max_i\{|\operatorname{cof} U_i e|, 1\}\},$$

where, for $F \in M^{3\times3}$, $\operatorname{cof} F$ stands for the matrix of all 2×2 subdeterminants of F and $|F| = \sqrt{\operatorname{Tr} F^T F}$ denotes the Euclidean norm in $M^{3\times3}$.

Theorem 1. [10] *Let Ω be a parallelepiped (not necessarily rectangular) with edges in the direction of vectors in $\mathcal{M}_s \cup U_s^{-1}\mathcal{M}_s^{-1}$. Assume that there exists a Young measure $\nu \in \mathcal{A}_i \cup \mathcal{A}_f \cup \mathcal{A}_e \cup \mathcal{A}_c$ such that $I(\nu) < I\left(\delta_{U_s}\right)$. Then, $\nu \in \mathcal{A}_c$.*

Proof. (sketch) Let Ω be as in the statement and let $\nu = (\nu_x)_{x\in\Omega}$ be an element of $\mathcal{A}_i \cup \mathcal{A}_f \cup \mathcal{A}_e \cup \mathcal{A}_c$ such that $I(\nu) < I\left(\delta_{U_s}\right)$. We first show that $\nu \notin \mathcal{A}_i$. Note that since $I\left(\delta_{U_s}\right) = 0$ we may assume that $\operatorname{supp} \nu_x \subset K$ as otherwise $I(\nu) = +\infty$ and the result is trivial. By averaging the measure ν (see Ref. [10]) we may also assume that ν is an x-independent Young measure and $\overline{\nu} = U_s$ without altering the energy $I(\nu)$. The minors relation for the determinant (see e.g. Ref. [9], [12]) says that $\det \overline{\nu} = \langle \nu, \det \rangle$ and hence,

$$\det U_s = \int_{SO(3)} \det A \; d\nu(A) + \int_{\bigcup_i SO(3)U_i} \det A \; d\nu(A)$$

$$= \int_{SO(3)} 1 \, d\nu(A) + \int_{\bigcup_i SO(3)U_i} \det U_s \; d\nu(A) \tag{4}$$

since $\det U_l = \det U_s$ for all l. Also, ν is a probability measure, i.e. $\int_K d\nu(A) = 1$, so that

$$\det U_s = \int_{SO(3)} \det U_s \; d\nu(A) + \int_{\bigcup_i SO(3)U_i} \det U_s \; d\nu(A)$$

and subtracting from (4),

$$\int_{SO(3)} (1 - \det U_s) \; d\nu(A) = 0.$$

Hence, $\nu(SO(3)) = \int_{SO(3)} d\nu(A) = 0$ or $\det U_s = 1$. The former case leads to a contradiction as then

$$I(\nu) = \int_\Omega \int_{\bigcup_i SO(3)U_i} W(A) \, d\nu(A) \, dx = 0 = I\left(\delta_{U_s}\right).$$

So, let $\det U_s = \alpha\beta\gamma = 1$. By the AM-GM inequality

$$\frac{|U_s|^2}{3} = \frac{\alpha^2 + \beta^2 + \gamma^2}{3} \geq \left(\alpha^2\beta^2\gamma^2\right)^{1/3} = 1$$

and thus $|U_s|^2 > 3 = |1|^2$. Note that the inequality is strict as otherwise $\alpha = \beta = \gamma = 1$ and $U_i = 1$ for all $i = 1, \ldots, 6$. The map $F \mapsto |F|^2$ is convex and so $|\overline{\nu}|^2 \leq \langle \nu, |\cdot|^2 \rangle$. Then

$$|U_s|^2 \leq \int_{SO(3)} |A|^2 \; d\nu(A) + \int_{\bigcup_i SO(3)U_i} |A|^2 \; d\nu(A)$$

$$= \int_{SO(3)} 3 \; d\nu(A) + \int_{\bigcup_i SO(3)U_i} |U_s|^2 \; d\nu(A) \tag{5}$$

since the norm does not change on martensitic variants. As ν is a probability measure,

$$|U_s|^2 = \int_{SO(3)} |U_s|^2 \; d\nu(A) + \int_{\bigcup_i SO(3)U_i} |U_s|^2 \; d\nu(A)$$

and subtracting from (5),

$$\int_{SO(3)} \left(|U_s|^2 - 3\right) \; d\nu(A) \leq 0.$$

However, $|U_s|^2 > 3$ and hence, $\nu(SO(3)) = 0$ completing the case of the interior. Note that the proof does not utilize (3) or the condition that $\det U_s \leq 1$; these are only relevant for faces and edges. Also, the result for the interior does not dependent on the orientation of Ω.

As for faces or edges, we wish to deduce that ν cannot be an element of $\mathcal{A}_f$ or $\mathcal{A}_e$. The proofs, though similar, are more involved and we refer the reader to Ref. [10] for details. The proofs essentially rely on showing that whenever a line segment joins points on

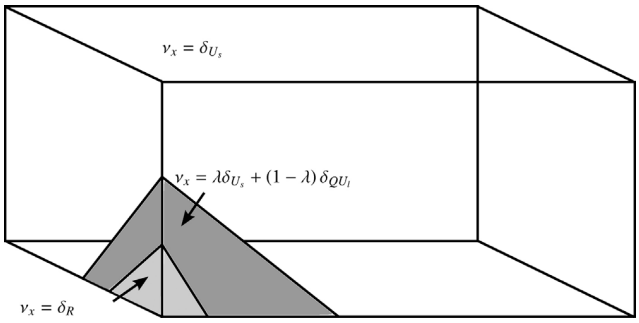

Fig. 5. Depiction of a measure $\nu \in \mathcal{A}_c$ such that $I(\nu) < I\left(\delta_{U_s}\right)$. In the light shaded region $\nu_x = \delta_R$ for some $R \in SO(3)$ so that austenite has nucleated at a corner; in the dark shaded region $\nu_x = \lambda\delta_{U_s} + (1-\lambda)\,\delta_{QU_l}$ for some $Q \in SO(3)$ and $l \in \{1, \ldots, 6\}$ such that the matrices R and $\lambda U_s + (1-\lambda)QU_l$ are rank-one connected, i.e. ν_x corresponds to a simple laminate between U_s and QU_l there forming a compatible interface with R. Note that the normals to the interfaces between austenite and the simple laminate (habit plane) and between the simple laminate and the pure phase of U_s (twinned-to-detwinned interface) are different.

the prescribed part of the boundary $\partial B_f \cap \Omega$ or $\partial B_e \cap \Omega$ of B_f or B_e, respectively, and lies in the direction of a vector in $\mathcal{M}_s \cup U_s^{-1}\mathcal{M}_s^{-1}$, then it must necessarily deform like $U_s x$ under any map y underlying an admissible measure $\nu \in \mathcal{A}_f$ or $\mathcal{A}_e$.

If the normal to a face is perpendicular to, or an edge is in the direction of, a vector in $\mathcal{M}_s \cup U_s^{-1}\mathcal{M}_s^{-1}$, the sets B_f or B_e can then be covered by such line segments so that $y(x) = U_s x$ in Ω. But this means that $\overline{\nu}_x = U_s$ and in a manner very similar to the proof for the interior, we can show that this implies $I(\nu) = 0$, i.e. for all $\nu \in \mathcal{A}_f$ or $\mathcal{A}_e$, $I(\nu) \geq I\left(\delta_{U_s}\right)$ and no admissible measure for a face or edge can lower the energy.□

On the other hand, a specific construction shows that for any given corner there always exists a measure $\nu \in \mathcal{A}_c$ such that $I(\nu) < I\left(\delta_{U_s}\right)$. In this construction (see Fig. 5) the measure ν takes the value δ_R in a small region at a corner, for some $R \in SO(3)$. The rotation R can itself form a compatible interface with a simple laminate as in Fig. 3 with $F = U_s$ and $G = QU_l$ for some variant chosen to form the interface with R. This laminate can trivially also form a compatible interface with a pure phase of the variant U_s and serves as the interfacial microstructure interpolating between R (austenite) and U_s making the entire microstructure compatible. Note that since the measure ν is supported on $SO(3)$ it must indeed lower the energy. Then, Theorem 1 combined with the existence of an admissible measure in $\mathcal{A}_c$ that lowers the energy imply that nucleation must, and does, occur at a corner.

5. Remarks and conclusions

For a general energy functional of the form

$$\int_\Omega W(\nabla y(x))\,dx,$$

known necessary conditions for a map y to be a local minimizer are that W is quasiconvex at $\nabla y(x_0)$ for all x_0 in the interior – quasiconvexity in the interior (Meyers [13]) – and at the boundary (faces) of Ω – quasiconvexity at the boundary (Ball and Marsden [14]). Recently, Grabovsky and Mengesha [15] showed that, along with the satisfaction of the Euler–Lagrange equations and the positivity of the second variation, strengthened versions of the quasiconvexity conditions are in fact sufficient for y to be a local minimizer; however, they showed this under smoothness assumptions on W and also on the domain Ω which do not allow for edges or corners.

In our work, the condition that

$$I(\nu) \geq I\left(\delta_{U_s}\right) \quad \text{forall } \nu \in \mathcal{A}_i\,(\text{resp. } \mathcal{A}_f,\ \mathcal{A}_e \text{ and } \mathcal{A}_c)$$

is the appropriate expression of quasiconvexity at U_s in the interior (resp. on faces, edges and corners). Then a way of interpreting Theorem 1 is that W is quasiconvex at U_s in the interior, at the boundary (faces) and edges but not at corners, so that U_s is a local minimizer in the interior, on faces and edges with respect to the localized variations defined before. We note that, to the best of the authors' knowledge, quasiconvexity conditions at edges and corners have not been considered before (see Ref. [10]).

The sets $\mathcal{M}_s$ and $\mathcal{M}_s^{-1}$ depend on the specific change of symmetry of the crystal lattice and, hence, on the lattice parameters of the material. For a range of parameters (see Ref. [10] for details), including those of the specimen studied here, the above sets have explicit representations making our result applicable to a variety of parallelepipeds; for $s = 1, 2$ these are given by

$$\mathcal{M}_s = \{e \in S^2 : (-1)^{s-1} e_2 e_3 \geq 0,\ |e_1| \leq \min\{|e_2|, |e_3|\}\},$$

$$\mathcal{M}_s^{-1} = \{e \in S^2 : (-1)^{s-1} e_2 e_3 \leq 0,\ |e_1| \geq \max\{|e_2|, |e_3|\}\}$$

whereas for $s = 3$, 4 and $s = 5$, 6 we simply interchange e_1 with e_2 and e_3 respectively. In particular, our result applies to the Cu–Al–Ni specimen of this paper for any $s = 1, \ldots, 6$. However, for these lattice parameters, $\mathcal{M}_s \cup U_s^{-1}\mathcal{M}_s^{-1}$ does not exhaust the unit sphere. Hence our result leaves open the possibility that for different specimens nucleation could occur at a face or an edge.

It is worth noting that the same nucleation mechanism was observed for a Cu–Al–Ni specimen stabilized as a compound twin. This microstructure is also not able to form directly compatible interfaces with austenite and our methods may be applicable to this case as well.

Lastly, similar situations in which the incompatibility of gradients results in hysterisis have been documented before in different contexts, e.g. Ref. [16]. There, though in a different way, the mathematical analysis argues that despite the existence of a state with lower energy than a certain martensitic variant, it is necessarily geometrically incompatible with it, giving rise to an energy barrier, which keeps the specific martensitic state stable. In general, in the context of microstructure formation, the incompatibility of gradients gives rise to very rich and interesting phenomena, such as the first genuinely non-classical austenite-martensite interfaces observed by Seiner and Landa [17], where austenite was able to form stress-free interfaces with a double laminate of martensite. In Ref. [18], the reader can find further details as well as a relevant mathematical analysis.

Acknowledgements

J.M. Ball and K. Koumatos were supported by the EPSRC New Frontiers in the Mathematics of Solids (OxMOS) programme (EP/D048400/1) and the EPSRC award to the Oxford Centre for Nonlinear PDE (EP/E035027/1). H. Seiner was supported by the Czech Science Foundation (project No. GAP107/10/0824) and the Institute of Thermomechanics ASCR v.v.i. (CEZ:AV0Z20760514).

Appendix A. Supplementary data

Supplementary data associated with this article can be found, in the online version, at doi:10.1016/j.jallcom.2011.11.070.

References

[1] C. Picornell, V. Lvov, J. Pons, E. Cesari, Materials Science and Engineering: A 438 (2006) 730–733.
[2] Y. Liu, D. Favier, Acta Materialia 48 (13) (2000) 3489–3499.

[3] M. Landa, P. Šittner, V. Novák, P. Sedlák, H. Seiner, 10th International Symposium on Physics of Materials, ISPMA-10, Prague, Czech Republic, August 30–September 2, 2005 (unpublished lecture).
[4] T. Černoch, M. Landa, V. Novák, P. Sedlák, P. Šittner, Journal of Alloys and Compounds 378 (1-2) (2004) 140–144.
[5] M. Landa, V. Novák, M. Blaháček, P. Šittner, Journal of Acoustic Emission 20 (2002) 163–171.
[6] H. Seiner, P. Sedlák, M. Landa, Phase Transitions 81 (6) (2008) 537–551.
[7] H. Seiner, M. Landa, P. Sedlák, Proceedings of the Estonian Academy of Sciences: Physics, Mathematics 56 (2) (2007) 218–225.
[8] J.M. Ball, R.D. James, Archive for Rational Mechanics and Analysis 100 (1) (1987) 13–52.
[9] J.M. Ball, R.D. James, Philosophical Transactions: Physical Sciences and Engineering (1992) 389–450.
[10] J.M. Ball, K. Koumatos, in preparation.
[11] P.G. Ciarlet, J. Nečas, Archive for Rational Mechanics and Analysis 97 (3) (1987) 171–188.
[12] K. Bhattacharya, Microstructure of Martensite: Why it Forms and How it Gives Rise to the Shape-Memory Effect, vol. 2, Oxford University Press, USA, 2003.
[13] N.G. Meyers, Transanctions American Mathathematical Society 119 (1965) 125–149.
[14] J.M. Ball, J.E. Marsden, Archive for Rational Mechanics and Analysis 86 (3) (1984) 251–277.
[15] Y. Grabovsky, T. Mengesha, Transanctions American Mathathematical Society 361 (3) (2009) 1495–1541.
[16] J.M. Ball, C. Chu, R.D. James, Journal de Physique IV C 5 (1) (1995) 245–251.
[17] H. Seiner, M. Landa, Phase Transitions 82 (11) (2009) 793–807.
[18] J.M. Ball, K. Koumatos, H. Seiner, Proceedings ICOMAT08, TMS, 2010, pp. 383–390 (also at arXiv:1108.6220v1).

2.5 Shrnutí získaných poznatků

Pohyblivé rozhraňové mokrostruktury ve slitině Cu-Al-Ni vznikají jako objekty umožňující kompatibilní přechod z mechanicky stabilizovaného martenzitu (monovarianta nebo laminát typu Compound) do vysokoteplotní asutenitické fáze. Byly pozorovány za různých termomechanických podmínek a pro různé orientace a geometrie vzorku; nicméně ve všech případech vykazují charakteristické morfologie typu X a λ.

Jak bylo ukázáno v podkapitolách 2.1 a 2.2, nelze tyto morfologie predikovat pomocí matematických modelů založených na minimalizaci energie, neboť neodpovídají ani lokálním minimům energie, a to jak na makro-škále (podkapitola 2.1), tak na mikro-škále (podkapitola 2.2). Zdá se, naopak, že vznik těchto morfologií je řízen disipačními procesy na makroškále, případně anelastickými procesy (vznik a zánik defektů) na mikroškále.

Že jsou takové efekty dominantní lze dobře dobře vidět na případech analyzovaných v podkapitolách 2.3 a 2.4. V prvním případě se ukazuje, že morfologie typu X nebo λ má tendenci vznikat i v případech, kdy výchozím mechanicky stabilizovaným martenzitem není monovarianta ale jemný laminát, a formování rozhraňové mikrostruktury tak vyžaduje vznik komplexních struktur (neklasická rozhraní). V druhém případě je pak experimentálně pozorováno a teoreticky vysvětleno, že specifické rozhraňové struktury vznikají i v případě, kdy je na vzorek aplikován lokalizovaný ohřev v jiném místě, než je z geometrických důvodů umožňena nukleace. Rozhraní tak vzniká v inverzním teplotním gradientu a pohybuje se směrem od chladnějšího nukleačního bodu k bodu lokalizovaného ohřevu. z toho vyplývá, že charakteristická morfologie typu X a λ nemůže být ani důsledkem teplotního gradientu.

Výsledky prezentované v této kapitole jsou shrnuty ve vyzvaném přehledovém článku [58], který vyjde v úvodním čísle časopisu *Shape Memory and Superelasticity*, vydávaného od května roku 2015 vydavatelstvím Springer Verlag.

Kapitola 3

Makrodvojčatová pohyblivá rozhraní ve slitině Ni-Mn-Ga

Slitina Ni-Mn-Ga patří mezi takzvané feromagnetické slitiny s tvarovou pamětí (FSMA), ve kterých je feroelastické chování úzce spjato s magnetismem. V jednotlivých variantách martenzitu určuje spontánní deformace (tj. orientace transformačního strainu) také orientaci osy snadné magnetizace. Díky velmi silné magnetokrystalické anizotropii těchto materiálů lze potom aplikací vnějšího magnetického pole indukovat reorientaci martenzitu: martenzit se reorientuje tak, aby osy snadné magnetizace ležely ve směru vnějšího pole. To je takzvaný jev *magnetické tvarové paměti* neboli *magneticky indukované reorientace* [10, 11].

Transformace ve slitině Ni-Mn-Ga je z krystalografického hlediska podstatně složitější než ve slitině Cu-Al-Ni. Podle přesného stechiometrického složení slitiny může vysokoteplotní fáze (austenit) přecházet při ochlazování do čtyř různých nízkoteplotních strukturních fází: kubického premartenzitu, dvou různě modulovaných monoklinických martenzitických fází (10 M a 14 M) nebo tetragonálního nemodulovaného martenzitu.

Z technologického hlediska je nejvýznamnější z těchto strukturních fází 10 M modulovaný martenzit (modulace na monoklinických rovinách s periodou deseti meziatomárních vzdáleností), protože v této fázi mohou vznikat takzvaná *vysoce pohyblivá rozhraní*, tedy rozhraní, která jsou schopna pohybu krystalem pod reorientačním napětím 1 MPa a menším nebo v odpovídajícím způsobem slabých magnetických polích.

Velikost reorientačního napětí u vysoce pohyblivých rozhraní záleží na konkrétním typu dvojčatění [59, 60]. Rozsáhlou experimentální studií [61] na velkém množství vzorků slitin s mírně rozdílnými stechiometriemi a tím pádem i mírně rozdílnými transformačními teplotami bylo prokázáno, že dvojčata Typu 1 vykazují výrazně vyšší reorientační napětí než dvojčata Typu 2 (Obr.**3.1**(a)), přičemž poměr mezi reorientačním napětím pro Typ 1 a pro Typ 2 je silně závislý na teplotě (Obr.**3.1**(a)).

Následující komentované publikace jsou zaměřeny právě analýzu rozdílu mezi rozhraními Typu 1 a Typu 2. V podkapitole 3.1 je zkoumána struktura těchto rozhraní experimentálně i pomocí matematické teorie martenzitických mikrostruktur; v této analýze je pokračováno i v pod-

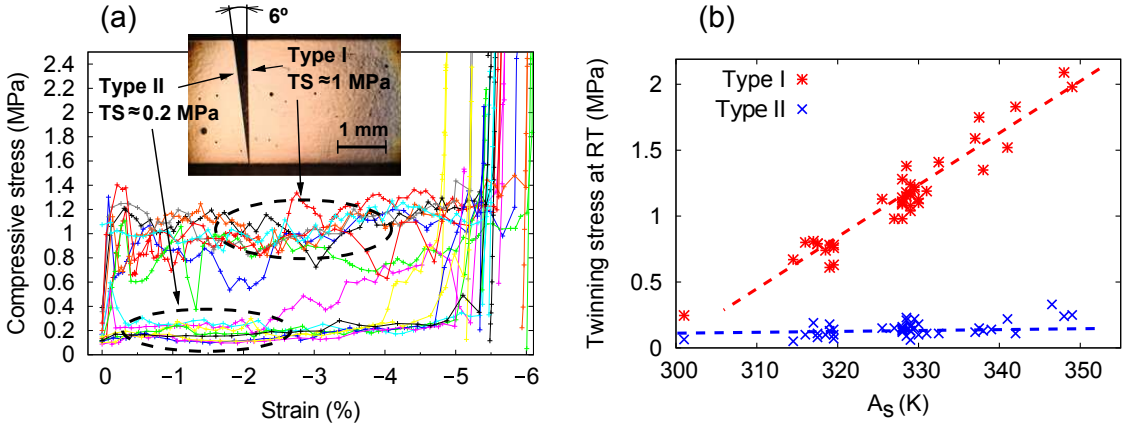

Obr. 3.1: Reorientační napětí pro dvojčatová rozhraní Typu 1 a 2: (a) reorientační křivky pro rozsáhlého soubor slitin s mírně rozdílnými transformačními teplotami (b) závislost reorientačního napětí jednotlivých typů dvojčatění na vzdálenosti od transformační teploty. Přejato z [59].

kapitole 3.2, kde jsou teoreticky navrženy a experimentálním pozorováním zdokumentovány různé přípustné (kinematicky kompatibilní) morfologie. V podkapitole 3.3 je pak navržen model pohybu těchto rozhraní s ohledem na jejich mikromorfologii na různých prostorových škálách.

Otázka pohyblivosti dvojčatových a makrodvojčatových rozhraní je jednou z aktuálně nejřešenějších otázek mechaniky termoelastických martenzitů. Se 44 citacemi od roku 2011 (podle databáze Scopus) patří publikace uvedená v podkapitole 3.3 mezi deset necitovanějších článků s tématikou Ni-Mn-Ga publikovaných za posledních 5 let (celkem asi 450 publikací podle téže databáze). Zároveň tento článek patří mezi 5 % nejcitovanějších článků daného ročníku Acta Materialia.

3.1 Publikace *Vysoce mobilní dvojčatová rozhraní v 10 M modulovaném Ni-Mn-Ga martenzitu: analýza za hranicí tetragonální aproximace mřížky.*

Bibliografická citace: Straka, L., Heczko, O., Seiner, H., Lanska, N., Drahokoupil, J., Soroka, A., Fähler, S., Hänninen, H., Sozinov, A. Highly mobile twinned interface in 10 M modulated Ni-Mn-Ga martensite: Analysis beyond the tetragonal approximation of lattice (2011) Acta Materialia, 59 (20), pp. 7450-7463.

Stručná anotace: V této publikaci bylo poprvé experimentálně i teoreticky prokázáno, že vysoce pohyblivá rozhraní v monokrystalech Ni-Mn-Ga jsou ve skutečnosti makrodvojčata Typu 1 a Typu 2, přičemž tyto dva typy se navzájem liší orientací a reorientačním napětím. Pro tuto analýzu bylo využito kombinace optické mikroskopie, rentgenové difrakce a matematické teorie martenzitických mikrostruktur. Tato publikace jako první rovněž přinesla plnou klasifikaci dvojčatových a makrodvojčatových systémů v 10 M martenzitu Ni-Mn-Ga, zavedla termín *modulačních dvojčat* a diskutovala kompatibilní vzájemné křížení jednotlivých dvojčatových systémů.

Příspěvek habilitanta: Článek vznikl v široké mezinárodní spolupráci, podíl habilitanta však byl relativně významný: veškeré výpočty založené na matematické teorii martenzitických mikrostruktur (shrnuté v příloze A tohoto článku), a interpretace pozorovaných morfologií na základě těchto výpočtů.

Available online at www.sciencedirect.com

SciVerse ScienceDirect

Acta Materialia 59 (2011) 7450–7463

Acta MATERIALIA

www.elsevier.com/locate/actamat

Highly mobile twinned interface in 10 M modulated Ni–Mn–Ga martensite: Analysis beyond the tetragonal approximation of lattice

L. Straka [a,*], O. Heczko [b], H. Seiner [c], N. Lanska [d], J. Drahokoupil [b], A. Soroka [d], S. Fähler [e], H. Hänninen [a], A. Sozinov [d]

[a] *Aalto University School of Science and Technology, Laboratory of Engineering Materials, PL 14200, FIN-00076 AALTO, Finland*
[b] *Institute of Physics, ASCR, Na Slovance 2, 182 02 Prague, Czech Republic*
[c] *Institute of Thermomechanics, ASCR, Dolejškova 1402/5, 182 00 Prague, Czech Republic*
[d] *AdaptaMat Ltd., Yrityspiha 5, Helsinki, FIN-00390, Finland*
[e] *IFW Dresden, Institute for Metallic Materials, PO Box 270116, D-01171 Dresden, Germany*

Received 11 July 2011; received in revised form 8 September 2011; accepted 9 September 2011

Abstract

The huge strains that Ni–Mn–Ga magnetic shape memory alloys can achieve are usually described in a tetragonal unit cell approximation of a five-layered modulated (10 M) crystal structure. Here we analyze the impact of a slight orthorhombic and monoclinic distortion of the 10 M structure in $Ni_{50.2}Mn_{28.3}Ga_{21.5at.\%}$ single crystal. Combining dedicated experiments to probe the microstructure, structure and mechanical properties with calculation using elastic continuum theory, we prove the existence of fine *a*/*b*-laminates within modulation macrotwins of the order of 100 micrometers in size. This complex twin microstructure containing a Type II macrotwin interface is associated with an extraordinarily low twinning stress of between 0.05 and 0.3 MPa, while Type I twins exhibit twinning stress of about 1 MPa. The findings provide important guidelines for designing the martensitic microstructure for more efficient actuators.

Keywords: Microstructure; Twinning; X-ray diffraction; Heusler phases; Magnetic shape memory

1. Introduction

Magnetic shape memory (MSM) alloys have the outstanding property that they can exhibit giant (up to 10% [1]) and simultaneously fast (≈1 kHz [2]) straining in a moderate magnetic field (<1 T). This magnetic-field-induced strain (MFIS), accompanied by a reasonable force output (≈1 MPa [3,4]), exceeds the strain reachable with the best magnetostrictive materials by about two orders of magnitude. The strain of the best ferroelectric materials is exceeded by up to about one order of magnitude [5]. The extraordinary properties of MSM alloys, and the new application possibilities they offer, have motivated intense research, which has resulted in active material in the form of single crystals [6,7], polycrystals [8], fibers [9], foam [10] and thin films [11,12]. Since the Ni–Mn–Ga alloys are not only the prototype MSM alloy but still the best MSM material available, here we focus on this system.

The existence of ferromagnetic twinned martensite microstructure is a precondition for the existence of the MFIS as the effect occurs by the rearrangement of the twinned microstructure in a magnetic field [13]. More specifically, Ullakko et al. [14] identified the movement of twin boundaries as the underlying mechanism of MFIS. When applying a magnetic field, the twin variants that have their easy magnetization axis along the field direction are energetically favored. These variants grow under the field by the motion of twin

* Corresponding author. Tel.: +358 9 470 25713; fax: +358 9 470 23518.
E-mail address: ladislav.straka@tkk.fi (L. Straka).

1359-6454/$36.00
doi:10.1016/j.actamat.2011.09.020

boundaries at the expense of unfavorably oriented variants, which results in the giant strain or MFIS. This effect has also been termed "magnetically induced reorientation" (MIR) as variants differ in crystallographic orientation, and thus a significant volume of the material changes its crystallographic orientation during this process. A high twin boundary mobility is essential, i.e. the forces opposing the twin boundary motion must be low.

The forces opposing the twin boundary motion are often determined using quasistatic mechanical tests. This determines so-called twinning stress, which is the stress under which the twin boundary moves [6,15,7]. The magnitude of the twinning stress is one of the major factors that determines the existence and efficiency of the MIR in quasistatic conditions or at low actuating frequencies (≈1–100 Hz) [15,4]. MIR is suppressed completely for twinning stresses higher than about 3 MPa [16,4,6] (breaching this limit is discussed in Ref. [17]). Conversely, the closer the twinning stress approaches zero, the higher the efficiency of the effect.

Twinning stress in single crystals is known to depend on defects already present in the austenitic crystal [18–20], the arrangement of twin boundaries in the martensitic state [21,22], the twin hierarchy [23], and training [21,24]. It has been found that Type I, Type II and compound twins can exist in Ni–Mn–Ga five-layered modulated (10 M) martensite after phase transformation [25–27]. Li et al. [26] have discussed how the reorientation of martensitic variants during MIR can occur either through Type I or through Type II twin boundary motion in 10 M martensite. However, despite having the same twinning shear, Type I and Type II twin boundaries exhibit considerably different twinning stresses in 10 M martensite [28]. This can result in variation of twinning stress in samples with complex twin microstructure and consequent unstable actuating performance. For example, the extraordinarily low twinning stress of about 0.05 MPa in 10 M martensite [7,6,29] significantly increased when a fine twin structure was created instead of a single twin boundary, which might be attributed to the change of twinning system.

The slight monoclinic and orthorhombic distortion of the lattice [30–32] and the experimental observation that two types of twin boundaries can participate in reorientation of martensitic variants [26,28] clearly indicate that the description of the twinned microstructure based on the tetragonal unit cell approximation is incomplete and that complex interfaces with various mobilities can occur in the material under applied stress or/and field. Consequently, the detailed identification of all the monoclinic twin variants and a method to prepare a specific microstructure are crucial for further development of MSM alloys.

This work reports a systematic investigation of the twin relation between martensite variants in MSM alloy with a very low twinning stress of about 0.2 MPa [7]. We experimentally demonstrate that complex twinned interfaces, in contrast with a plane twin boundary, can be highly mobile under application of stress or a magnetic field. As this microstructure cannot be described using a tetragonal approximation of the lattice, we first analyze the martensitic microstructure and local structure with dedicated high-resolution structural methods. Using these methods/calculation, the consequences of the slight orthorhombic and monoclinic distortions become clear. These distortions result in modulation twin boundaries and *a*/*b*-laminates. Comparing the experimental observations with a theoretical calculation for all possible twin variant configurations we were able to identify fully the observed twin variants and to explain the observed morphological features of the highly mobile twinned interface. At the end of this paper, we show how the specific martensitic microstructure can dramatically reduce the twinning stress by a factor of about five.

2. Experimental methods

The experimental methods employed to understand and describe the twin variants and microstructure associated with the complex twinned interfaces studied here include: mechanical testing, optical observations with polarized light and with reflective differential interference (Nomarski) contrast (DIC) [33], atomic and magnetic force microscopy (AFM and MFM), scanning electron microscopy (SEM) with electron backscatter diffraction (EBSD), SEM with Lorenz contrast [34,35], X-ray diffraction (XRD) and, finally, XRD with a microdiffraction probe (XRμD).

Systematic investigation of twin boundary mobility and microstructure was performed on more than 20 alloys with nominal composition $Ni_{50}Mn_{25+x}Ga_{25-x}$ (at.%), where x was between 3 and 4. All alloys in this composition range exhibited approximately similar microstructural features and twinned-interface mobility. The observations presented in this paper were performed on $Ni_{50.2}Mn_{28.3}Ga_{21.5}$ (±0.2 at.%) alloy (composition determined by X-ray fluorescence spectroscopy).

The $Ni_{50.2}Mn_{28.3}Ga_{21.5}$ single-crystal samples were cut approximately along the $\{1\,0\,0\}_P$ planes of parent cubic austenite, which exhibited a lattice parameter $a_P = 5.832$ Å near the martensitic transformation, which occurred at $M_s = 323$ K. The crystal structure at room temperature as determined by XRD was five-layered modulated, i.e. 10 M martensite structure. The cell parameters of the martensitic phases in Ni–Mn–Ga are often described in cubic coordinates, on the basis of the original $L2_1$ lattice of austenite [32] (see also Fig. 2), and we use this description of the lattice also here. Using the tetragonal approximation, the lattice parameters determined by XRD were $a_T = 5.958$ Å and $c_T = 5.584$ Å using the cubic coordinates of austenite. For the monoclinic approximation the parameters were $a = 5.972$ Å, $b = 5.944$ Å, $c = 5.584$ Å and $\gamma = 90.37°$ again using cubic coordinates. All experiments were performed at room temperature, well below the martensite finish temperature of 321 K and the Curie temperature of 370 K.

The optical observations of twinned interfaces were performed using a Meiji MX8100 microscope with crossed

polarizers and a Zeiss microscope with reflective DIC. The XRD measurements were performed using an X'Pert MRD four-circle diffractometer with a Co anode. The XRμD was performed using an X'Pert PRO PANalytical powder diffractometer with a Co anode ($\lambda = 1.78901$ Å) using point focus. The irradiated area was defined by using a monocapillary with inner radius 0.1 mm and the beam radius at the sample surface was approximately 0.12–0.14 mm. The sample was mounted on an ATC-3 texture cradle enabling rotation, inclination (ψ) and linear movement of the sample. The simultaneous movement of the tube and detector allowed precise change of the incident angle (ω). The diffracted beam was either limited by Soller slits to limit the ψ-range of diffracting planes (up to $\approx$1°) or the slits were removed which enabled simultaneous detection of two diffraction peaks, the positions of which could differ by up to $\approx$3°. An X'Celerator multiple strip detector was used to detect the diffracted beam, which considerably shortened the acquisition times.

Full identification of twin variants and their orientation was achieved by XRμD mapping using 2θ, ω and ψ scans. The mapping was performed along the twinned interface (details are given further in the text and in Fig. 3). In the ω scan the angles 2θ and ψ were fixed. In the ψ scan the angles 2θ and ω were fixed. The intervals of angular acceptance of the detector were $\approx$3° for ψ and 2.17° for 2θ. The scans enable precise mapping of the crystal orientation. Using the 2θ scan for a single crystal, the single orientation of planes can be detected for given ψ and ω. We used mostly primary {400} planes. Due to the chemical order of Heusler alloys {200} and {600} could also be detected as weak superstructure peaks [36]. Using all three peaks improved the precision of the lattice parameter determination.

First, several ω and ψ scans were performed until the maximum intensities of the (400), (040) and (004) peaks were found. The 2θ scan along the x-axis was then used to identify different martensitic variants. However, due to the closeness of a and b lattice constants the (400) and (040) peaks could not be resolved. Instead we chose to analyze the (600) and (060) peaks, which have the same diffraction vector orientation as the (400) or (040) peaks. These peaks are well separated and individual integral intensities of the peaks can be easily determined. The (006) peak was out of range.

3. Microstructural analysis: failure of the tetragonal approximation

A typical optical micrograph of the complex, highly mobile twinned interface often observed in all the studied alloys is shown in Fig. 1a. This type of interface advanced under a compressive stress of $\approx$0.2 MPa in the alloy presented here, and thus the twinning stress was taken to be $\approx$0.2 MPa (the mobility is described in more detail below). The interface was easily recognized as the two regions forming the interface reflected different amounts of light

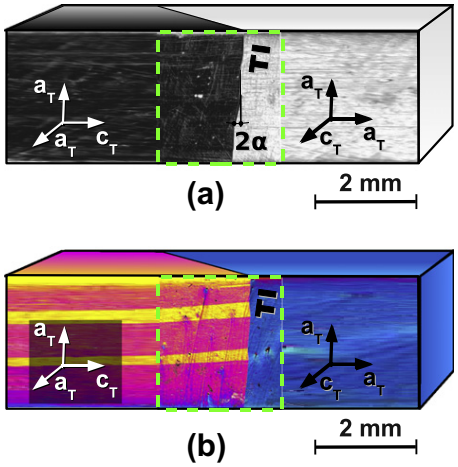

Fig. 1. Typical microstructure of highly mobile twinned interface. Regions inside the red dashed frames are optical micrographs, regions outside are schematic drawings. Approximate directions of tetragonal lattice axes are marked. (a) Highly mobile twinned interface (TI) in the studied material often consists of straight segments with size of the order of 100 μm, tilted relative to each other by an angle of $2\alpha \approx 12°$. (b) Differential interference (Nomarski) contrast reveals that each segment is associated with a slight surface inclination about c-axis on one side of the interface. This is manifested as stripe contrast with light (yellow) and dark (blue) bands oriented perpendicularly to the interface.

due to the 3.6° tilt on the observed surface, caused by twinning [7].

Based on the tetragonal approximation of the lattice, the region on the left of the interface was identified using XRD as a twin variant with the short c_T-axis aligned horizontally and the a_T-axis oriented perpendicularly to the plane of observation (further referred as a-oriented variant). This variant was energetically favored when compressive stress was applied (oriented horizontally in the figure) as it had the short c_T-axis along the stress. Thus, it grew during the compression, and consequently the twinned interface (TI) moved to the right. The region on the right of the interface, Fig. 1a, was identified as the twin variant with the a_T-axis aligned along and the c_T-axis oriented perpendicularly to the plane of observation (c-oriented variant). This twin variant was consumed during the compression.

Close inspection of the interface, however, indicated that the twin microstructure associated with the interface was more complex than was suggested based on XRD and the tetragonal approximation of the lattice. The interface was not straight but consisted of segments of the order of 100 μm in size, which formed a low-angle zig–zag pattern with the relative angle between the individual segments being about 12° (Fig. 1a). Employing DIC, an additional contrast was revealed in the a-oriented variant in the form of stripes along the c_T-axis (Fig. 1b). This stripe contrast was directly connected with the segment or zig–zag character of the twinned interface. The DIC contrast indicated a different surface inclination [33] of individual stripes, and AFM (not shown) revealed that the surfaces were inclined by approximately $\pm$0.4° about the c_T-axis. As about the

same stripe pattern was observed also at the "back" face of the sample, it was concluded that the stripes extended through the volume of the sample with the boundaries between stripes being approximately along the (0 1 0) plane. Hence, these boundaries cannot be twin boundaries of a tetragonal martensite, which are (1 0 1) oriented.

Both XRD performed on individual stripes and complementary SEM investigation using EBSD (not shown) also showed that the stripe contrast (surface inclination) is not caused by tetragonal variants with differing orientation of the c_T-axis. The orientation of the c_T-axis between the individual stripes causing the DIC contrast differed less than the resolution of the experimental methods (≈1°).

We excluded the possibility that the stripe contrast was caused by residual surface relief as the stripes always disappeared suddenly when the reverse martensitic transformation occurred during heating of the sample. The experimental observation of the magnetic domain structure by MFM and SEM using Lorenz contrast [34,35] (not shown) excluded the possibility that the stripe contrast or surface inclination was caused by the magnetic domain structure as observed in Ref. [37]. Thus, this microstructure cannot be explained using a simple tetragonal crystal lattice structure model. Hence, a more accurate description of the 10 M crystal structure is required.

3.1. Orthorhombic and monoclinic distortions of the unit cell

The tetragonal crystal lattice structure model of five-layered martensite (10 M) with $a_T = b_T > c_T$ expressed in terms of the lattice corresponding to the original austenite (Fig. 2a) serves well to describe the MIR, particularly for magnetic experiments and phenomenological modeling. From more precise structural analyses it is known that 10 M martensite can exhibit a slight monoclinic distortion ($\gamma \neq 90°$) and a slight orthorhombic distortion, which makes it necessary to distinguish between *a*- and *b*-axes [31,38,32]. This lattice is sketched in Fig. 2b. The orientation and length of the short *c*-axis remains the same as in the tetragonal approximation, i.e. $c \equiv c_T$.

The lattice modulation can be expressed by periodic shifting along the $(1\,1\,0)[1\,\bar{1}\,0]_P$ system [31,38,32,39]. The lattice parameters in "diagonal coordinates" (space group I2/m, see Fig. 2b) determined for different 10 M Ni–Mn–Ga alloys [25,30,31] are always in relation $a_{I2/m} > c_{I2/m}/5$ and the modulation acts by shifting the basic atomic positions exclusively along the $a_{I2/m}$-axis and the modulation points along the $c_{I2/m}$-axis [32]. It immediately follows that the modulation direction also has an exact orientation in relation to the *a*- and *b*-axes of the lattice considered here. More specifically, the modulation direction always points in the direction which is close to parallel to the shortest diagonal of the unit cell face formed by the *a*- and *b*-axes, i.e. it is intersecting the obtuse angle γ between the *a*- and *b*-axes (Fig. 2b) (see also Fig. A.1 in Appendix A). In the concept of adaptive martensite [40], the lattice distortions can be directly calculated by elementary geometry (see

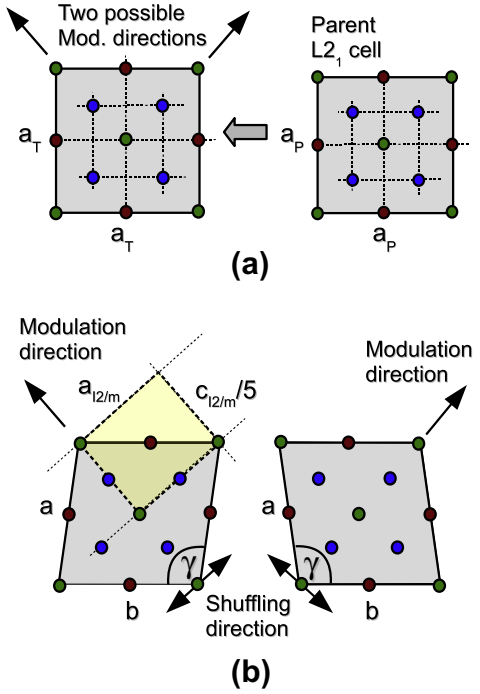

Fig. 2. Mutual orientation of crystallographic axes and modulation direction. (a) Tetragonal approximation. Modulation direction can point in two possible equivalent directions. (b) Monoclinic approximation. Modulation direction is close to parallel to the shortest diagonal of the parallelogram formed by the *a* and *b* crystallographic axes. Left and right latices are in mirror orientation to each other. Orientations of crystallographic axes $a_{I2/m}$ and $c_{I2/m}$ used in Refs. [25–27,32] are shown for comparison ($a_{I2/m}$ and $c_{I2/m}$ are so called "diagonal coordinates", space group I2/m).

supplementary information of Ref. [41] for 10 M martensite) and the modulation direction is determined as the normal to the nanotwin boundaries.

3.2. Studied twinned interface

In order to understand the crystallographic origin of the observed microstructure, we used XRμD. The sample and region probed are shown in detail in Fig. 3. First, the {4 0 0} set of reflections was used which allows the crystal orientation to be probed in the tetragonal approximation (not shown). We confirmed that the upper part has the c_T-axis perpendicular to the plane of observation, i.e. it is the *c*-oriented variant. The lower part has a_T-axis oriented perpendicularly to the plane of observation (the difference between the *a*- and *b*-axis cannot be distinguished when using the {4 0 0} reflections). The angle between the c_T-axis in the upper and the a_T-axis in the lower variants determined by XRD was close to 3.6°, in agreement with the calculation for the macroscopic variants using given lattice constants. However, the vertical stripe pattern in the lower variant cannot be identified within the tetragonal approximation of the lattice. Thus, we performed detailed XRμD investigation to determine the origin of the observed stripe pattern.

Several XRμD mappings were performed along the twin boundary in such a way as to obtain diffractions from both

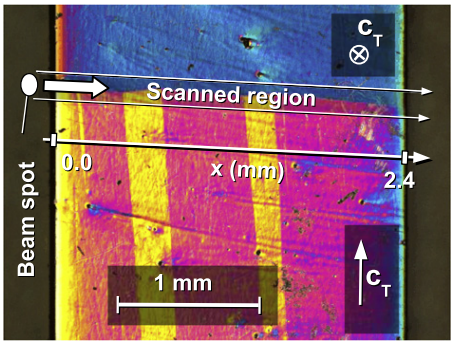

Fig. 3. Detail of the highly mobile twinned interface (oriented horizontally) and associated microstructure visible as the stripe contrast (oriented vertically) using Nomarski (DIC) contrast. The XRμD scans were performed along the interface in the region marked. The approximate size of the X-ray beam spot is marked on the left, x-axis used in mapping is marked along the interface. Approximate direction of c-axis is marked by an arrow and crossed circle ($\otimes$).

the upper and lower regions surrounding the interface simultaneously. The scanned region is marked in Fig. 3.

3.3. Mosaic structure of the crystal

A mosaic structure (cell misorientation) often appears in during crystal growth due to the formation of low-angle boundaries. Thus, we analyzed the local orientation of the monocrystal to ensure that the stripe contrast was not caused by the mosaic structure. The XRμD mapping by ω scans was performed along the segmented twin boundary (Fig. 3). Mosaic structure results in rapid changes of the ω angle. The magnitude of changes in the ω angle shows that the sample consisted of areas misaligned up to 0.5° (Fig. 4). Although the variation of the ω angle is comparable to the tilt associated with the stripe pattern ($2 \times 0.4°$) there is no local correlation with the DIC contrast. Thus, we conclude that the observed stripe pattern does not originate from the mosaic structure of the crystal.

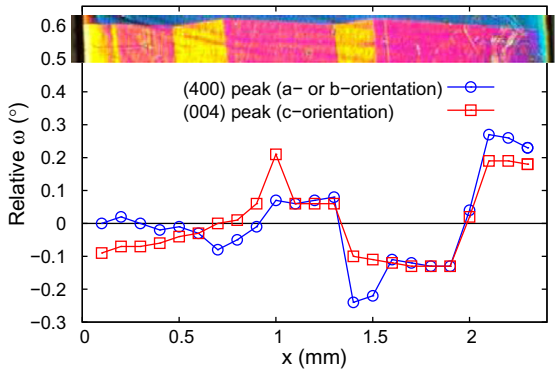

Fig. 4. Mosaic structure of the studied part of the crystal expressed as the relative change of the ω angle of the (400) and (004) peaks as a function of position x. The investigated stripe contrast (inset placed at corresponding position x) is given for comparison.

3.4. Orientation of the a- and b-axes

An alternative possibility is that the stripes are caused by alternating twin variants with a- and b-orientation. Due to the slight orthorhombic distortion, this should result in a–b twin boundaries, which are not considered in the tetragonal approximation. We used XRμD to probe the lattice spacings approximately normal to the sample. Thus, within the lower part of the sample (Fig. 3), we probe an alternating arrangement of variants with their a- and b-axes perpendicular to the plane of observation.

The lattice parameters a and b, however, are very close, and thus cannot be resolved from the (400) and (040) peaks (Fig. 5a). Thus, for proper resolution we performed diffraction at higher angles. As shown in Fig. 5b, the diffraction peaks (600) and (060) are well separated on 2θ despite their substantially lower intensity.

As a measure of the fraction of a- (or b-) oriented variants, we take the ratio between the (600) (or (060)) peak area and the area of both (600) and (060) peaks. The determined relative integral intensity of the (600) and (060) peaks as a function of position along the interface is shown in Fig. 5c. Variation of between 20% and 80% was observed but no local correlation with the stripe contrast existed. This shows that both a- and b-orientations are present in the diffraction volume ($\approx 0.12 \times 0.14 \times 0.01$ mm^3) simultaneously and implies the presence of a/b-laminates at a length scale that is below the local resolution of the XRμD used. These laminates are discussed in more detail later.

Although the relative intensities exhibited some local variation, no correlation between the relative integral intensities and the stripe contrast is found. Although the presence of a/b-laminates is evident within each stripe, the orthorhombic approximation is obviously not sufficient to explain the stripe contrast.

3.5. Modulation domains

We considered also that the stripe contrast could be connected with different directions of modulation in neighboring stripes constituting the stripe contrast. The modulation direction is typically determined using reciprocal space mapping. In reciprocal space, the extra reflections associated with 10 M lattice modulation divide the distance between the basic diffraction peaks along $[1\,1\,0]^*$ (or $[1\,\bar{1}\,0]^*$, depending on modulation direction) into five parts [30,32]. As an example, a part of the reciprocal space map of 10 M martensite containing (400), (620) and (6$\bar{2}$0) basic peaks is shown schematically in Fig. 6a. Two possible modulation directions are marked by different colors[1] ($[1\,1\,0]^*$, blue, $[1\,\bar{1}\,0]^*$, red). However, performing a complete scan of the reciprocal space for each location was not

[1] For interpretation of color in Figs. 1–9, the reader is referred to the web version of this article.

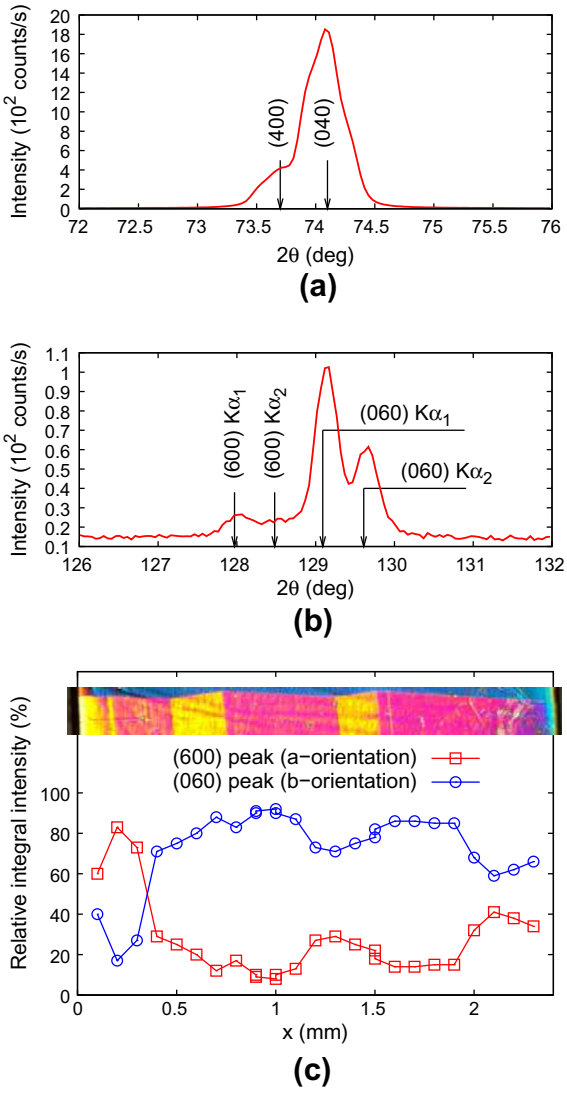

Fig. 5. Two theta scan for the {400} and {600} peaks to determine the orientation of the twin variants. (a) Resolution between (400) and (040) is not enough to distinguish between *a*- and *b*-orientation. (b) (600) and (060) peaks have enough resolution, in spite of their lower intensity. (c) Relative integral intensity of the (600) and (060) peaks as a function of position *x* along the interface as a direct measure of the fraction of *a*- and *b*-orientation. The investigated stripe contrast (inset placed at corresponding positions *x*) is given for comparison.

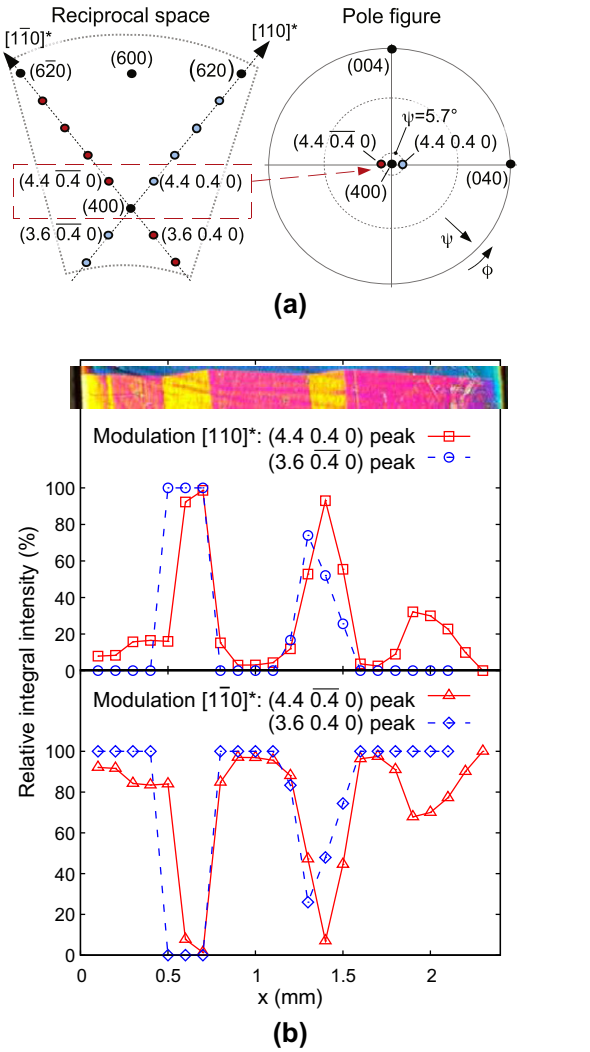

Fig. 6. Determination of the modulation orientation. (a) In reciprocal space, the peaks associated with modulation of the lattice (satellite peaks) are found either in direction $[1\,1\,0]^*$ from (400) (modulation $[1\,1\,0]^*$, blue dots) or in direction $[1\,\bar{1}\,0]^*$ (modulation $[1\,\bar{1}\,0]^*$, red dots). These peaks with non-integral indexes can be found in the pole figure as demonstrated for the (4.40.40) peak. (b) The relative integral intensity of the satellite peaks nearest to (400) as a function of position *x* along the interface as a direct measure of modulation direction (the (3.60.40) and (3.6$\overline{0.4}$0) dependences are only informative as the relevant peak intensities were very weak, ≈ 10 counts/s). The investigated stripe contrast (inset placed at corresponding positions *x*) is given for comparison.

possible with XRμD due to the geometrical constraints of the instrument we used. Instead, we developed a different approach which also reduced measurement time considerably without loss of information.

To determine the modulation direction it is sufficient to search for the first satellite reflections denoting the modulation. In our definition of the monoclinic unit cell in cubic coordinates this means searching for the diffraction peaks with non-integral indexes (4.4±0.40) or (3.6±0.40). This is illustrated in Fig. 6a, which shows the correspondence between the positions of the (4.4$\overline{0.4}$0) and (4.40.40) peaks in reciprocal space and in a pole figure. The presence or intensity of these peaks in the pole figure then reveals the direction of the modulation at each studied position. For example, the presence of the (4.40.40) peak at $\psi = 5.7°$ and the absence of the (4.4$\overline{0.4}$0) peak at $\psi = -5.7°$ indicates that the modulation direction is $[1\,1\,0]^*$ or $+\psi$ (blue dots in reciprocal space figure shown in Fig. 6a); a similar consideration applies also for the (3.60.40) and (3.6$\overline{0.4}$0) peaks.

For each measured position along the scanned interface we performed several ψ and ω scans to find the maximum for each satellite peak, and the integral intensity of these peaks was then calculated. The relative intensities of both modulation directions as a function of their position along

the twin interface are shown in Fig. 6. For all satellite peaks probed, we observe an almost perfect correlation with the stripe contrast. Differences are found at the sample edges ($x = 0$ mm and $x = 2.4$ mm) and can be attributed to rounding of the sample surface causing DIC contrast near the edges. The largest misfit is located around $x = 2$ mm, where an abrupt change of crystal misorientation (mosaic) occurs (see Fig. 4). This might result in a change modulation on a scale not discernible by DIC.

From the good correlation between the position map and the stripe contrast we can conclude that the stripe contrast originates from the different directions of modulation in neighboring stripes. Hence, the neighboring stripes may be considered as twins with twinning plane (0 1 0) (see Fig. 2b). However, more sophisticated theoretical analysis is required to understand the observed microstructure. In the following section we will show that with just the input of the monoclinic lattice constants one can directly obtain all the features of the stripe pattern: their (0 1 0) orientation, the angle of 12° observed at the surface between two segments of the interface, and the surface relief of ±0.4°.

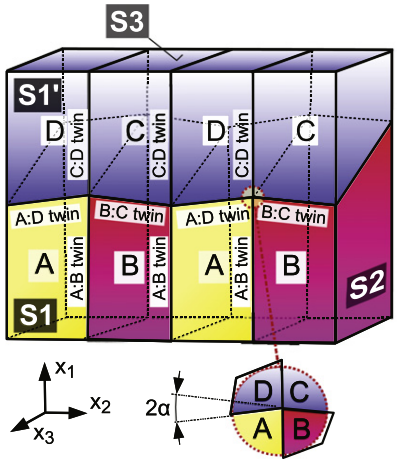

Fig. 7. Schematic sketch of the investigated microstructure (Figs. 1, 3). Surface relief (inclination of the surface ± 0.4° about *c*-axis) resulting in stripe contrast is found on surface S1; no relief is observed on S1' nor on S2 (Fig. 1). Relief at S3 cannot be confidently determined in our experimental arrangement. Surfaces S1 and S1' are tilted 3.6° relative to each other. Reference coordinate system and detail of tilting of the twinned interface by angle 2α are marked at the bottom.

4. Theoretical part—identification of variants and twinning systems and compatibility analysis

In the continuum theory of martensitic microstructures, the observed morphology of the interface (Fig. 3) is similar to the morphology known as the crossing-twins microstructure [42], or the parallelogram microstructure [43] or as a part of the herring-bone microstructure [44]. This microstructure consists of two mutually intersecting twinning systems, as sketched in Fig. 7. Although only three contrast parts are apparent when using optical microscopy, there are four variants involved in the crossing-twins microstructure, denoted by uppercase letters A, B, C and D. The twins between the variants A and B and between the variants C and D (denoted A:B and C:D, respectively) belong to the first twinning system, and the A:D and B:C twins to the second twinning system, which intersects the first one.

Such a microstructure can exist in a stress-free state if these two systems cross compatibly, i.e. the conditions of kinematic compatibility [45,46,42] are satisfied not only at the individual twinning planes, but also at their intersection. These conditions can be written in the form of a set of algebraic equations for the Bain tensors describing the individual variants involved in the microstructure. Here we briefly summarize the results in order to identify the twinning systems in the experimentally observed microstructure. The solution of this set of equations for the 10 M martensite is given in Appendix A. For the details on the mathematical background, see Refs. [42–44].

The structural and morphological features experimentally observed for the studied interface are schematically redrawn in Fig. 7 and summarized here:

1. The observed surface (a cut approximately along the (1 0 0) plane) is flat across the C and D variants, i.e. across the C:D twinning plane, but there is an observable surface relief between the A and B variants, i.e. across the A:B twinning plane (≈0.8°). There is a much larger inclination between the B and C or A and D variants, i.e. across the B:C and A:D twinning planes (3.6°).
2. The orientation of the *c*-axis does not change over the A:B and C:D twinning planes, but changes over the A:D and B:C twinning planes from the direction parallel to the observed surface (S1) in variants A and B (*a*- and/or *b*-oriented variants) into the direction perpendicular to the observed surface (S1′) in the variants C and D (*c*-oriented variants).
3. The A:B and C:D twinning planes are parallel to the (0 1 0) plane, and the A:D and B:C twinning planes are slightly declined from the (1 0 1) plane. As a result the traces of the B:C and A:D twinning planes on the surface (approximately (1 0 0) plane) are inclined with angle 2α, which is approximately equal to 12°.

To identify the individual variants and the twinning systems we searched for those combinations of the variants that can form the crossing-twins microstructure and, more importantly, are in agreement with all experimentally observed features. All possible variants and twinning systems of 10 M martensite are listed in Table A.1 of Appendix A for the cubic-to-monoclinic II transition.

Among all these variants and twinning systems there are two combinations of the variants listed in Table 1 that can form the crossing-twins microstructure. These two combinations are very similar. In both cases the mutually crossing systems are the modulation twins, i.e. the modulation

direction changes at twinning planes (in agreement with Fig. 6) and Type II twins, where the orientation of the *c*-axis changes from in-plane to perpendicular to the surface. Further, the angle α is approximately equal to 6° for both combinations in agreement with the experiment. This similarity results in the morphologies of these crossing-twins microstructures being almost indistinguishable from each other, and the optical observation is not sufficient to determine which of these combinations is observed in the experiments.

On the other hand, these two combinations can be easily distinguished from each other using a structure probe. In the first combination, variants A and B are *a*-oriented, and in the second combination, A and B are *b*-oriented variants. However, as shown in Fig. 5, XRμD showed that the orientation is neither only *a*- nor *b*-variant, but that there is always a mixture. The fraction of *a*/*b*-variants varies more or less smoothly along the mobile interface without any abrupt changes at modulation twinning, i.e. at the A:B twinning planes. This suggests that the real microstructure is more complicated compared with Fig. 7.

In particular, the experiment suggests that the individual components of the crossing-twins microstructure are not single variants, but can have a structure comprising a fine laminate of variants. The laminate must be very fine, below the resolution of XRμD. The variants in the laminate have different orientations of *a*- or *b*-axis but have the same modulation direction, which changes only on the modulation twin plane. The experiment showed that the modulation direction changes at the A:B interface from 0%/100% to 100%/0%. Thus, the fine microstructure in each of the macroscopically homogeneous regions A, B, C and D can consist of only two variants with the same modulation. This microstructure is usually called *a*/*b*-laminate. Within the approach of elastic continuum these microstructures are first-order laminates, i.e. the simplest possible laminates of two variants (e.g. [47]). The consequence of the existence of this fine *a*/*b*-laminate is that the individual segments of the studied interface cannot be the simple twinning planes, but the segments are macrotwin boundaries between *a*/*b*-laminates.

As described in Appendix A, the 10 M martensite can form macrotwin boundaries between fine first-order laminates of in-plane twins. By constructing all such laminates and all the possible macrotwin boundaries between them, it can be proved that the experimentally observed microstructure is the microstructure shown in Fig. 8. This microstructure consists of four compound twin laminates, i.e. *a*/*b*-laminates denoted by μ_A, μ_B, μ_C and μ_D, with different orientations of modulation, two modulation macrotwin boundaries and two Type II macrotwin boundaries.

It can be further demonstrated that the fine, homogeneous compound laminates (in Fig. 8) can also fulfill the conditions for the stress-free existence of the crossing-twins microstructure as for the simple case without laminates. This stress-free state can occur if the volume fraction λ of *a*-oriented variant in Eq. (A.3) of Appendix A is a constant in the vicinity of the macrotwin boundaries. The experiment showed that this condition is probably fulfilled, since the *a*/*b* ratio in Fig. 5 does not exhibit any correlation with the individual boundaries. Since the resulting morphology is a mixture of the morphology for the two possible combinations of variants listed in Table 1, the angle α varies between 6.28° and 5.87° depending on the exact volume fraction λ.

Table 1
Possible compatible combinations of twin variants and twin systems for the crossing-twins microstructure. For the notation of the individual variants and the terminology of the twinning systems, see Appendix A. The angle α is calculated based on the assumption that the free surface is exactly the (001) plane for the variants C and D.

	Combination 1	Combination 2
Variant A	No. 11	No. 9
Variant B	No. 12	No. 10
Variant C	No. 2	No. 4
Variant D	No. 1	No. 3
A:B system	Modulation	Modulation
B:C system	Type II	Type II
C:D system	Modulation	Modulation
D:A system	Type II	Type II
α	5.87°	6.28°

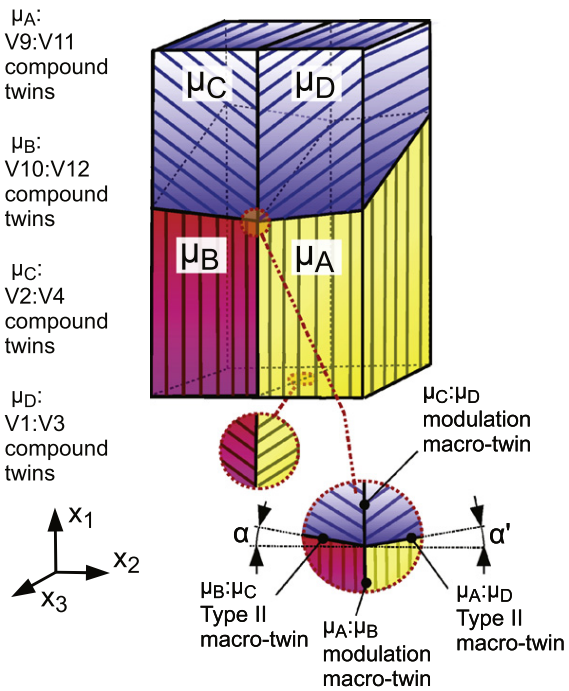

Fig. 8. Schematic of the theoretically suggested complete description of the investigated microstructure (Figs. 1 and 3). The twin microstructure consists of compound laminates μ_A–μ_D. The orientations of the twin boundaries internal to the laminates are marked by fine lines. The laminates are formed by variants identified on the left, and meet at macrotwin boundaries identified at the bottom of the figure. The labels V1,...,V12 denote the individual variants with the notation summarized in Appendix A.

The direct calculation also showed that the real microstructure stays very close to the stress-free state even if the volume fraction λ varies. The reason for this is that the compound twins forming the laminates, e.g. the V1:V3 system, can also cross nearly compatibly the Type II twinning planes, e.g. the planes of the V1:V11 system, and thus nearly fulfill the conditions for the stress-free existence of the crossing-twins microstructure. This would ensure full or nearly full microstructure compatibility regardless how the thickness of individual layer in the laminate changes along the interface. Based on this calculation we can conclude that the experimentally observed highly mobile twinned interface is kinematically compatible, or very close to compatible without the presence of any elastic strains, i.e. that the material can form such interfaces without significant energetic penalty.

The existence of Type I and Type II twins instead of compound twinning (1 0 1) [$\bar{1}$ 0 1] (or equivalent crystallographic twinning system) in a tetragonal lattice is a direct consequence of the monoclinic lattice distortion. The twin boundaries with exact twin plane orientation of (1 0 1) (or equivalent crystallographic planes) are twin boundaries of Type I. The twin boundaries deviating approximately 4° (see Table A.1 in Appendix A) from plane (1 0 1) by rotation about axis [1 0 1] (or equivalent crystallographic planes and directions) are Type II twin boundaries and they have approximately (10 1 10) or equivalent orientation (Table A.1; see also Ref. [28]). The existence of Type II (and Type I) twins due to monoclinic distortion in Ni–Mn–Ga has been demonstrated and partly discussed before [27,26]; however, no relation with boundary mobility has been drawn and in the next section we try to fill this gap.

5. Relation between twinning system and mobility of twin boundaries

In order to understand the impact of monoclinic distortion on twin boundary mobility we examined the correlation of stress–strain curves and the martensitic microstructure before and during the deformation. This is facilitated in the studied material since it tends to form only single or few twinned interfaces. During the mechanical testing, only one twinned interface propagates through the sample. Thus, the testing and the resulting twinning stress cannot be influenced by the interaction (pinning) of intersecting (1 0 1) twin boundaries [21,22]. The result of mechanical testing performed several times on 18 samples with only one active twinned interface advancing through the sample during compression is shown in Fig. 9. Although all these samples were cut from the same single crystal, the detwinning plateaus clearly separate in two classes with different stress levels of around 0.2 MPa and around 1 MPa. Moreover, the plateaus at the two different stress levels are quite frequently observed on the same sample in subsequent experiments after recreating the twin interface. Similar behavior was observed on more than 20 studied alloys with slightly varying composition with lower

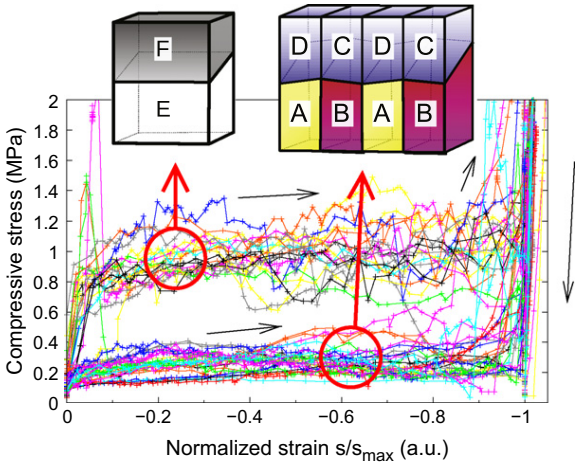

Fig. 9. Relation between the mobility of twinned interface and observed twin microstructure. (a) Result of the compressive testing performed on 18 samples. Each of the samples was compressed 1–4 times, maximum strain s_{max} was 4–6%. Two distinct plateaus are associated with different twin microstructures. The plateau at ≈1 MPa is associated with Type I twin boundaries (example twin variants in inset are E ≡ V1, F ≡ V11). The plateau at 0.2 MPa is associated with the twinned interface formed by Type II (macro) twin boundaries. An example of a segmented Type II twin boundary is given as an inset. The individual variants or laminates are of the same type as identified in the text for Figs. 7, 8, or equivalent.

plateaus varying between 0.05 and 0.3 MPa and the higher plateaus being near 1 MPa.

The simultaneous characterization of the martensitic microstructure allows us to correlate these two classes of twinning stress with two classes of microstructure, sketched in Fig. 9. (i) A high stress plateau around 1 MPa is observed when the twin boundary has an orientation of exactly (1 0 1) (or equivalent), indicating a Type I twin boundary [28]. (ii) The low stress plateau of about 0.2 MPa (varying between 0.05 and 0.3 MPa for all 20 alloys studied) is only observed when the twin boundary deviates by several degrees from (1 0 1), indicating a Type II twin boundary [28], or it consists of large segments of Type II twin boundaries and modulation twins as described in Section 4. This directly indicates that a Type II twin boundary is beneficial for a high mobility. With hindsight it is also clear that the previous reports on highly mobile twin boundaries and MIR in very small magnetic field [7,6,29] were related to Type II twin boundaries. Conversely, the larger twinning stress in a specimen with fine twins reported in Ref. [7] might be caused by the presence of Type I twin boundaries.

At first glance it seems that the tetragonal approximation can be sufficient for a simple interface of Type I with 1 MPa twinning stress, and indeed this approximation has been successfully used in the past. However, XRμD measurements (not shown) indicate that even this twin microstructure contains *a*/*b*-laminates, i.e. *a*- and *b*-oriented variants coexist along the twin boundary.

We would like to add that our analysis is incomplete with respect to the *a*/*b*-laminates. We observed the coexistence of *a*- and *b*-oriented variants in all cases, but the

methods available do not allow the postulated laminates to be resolved locally. We can speculate that these laminates form in order to reduce higher terms of the elastic energy in a hierarchical "twin within twins" microstructure [48] but have to leave proof of this to future experiments.

6. Conclusions

The results show that a complete monoclinic description is required to explain the observed highly mobile complex twinned interface with a twinning stress of approximately 0.2 MPa in the present alloy and between 0.05 and 0.3 MPa for a broader spectrum of investigated alloys. The tetragonal approximation is clearly not sufficient to describe the martensitic microstructure observed in 10 M modulated Ni–Mn–Ga MSM alloys with very low twinning stress.

The highly mobile interface consists of *a*/*b*-laminates and mesoscopic Type II twin boundary segments and modulation twins. It is surprising that such a complex arrangement exhibits very high mobility, while in the cases of more simple twin microstructure with Type I twins, the twinning stress increases to about 1 MPa. Our calculation shows that the described twin microstructure of highly mobile twinned interface is kinematically compatible and has stress-free interfaces. Since only in the presence of Type II macrotwin boundaries is a low twinning stress of the order of 0.1 MPa observed, we conclude that the monoclinic distortion may be the decisive factor explaining the very high twin boundary mobility.

The analysis also shows that very detailed control of twin microstructure is essential for practical exploitation of the MSM effect. Additionally, based on this analysis, we suggest that evolving monoclinic twin variants may be an additional mechanism contributing to the decrease of twinning stress during the training of an alloy [24,21].

Acknowledgements

We acknowledge a fruitful discussion with Manfred Wuttig and Robert Niemann. This work was funded by the Academy of Finland, Tekes—the Finnish Funding Agency for Technology and Innovation, the Academy of Sciences of the Czech Republic, the Czech Scientific Foundation (Grants P107/11/0391 and P107/10/0824), and the German Research Society (DFG, Grant FA 453/8 through SPP 1239 and Grant FA 453/8).

Appendix A. Twinning systems in the 10 M martensite of the Ni–Mn–Ga alloy

This appendix summarizes the notation of the monoclinic variants of the 10 M martensite and explains the nomenclature used for the individual twinning systems in the theoretical part of the article. The austenite-to-10 M martensite transition in the Ni–Mn–Ga alloy belongs to the cubic-to-monoclinic II transition class (according to the terminology used in Ref. [42]; Zanzotto and Pitteri [49] use the term "cubic axes" structure for the resulting martensitic variants). This means that there exist 12 different variants of martensite that can form up to four different types of twins (compound, Type I, Type II and non-conventional [49]). The main properties of this transition class are described in Ref. [42,49]. However, since the monoclinicity of the 10 M lattice is connected with modulation, it may be useful to introduce a more detailed categorization of the variants and the twinning systems, which would take the possible changes of the modulation direction at the individual twinning planes into account.

A.1. Notation of variants

In the framework of continuum mechanics, the individual variants of martensite are uniquely described by so-called Bain tensors which are symmetric parts of the polar decompositions of the respective deformation gradients **F** (for more details, see Ref. [45,42]). The deformation gradient is defined by the geometry of transformation and lattice constants of transforming phases. With the numbering taken from Ref. [42], these Bain tensors for the cubic-to-monoclinic II transition are:

$$\mathbf{U}_1=\begin{pmatrix} e_a & e_{ab} & 0\\ e_{ab} & e_b & 0\\ 0 & 0 & e_c\end{pmatrix},\quad \mathbf{U}_2=\begin{pmatrix} e_a & -e_{ab} & 0\\ -e_{ab} & e_b & 0\\ 0 & 0 & e_c\end{pmatrix},$$

$$\mathbf{U}_3=\begin{pmatrix} e_b & e_{ab} & 0\\ e_{ab} & e_a & 0\\ 0 & 0 & e_c\end{pmatrix},\quad \mathbf{U}_4=\begin{pmatrix} e_b & -e_{ab} & 0\\ -e_{ab} & e_a & 0\\ 0 & 0 & e_c\end{pmatrix},$$

$$\mathbf{U}_5=\begin{pmatrix} e_a & 0 & e_{ab}\\ 0 & e_c & 0\\ e_{ab} & 0 & e_b\end{pmatrix},\quad \mathbf{U}_6=\begin{pmatrix} e_a & 0 & -e_{ab}\\ 0 & e_c & 0\\ -e_{ab} & 0 & e_b\end{pmatrix},$$

$$\mathbf{U}_7=\begin{pmatrix} e_b & 0 & e_{ab}\\ 0 & e_c & 0\\ e_{ab} & 0 & e_a\end{pmatrix},\quad \mathbf{U}_8=\begin{pmatrix} e_b & 0 & -e_{ab}\\ 0 & e_c & 0\\ -e_{ab} & 0 & e_a\end{pmatrix},$$

$$\mathbf{U}_9=\begin{pmatrix} e_c & 0 & 0\\ 0 & e_a & e_{ab}\\ 0 & e_{ab} & e_b\end{pmatrix},\quad \mathbf{U}_{10}=\begin{pmatrix} e_c & 0 & 0\\ 0 & e_a & -e_{ab}\\ 0 & -e_{ab} & e_b\end{pmatrix},$$

$$\mathbf{U}_{11}=\begin{pmatrix} e_c & 0 & 0\\ 0 & e_b & e_{ab}\\ 0 & e_{ab} & e_a\end{pmatrix},\ \text{and}\ \mathbf{U}_{12}=\begin{pmatrix} e_c & 0 & 0\\ 0 & e_b & -e_{ab}\\ 0 & -e_{ab} & e_a\end{pmatrix}. \tag{A.1}$$

Using the lattice parameters of the austenite and 10 M martensite listed in Section 2, the individual components of the above listed Bain tensors are $e_a = 1.0240$, $e_b = 1.0192$, $e_c = 0.9575$ and $e_{ab} = 0.0033$.

The variants described by the Bain tensors $\mathbf{U}_1$–$\mathbf{U}_4$, i.e. variants No. 1–4, have the resulting *c*-axis aligned parallel

to the $[001]_P$ direction. The subscript P denotes that this direction is taken in the parent lattice of austenite, i.e. in the reference configuration. In other words, these variants can be mapped onto each other by rotations about the $[001]_P$ axis and by mirror reflections about the planes perpendicular to the $(001)_P$ plane. However, these four variants differ from each other by the directions of the *a*- and *b*-axis and by the modulation directions. The variants Nos. 1 and 2 have the *b*-axis aligned with the $[010]_P$ direction, and variants Nos. 3 and 4 with the $[100]_P$ direction. The variants Nos. 1 and 3 correspond to modulation along $[110]_P$, and variants Nos. 2 and 4 to modulation along $[1\bar{1}0]_P$. Similarly, the variants Nos. 5–8 have the *c*-axis oriented parallel to the $[010]_P$ direction, and the variants No. 9–12 to the $[100]_P$ direction with the corresponding changes of *a*- and *b*-axis and modulation directions.

A.2. The twinning systems

According to the Hadamard condition [45,46,42], two variants of martensite described by the Bain tensors $\mathbf{U}_a$ and $\mathbf{U}_b$ can form a twin whenever there exist a matrix $\mathbf{R} \in SO(3)$, a non-zero vector $\mathbf{b}$ and a unit vector $\mathbf{n}$, such that

$$\mathbf{R}\mathbf{U}_a - \mathbf{U}_b = \mathbf{b} \otimes \mathbf{n}, \tag{A.2}$$

where $\mathbf{b} \otimes \mathbf{n}$ is a dyadic product of vectors $\mathbf{b}$ and $\mathbf{n}$. The vector $\mathbf{n}$ is perpendicular to the twinning plane in the reference cubic configuration, the vector $\mathbf{b}$ is the so-called shearing vector, and the matrix $\mathbf{R}$ corresponds to the rotation of the variant $\mathbf{U}_a$ with respect to the variant $\mathbf{U}_b$ when the twin is formed. The properties of the vectors $\mathbf{n}$ and $\mathbf{b}$, or, more precisely, of the transformation of this vector into the reference configuration, i.e. $\mathbf{F}^{-1}\mathbf{b}$, where $\mathbf{F}$ is the corresponding deformation gradient, are used for the identification of the twinning systems. If both these vectors are parallel to some lattice vectors in the reference configuration, the resulting twin is of the compound type (we will distinguish between two different types of the compound twins later in this appendix); if only the vector $\mathbf{n}$ is a lattice vector, the resulting twin is of Type I; if only the vector $\mathbf{F}^{-1}\mathbf{b}$ is a lattice vector, the resulting twin is of Type II; if none of the vectors $\mathbf{F}^{-1}\mathbf{b}$ and $\mathbf{n}$ is a lattice vector, the resulting twin can be classified as a non-conventional twin.

For any chosen pair of variants, all the possible solutions of Eq. (A.2) can be found by using a theorem introduced in Ref. [45,46]. This theorem states that this equation has a solution if and only if the middle eigenvalue (denoted usually as λ_2) of a matrix $\mathbf{C} = \mathbf{U}_b^{-1}\mathbf{U}_a^2\mathbf{U}_b^{-1}$ is equal to 1. If this condition is fulfilled, then there are exactly two solutions of Eq. (A.2) (we will denote them T_1 and T_2), for which the vectors $\mathbf{n}$ and $\mathbf{b}$ and the matrix $\mathbf{R}$ can be calculated by an algorithm also described in Ref. [45,46].

The list of all possible solutions found by applying this theorem for the twins with variant No. 1 and variants No. $2 \div 12$ is given in Table A.1. Since all the other variants can be obtained from the variant No. 1 by rotations and mirror reflections, Table A.1 gives a complete summary of all the possible twinning systems in the examined material.

To be more specific we discuss in more detail the twins between the variants Nos. 1–4. It is obvious that all the twinning systems in which these four variants can form must have the twinning planes perpendicular to the $(001)_P$ plane and that the shearing vectors must lie in this plane. For this reason, we will call these twinning systems in-plane systems and distinguish between them as outlined in Fig. A.1:

- The variants Nos. 1 and 2 have approximately the same orientations of the *a*- and *b*-axis, but differ in the modulation direction as discussed above, so the twins between them are referred to as modulation twins. Obviously, these twins can be also categorized as compound twins, since both the vectors $\mathbf{n}$ and $\mathbf{F}^{-1}\mathbf{b}$ for them are the lattice vectors. However, we will use the term modulation twins instead, to emphasize that the twining planes of this system are associated with the change of the modulation direction, and to distinguish them clearly from the compound twins defined next.
- The variants Nos. 1 and 3 have the same modulation direction but are mirror symmetric about the $\{110\}_P$ plane; such twins are fully analogous to the compound twins in the cubic-to-tetragonal and cubic-to-orthorhombic systems, so we will call them the compound twins.
- The variants Nos. 1 and 4 differ both in the orientations of the *a*- and *b*-axis and in the modulation direction; according to the terminology used in Ref. [49], we will call them non-conventional twins. These non-conventional twins are generic, i.e. they exist in any cubic-to-monoclinic II system, regardless of the exact lattice parameters.

As seen in Table A.1, none of the out-of-plane twinning systems, i.e. the twins between the variants with different orientations of the *c*-axis, can be classified as modulation twins, compound twins or non-conventional twins. Instead, all the possible out-of-plane systems belong to Type I or Type II class, which means that either the vector $\mathbf{F}^{-1}\mathbf{b}$ or the vector $\mathbf{n}$ is always a lattice vector, but never both of them. Only these twinning systems can be reoriented by a magnetic field as the easy magnetization axis or *c*-axis has a different direction for each twin variant.

Importantly the variant No. 1 cannot form any twins with the variants No. $7 \div 10$ as the middle eigenvalue is not equal to 1. This means that no non-generic non-conventional twins (for a definition see Ref. [49]) are allowed in this material.

A.3. Macrotwins between in-plane laminates

Motivated by the experiment, which suggests the existence of laminate, we show in this section that 10 M mar-

Table A.1
All possible twinning systems in the 10 M martensite resulting from the cubic-to-monoclinic II transition. See text for explanation of individual symbols.

Variants	λ_2		n	$(\mathbf{F}^{-1}\mathbf{b})/\lvert\mathbf{F}^{-1}\mathbf{b}\rvert$	Twinning type
1:2	1.0000	T_1	$[0;1;0]$	$[1;0;0]$	Modulation
		T_2	$[1;0;0]$	$[0;1;0]$	Modulation
1:3	1.0000	T_1	$1/\sqrt{2}[1;-1;0]$	$1/\sqrt{2}[1;1;0]$	Compound
		T_2	$1/\sqrt{2}[1;1;0]$	$1/\sqrt{2}[1;-1;0]$	Compound
1:4	1.0000	T_1	$[-0.9509;0.3094;0]$	$[0.3094;0.9509;0]$	Non-conventional[a]
		T_2	$[0.3094;0.9509;0]$	$[0.9509;-0.3094;0]$	Non-conventional[a]
1:5	1.0000	T_1	$1/\sqrt{2}[0;1;-1]$	$[0.0682;0.7055;0.7055]$	Type I
		T_2	$[0.0779;0.7050;0.7050]$	$1/\sqrt{2}[0;-1;1]$	Type II[b]
1:6	1.0000	T_1	$[0.0779;0.7050;-0.7050]$	$1/\sqrt{2}[0;1;1]$	Type II[b]
		T_2	$1/\sqrt{2}[0;1;1]$	$[-0.0682;-0.7055;0.7055]$	Type I
1:7	1.0094				
1:8	1.0094				
1:9	0.9907				
1:10	0.9907				
1:11	1.0000	T_1	$1/\sqrt{2}[1;0;-1]$	$[0.7057;0.0637;0.7057]$	Type I
		T_2	$[0.7053;0.0721;0.7053]$	$1/\sqrt{2}[-1;0;1]$	Type II[c]
1:12	1.0000	T_1	$[0.7053;0.0721;-0.7053]$	$1/\sqrt{2}[1;0;1]$	Type II[c]
		T_2	$1/\sqrt{2}[1;0;1]$	$[-0.7057;-0.0637;0.7057]$	Type I

[a] The twinning plane is inclined by 17.98° from the nearest principal plane of variant No. 1.
[b] The twinning plane is inclined by 4.31° from the nearest {0 1 1} plane of variant No. 1.
[c] The twinning plane is inclined by 4.01° from the nearest {1 0 1} plane of variant No. 1.

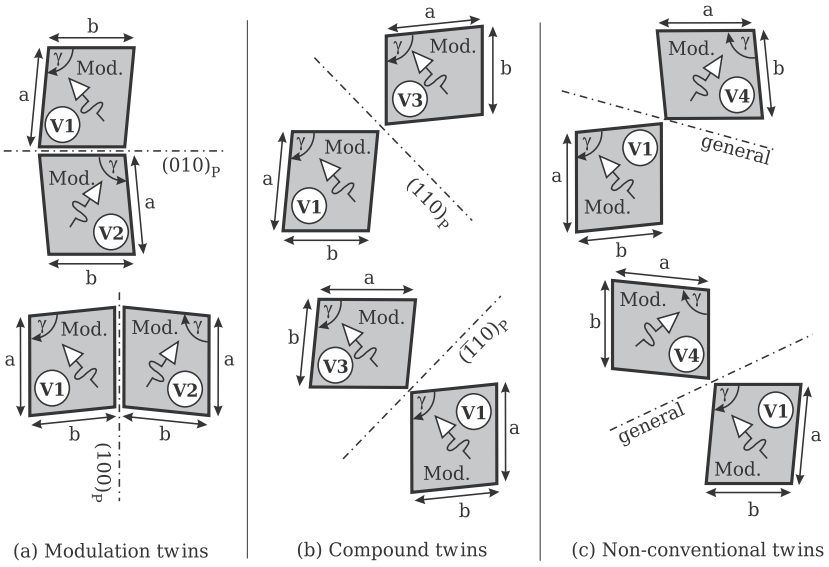

Fig. A.1. Visualization of the three possible in-plane twinning systems between variants No. 1 ÷ 4. The dash-dot lines outline the twinning planes. The view is perpendicular to the $[0\,0\,1]_P$ direction, i.e. to the c-axis of all the variants. Modulation direction is marked by empty-head arrows.

tensite can easily form higher-order laminates, i.e. with microstructures consisting of fine laminates forming the macrotwins, and summarize the main features of such microstructures.

If we consider a fine laminate of any of the in-plane twinning systems formed by the variants Nos. 1–4, the macroscopic deformation gradient describing such microstructure can be (neglecting some small rotation) written as:

$$\boldsymbol{\mu} = \lambda\mathbf{R}\mathbf{U}_a + (1-\lambda)\mathbf{U}_b, \tag{A.3}$$

where λ is a volume fraction of variant $\mathbf{U}_a$ in the laminate. Because of the in-plane character of the twinning system, the matrix $\mathbf{R}$ must represent a rotation about the $[0\,0\,1]_P$ axis only. This means that $R_{33} = 1$, from which it directly follows that $\mu_{33} = e_c$ and that $\mu_{13} = \mu_{23} = \mu_{31} = \mu_{32} = 0$. Consequently, the Bain tensors representing the laminate must be of the form:

$$\mathbf{U}_\mu = \begin{pmatrix} m_a(\lambda) & m_{ab}(\lambda) & 0 \\ m_{ab}(\lambda) & m_b(\lambda) & 0 \\ 0 & 0 & e_c \end{pmatrix}, \tag{A.4}$$

Table A.2
Macrotwinning plane orientations for different volume fraction λ of laminate in the experimentally observed macrotwins.

Microstructures	Volume fraction	n	Description
μ_A:μ_B	$\lambda \in [0,1]$	[0;1;0]	Modulation macrotwin
μ_B:μ_C	$\lambda = 0$	[0.7053; −0.0721; 0.7053]	Type II macrotwin
	$\lambda = 0.25$	[0.7052; −0.0734; 0.7052]	
	$\lambda = 0.5$	[0.7051; −0.0748; 0.7051]	
	$\lambda = 0.75$	[0.7050; −0.0763; 0.7050]	
	$\lambda = 1.0$	[0.7050; −0.0779; 0.7050]	
μ_C:μ_D	$\lambda \in [0,1]$	[0;1;0]	Modulation macrotwin
μ_D:μ_A	$\lambda = 0$	[0.7053; 0.0721; 0.7053]	Type II macrotwin
	$\lambda = 0.25$	[0.7052; 0.0734; 0.7052]	
	$\lambda = 0.5$	[0.7051; 0.0748; 0.7051]	
	$\lambda = 0.75$	[0.7050; 0.0763; 0.7050]	
	$\lambda = 1.0$	[0.7050; 0.0779; 0.7050]	

where the components m_a, m_b and m_{ab} depend on the volume fraction λ. For reasons of symmetry there are 11 similar laminates of the same twinning system. The components of the corresponding Bain tensors are arranged the same way as the components e_a, e_b and e_{ab} are arranged in the matrices $\mathbf{U}_2 \div \mathbf{U}_{12}$ (Eq. (A.1)). This enables us to analyze the ability of these laminates to form macrotwins using exactly the same method as for the twinning between the individual variants described in the previous section.

Since there are three in-plane twinning systems for each orientation of the c-axis, and since the laminates of these systems can form up to four different macrotwins, e.g. the modulation laminates can form compound and non-conventional in-plane macrotwins and Type I and Type II out-of-plane macrotwins, there are up to 12 different macrotwinning systems predicted by the theory. However, instead of calculating the orientations of all macrotwinning planes for all combinations, here we list only those that are observed experimentally. These are the macrotwins between the compound a/b-laminates:

$$\mu_A = \lambda \mathbf{R}_{9:11}\mathbf{U}_9 + (1-\lambda)\mathbf{U}_{11}, \tag{A.5}$$

$$\mu_B = \lambda \mathbf{R}_{10:12}\mathbf{U}_{10} + (1-\lambda)\mathbf{U}_{12}, \tag{A.6}$$

$$\mu_C = \lambda \mathbf{R}_{2:4}\mathbf{U}_4 + (1-\lambda)\mathbf{U}_2, \tag{A.7}$$

$$\text{and } \mu_D = \lambda \mathbf{R}_{1:3}\mathbf{U}_3 + (1-\lambda)\mathbf{U}_1. \tag{A.8}$$

The resulting twinning planes for the volume fraction λ changing from 0 to 1 are summarized in Table A.2. The modulation macrotwins between the a/b-laminates μ_A and μ_B (or, respectively, μ_C and μ_D) have exactly the same orientation for all admissible volume fractions. The orientation of the Type II macrotwinning plane changes slightly between the two degenerate cases ($\lambda = 0$ and $\lambda = 1$), which are geometrically identical to the 1:5 and 1:11 Type II twins in Table A.1. This means that in the deformed configuration using variant No. 1 the declination of the macrotwin boundary from the nearest {110} plane varies between 4.01° and 4.31°, which in projection onto the (100) plane gives a deviation of between 5.87° and 6.28° in agreement with the experiment.

References

[1] Sozinov A, Likhachev AA, Lanska N, Söderberg O, Ullakko K, Lindroos VK. Mat Sci Eng A 2004;378:399.
[2] Marioni MA, O'Handley RC, Allen SM. Appl Phys Lett 2003;83:3966.
[3] Tickle R, James RD. J Mag Mag Mat 1999;195:627.
[4] Likhachev AA, Sozinov A, Ullakko K. Mech Mater 2006;38:551.
[5] Park SE, Shrout TR. J Appl Phys 1997;82:1804.
[6] Straka L, Hänninen H, A Soroka, Sozinov A. J Phys: Conf Ser 2011;303:012079.
[7] Straka L, Lanska N, Ullakko K, Sozinov A. Appl Phys Lett 2010;96:131903.
[8] Gaitzsch U, Pötschke M, Roth S, Rellinghaus B, Schultz L. Acta Mat 2009;57:365.
[9] Scheerbaum N, Heczko O, Liu J, Hinz D, Schultz L, Gutfleisch O. New J Phys 2008;10:073002.
[10] Chmielus M, Zhang XX, Witherspoon C, Dunand DC, Müllner P. Nature Mat 2009;8:863.
[11] Thomas M, Heczko O, Buschbeck J, Lai YW, McCord J, Kaufmann S, et al. Adv Mater 2009;21:3708.
[12] Heczko O, Thomas M, Buschbeck J, Schultz L, Fähler S. Appl Phys Lett 2008;92:072502.
[13] James RD, Wuttig M. Phil Mag A 1998;77:1273.
[14] Ullakko K, Huang JK, Kanter C, O'Handley RC, Kokorin VV. Appl Phys Lett 1996;69:1966.
[15] Faran E, Shilo D. J Mech Phys Sol 2011;59:975.
[16] Heczko O, Sozinov A, Ullakko K. IEEE Trans Mag 2000;36:3266.
[17] Ganor Y, Shilo D, Shield TW, James RD. App Phys Lett 2008;93:122509.
[18] Dunand DC, Müllner P. Adv Mater 2011;23:216.
[19] Heczko O, Soroka A, Hannula S-P. App Phys Lett 2008;93:022503.
[20] O'Handley RC, Lograsso TA. private communication.
[21] Straka L, Heczko O, Hänninen H. Acta Mat 2008;56:5492.
[22] Müllner P, Chernenko VA, Kostorz G. J Mag Mag Mat 2003;267:325.
[23] Müllner P, King AH. Acta Mat 2010;58:5242.
[24] Müllner P, Chernenko VA, Kostorz G. J App Phys 2005;95:1531.
[25] Mogylnyy G, Glavatskyy I, Glavatska N, Soderberg O, Ge Y, Lindroos VK. Scripta Mat. 2003;48:1427.
[26] Li Z, Zhang Y, Esling C, Zhao X, Zuo L. Acta Mat 2011;59:2762.
[27] Nishida M, Hara T, Matsuda M, Ii S. Mat Sci Eng A 2008;481–482:18.
[28] Sozinov A, Lanska N, Soroka A, Straka L. Appl Phys Lett. 2011;99:124103.
[29] Straka L, Hänninen H, Heczko O. Appl Phys Lett 2011;98:141902.
[30] Ge Y, Jiang H, Sozinov A, Söderberg O, Lanska N, Keränen J, et al. Mat Sci Eng A 2006;438:961.
[31] Lanska N, Söderberg O, Sozinov A, Ge Y, Ullakko K, Lindroos VK. J Appl Phys 2004;95:8074.
[32] Righi L, Albertini F, Pareti L, Paoluzi A, Calestani G. Acta Mat 2007;55:5237.
[33] Hartman JS, Gordon RL, Lessor DL. App Opt 1981;20:2665.
[34] Heczko O, Jurek K, Ullakko K. J Mag Mag Mat 2001;226–230:996.
[35] Pogany L, Ramstock K, Hubert A. Scanning 1992;14:263.
[36] Cullity BD, Stock SR. Elements of X-Ray diffraction. 3rd ed. Englewood Cliffs, NJ: Prentice Hall; 2001.
[37] Ge Y, Heczko O, Söderberg O, Hannula S-P. App Phys Lett 2006;89:082502.
[38] Ge Y, Söderberg O, Lanska N, Sozinov A, Ullakko K, Lindroos VK. J Phys IV 2003;112:921.
[39] Martynov VV, Kokorin VV. J de Phys III 1992;2:739.

[40] Khachaturyan AG, Shapiro SM, Semenovskaya S. Phys Rev B 1991;43:10832.
[41] Kaufmann S, Rößler UK, Heczko O, Wuttig M, Buschbeck J, Schultz L, et al. Phys Rev Lett 2010;104:145702.
[42] Bhattacharya K. Microstructure of martensite. New York: Oxford University Press; 2003.
[43] Ball JM, Koumatos K, Seiner H. An analysis of non-classical austenite–martensite interfaces in CuAlNi. In: Olson GB, Lieberman DS, Saxena A. editors. Proceedings of the international conference on martensitic transformations, ICOMAT-08. TMS, Pennsylvania; 2009. p. 383 <http://arxiv.org/abs/1108.6220>.
[44] Waitz T. Acta Mat 2005;53:2273.
[45] Ball JM, James RD. Arch Rat Mech Anal 1987;100:13.
[46] Ball JM, James RD. Phil Trans R Soc Lond A 1992;338:389.
[47] Bhattacharya K, Li B, Luskin M. Arch Rat Mech Anal 1999;149:123.
[48] Kaufmann S, Niemann R, Thersleff T, Rößler UK, Heczko O, Buschbeck J, et al. New J Phys 2011;13:053029.
[49] Pitteri M, Zanzotto G. Acta Mat 1998;46:225.

3.2 Publikace *Rozdílné mikrostruktury pohyblivých dvojčatových hranic v 10 M modulovaném martenzitu slitiny Ni-Mn-Ga.*

Bibliografická citace: Heczko, O., Straka, L., Seiner, H. Different microstructures of mobile twin boundaries in 10 M modulated Ni-Mn-Ga martensite (2013) Acta Materialia, 61 (2), pp. 622-631.

Stručná anotace: Tato publikace v podstatě navazuje na publikaci uvedenou v podkapitole 3.1, rozšiřuje ji o diskuzi přípustných mikrostruktur, jejich analýzu z hlediska kinematické kompatibility a jejich energetickou náročnost, k čemuž je využito konceptu takzvaných *indikátorů kompatibility* [63]. Rovněž je zde započata diskuze mechanismů pohybu makrodvojčatových rozhraní, která je dále podrobně rozvinuta v podkapitole 3.3.

Příspěvek habilitanta: Příspěvkem habilitanta byly všechny výpočty a teoretické diskuze týkající se elastické napjatosti a kinematické kompatibility.

Available online at www.sciencedirect.com

SciVerse ScienceDirect

Acta Materialia 61 (2013) 622–631

Acta MATERIALIA

www.elsevier.com/locate/actamat

Different microstructures of mobile twin boundaries in 10 M modulated Ni–Mn–Ga martensite

O. Heczko [a,*], L. Straka [b], H. Seiner [c]

[a] Institute of Physics, ASCR, Na Slovance 2, 182 02 Prague, Czech Republic
[b] Aalto University School of Engineering, Laboratory of Engineering Materials, PL 14200, FIN-00076 AALTO, Finland
[c] Institute of Thermomechanics, ASCR, Dolejškova 1402/5, 182 00 Prague, Czech Republic

Received 10 June 2012; received in revised form 18 September 2012; accepted 9 October 2012
Available online 3 November 2012

Abstract

The morphology and microstructure of a single, macroscopically straight twin interface with a twinning stress of about 1 MPa was analysed in detail by differential interference contrast optical microscopy and X-ray diffraction. The interface was identified as a Type I macrotwin boundary between two variants with *a*/*b*-laminates and constant modulation direction, in contrast with a highly mobile twinned interface consisting of Type II macrotwin boundary segments with changing modulation direction and *a*/*b*-laminate reported earlier. Theoretical analysis using elastic continuum theory shows that only pure Type I or Type II boundaries are fully compatible with *a*/*b*-laminate. Other hypothetical twin microstructures combining these two mobile interfaces are shown to be incompatible to various degrees. A weakly incompatible combination of Type I and II boundaries was experimentally observed. The large difference in mobility between Type I and Type II macrotwin boundaries created at the same location of the same sample indicates that the mobility depends on the internal structure of these boundaries. A possible origin of this different mobility is discussed.

Keywords: Martensitic twin microstructure; Twinning interfaces; Ni–Mn–Ga martensite; Mobility of twin boundary; Magnetic shape memory

1. Introduction

The magnetically induced reorientation (MIR) of martensite [1], one of the family of magnetic shape memory (MSM) effects [2], depends critically on the high mobility of twin boundaries as the driving force generated by magnetic fields is limited. In Ni–Mn–Ga the maximum magnetic force is equivalent to a mechanical stress of about 3 MPa [3–5]. The magnetic-field- or stress-driven propagation of twin boundaries reorients the non-cubic lattice by about 90°, resulting in large macroscopic strain [1,3]. The stress needed for the twin boundary motion is called twinning stress and the twin boundaries with low twinning stress can be called highly mobile or to possess high mobility. The lower the twinning stress, the higher the efficiency of MIR-based magnetic actuation and the lower the magnetic field needed for the effect to occur [4,5]. The very low twinning stress of ≈0.1 MPa reported recently for a single twin boundary moving in Ni–Mn–Ga single crystal [6,7] makes MIR possible under very low fields, down to ≈200 Oe or ≈1600 A m^{-1} [7], which is easily generated and controlled. Such low twinning stress suggests an actuation efficiency of up to ≈90% in magnetic saturation [8].

Modulated 10 M martensite is often approximated as a tetragonal structure [9,10]. In this case the mobile twin boundary can be considered as compound twinning without any fine features. However, using a more precise description including monoclinic and orthorhombic distortion of 10 M martensite lattice, various new types of twin interfaces can emerge [11–13]. These twin boundaries can exhibit considerably different twinning stresses [14,15]. Using optical microscopy and X-ray diffraction analysis we showed that very low twinning stress, ≈0.1 MPa, occurs

* Corresponding author. Tel.: +420 266 052714; fax: +420 286 890 527.
E-mail address: heczko@fzu.cz (O. Heczko).

1359-6454/$36.00
http://dx.doi.org/10.1016/j.actamat.2012.10.007

only when the twinned interface consists of Type II macrotwin boundaries. This complex twinned interface connects two variants with different orientations of the *c*-axis, which themselves consist of modulation twins and twinned *a*/*b* laminate. The calculation showed that this arrangement of various twinning systems is fully elastically compatible. In contrast to twin boundaries of Type II with very low twinning stress, the one order higher twinning stress, about 1 MPa, was tentatively ascribed to Type I twin boundaries [14,15]. However, the microstructure analysis of this less mobile twin interface has not been done. Additionally, due to multiple twinning systems, many different combinations of macrotwin interfaces can arise and these interfaces might differ in their mobility.

In this paper, we investigate both experimentally and theoretically the microstructure of different types of twin boundaries and examine in detail the twin boundary with lower mobility, i.e. the boundary with 1 MPa twinning stress. Combining the knowledge obtained from the experiments and elastic continuum theory, we categorize and discuss various possible twin microstructures and combined interfaces consisting of Type I and Type II twin boundary segments. Finally, we offer a qualitative interpretation and look at what underlies the different mobilities and twinning stresses of Type I and Type II twin boundaries.

2. Experimental methods

$Ni_{50.2}Mn_{28.3}Ga_{21.5}$ at.% (determined from X-ray fluorescence spectroscopy) single-crystal samples produced by AdaptaMat Ltd. were cut approximately along the {1 0 0} planes of the parent cubic austenite. The electropolished samples were $0.9 \times 2.4 \times 20\ mm^3$ in size. The lattice parameter of austenite was $a_P = 5.832$ Å near the martensitic transformation which occurs at $M_s = 323$ K. The material is ferromagnetic with a Curie temperature of 370 K. For the description of the lattice of 10 M martensite we used the cell derived from the cubic cell of the austenite (cubic coordinates) [9,10]. All experiments were performed at room temperature where the structure is 10 M martensite with lattice parameters $a = 5.972$ Å, $b = 5.944$ Å, $c = 5.584$ Å and $\gamma = 90.37°$. The experimental methods used were described in detail in Ref. [15] and here we provide only a brief summary.

The various types and numbers of twin boundaries were created from a single variant sample using repeated tensile and compression stress applied parallel to the long axis of the sample [6]. The compressive mechanical testing of the samples with a single twin boundary was performed using the instrument described in Ref. [8]. Placing this instrument in the optical microscope allowed the mobility of the twin boundary to be determined during observation of its movement, and enabled the twin boundary to be positioned in a selected orientation. The type of boundary was identified from additional optical micrographs using reflective differential interference contrast (DIC) or Nomarski contrast. This contrast visualizes differently tilted surface by different colors or shades of gray [16].

For detailed microstructural analysis of twinned interface and variants we used X-ray diffraction with a microdiffraction probe (XRμD) using point focus and line detector with an X'Pert PRO PANalytical powder diffractometer (Co anode, $\lambda = 1.78901$ Å). The irradiated area was defined by a monocapillary with inner radius 0.1 mm resulting in a beam radius at the sample surface 0.12–0.14 mm. Full identification of the twin variants and their orientation was achieved by XRμD mapping using 2θ-scan, ω-scan and ψ-scan along the studied twinned interface. First, several ω- and ψ-scans were performed until the maximum intensities of the (4 0 0), (0 4 0) and (0 0 4) peaks were found in order to obtain the precise orientation of the crystal. The 2θ-scan along the boundary was then used to identify the different martensitic variants. Due to the chemical order of Heusler alloys, {2 0 0} and {6 0 0} planes could also be detected as weak superstructure peaks [17,18]. The (6 0 0) and (0 6 0) lines were used to resolve the *a* and *b* lattice constants. A combination of ω-scan and ψ-scan for selected 2θ was used to identify the modulation direction. To determine the modulation direction it is sufficient to search for the first satellite reflections particular to the modulation. This means searching for the diffraction peaks with non-integral indexes , i. e. h = 4.4, k = ± 0.4, l = 0 or (4.4 ± 0.4 0) or similarly (3.6 ± 0.4 0) in cubic coordinates using proper ω and ψ [15,19].

3. Results and discussion

3.1. Microstructural analysis

Two different twin interfaces with different mobilities located next to each other in the sample are shown in Fig. 1. Both boundaries are macroscopically straight and differ only in terms of the angle. The twin boundaries, or more precisely traces of twin boundaries, in the observation plane are visible in the micrographs due to the surface tilt associated with the twinning. According to Ref. [14], the interface with higher mobility or lower twinning stress ≈0.1 MPa is a Type II twin boundary, while the less mobile twin interface with twinning stress ≈1 MPa is assumed to be a Type I twin boundary. The Type I twin boundaries are parallel to the (1 0 1) plane and the Type II boundaries are approximately along the (10 1 10) (or equivalent) plane using cubic coordinates. The angle between the traces of the boundaries is about 6°, in agreement with the calculation. The Type II twin boundary shown here is macroscopically straight, in contrast with the segmented zigzag character of the highly mobile Type II twinned interface studied previously [15] (see also Figs. 4 and 6a). The boundary consists of only one segment with no modulation twins, i.e. the modulation is the same along the interface. In contrast, the assumed Type I twin boundary coincides with the (1 0 1) plane and is straight.

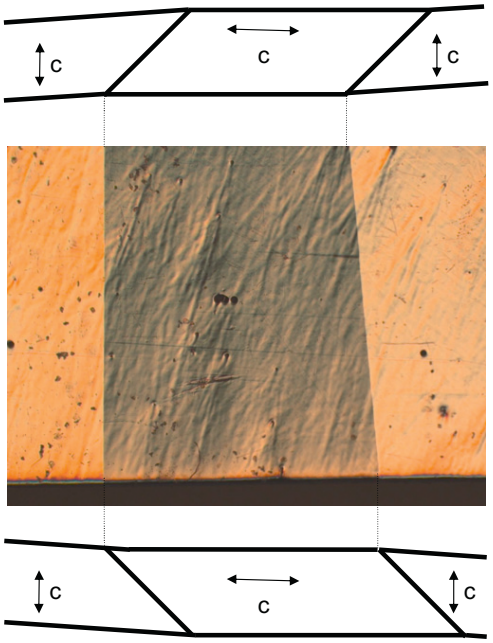

Fig. 1. Optical micrograph showing the traces of the hard (left) and easy (right) moving twin boundaries in the plane (001) having the same orientation as the twin plane normal [011] (differential interference contrast (DIC)). On the side of the sample, i.e. in the (100) plane, there is no DIC contrast and the different variants on the sides were identified by polarization contrast. Since the contrast is weak, both sides are drawn. The orientation of the *c*-axis is shown in the figure. The width of the image is approximately 2 mm.

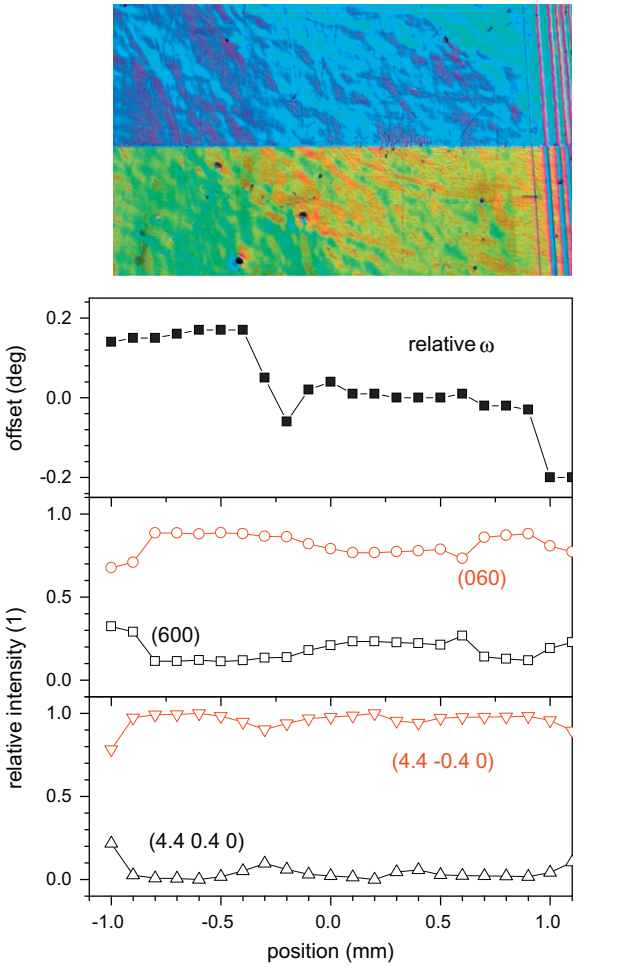

Fig. 2. (a) Optical micrographs (DIC) of a macrotwin boundary. The orientation of the *c*-axis is perpendicular in the upper variant and vertical in plane in the lower variant. X-ray analysis along the twin interface: (b) ω-scan using the (400) reflection to probe the presence of low-angle boundaries or the mozaicity of the crystal. (c) Relative volume of the variants with *a*- or *b*-orientation perpendicular to the surface calculated from the (600) and (060) reflections. (d) The relative integral intensity of the satellite peaks nearest to the (400) reflection. This provides a direct measure of the amount of variants with different modulation directions.

However, the very finely segmented Type II twin boundary, with segments below the resolution of optical microscopy, i.e. variants containing very fine modulation domains, could also appear exactly aligned along the (101) plane. The fine modulation domains in 10 M martensite have been observed in thin foil by TEM [20]. Therefore the simple refinement of the modulation twinning can produce a straight interface. This very fine modulation twinning can hinder the movement of the twinned interface and the sample could exhibit higher twinning stress. In this case there would be only one type of boundary (Type II) differing only by the scale of modulation twinning. To exclude fine modulation twinning and to prove that a particular observed twin interface aligned along (101) is a Type I boundary, we analyzed in detail the structure of the single twin boundary with high twinning stress using X-ray microdiffraction. To render the analysis unambiguous, we recreated a single straight twin boundary in the sample from the single variant state by mechanical loading. The optical micrograph of this single boundary and various X-ray scans along the boundary are shown in Fig. 2. The optical contrast arises from the tilt between variants corresponding to the twinned interface ($90 - 2 * \arctan(a/c) = 3.8°$). There is no other observable relief apart from surface irregularities due to electropolishing.

After proper orientation of the crystal using the {400} reflections we determined the mozaicity or crystal misorientation (perfectness) of the crystal using an ω-scan. Along the boundary there are a few low-angle boundaries with crystal misorientations up to 0.4°, similar to a previous report [15] and other crystals from AdaptaMat. The presence of both (600) and (060) reflections in the scan along the twin boundary shows the presence of variants with *a*- and *b*-axes perpendicular to the analysed surface. This indicates twinned layers of *a*- and *b*-variants or fine *a*/*b*-laminate (Fig. 3). This twinning was previously identified as compound twinning [15]. The ratio of the variants is not constant along the boundary, but slightly varies with an average ratio of about 1:4 (Fig. 2c). There should be slight surface relief associated with *a*/*b* twinning about 0.3° ($90 - 2 * \arctan(b/a)$) but the individual variants with *a*- and *b*-orientations could not be resolved by either optical microscopy or atomic force microscopy.

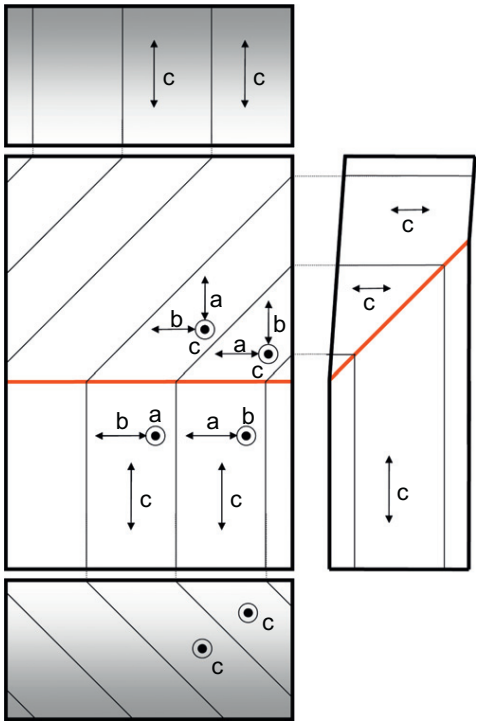

Fig. 3. Sketch of analyzed twinned interface (thick, red line) with marked orientation of crystal axes. The interface is a Type I macrotwin boundary, which connects two variants with differently oriented *a*/*b*-laminate (thin lines). The thickness of the laminate bands is strongly exaggerated for the sake of clarity. (For interpretation of the references to colour in this figure legend, the reader is referred to the web version of this article.)

Finally we investigated the modulation direction in variants with their *a*- or *b*-axis perpendicular to surface. As speculated above, the modulation direction could either fluctuate on a very fine scale or can have the same direction along the interface depending on the type of the mobile interface. X-ray diffraction can be used to determine the average amount of variants with different modulation orientations, and therefore can identify any changes in the modulation direction regardless of scale. The relative intensities of the $(4.4 \pm 0.4\ 0)$ peaks corresponding to the relative volume fractions of two variants with different modulation directions are shown in Fig. 2d. The measurement indicates that there is only one direction of the modulation in most of the scanned region, except on the edges of the sample where some mixing of the two directions occurs. This mixing on the edges can be caused by additional twinning originating from sample manipulation. This twinning feature is also apparent on optical micrographs. The observed single modulation direction along most of the studied region indicates that the boundary does not consist of fine Type II segments. The single modulation direction and the simultaneous alignment along (1 0 1) confirms the Type I character of the boundary. The detailed microstructure of Type I boundary is sketched in Fig. 3. In agreement with this experiment the calculation, presented in the next section, indicated that in this geometry the modulation twinning is not compatible with the Type I boundary.

From the experiment we can conclude that the optical observation may be enough to distinguish the type of the boundary according the tilt of the twinned interface trace in the (1 0 0) or (0 1 0) plane. To show that different boundaries can be created at the same place, we annihilated the analyzed Type I boundary and recreated a Type II segmented interface by mechanical stress from the single-variant sample and moved it to approximately the same position. For comparison, the optical micrographs of both interfaces are shown in Fig. 4. The segmented interface exhibits a typical zigzag pattern and bands in the variant with the in-plane *c*-axis, indicating the modulation twinning similar to the boundary analyzed previously [15]. The tilt of the zigzag lines from the analyzed Type I boundary is $\pm 6°$. This experiment shows that modulation twins not present before can be formed together with the Type II boundary since this macrotwin interface is compatible with modulation twinning. In contrast with TEM studies on foil [20], modulation twinning is macroscopically straight with a [0 1 0] overall direction. In the same sample we observed that modulation domains often appear, disappear or rearrange during the subsequent annihilation and new formation of the mobile interfaces by mechanical loading. In addition to Type I boundary, both Type II macroscopic planar and segmented interfaces with large segments can appear during subsequent loadings. Perhaps, then, it is no great surprise that, apart of these analyzed relatively simple cases, sometimes more complex microstructure of twinned interfaces can be observed. An example is shown in Fig. 5. The observed microstructure consists of alternating segments of Type I and Type II macrotwins with the bands of modulation twinning. These are only occasionally observed and these configurations have not yet been studied in detail [21]. The compatibility of the microstructure involving both Type I and Type II boundary is discussed in the end of next section.

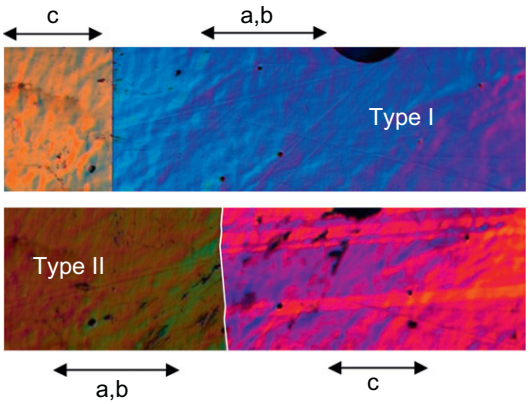

Fig. 4. Type I (upper) and Type II (lower) twin boundaries successively created and shown in nearly the same place on the sample. For better visibility the Type II boundary is enhanced by a white zigzag line; weak horizontal bands are modulation twinning.

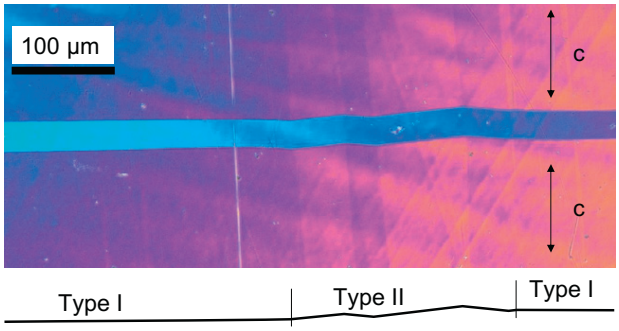

Fig. 5. Optical micrograph showing an example of the weakly incompatible two parallel macrotwin interfaces identified as the combination of Type I and Type II macrotwin boundaries. The line following the interface demonstrates the different angles between segments of boundaries: about 6° between Type I and Type II boundaries, and about 12° between two segments of Type II boundary. The weak contrast of nearly vertical bands is due to modulation twinning in the variant with the *c*-axis in plane [15]. In the narrow middle band the *c*-axis is perpendicular to the plane.

3.2. Compatibility analysis

As shown by the X-ray results, the experimentally observed Type I boundaries are planar interfaces between two fine microstructures, each containing variable amounts of *a*/*b* (compound) twins (Fig. 3). In this section, we will analyze the kinematic compatibility, i.e. geometric admissibility, of such interfaces within the framework of continuum mechanics, and discuss some of the possible more complex morphologies from this point of view. Throughout this section, we will use the terminology introduced in Ref. [15]. In particular, we will use the term "compound twins" only for the (1 1 0)-compound twinning system (twins between variants with the same modulation direction but different orientations of the *a*- and *b*-axes), and the term "modulation twins" for the (1 0 0)-compound twinning system formed by two variants with different modulation directions and the same orientations of the *a*- and *b*-axes. We will also use the term "modulation macrotwin" for a compatible planar interface between two fine compound laminates at which the modulation direction changes (but the *a*/*b* ratio and the orientation of the *c*-axis does not change). In a similar sense, we will use the terms "Type I macrotwins" and "Type II macrotwins" for interfaces between the *a*/*b* laminates at which the orientation of the *c*-axis changes. Further details on the ability of the 10 M martensite to form such macrotwins can be found in Ref. [15].

In this reference it was shown that the highly mobile interface has the complex morphology sketched in Fig. 6a. This morphology consists of fine compound *a*/*b* laminates marked μ_A, μ_B, μ_C and μ_D, from which the μ_A and μ_B laminates contain the martensitic variants with the *c*-axis oriented parallel to the x_3 axis (approximately perpendicular to the observed surface of the sample) and the μ_C and μ_D laminates contain the variants with the *c*-axis parallel to the x_1-axis (lying approximately on the observed surface of the sample and parallel to the long edge). The involved macrotwinning systems are the modulation macrotwins μ_A:μ_B and μ_C:μ_D, and Type II macrotwins μ_A:μ_C and μ_B:μ_D. If all laminates $\mu_{A,\ldots,D}$ are homogeneous and of first order, this morphology is fully compatible, i.e.

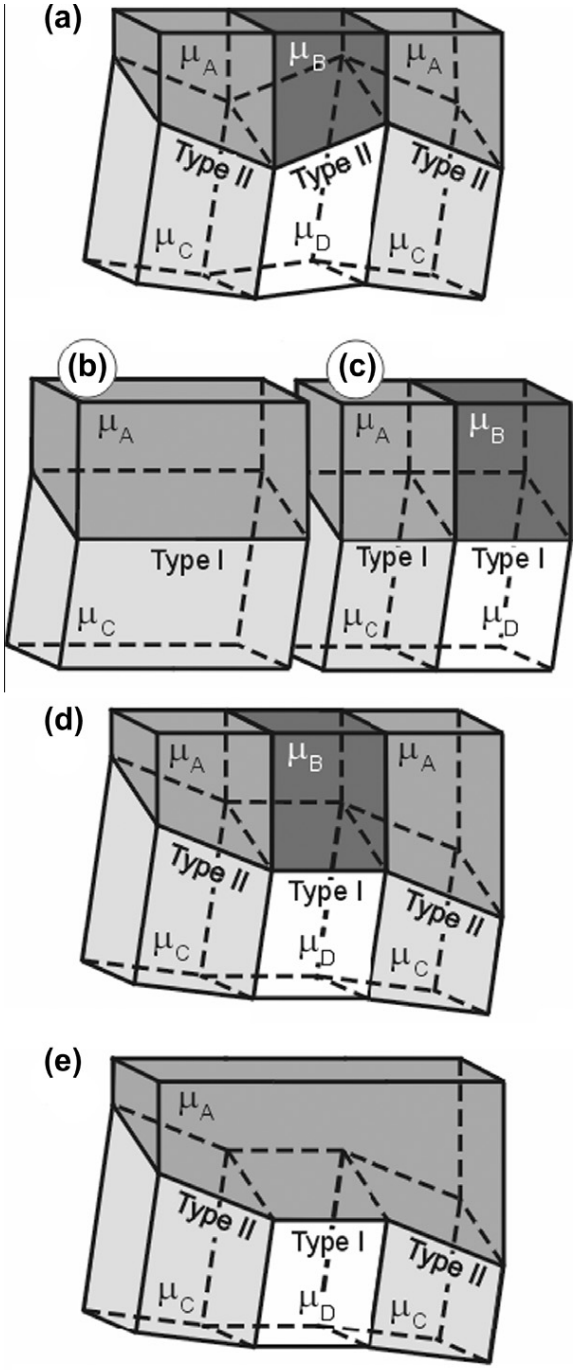

Fig. 6. Possible morphologies of the interface: (a) the highly mobile morphology; (b) the low-mobility morphology—hard boundary; (c) the hard boundary intersected by a modulation macrotwin; (d) a combination of the low and highly mobile interfaces; (e) a degenerate case of (d) for which $\psi = 0$. The unlabeled interfaces parallel to the x_1x_3-plane are the modulation macrotwinning planes.

it can exist without additional elastic strains [15]. Further we demonstrated that the compound laminates can also form Type I macrotwins, which is exactly the boundary with high twinning stress (Fig. 6b), consisting of a single Type I macrotwin boundary between two compound laminates μ_A and μ_C (or μ_B and μ_D). If these laminates are both homogeneous first-order laminates with the same volume fraction of a/b variants, then the condition of the macroscopic compatibility is fulfilled and this interface can exist without elastic strains. This particular structure was experimentally analyzed in a previous section and is sketched in Fig. 3, which shows a/b compound twins (laminate) and Type I macrotwins.

The question is whether the highly mobile boundary (Fig. 6a) and the rigid boundary (Fig. 6b) are the only two admissible morphologies of the interface. A simple extension of the analyzed case is the morphology outlined in Fig. 6c. This morphology consists of four homogeneous laminates $\mu_{A,\ldots,D}$ separated by the Type I and modulation macrotwins, which cross each other. As explained in detail in Ref. [22], the crossing morphology can be fully kinematically compatible, i.e. can exist without additional elastic strains, if the following three conditions are simultaneously fulfilled:

1. The four homogeneous laminates involved in the morphology can pairwise form compatible planar interfaces. This means that there exist four unit vectors $\mathbf{n}_{\mu_A:\mu_B}$, $\mathbf{n}_{\mu_B:\mu_D}$, $\mathbf{n}_{\mu_D:\mu_C}$, and $\mathbf{n}_{\mu_C:\mu_A}$, four shearing vectors $\mathbf{b}_{\mu_A:\mu_B}$, $\mathbf{b}_{\mu_B:\mu_D}$, $\mathbf{b}_{\mu_D:\mu_C}$, and $\mathbf{b}_{\mu_C:\mu_A}$ and four rotation matrices $\mathbf{R}_{\mu_A:\mu_B}$, $\mathbf{R}_{\mu_B:\mu_D}$, $\mathbf{R}_{\mu_D:\mu_C}$, and $\mathbf{R}_{\mu_C:\mu_A}(\mathbf{R}\in SO(3))$, such that

$$\mathbf{R}_{\mu_A:\mu_B}\mathbf{U}_{\mu_B}-\mathbf{U}_{\mu_A}=\mathbf{b}_{\mu_A:\mu_B}\otimes\mathbf{n}_{\mu_A:\mu_B}, \quad (1)$$

$$\mathbf{R}_{\mu_B:\mu_D}\mathbf{U}_{\mu_D}-\mathbf{U}_{\mu_B}=\mathbf{b}_{\mu_B:\mu_D}\otimes\mathbf{n}_{\mu_B:\mu_D}, \quad (2)$$

$$\mathbf{R}_{\mu_D:\mu_C}\mathbf{U}_{\mu_C}-\mathbf{U}_{\mu_D}=\mathbf{b}_{\mu_D:\mu_C}\otimes\mathbf{n}_{\mu_D:\mu_C}, \quad (3)$$

$$\mathbf{R}_{\mu_C:\mu_A}\mathbf{U}_{\mu_A}-\mathbf{U}_{\mu_C}=\mathbf{b}_{\mu_C:\mu_A}\otimes\mathbf{n}_{\mu_C:\mu_A}, \quad (4)$$

where $\mathbf{U}_{\mu_{A,\ldots,D}}$ are Bain matrices of the individual homogeneous laminates. Then the vectors $\mathbf{n}$ have the meaning of unit vectors perpendicular to the individual macrotwinning planes in the reference configuration. We would like to point out that these conditions ensure only the ability of the involved homogeneous laminates to form the individual interfaces. In addition, however, the solution of Eqs. (1)–(4) provides also the values of vectors $\mathbf{n}$ and matrices $\mathbf{R}$ for each such possible interface, which are further used in the second and the third conditions given below.

2. The stress-free macrotwinning planes intersect on one line, which means that all unit vectors $\mathbf{n}$ from the first condition lie in one plane. The fulfilment of this condition can be parameterized by a scalar parameter ϕ defined as

$$\phi=\arcsin\left|\frac{\mathbf{n}_{\mu_A:\mu_B}\times\mathbf{n}_{\mu_C:\mu_A}}{|\mathbf{n}_{\mu_A:\mu_B}\times\mathbf{n}_{\mu_C:\mu_A}|}\times\frac{\mathbf{n}_{\mu_D:\mu_C}\times\mathbf{n}_{\mu_B:\mu_D}}{|\mathbf{n}_{\mu_D:\mu_C}\times\mathbf{n}_{\mu_B:\mu_D}|}\right|, \quad (5)$$

which is equal to zero if this condition is fulfilled and different from zero otherwise.

3. The mutual rotations between the laminates over the macrotwinning planes compensate each other, i.e. the matrices $\mathbf{R}$ from the first condition satisfy the relation

$$\mathbf{R}_{\mu_A:\mu_B}\mathbf{R}_{\mu_B:\mu_D}\mathbf{R}_{\mu_D:\mu_C}\mathbf{R}_{\mu_C:\mu_A}=\mathbb{I} \quad (6)$$

(see Ref. [22] for a more detailed explanation). The fulfilment of this condition can be parameterized by one scalar parameter, the angle ψ defined as

$$\psi=\arccos\left(\frac{\mathrm{tr}(\mathbf{R}_{\mu_A:\mu_B}\mathbf{R}_{\mu_B:\mu_D}\mathbf{R}_{\mu_D:\mu_C}\mathbf{R}_{\mu_C:\mu_A})-1}{2}\right). \quad (7)$$

The parameter is equal to zero if this third condition is fulfilled and different from zero otherwise.

The scalar parameters ϕ and ψ were first introduced by Stupkiewicz and Górzyńska-Lengiewicz [23], who called them "incompatibility indicators", which is a term we will adopt here as well. If the first condition is fulfilled, the values of ϕ and ψ then indicate how much the resulting morphology deviates from full compatibility. The incompatibility parameter with a very similar meaning to ψ was also introduced by Balandraud et al. [24,25] for special microstructures for which $\phi\equiv 0$.

Following the work of Koumatos [26], these three conditions can be further simplified if $\mathbf{n}_{\mu_A:\mu_B}=\mathbf{n}_{\mu_D:\mu_C}$, i.e. if the crossing of the two twinning systems involved does not change the twinning plane orientation of one of them. Then the second condition (coplanarity of the vectors $\mathbf{n}$) is a direct consequence of the first and the third conditions. Nevertheless, even in such a simplified case it is necessary to use both the scalar indicators ϕ and ψ to measure possible incompatibility. The reason is that if the third condition is satisfied only approximately (e.g. $\psi\lesssim 0.1°$), the implication from Ref. [26] does not tell us anything about the value of the indicator ϕ, so the discussed microstructure can be both very close to full compatibility or completely incompatible.

Additionally, as both the macrotwinning plane orientations $\mathbf{n}$ and the rotation matrices $\mathbf{R}$ can be dependent on the a/b volume fraction of the laminates, the incompatibility indicators can also change with this fraction. For the orientations $\mathbf{n}$, an example of such dependence was calculated numerically in Ref. [15] with the following result: if μ_A is a compound laminate with the c-axis oriented along the x_1 direction of some Cartesian coordinate system and with the modulation along the $[0;\sqrt{2}/2;-\sqrt{2}/2]$ direction in this system and this compound laminate forms a Type II macrotwin boundary with a laminate μ_C having the c-axis oriented along the x_3 direction and with the modulation along the $[\sqrt{2}/2;-\sqrt{2}/2;0]$ direction, the vector $\mathbf{n}_{\mu_C:\mu_A}$ is equal to $[0.7053;-0.0721;0.70530]$ providing that all unit cells in the laminates have the b-axis parallel to the macrotwinning plane, i.e. contains only b-variant. If, on the contrary, all a-dimensions are parallel to the macrotwinning plane, i.e. containing only a-variant, the vector is equal

to [0.7050; −0.0779; 0.7050]. For the volume fraction of *a*/*b* variants between 0 and 1 the vector is between these two limits. As far as the dependence of the rotation matrices **R** is concerned, the effect of the *a*/*b* volume fraction is schematically sketched in Fig. 7; the rotation compensates the declinations of the diagonal planes forming the interface, so it is obviously dependent on the *a*/*b* orientations of the unit cells.

For the morphology shown in Fig. 6c, the first condition is satisfied. The planar interfaces of the modulation macrotwins (μ_A:μ_B and μ_C:μ_D) and of the Type I macrotwins (μ_A:μ_C and μ_A:μ_D) is fully compatible as explained above and in Ref. [15]. Thus, the incompatibility or compatibility of the entire crossing morphology depends only on the values of ϕ and ψ. The value of the indicator ϕ can be calculated as follows. The orientation of the Type I macrotwinning is independent of the modulation direction and of the *a*/*b* volume fraction in the neighboring laminates, in definite terms:

$$\mathbf{n}_{\mu_C:\mu_A} = \mathbf{n}_{\mu_B:\mu_D} = \begin{pmatrix} 1 \\ 1 \\ 0 \end{pmatrix}. \tag{8}$$

Similarly, the modulation macrotwinning plane has the same orientation on the both sides of the macrotwin boundary. For the choice (8), the morphology in Fig. 6c is obtained when:

$$\mathbf{n}_{\mu_A:\mu_B} = \mathbf{n}_{\mu_D:\mu_C} = \begin{pmatrix} 0 \\ 0 \\ 1 \end{pmatrix}. \tag{9}$$

For these orientations of the macrotwinning planes the argument in (5) is equal to zero and consequently $\phi = 0$. The same conclusion was reached for all possible choices of the macrotwin orientations using Eq. (8). The value of the second indicator is slightly dependent on the volume fraction of *a*/*b* variants in the laminates $\mu_{A,\ldots,D}$ due to the above-mentioned dependence of the rotation matrices on this parameter. When only the *a*-axis is lying parallel to the μ_A:μ_C interface, the value is $\psi = 1.0134°$; when only the *b*-axis is lying parallel to the interface, the calculation gives $\psi = 1.0108°$; and for any other volume fraction of *a*/*b* variants ψ is somewhere in between.

The experimentally observed, weakly incompatible microstructures reported in Ref. [23–25] have the value of the incompatibility indicator typically $0.1° - 0.4°$; therefore it is plausible that the value $\psi > 1°$ obtained for Fig. 6c is large enough to prevent the formation of such morphology. This conclusion is in good agreement with the fact that crossing between the modulation macrotwins and Type I macrotwins was never observed in our experiments. The meaning of the indicator ϕ in this case can be qualitatively understood from a simple consideration of the surface relief. The twin variants or domains with an in-plane *c*-axis and different modulation directions form roofs and valleys on one side of macrotwin boundary, while on other side the variants with the *c*-axis perpendicular have no relief and their surfaces are flat. Since the macrotwin Type I boundary is straight, this arrangement would form a discontinuity on the macrotwin boundary. However, the segmented Type II macrotwin boundary is compatible on the surface as the relief due to modulation

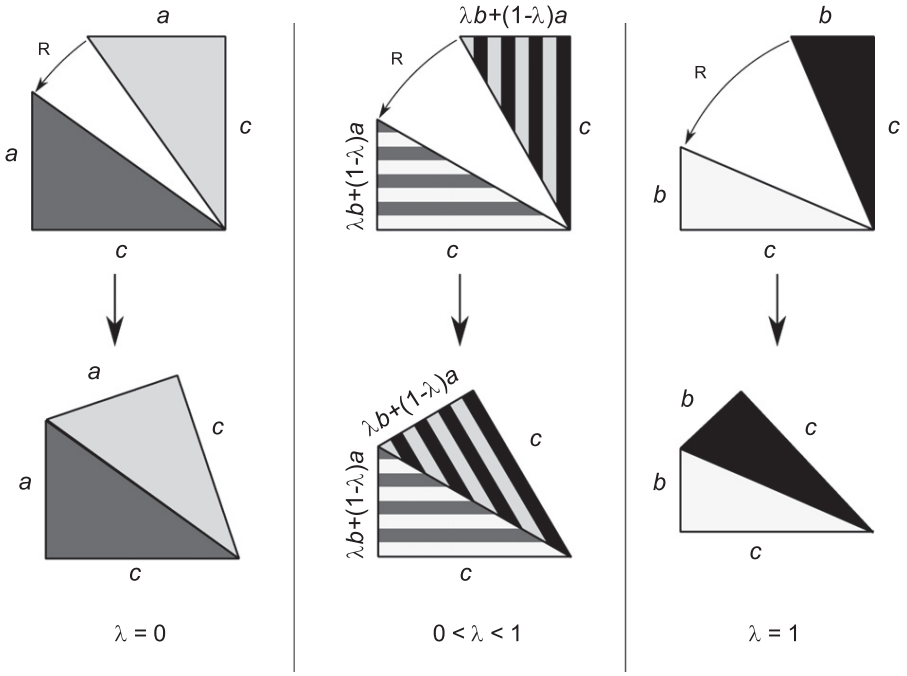

Fig. 7. Two-dimensional illustration of the dependence of the rotation matrix **R** on the *a*/*b* volume fraction.

twinning is compensated by the zigzag pattern and boundary tilt and no discontinuity occurs (Fig. 6a).

Another possible generalization of the macrotwin morphology is outlined in Fig. 6d. In this case, the hypothetical boundary would consist of alternating segments of Type I and Type II macrotwins, with these segments separated from each other by modulation macrotwins. Again the first condition for such morphology is always fulfilled, i.e. the involved laminates can pairwise form fully compatible planar macrotwinning interfaces. Considering all possible combinations of laminates and calculating the Type I and Type II macrotwin orientations for them, we have reached the following conclusion. For any quadruplet of laminates $\mu_{A,\ldots,D}$ such that the μ_A:μ_B and μ_C:μ_D pairs are able to form modulation macrotwins, the Type I macrotwinning plane μ_B:μ_D is always nearly perpendicular to the Type II macrotwinning plane μ_A:μ_C, so this morphology can never be nearly compatible, since the value of the first indicator is typically $\phi \sim 90°$.

The only exception is the degenerate case shown in Fig. 6e, where $\mu_A = \mu_B$. In this special case, all three involved macrotwinning planes intersect again in the $[1\,\bar{1}\,0]$ (or $[\bar{1}\,1\,0]$) direction and consequently $\phi = 0$. For this case, the indicator ψ can be calculated from the relation (7) with $\mathbf{R}_{\mu_A:\mu_B} = \mathbb{I}$. The result is again dependent on the volume fraction of a/b variants, ranging from $\psi = 0.5067°$ for all unit cells having the b-axis oriented along the interface to $\psi = 0.5405°$ for all unit cells having the a-axis oriented along the interface. This means that the incompatibility is about two times lower than for Fig. 6c, and becomes comparable to the incompatibility of the experimentally observed microstructures analyzed in Refs. [23–25]. Unfortunately, the suggested arrangement of segments cannot be resolved in our X-ray diffraction set-up; however, it can be resolved by optical observation and careful measurement of the angles in the zigzag pattern which should differ by about 6°, in contrast with Type II segments where the deviation is about 12°. An example of this assumed morphology is presented in Fig. 5. A slight incompatibility results in the small continuous bending on the edge of the Type I boundary when connected to the Type II boundary. The formation mechanism of such a bent macrotwin interface is similar to that described for curved non-classical interfaces in CuAlNi in Ref. [27]. Since these interfaces are not fully compatible and were observed only rarely, they could be only transitional. During repeated movement of the interface under tensile and compression stress, they might evolve and settle either to Type I or Type II compatible interfaces.

3.3. Mobility of twinned interfaces

We showed that a macrotwin boundary with higher twinning stress has a relatively simple structure. It coincides with the (1 0 1) plane in the tetragonal approximation of the lattice. Compared with the highly mobile interface identified as a Type II macrotwin boundary, it also contains a/b laminate but cannot contain the modulation twinning in the same geometry. Theoretical analysis shows it is a Type I twin boundary. Additionally, we showed experimentally that both interfaces could be created at the same location in the same sample. While the theory shows that Type I and Type II twin boundary (macrointerface) are both compatible, the boundaries differ radically in the magnitude of twinning stress. This suggests that the mobility of the boundary depends mainly on the internal structure of the boundary itself and not on external parameters such as the quality of the crystal or inclusions.

Following the reasoning of Salje [28,29] one can tentatively explain this high mobility or very low twinning stress by considering the potential energy landscape on an atomic scale. Compared with Type I boundary, the Type II boundary is tilted from the (1 0 1) plane having irrational indices but is relatively close to the (10 1 10) plane. Therefore the atoms in this plane are in positions that are not local minima compared with the atoms of the Type I boundary that occupy certain minima of the energy landscape. A very simplified one-dimensional case is sketched in Fig. 8. It suggests how the atoms in the Type II interface are distributed over the energy landscape. If we integrate the energy needed to overcome the barrier (Peierls energy), the total energy to move the whole boundary is about zero. In the first approximation no force is therefore needed for atomic rearrangement, resulting in extremely low twinning stress. As the energy to move the boundary is about zero, this also implies no temperature dependence of twinning stress for the Type II boundary in agreement with experimental findings [7]. Although this picture is grossly simplified it offers an explanation for the different twin boundary mobilities and it might be relevant for ab initio calculations and ultimately for the search of new alloys showing the MSM effect.

One can extend this consideration further. Even for the Type I macrotwin boundary there are not very well defined positions in the modulated lattice compared with a simple tetragonal one. Due to modulation the atoms of the Type I boundary do not sit in relevant minima, which might

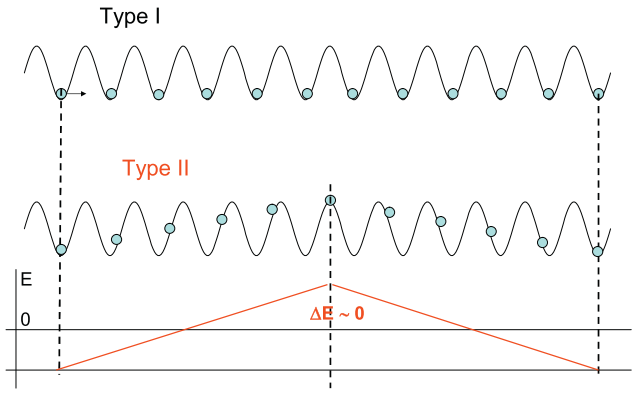

Fig. 8. Simplified energy landscape in one dimension for Type I and Type II boundaries. Integration along the landscape for the Type II boundary gives zero energy.

increase the mobility in a similar manner. In comparison, in non-modulated Ni–Mn–Ga martensite the observed twinning stress is always higher than 10 MPa. Therefore one can speculate that only a modulation structure can create enough mobile boundaries and thus cause a MSM effect.

Another model to explain the high mobility and low twinning stress considers the movable twin boundaries as a broad interface having high energy, which is not pinned on defects [30]. As the Type II is tilted from its precise crystallographic plane position, it can be considered even broader, resulting in even lower twinning stress. However, since this model regards pinning as the cause of the twinning stress, it can be expected that the temperature dependence of the twinning stress should be similar for both types of twin boundaries, in disagreement with experiment.

The different temperature dependence of twinning stress of Type I and II macrotwin boundaries offers a further insight into the mobility. In contrast with the strong increase in twinning stress with decreasing temperature for the Type I boundary [31], the dependence of the Type II boundary is flat and nearly constant [7,32]. This indicates that the mobility of the Type I boundary depends on the evolution of the intrinsic material properties, e.g. lattice parameters and elastic properties, with temperature. Close to the martensitic transformation temperature the twinning stresses of the Type I and Type II boundaries are about the same. This probably originates from the fact that on the atomic scale the distinction between Type I and II twin boundaries gradually disappears as the monoclinic distortion becomes smaller and a and b approach the same value, resulting in an approximately tetragonal lattice [33]. Both twin interfaces become similar to compound twinning. Interestingly, the twinning stress of this compound-like interface is low. This lowering of twinning stress near transformation may originate not only from the changing microstructure of the interface but also from the lattice softening at the transformation [34–36].

Considering the complex microstructure of these interfaces, the questions remain as to whether the modulation twinning has any effect on the mobility and what the role of the a/b-laminate is. A preliminary model based on the theory of elastic continuum suggests that a/b-laminate hinders twin boundary motion in Type I twin boundary but not in Type II. Thus near the transformation the mobility of the Type I boundary can be as high as $a \approx b$ and there is virtually no laminate.

Apart from the elastically compatible pure Type I and Type II boundaries analyzed here and in Ref. [15], theory predicts that a particular mixture of Type I and Type II boundaries with low elastic incompatibility can also constitute a mobile macrotwin interface (Fig. 6e). This interface was observed (Fig. 5). Since such a boundary contains both the highly mobile Type II macrotwins and more rigid Type I macrotwins, it can be expected that the mobility of this microstructure should be somewhere between the mobilities of the of Type II and Type I boundaries. This was confirmed by a preliminary mechanical testing experiment [21]. Similarly, the temperature dependence of twinning stress can be expected to be weaker than for Type I itself. We can conclude that for an optimal performance, the twin microstructure must not contain Type I twins and must be based primarily on Type II twins. Any other combinations will result in higher twinning stress and an unfavorable temperature dependence of the MSM effect.

Acknowledgements

The authors thank J. Drahokoupil for X-ray analysis and acknowledge kind support from AdaptaMat Ltd. and fruitful discussions with A. Sozinov, N. Lanska and A. Soroka. This work was funded by the Academy of Sciences of the Czech Republic by a grant for supporting international cooperation and Czech Scientific Foundation grants No. P107/11/0391 and P107/10/0824, and by the Academy of Finland. H.S. would like to acknowledge K. Koumatos (Oxford) for help with revision of the manuscript.

References

[1] Ullakko K, Huang JK, Kanter C, O'Handley RC, Kokorin VV. Appl Phys Lett 1996;69:1966.
[2] Heczko O, Scheerbaum N, Gutfleisch O. Magnetic shape memory phenomena. In: Nanoscale magnetic materials and applications. Springer Science+Business Media; 2009.
[3] Heczko O, Sozinov A, Ullakko K. IEEE Trans Mag 2000;36:3266.
[4] Likhachev AA, Sozinov A, Ullakko K. Mech Mater 2006;38:551.
[5] Straka L, Heczko O, Haenninen H. Acta Mater 2006;56:5492.
[6] Straka L, Lanska N, Ullakko K, Sozinov A. Appl Phys Lett 2010;96:131903.
[7] Straka L, Hänninen H, Heczko O. Appl Phys Lett 2011;98:141902.
[8] Straka L, Hänninen H, Soroka A, Sozinov A. J Phys: Conf Ser 2011;303:012079.
[9] Ge Y, Söderberg O, Lanska N, Sozinov A, Ullakko K, Lindroos VK. J Phys IV 2003;112:921.
[10] Righi L, Albertini F, Pareti L, Paoluzi A, Calestani G. Acta Mater 2007;55:5237.
[11] Mogylnyy G, Glavatskyy I, Glavatska N, Soderberg O, Ge Y, Lindroos VK. Scripta Mater 2003;48:1427.
[12] Nishida M, Hara T, Matsuda M, Ii S. Mater Sci Eng A 2008;481–482:18.
[13] Li Z, Zhang Y, Esling C, Zhao X, Zuo L. Acta Mater 2011;59:2762.
[14] Sozinov A, Lanska N, Soroka A, Straka L. Appl Phys Lett 2011;99:124103.
[15] Straka L, Heczko O, Seiner H, Lanska N, Drahokoupil J, Soroka A, et al. Acta Mater 2011;59:4750.
[16] Hartman JS, Gordon RL, Lessor DL. Appl Opt 1981;20:2665.
[17] Cullity BD, Stock SR. Elements of X-ray diffraction. 3rd ed. Englewood Cliffs, NJ: Prentice Hall; 2001.
[18] Webster JP. Contemp Phys 1969;10:559.
[19] Ge Y, Heczko O, Hannula S-P, Fähler S. Acta Mater 2010;58:6665.
[20] Ge Y, Jiang H, Sozinov A, Söderberg O, Lanska N, Keränen J, et al. Mater Sci Eng A 2006;438:961.
[21] Soroka A, private communication.
[22] Bhattacharya K. Microstructure of martensite. New York: Oxford University Press; 2003.
[23] Stupkiewicz S, Górzyńska-Lengiewicz A. Continuum Mech Thermodyn 2012;24:149.
[24] Balandraud X, Zanzotto G. J Mech Phys Solids 2007;55:194.

[25] Balandraud X, Delpueyo D, Grediac M, Zanzotto G. Acta Mater 2010;58:455.
[26] Koumatos K. The formation of microstructure in shape memory alloys. Ph.D. thesis, University of Oxford; 2012.
[27] Seiner H, Landa M. Phase Transitions 2009;82:793.
[28] Salje EKH. Phase Transitions 2010;83:657.
[29] Lee WT, Salje EKH, et al. Phys Rev B 2006;73:214110.
[30] Kaufmann S, Niemann R, Thersleff T, Rossler UK, Heczko O, Buschbeck J, et al. New J Phys 2011;13:053029.
[31] Heczko O, Straka L. J Appl Phys 2003;94:7139.
[32] Straka L, Soroka A, Seiner H, Hänninen H, Sozinov A. Scripta Mater 2012;67:25.
[33] Lanska N, Söderberg O, Sozinov A, Ge Y, Ullakko K, Lindroos VK. J Appl Phys 2004;95:8074.
[34] Aaltio I, Lahelin M, Soderberg O, Heczko O, Lofgren B, Ge Y, et al. Mater Sci Eng A 2008;481:314.
[35] Pérez-Landazábal JI, Sanchéz-Alarcos V, Góméz-Polo C, Recarte V, Chernenko VA. Phys Rev B 2007;76:092101.
[36] Segui C, Chernenko VA, Pons J, Cesari E, Khovailo V, Takagi T. Acta Mater 2005;53:111.

3.3 Publikace *Mikrostrukturní model pohybu makrodvojčatových rozhraní v 10 M martenzitu slitiny Ni-Mn-Ga.*

Bibliografická citace: Seiner, H., Straka, L., Heczko, O. A microstructural model of motion of macro-twin interfaces in Ni-Mn-Ga 10 M martensite (2014) Journal of the Mechanics and Physics of Solids, 64 (1), pp. 198-211.

Stručná anotace: V této publikaci je prezentován obecný model pohybu makro-dvojčatových rozhraní v termoelastických martenzitech, motivovaný rozdílnou pohyblivostí rozhraní Typu 1 a 2 v 10 M modulovaném Ni-Mn-Ga. Model plně vysvětluje sníženou pohyblivost Typu 1 (vůči Typu 2) mechanismem pinování pohybujícího se rozhraní na lokálních energeticky výhodných stavech. Model je aplikován postupně na třech prostorových měřítkách: meso-škále (modulační dvojčata), mikro-škále (dvojčata typu Compound) a nano-škále (modulace martenzitu).

Příspěvek habilitanta: Celá koncepce modelu, jeho konstrukce a numerická implementace jsou prací habilitanta, diskuze výsledků ve srovnání s experimenty (sekce 5) proběhla ve spolupráci s oběma spoluautory.

Journal of the Mechanics and Physics of Solids 64 (2014) 198–211

Contents lists available at ScienceDirect

Journal of the Mechanics and Physics of Solids

journal homepage: www.elsevier.com/locate/jmps

A microstructural model of motion of macro-twin interfaces in Ni–Mn–Ga 10 M martensite

Hanuš Seiner [a,*], Ladislav Straka [b], Oleg Heczko [c]

[a] Institute of Thermomechanics, Academy of Sciences of Czech Republic, Dolejškova 5, 18200 Prague, Czech Republic
[b] Aalto University School of Engineering, Laboratory of Engineering Materials, PL 14200, FIN-00076 Aalto, Finland
[c] Institute of Physics, Academy of Sciences of the Czech Republic, Na Slovance 2, 182 21 Prague 8, Czech Republic

ARTICLE INFO

Article history:
Received 24 February 2013
Received in revised form
1 October 2013
Accepted 6 November 2013
Available online 18 November 2013

Keywords:
Twinning
Strain compatibility
Layered material
Numerical algorithms
Shape memory alloys

ABSTRACT

We present a continuum-based model of microstructures forming at the macro-twin interfaces in thermoelastic martensites and apply this model to highly mobile interfaces in 10 M modulated Ni–Mn–Ga martensite. The model is applied at three distinct spatial scales observed in the experiment: meso-scale (modulation twinning), micro-scale (compound *a*–*b* lamination), and nano-scale (nanotwining in the concept of adaptive martensite). We show that two mobile interfaces (Type I and Type II macro-twins) have different micromorphologies at all considered spatial scales, which can directly explain their different twinning stress observed in experiments. The results of the model are discussed with respect to various experimental observations at all three considered spatial scales.

1. Introduction

Ferromagnetic shape memory alloys (FSMAs) of the Ni–Mn–Ga system (Chernenko et al., 1995; O'Handley et al., 2000; Heczko et al., 2000) are smart materials with potential for applications in actuation and micromanipulation. The decisive factor for magnetic shape memory effect is the high mobility of the twin boundaries, which enables fast actuation with large strain amplitudes. This high mobility was observed mainly in the five-layered (10 M) modulated martensite phase of Ni–Mn–Ga alloy. In particular, as recently shown by Sozinov et al. (2011) and Straka et al. (2011), two different types of mobile twin interfaces relevant for actuation can arise in the 10 M phase: Type I (twinning stress ≈ 1 MPa at room temperature and strongly temperature-dependent) and Type II (twinning stress less than 0.2 MPa and nearly temperature-independent). The respective temperature dependences were analyzed by Straka et al. (2012) and measured by Straka et al. (2013) and Heczko et al. (2013a). Understanding the difference between these two types requires a crystallographic analysis beyond the tetragonal approximation of the 10 M unit cell, taking into account the weak monoclinicity of the modulated phase (Lanska et al., 2004; Righi et al., 2007). In addition, as proved by X-ray microdiffraction in Straka et al. (2011) and Heczko et al. (2013b), and discussed *ibid* theoretically, these mobile interfaces are not simple twinning planes, but they are macro-twinning planes between fine 1st or 2nd order laminates. Furthermore, according to the so-called *adaptive concept of martensite* (Kaufmann et al., 2010, 2011; Niemann et al., 2012), the 10 M modulated phase itself is built up from a stacking sequence of tetragonal unit cells of the non-modulated (NM) martensite, which adds even one more level of lamination. Thus, the observed mobile interfaces are in fact macro-twin boundaries between relatively complex twinned structures.

* Corresponding author. Tel.: +420 266 053712.
E-mail address: hseiner@it.cas.cz (H. Seiner).

0022-5096/$ - see front matter © 2013 Elsevier Ltd. All rights reserved.
http://dx.doi.org/10.1016/j.jmps.2013.11.004

This opens the questions how such microstructures can be connected compatibly over a single interface, and how the micromorphologies forming at these interfaces can affect their motion. Such analysis is the subject of this paper.

Recently, Faran and Shilo (2011, 2013) analyzed the kinetics of Type I and Type II interfaces under pulse-like magnetic loadings and obtained extensive data on mobility of both the types for a wide range of amplitudes of the driving force. They concluded that for small amplitudes of the applied magnetic pulses (small driving force, slow propagation), the kinetics of both the Type I and Type II interfaces is driven mainly by nucleation and growth of steps along the interfaces. This macroscopically appears as a smooth, continuous sideways motion of the mobile boundary. Under such condition, Faran and Shilo (2011, 2013) showed that the energy of such steps is smaller for the Type II twins, for which also the Peierls barrier seems to be smaller, and, consequently, the mobility to be higher. On the other hand, they did not take into account the complex microstructure of the analyzed macro-twins known from the experiments. The presence of fine lamination (possibly of higher orders) close to the interface does not contradict the concept of nucleation and growth of the steps. It is plausible that, in addition to the Peierls landscape, the microstructure can create energetic barriers against the nucleation and motion of such steps. Such conjecture is supported by the fact that Faran and Shilo (2013) have observed some variation of the mobility with periodicity of about 10–50 μm, which could be a characteristic length-scale of some particular microstructure. Similar periodicity was also detected on quasi-static curves for the Type I interface measured by Faran and Shilo (2012).

In this paper, we examine the influence of the complex microstructures on the quasi-static motion of the Type I and Type II boundaries. Within the frame of continuum mechanics, we present a theoretical model of such interfaces, employing the description of thermoelastic martensites. We solve the compatibility problems in the interfacial region where the two laminates meet, and discuss what effect the resulting microstructure can have on the motion of the macro-twin. Our discussion is restricted to the 1st order of lamination only; which is, however, sufficient for application of the model for the case of 10 M martensite of Ni–Mn–Ga. The reason is that the individual laminations in 10 M martensite appear at completely different spatial scales, and their interactions in the interfacial region can be, thus, discussed separately. By using this model, we obtain a multi-scale picture of the micromorphology at the studied macro-twin boundaries, and we are able to explain the possible origins of the different twinning stress.

2. Martensitic microstructures in 10 M martensite of Ni–Mn–Ga

In this section we summarize the main properties of the martenstic transition in Ni–Mn–Ga alloys and resulting 10 M microstructures known from previously published experimental observations or calculations. The austenite-to-10 M transition in Ni–Mn–Ga belongs to the cubic-to-monoclinic class. The geometric parameters of this transition, including the complete classification of twinning system and the construction of macro-twins, were in detail described in Straka et al. (2011). Here only a brief summary is given.

2.1. Lattice parameters and twinning systems

We use a reference coordinate system x_i taken identically with the principal directions of a cubic unit cell of the austenite phase. In this reference coordinate system we express all the geometric parameters describing the discussed microstructures: the Bain matrices, the directions of the twinning and macro-twinning planes, the rotations, etc. For clarity, we denote all quantities expressed in this coordinate system by the subscript P, meaning the *parent phase*.

As the lattice parameters are significantly dependent on composition (Lanska et al., 2004), for matter of uniqueness we select the lattice constant for one particular alloy. We choose the same alloy as used in the previous works (Straka et al., 2011; Heczko et al., 2013b). The unit cell of austenite has one lattice constant $a_P = 0.5832$ nm. In the transformed state, i.e. in 10 M martensite, the equivalent (effective) unit cell has three different lattice constants, $a = 0.5972$ nm, $b = 0.5944$ nm and $c = 0.5584$ nm, and the angle contained between the edges of dimensions a and b is $\gamma = 90.37^\circ$. Twelve different variants can be formed (Pitteri and Zanzotto, 1998; Bhattacharya, 2003). In the reference configuration, the Bain matrices representing these twelve variants are

$$\mathbf{U}_1 = \begin{pmatrix} e_a & e_{ab} & 0 \\ e_{ab} & e_b & 0 \\ 0 & 0 & e_c \end{pmatrix}_P, \quad \mathbf{U}_2 = \begin{pmatrix} e_a & -e_{ab} & 0 \\ -e_{ab} & e_b & 0 \\ 0 & 0 & e_c \end{pmatrix}_P,$$

$$\mathbf{U}_3 = \begin{pmatrix} e_b & e_{ab} & 0 \\ e_{ab} & e_a & 0 \\ 0 & 0 & e_c \end{pmatrix}_P, \quad \mathbf{U}_4 = \begin{pmatrix} e_b & -e_{ab} & 0 \\ -e_{ab} & e_a & 0 \\ 0 & 0 & e_c \end{pmatrix}_P,$$

$$\mathbf{U}_5 = \begin{pmatrix} e_a & 0 & e_{ab} \\ 0 & e_c & 0 \\ e_{ab} & 0 & e_b \end{pmatrix}_P, \quad \mathbf{U}_6 = \begin{pmatrix} e_a & 0 & -e_{ab} \\ 0 & e_c & 0 \\ -e_{ab} & 0 & e_b \end{pmatrix}_P,$$

$$\mathbf{U}_7=\begin{pmatrix} e_b & 0 & e_{ab} \\ 0 & e_c & 0 \\ e_{ab} & 0 & e_a \end{pmatrix}_P, \quad \mathbf{U}_8=\begin{pmatrix} e_b & 0 & -e_{ab} \\ 0 & e_c & 0 \\ -e_{ab} & 0 & e_a \end{pmatrix}_P,$$

$$\mathbf{U}_9=\begin{pmatrix} e_c & 0 & 0 \\ 0 & e_a & e_{ab} \\ 0 & e_{ab} & e_b \end{pmatrix}_P, \quad \mathbf{U}_{10}=\begin{pmatrix} e_c & 0 & 0 \\ 0 & e_a & -e_{ab} \\ 0 & -e_{ab} & e_b \end{pmatrix}_P,$$

$$\mathbf{U}_{11}=\begin{pmatrix} e_c & 0 & 0 \\ 0 & e_b & e_{ab} \\ 0 & e_{ab} & e_a \end{pmatrix}_P, \quad \text{and} \quad \mathbf{U}_{12}=\begin{pmatrix} e_c & 0 & 0 \\ 0 & e_b & -e_{ab} \\ 0 & -e_{ab} & e_a \end{pmatrix}_P, \tag{1}$$

where $e_a=1.0240$, $e_b=1.0192$, $e_c=0.9575$ and $e_{ab}=0.0033$. For each variant, the so-called *modulation direction* is the direction perpendicular to the *c*-axis (magnetization easy axis) and pointing along the shorter diagonal of the *a*–*b* parallelogram.

There are up to five twinning systems that can appear between particular pairs of 10 M martensitic variants, and, with one exception, all of them were observed in the experiments:

1. The twins between variants differing only in the direction of modulation (for example Nos. 1 and 2); according to the classification by Bhattacharya (2003), these twins are of a compound type. For clarity, however, we will call them *modulation twins*.
2. The twins between variants differing only in the orientation of the *a*- and *b*-dimensions of the unit cell (for example Nos. 1 and 3), which are also of the compound type; we will call them *a*–*b twins*.
3. The *non-conventional twins* between variants differing in both the *a*–*b* orientations and modulation direction (but with the same orientation of the *c*-axis, for example Nos. 1 and 4). This type of twinning has not been observed yet.
4. Type I twins between variants with different orientations of the *c*-axis (for example Nos. 1 and 5); the twinning plane in this case is the lattice plane of the 10 M lattice.
5. Type II twins between variants with different orientations of the *c*-axis (again, for example Nos. 1 and 5); the twinning plane in this case is irrational in the 10 M lattice.

We will use this terminology throughout the whole paper and adopt it also for the macro-twins, i.e. for the compatible interfaces between homogeneous twinned structures. In this sense, we will use the term *modulation macro-twin* for a macro-twin between two laminates differing mainly in the modulation direction; in a similar sense we will use the terms *Type I* and *Type II macro-twins* for macro-twins between laminates with different orientations of the *c*-axis. In this case the distinguishing between Types I and II will be based on whether the macro-twinning plane is a lattice plane, or not.

Over all spatial scales we will also use the term *mobile interface* for the Type I and Type II twins or macro-twins, i.e. for those interfaces at which the orientation of the *c*-axis of the 10 M unit cell changes. Such interfaces are the only ones that can be set into motion by the magnetic field; we will call them *mobile* to distinguish them from all other interfaces, in particular from the interfaces forming the individual laminates, which are considered as fully static in our model.

2.2. The length-scales observed in experiments

As mentioned in the Introduction, it is known from the experiments that the lamination (and, thus, macro-twinning) in 10 M martensite can appear at three different length-scales. The observed spatial hierarchy of the laminates at the mobile interface is schematically outlined in Fig. 1 and summarized here:

- At the *macro-scale*, there is a single flat interface between two regions with different orientation of the *c*-axis. This interface is the mobile interface with effective macroscopic twinning stress of $\lesssim$0.2 MPa (for the Type II case) or 1 MPa (for the Type I case).
- At the *meso-scale*,[1] a closer look reveals that these two regions in the vicinity of the single flat interface are often not homogeneous. They can be composed of segments with altering orientation of the modulation direction. At this scale we can treat each such segment as homogeneous and, thus, the mobile interface can be at this length-scale understood as a macro-twin between two 1st order laminates of modulation twins. The presence of lamination at the meso-scale was observed by optical microscopy and X-ray microdiffraction (Straka et al., 2011; Heczko et al., 2013b) and by electron backscattered diffraction (EBSD) (Chulist et al., 2013; Heczko et al., 2013c).

[1] In this paper, we use the prefix meso– to describe a spatial scale between the macro-scale (characteristic lengthscales in the order of millimeters) and the micro-scale (characteristic lengthscales in the order of micrometers). Such use of the term meso-scale is common in some literature concerned with multi-scale mathematical modelling of shape memory alloys (Turteltaub and Suiker, 2006; Kouznetsova and Geers, 2008), but slightly different from the meaning used in solid state physics or materials science, for example in the works dealing with the adaptive concept of Ni–Mn–Ga martensites (Kaufmann et al., 2011; Niemann et al., 2012), where this intermediate scale appears between the atomistic scale and the micro-scale.

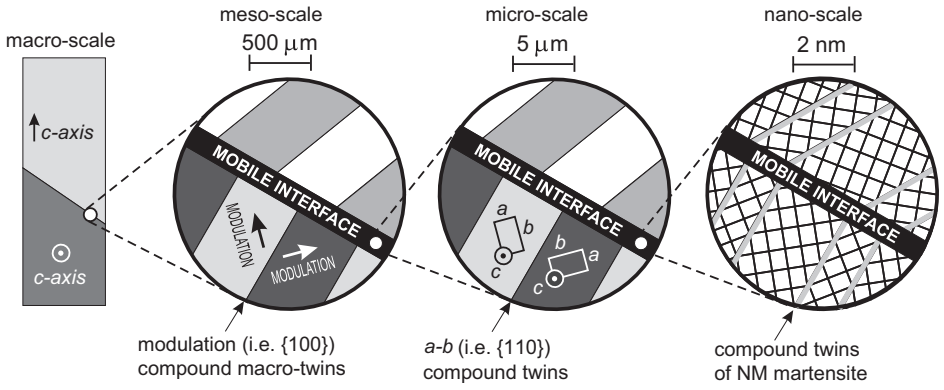

Fig. 1. Possible hierarchy of laminations in the vicinity of the mobile interface. Note: the geometry of the sketch is quite general and illustrative, and its relation to possible real morphologies is only very approximate.

- At the *micro-scale,* further lamination can appear. If the mobile macro-twin interface is planar at the meso-scale, or if the alterations of the modulation directions are absent (i.e. no modulation twinning at the meso-scale appears), two regions, each with homogeneous modulation direction, necessarily meet at the mobile interface. These two regions are thus homogeneous at the meso-scale, but at the *micro-scale* they are 1st order laminates of *a*–*b* compound twins. The presence of this *a*–*b* lamination in the vicinity of the mobile interfaces of both types was proved indirectly by X-ray microdiffraction in Straka et al. (2011), Heczko et al. (2013b), and Sozinov et al. (2011) and directly by EBSD in Chulist et al. (2013).
- At the *nano-scale,* considering the concept of adaptive martensite (Khachaturyan et al., 1991a,b; Kaufmann et al., 2010, 2011; Niemann et al., 2012), there can be another level of lamination. If the mobile interface is flat at the micro-scale, or if the *a*–*b* twinning does not appear at the micro-scale, two regions with homogeneous orientation of *a* and *b* dimensions and with homogeneous direction of the modulation meet at the mobile interface. In fact, these two regions are only two single variants of the 10 M martensite. However, within the concept of the adaptive martensite, the mobile interface is again a macro-twin at the laminates of tetragonal NM martensite at the atomistic scale, i.e. at the nano-scale.

It is apparent that this construction of the multi-scale hierarchy of the twinning systems shown in Fig. 1 is inductive: the micro-scale can be discussed if and only if the interface appears flat at the meso-scale, the same is valid for the nano- and micro-scales.

Hence, we can also follow the same approach when discussing the effect of the martensitic microstructure on the twinning stress; we start the analysis at the macro-scale and follow the possible special morphologies down to the nano-scale. At all these spatial scales we apply a simple model formulated in the next section.

3. Model formulation

In this section we construct a model of morphology and motion of macro-twins. For this purpose, we use (without giving any detailed explanations) some common terms and approaches of the continuum mechanics of martensitic microstructures, which treat the individual variants of martensite as deformed states of the reference configuration (i.e. of the parent phase). The fundamentals of this theory are sufficiently described in Bhattacharya (2003) and Ball and James (1987, 1992), some brief summary with particular focus on the Ni–Mn–Ga alloy is also given in Straka et al. (2011, Appendix A).

3.1. Micromorphology at the macro-twin interface

Let us consider two homogeneous laminates of the first order, i.e. two martensitic microstructures each consisting of parallel lamina of two altering variants of martensite (Bhattacharya et al., 1999). Let one of these laminates consists of variants denoted as *A* and *B* (this laminate will be further referred to as the *A*:*B-laminate*), which are able to form a twin. The twinning plane of this twin is characterized by the vector $\mathbf{n}_{A:B}$, which is a unit vector perpendicular to this plane in the reference configuration. The second laminate consist of variants *C* and *D* (i.e. it is a *C*:*D-laminate*) with the twinning plane $\mathbf{n}_{C:D}$. The existence of these two laminates is conditioned by the existence of rotations $\mathbf{R}_{I:J} \in SO(3)$ and shearing vectors $\mathbf{a}_{I:J} \in \mathbb{R}^3$ such that

$$\mathbf{U}_A - \mathbf{R}_{A:B}\mathbf{U}_B = \mathbf{a}_{A:B} \otimes \mathbf{n}_{A:B}, \tag{2}$$

$$\mathbf{U}_C - \mathbf{R}_{C:D}\mathbf{U}_D = \mathbf{a}_{C:D} \otimes \mathbf{n}_{C:D}, \tag{3}$$

where U_I are the Bain tensors of the individual variants and $\mathbf{x} \otimes \mathbf{y}$ denotes the dyadic product of vectors $\mathbf{x}$ and $\mathbf{y}$.

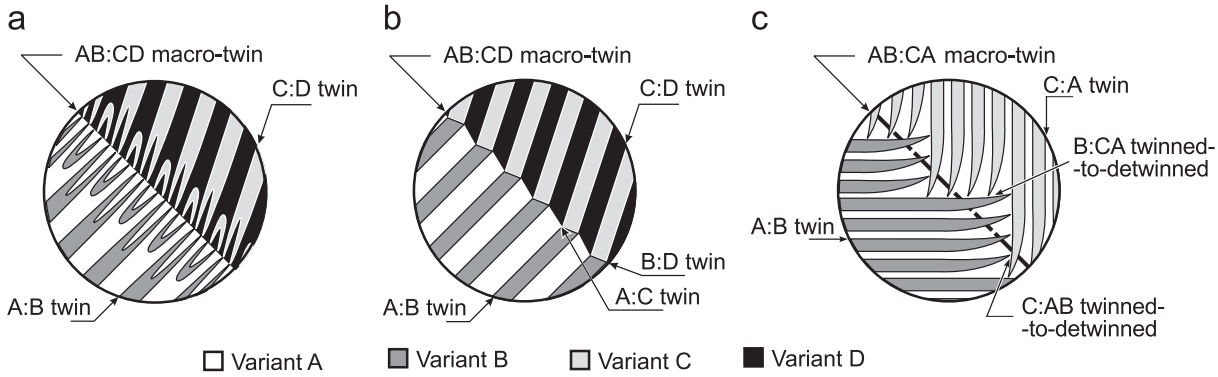

Fig. 2. Possible morphologies of the macro-twin boundary: (a) the general morphology; (b) the crossing-twins morphology; (c) the zig-zag morphology.

To allow the existence of a macroscopically compatible interface (i.e. the macro-twin) between these two laminates, a similar condition must be satisfied. In particular, there must exist a rotation $\mathbf{R}_{AB:CD} \in SO(3)$ and a shearing vector $\mathbf{a}_{AB:CD} \in \mathbb{R}^3$ such that

$$\mathbf{M}_{AB} - \mathbf{R}_{AB:CD}\mathbf{M}_{CD} = \mathbf{a}_{AB:CD} \otimes \mathbf{n}_{AB:CD}, \tag{4}$$

where

$$\begin{aligned} \mathbf{M}_{AB} &= \lambda_{A:B}\mathbf{U}_A + (1-\lambda_{A:B})\mathbf{R}_{A:B}\mathbf{U}_B, \\ \mathbf{M}_{CD} &= \lambda_{C:D}\mathbf{U}_C + (1-\lambda_{C:D})\mathbf{R}_{C:D}\mathbf{U}_D. \end{aligned} \tag{5}$$

$\mathbf{M}_{AB}$ and $\mathbf{M}_{CD}$ are, up to some rotation, the mesoscopic deformation gradients of the laminates, the vector $\mathbf{n}_{AB:CD}$ is a unit vector perpendicular to the macro-twin boundary in the reference configuration, and $\lambda_{A:B}$ and $\lambda_{C:D}$ are the volume fractions of variant A in the A:B-laminate and of variant C in the C:D-laminate, respectively.

The condition (4) treats the A:B- and C:D-laminates as infinitely fine. However, in real laminates the surface energy of the twinning planes induces some final width of the individual lamina. For this reason, the macro-twin boundary between two such laminates should have the morphology sketched in Fig. 2a, where both the laminates are getting finer *via* branching in the vicinity of the macro-twin boundary, and the minor variant in each laminate forms thin, tapering needles ending at the interface (see e.g Bhattacharya, 2003 for an optical micrograph or Chulist et al., 2010 for an EBSD micrograph of such interface). A macro-twin interface with such morphology can exist between any two laminates fulfilling the condition (4); for this reason we will call this morphology *a general morphology*.

Under some additional conditions, two laminates of finite widths of the lamina can form a compatible macro-twin boundary without branching and without the formation of the needles. The morphology of such interface is sketched in Fig. 2b, and will be called from hereafter *the crossing-twins morphology*, since it consists of two mutually crossing twinning systems. The conditions under which the crossing-twins morphology can exist are the following:

1. The variants A and C can form an A:C twin (over a twinning plane with normal $\mathbf{n}_{A:C}$); similarly, the variants B and D can form a B:D twin (over a twinning plane with normal $\mathbf{n}_{B:D}$). This means that there exist the shearing vectors $\mathbf{a}_{A:C}$ and $\mathbf{a}_{B:D}$ and the rotations $\mathbf{R}_{A:C}$ and $\mathbf{R}_{B:D}$ such that the conditions analogous to (2) and (3) are fulfilled between the Bain tensors U_A and U_C, and between U_B and U_D, respectively. (It is also necessary that these two twinning planes can compose into the macroscopic macro-twinning plane, i.e. the vector $\mathbf{n}_{AB:CD}$ can be expressed as a linear combination of vectors $\mathbf{n}_{A:C}$ and $\mathbf{n}_{B:D}$. This condition is, however, usually automatically fulfilled, since it is a direct consequence of the conditions (Nos. 2. and 3) given below.)
2. The A:B, A:C, C:D and B:D twinning planes intersect in one line, i.e.

$$\phi = \arcsin\left|\frac{\mathbf{n}_{A:B}\times\mathbf{n}_{A:C}}{|\mathbf{n}_{A:B}\times\mathbf{n}_{A:C}|}\times\frac{\mathbf{n}_{B:C}\times\mathbf{n}_{C:D}}{|\mathbf{n}_{B:C}\times\mathbf{n}_{C:D}|}\right| = 0. \tag{6}$$

   If this condition is satisfied, then it is also true that the twinning planes A:B, and C:D intersect at the macro-twinning plane AB:CD , i.e.

$$\tilde{\phi} = \arcsin\left|\frac{\mathbf{n}_{A:B}\times\mathbf{n}_{AB:CD}}{|\mathbf{n}_{A:B}\times\mathbf{n}_{AB:CD}|}\times\frac{\mathbf{n}_{C:D}\times\mathbf{n}_{AB:CD}}{|\mathbf{n}_{C:D}\times\mathbf{n}_{AB:CD}|}\right| = 0, \tag{7}$$

   (but the inverse implication does not hold).
3. The mutual rotations between the individual variants fully compensate each other (Bhattacharya, 2003). Explicitly written, this condition reads

$$\psi = \arccos\left(\frac{\mathrm{tr}(\mathbf{R}_{A:B}\mathbf{R}_{B:D}\mathbf{R}^{\mathrm{T}}_{C:D}\mathbf{R}^{\mathrm{T}}_{A:C})-1}{2}\right) = 0. \tag{8}$$

4. The volume fractions $\lambda_{A:B}$ and $\lambda_{C:D}$ and the thicknesses of the lamina in the both laminates are tuned such that the all A:B and C:D twinning planes can exactly meet at the macro-twin boundary.

The scalar parameters ϕ and ψ are the so-called *incompatibility indicators*, firstly introduced by Stupkiewicz and Górzyńska-Lengiewicz (2012); these parameters quantify the compatibility of the crossing of the two involved twinning systems.

The four conditions given above are quite restrictive; only very specific pairs of laminates can form the crossing-twins morphology. Experimentally observed examples of compatible crossings of two twinning systems are the nanotwins in B19' martensite of Ni–Ti (Waitz, 2005) or the intersection of the Compound and Type II twins 2H martensite of Cu–Al–Ni (Ball et al., 2009; Seiner and Landa, 2009).

It is obvious that the energy of the general morphology is much higher than that of the crossing-twins morphology: the latter consists of the surface energies of the two involved twinning systems only, whereas the energy of the general morphology contains also the additional surface energy resulting from branching and the energy of the elastic strains accompanying both the branching and the formation of the needles of the minor variant. Thus, according to the assumption that the material near the macro-twin boundary tends to minimize its energy, the crossing-twins morphology should form as soon as the above listed conditions are satisfied.

The question is which morphology is preferred when these four conditions are satisfied only approximately, i.e. if, for example, the vectors $\mathbf{n}_{A:B} \times \mathbf{n}_{A:C}$ and $\mathbf{n}_{A:B} \times \mathbf{n}_{B:D}$ differ by less than 1°, or if all the A:B and C:D twinning planes do not exactly meet at the interface. In such case, the exact crossing-twins morphology can form only if these small differences from the compatibility are compensated by elastic strains. Such compensation is indeed possible, as it follows from the analyses of some experimentally observed microstructures in In–Tl (Ruddock, 1994), in Cu–Zn–Al (Balandraud and Zanzotto, 2007) and in Cu–Al–Ni (Seiner et al., 2009; Stupkiewicz and Górzyńska-Lengiewicz, 2012). Alternatively, these small differences can also be compensated by branching and by the formation of a fine microstructure close to the macro-twin boundary, and thus the resulting morphology may have some similar features as the general morphology shown in Fig. 2a. However, since the geometric misfit between two laminates satisfying approximately the four conditions for the crossing-twins morphology is much smaller than in the fully general case, it is reasonable to assume that the energy of branching and additional twinning in such case can be much lower. Thus, it is plausible that such two laminates always form either the elastically strained crossing-twins morphology, or a general morphology with significantly lower energy than in a fully general case.

For real laminates, in which the volume fraction is never exactly constant and the spacing between the lamina is never exactly periodic, the fourth condition cannot be fully satisfied. On the other hand, wherever two A:B and C:D twinning planes meet at the macro-twin boundary, and providing that the first three conditions are fulfilled, the energy of the macro-twin is locally lowered by compatible crossing of the twins, i.e by local formation of the crossing-twins morphology.

A special case of the 'approximate' fulfillment of these four conditions occurs when the A:C and B:D twinning planes do not exist. This happens for example for the cubic-to-tetragonal transition, where there are only three variants of martensite and six possible orientations of the twinning planes, which is insufficient for the crossing-twins morphology. In other words, the crossing-twins morphology can never form if two laminates meeting at the macro-twin interface contain both the same variant, for example $A=D$. In such case, another special morphology can form providing that the intersection of the A:B and A:C twinning planes is parallel with the macro-twinning plane. This can be quantified by the indicator $\tilde{\phi}$ defined by (7), but with $A=D$:

$$\tilde{\phi} = \arcsin\left| \frac{\mathbf{n}_{A:B} \times \mathbf{n}_{AB:CA}}{|\mathbf{n}_{A:B} \times \mathbf{n}_{AB:CA}|} \times \frac{\mathbf{n}_{C:A} \times \mathbf{n}_{AB:CA}}{|\mathbf{n}_{C:A} \times \mathbf{n}_{AB:CA}|} \right| = 0. \tag{9}$$

If this condition is satisfied, the laminates of the variants B can form tapering needles ending at the A:C twinning planes (with possible branchings close to these twinning planes), and the tips of these needles are then parallel to the macro-twinning interface. This leads to the morphology sketched in Fig. 2c, which we will call the *zig-zag morphology*. The length of the individual 'steps' at the zig-zag interface depends on other conditions: if there can exist compatible interfaces between the A:B laminate and the single variant C, and similarly between the A:C laminate and pure variant B (so called twinned-to-detwinned interfaces), the segments can be long, since the compatibility conditions along them are satisfied. If this is not the case, the steps must be fine, since the compatibility is achieved only in the macroscopic sense, i.e. between the homogeneous laminates A:B and A:C. Let us point out that the condition (9) is indeed essential for the zig-zag morphology; if this equality does not hold (at least approximately), the continuity of the variant A over the interfacial region is broken and the tips of the B and C needles cannot run undisturbed along the twinning planes of the opposing laminates. In such case, the general morphology probably forms.

The zig-zag morphology seems to be energetically preferred compared with the general one, since the necessary tapering and branching of the needles appears on one side of the interface only. On the other hand, the interface is, due to the steps, up to $\sqrt{2}$ times longer. Experimentally, the zig-zag morphology was observed for example in Ni–Al (Schryvers et al., 2002; Boullay et al., 2001) or at the *modulation macro-twins* of 10 M Ni–Mn–Ga (Ge et al., 2006). The so-called *L-interface*, observed in Cu–Al–Ni by Chu (1993), can be also understood as some degenerate form of the zig-zag morphology. Let us mention that some of these observations of the zig-zag morphology show that the thin needles of the variants B and C can partially intersect and form more complex patterns close to the macro twin. We will not discuss this special case in details; since the condition (9) is satisfied in this case, such morphologies will be classified as zig-zag morphology as well.

In summary, both the discussed special morphologies (crossing-twins and zig-zag) can appear only if the two laminates coming into play have suitable volume fractions and suitable characteristic length-scales, and if $\tilde{\phi}=0$. Then, the microstructure at the interface can be considered as two-dimensional, since all planes perpendicular to $\mathbf{n}_{A:B} \times \mathbf{n}_{C:D}$ are

fully equivalent. Furthermore, under these two conditions the lamina of the variants A and C (and, analogously, of the variants B and D) can either meet 'head-to-head' at the interface and form the A:C and B:D twinning planes of the crossing-twins morphology, or accommodate into the steps of the zig-zag morphology. However, even if the exact micromorphology at the interface is not known and cannot be fully predicted by a calculation, the interfaces fulfilling the condition (7) differ in their twinning stress from the fully general ones. This is shown in the following part of the paper.

3.2. Motion of the macro-twins

Let us consider that the macro-twin boundary moves from its original position x to some new position $x+\Delta x$ along the direction given by the normal $\mathbf{n}_{AB:CD}$, such that the A:B- and C:D-laminates far from the interface remain unchanged. For the general morphology, the fine microstructure at the macro-twin boundary can remain the same for any Δx (Fig. 3(a)), as the branching points and the tips of the needles of the minor variant move together with the interface. This means that the energy of the macro-twin boundary is constant during the propagation (as sketched by the solid line in Fig. 4(a)).

For the crossing-twins morphology, the situation is completely different. For some increments Δx, the compatible connection between the A:B and C:D twinning planes is fully broken and the fourth condition for the existence of this morphology is not satisfied, not even in any approximate sense (Fig. 3(b)). Consequently, the general morphology must form and the energy of the interface significantly increases. By further propagation, the macro-twin boundary may again reach some position in which the A:B and C:D twinning planes meet exactly each other and the low-energy crossing-twins morphology forms again. Therefore the energy of the interface is strongly dependent on its position, passing though periodically repeating deep minima corresponding to the crossing-twins morphologies (see the solid line in Fig. 4(b)). The boundary is then pinned in these energetically preferred positions and its twinning stress increases. From other point of view, the motion of the interface is always accompanied by dissipation. If the above described pinning mechanism is present, the dissipated energy includes the energy of the barriers that the boundary must overcome; hence, the energy dissipated by motion of the boundary jumping between the crossing-twins morphologies is higher than for the continuously moving general one.

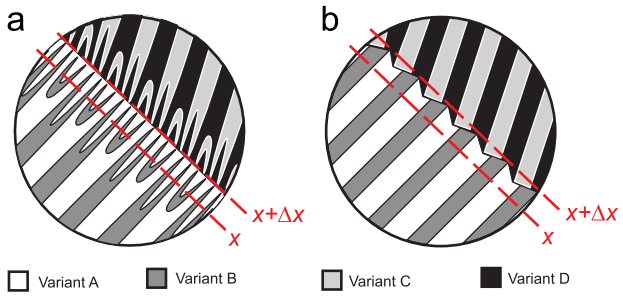

Fig. 3. Macro-twin boundary motion mechanism for the general (a) and the crossing-twins (b) morphologies.

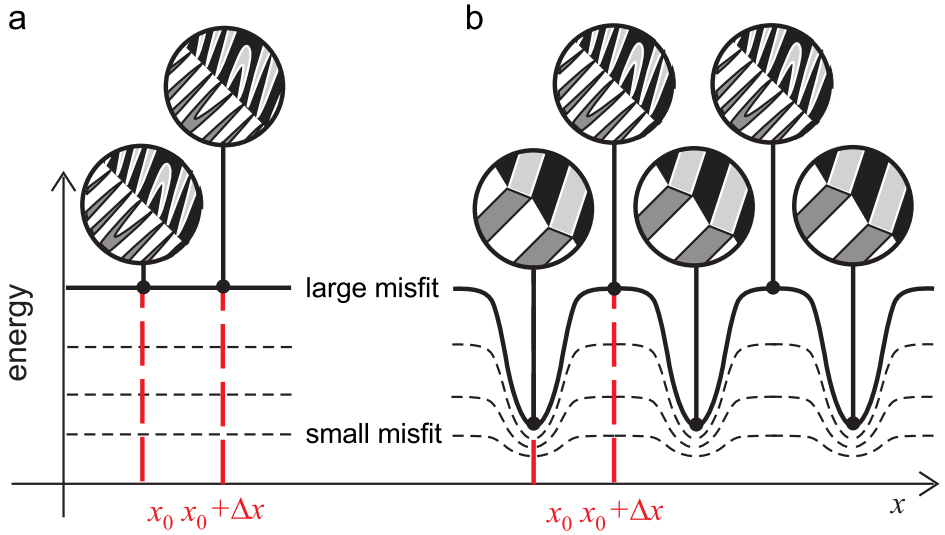

Fig. 4. The changes of energy of a macro-twin during the motion: (a) the general morphology; (b) the crossing-twins morphology. The dashed lines outline the evolution of the energy landscapes with the geometrical misfit to be compensated at the interface (see the text for more details).

Similar conclusion can be drawn for real macro-twin boundaries between laminates with non-perfect periodicity and slightly varying volume fractions. If the first three condition are satisfied, the crossing-twins morphology locally forms at several points along the interface, and the boundary becomes pinned in these points. During the propagation, the position of the pinning point changes, but the twinning stress is permanently increased. So it can be expected that the macro-twin boundaries at which the first three conditions are (at least approximately) satisfied are less mobile than the fully general ones, for which no such pinning mechanism occurs.

Using this theoretical concept, we can discuss which parameters may affect the twinning stress. Let us consider, for instance, that the macro-twin forms between laminates of orthorhombic martensitic variant such that the unit cells over the A:B and C:D twinning planes differ always only by the orientation of the a and b dimensions of the unit cell while the orientation of the third dimension c remains unchanged within each laminate. Or that the variants are monoclinic, and that the A:B and C:D twinning planes just separate the variants with different sign of the angle of the monoclinic distortion $\gamma-\pi/2$ (but the orientations of the a, b, and c are always the same in the whole laminate). Then, the possible misfit at the interface is always described by a single parameter: in the first case this parameter is the difference between a and b, in the latter case this parameter is the magnitude of the angle $\gamma-\pi/2$. If this parameter goes to zero (i.e. $a\to b$ or $\gamma\to\pi/2$) the laminate disappears and the macro-twin degenerates into a simple twin. Thus, this parameter quantifies not only the misfit between the individual variants inside the laminate, but, simultaneously, also the misfit that must be compensated at the macro-twin interface if the exact crossing-twins morphology cannot form. The effect of this parameter on the twinning stress is marked by the dashed lines in Fig. 4: if the misfit is large, the minima corresponding to the crossing-twins morphology are deeper and the pinning is thus stronger. With vanishing misfit the pinning disappears, and the twinning stress is expected to decrease.

The obtained theoretical conclusion that the twinning stress for the crossing-twins morphology is increased by such pinning mechanism can be easily applied to any macro-twin, for which the intersection of the A:B and C:D twinning planes lies in the macro-twinning plane ($\tilde{\phi}=0$), and for which the periodicity of both the laminates is the same (the same volume fraction and the same spatial period of lamination). It is obvious that in such case some positions of the macro-twinning planes are energetically more favourable than the others. As the macro-twin moves through the crystal, the lamina are meeting each other and passing away periodically, which results in periodic changes of the energy of the microstructure forming at the interface during the propagation. The moving interface has to overcome this periodic energetic barriers, which leads to energy dissipation and pinning.

4. Application to 10 M Ni–Mn–Ga Type I and Type II macro-twins

Now we apply the above described general model to the 10 M martensite of Ni–Mn–Ga in order to analyse the observed large difference of the twinning stress of the Type I and Type II macro-twin boundaries. Our broader aim is to analyze the micromorphologies appearing at the macro-twinning interfaces at all length scales observed in the experiment and to discuss how they may affect the twinning stress.

4.1. The choice of the geometry

For the sake of simplicity, we consider only the following given geometry of the macro-twins: the mobile interface will be an interface between one region with the c-axis oriented along the $[0;0;1]_P$ direction and a region with the c-axis oriented along the $[1;0;0]_P$ direction. This means that the first region will be composed of variants 1, 2, 3 and 4, while the second region of variants 9, 10, 11 and 12. For symmetry reasons, this choice is sufficiently general.

Furthermore, we restrict our analysis to two possible interfaces: the Type I interfaces along the $(1/\sqrt{2})(1;0;-1)_P$ plane, and the Type II interface approximately along the $(1/\sqrt{2})(1;0;1)_P$ plane.[2] The reason why we choose the Type I and Type II interfaces nearly perpendicular to each other is the following: if we take two fixed single variants that are able to form Type I and Type II twins, for example No.1 and No. 11, the orientations of the twinning planes are $\mathbf{n}^{\mathrm{TypeI}}=1/\sqrt{2}[1;0;-1]_P$ and $\mathbf{n}^{\mathrm{TypeII}}=[0.7053;0.0721;0.7053]_P$, i.e. in agreement with our choice of the orientations of the macro-twins. Thus, when downscaling to the nano-scale, we can end up with a single interface between two modulated single variants of martensite with the same two possible orientations of the twin. Again, this choice captures all possible cases, and the results for any other orientation would be equivalent, as it follows from the symmetry of the monoclinic lattice.

Finally we choose fixed volume fractions and fixed crystallographic orientations of the laminates. Then we can work with specific numbers and do the calculations without giving lengthy explanation of for which volume fraction which exact orientation of the macro-twinning plane is valid. Although the results obtained for different volume fractions may differ quantitatively (but the differences are rather negligible, as seen for example in the calculations of the Type II macro-twin orientation in Straka et al. (2011) or of the incompatibility indicators in Heczko et al., 2013b), the qualitative results, which are the most desired in this case, are always the same. In this sense, we will use the fixed orientations and volume fractions

[2] At the meso-scale, the angle of declination of the Type II interface from the $(1/\sqrt{2})(1;0;1)_P$ plane in the reference configuration depends on the volume fractions of the individual variants in the modulation laminates, ranging from 0° to 4.3°; at the micro-scale, this angle depends on the volume fraction of the a–b laminates, ranging from 4.1° to 4.3°; at the nano-scale this angle is either 4.1° or 4.3°, depending on which particular variants are involved, see Straka et al. (2011) for the calculations.

Table 1
Parameters of the microstructures taken for the calculations: definition of regions $A, \ldots, D$ at different spatial scales, the orientations of interfaces between them and the respective volume fractions. (If not stated otherwise, all values at each scale are taken the same for the Type I and Type II macro-twin.)

		A	B	C	D
Meso-scale	c-axis (10 M)	$[0;0;1]_P$	$[0;0;1]_P$	$[1;0;0]_P$	$[1;0;0]_P$
	Modulation direction	$\frac{1}{\sqrt{2}}[1;1;0]_P$	$\frac{1}{\sqrt{2}}[1;-1;0]_P$	$\frac{1}{\sqrt{2}}[0;1;1]_P$	$\frac{1}{\sqrt{2}}[0;1;1]_P$
	Variants (10 M)	Nos. 1 and 3	Nos. 2 and 4	Nos. 9 and 11	Nos. 10 and 12
	Interfaces (for Type I)	$\mathbf{n}_{A:B}=[1;0;0]_P$		$\mathbf{n}_{C:D}=[0;0;1]_P$	
	Interfaces (for Type II)	$\mathbf{n}_{A:B}=[0;1;0]_P$		$\mathbf{n}_{C:D}=[0;1;0]_P$	
	Volume fractions	$\lambda_{A:B}=1/2$		$\lambda_{C:D}=1/2$	
Micro-scale	c-axis (10 M)	$[0;0;1]_P$	$[0;0;1]_P$	$[1;0;0]_P$	$[1;0;0]_P$
	a-axis (10 M)	$[1;0;0]_P$	$[0;1;0]_P$	$[0;0;1]_P$	$[0;1;0]_P$
	b-axis (10 M)	$[0;1;0]_P$	$[1;0;0]_P$	$[0;1;0]_P$	$[0;0;1]_P$
	Variants (10 M)	No. 1	No. 3	No. 11	No.9
	Interfaces	$\mathbf{n}_{A:B}=\frac{1}{\sqrt{2}}[1;1;0]_P$		$\mathbf{n}_{C:D}=\frac{1}{\sqrt{2}}[0;1;1]_P$	
	Volume fractions	$\lambda_{A:B}=0.2$		$\lambda_{C:D}=0.2$	
Nano-scale	c-axis (NM)	$[1;0;0]_P$	$[0;1;0]_P$	$[0;0;1]_P$	$[0;1;0]_P$
	Variants (10 M)	A:B-laminate = No.1		C:D-laminate = No.11	
	Interfaces	$\mathbf{n}_{A:B}=\frac{1}{\sqrt{2}}[1;-1;0]_P$		$\mathbf{n}_{C:D}=\frac{1}{\sqrt{2}}[0;1;-1]_P$	
	Volume fractions	$\lambda_{A:B}=3/5$		$\lambda_{C:D}=3/5$	

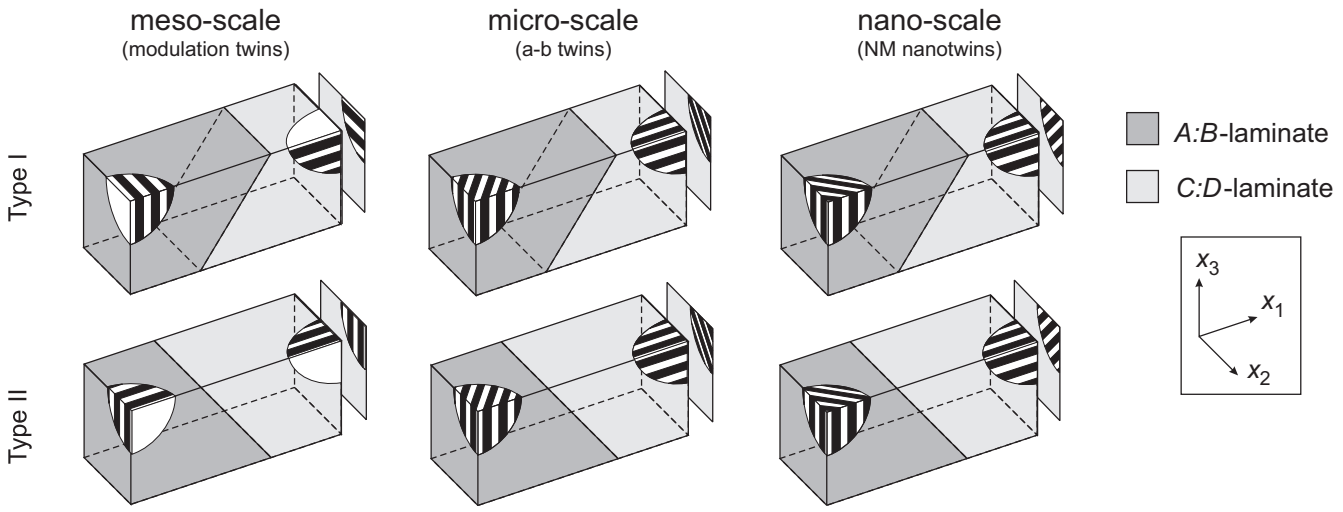

Fig. 5. Overview of orientations of A:B and C:D laminates (black/white stripes shown in the corners) at all discussed length-scales drawn in the reference coordinate system. Upper row: Type I interface along the $(1/\sqrt{2})(1;0;-1)_P$ plane; lower row: Type II interface approximately along the $(1/\sqrt{2})(1;0;1)_P$ plane.

as summarized in Table 1 and outlined in Fig. 5. For defining these particular geometries we use the notation introduced in Section 2 and used in Fig. 2, i.e we use the capital letters A, B, C and D for homogeneous regions forming the A:B- and C:D-laminates that meet at the macro-twin boundary.

- At the *meso-scale* (upper part of Table 1), the A:B- and C:D-laminates are the modulation laminates. We will take two possible orientations of the modulation laminates observed experimentally (Straka et al., 2011; Chulist et al., 2013): for the case of the Type I it is $\mathbf{n}_{A:B}=[1;0;0]_P$ and $\mathbf{n}_{C:D}=[0;0;1]_P$; for the case of Type II it is $\mathbf{n}_{A:B}=[0;1;0]_P$ and $\mathbf{n}_{C:D}=[0;1;0]_P$. The respective volume fractions will be $\lambda_{A:B}=\lambda_{C:D}=1/2$, chosen according to the optical observations by Straka et al. (2011).
- At the *micro-scale* (middle part of Table 1), we describe the case of four martensitic variants $A=$ No. 1, $B=$ No. 3, $C=$ No. 11 and $D=$ No. 9. From the possible orientation of the a–b twinning planes, we take (without loss of generality) $\mathbf{n}_{A:B}=(1/\sqrt{2})[1;1;0]_P$ and $\mathbf{n}_{C:D}=(1/\sqrt{2})[0;1;1]_P$. In order to be specific and guided by experiment (Straka et al., 2011), the respective volume fractions are $\lambda_{A:B}=\lambda_{C:D}=0.2$. (The necessity of $\lambda_{A:B}=\lambda_{C:D}$ follows from the condition of the mesoscopic compatibility between the a–b laminates.)
- At the *nano-scale* (lower part of Table 1), the volume fractions are given by the stacking sequence in which the tetragonal NM martensite arranges into the modulated phase. We work with three variants of tetragonal NM martensite: A (c-axis oriented along the $[1;0;0]_P$ direction), B (c-axis oriented along the $[0;1;0]_P$ direction) and C (c-axis oriented along the $[0;0;1]_P$ direction). To obtain the twin boundary between the variants No. 1 and No. 11 of the 10 M modulated phase, the

Table 2
Results of the calculation of the incompatibility indicators for all discussed macro-twins. The vector $\mathbf{m}_{A:B:C:D}$ is the vector of mutual intersection of the A:B and B:D twinning planes with the macro-twin, that does not exist unless $\phi=0$ (or $\tilde{\phi}=0$).

		ϕ	ψ	$\mathbf{m}_{A:B:C:D}$	Morphology	Comments
Meso-scale	Type I	0°	0°	$[0;1;0]_P$	Crossing-twins	See Fig. 6(a)
(Modulation twins)	Type II	0°	0°	$\frac{1}{\sqrt{2}}[1;0;-1]_P$	Crossing-twins	See Fig. 6(b)
Micro-scale	Type I	0°	0.458°	$\frac{1}{\sqrt{3}}[1;1;1]_P$	Crossing-twins	Elastic strains needed
(a–b twins)	Type II	$\sim 75^\circ$	$\sim 10^\circ$	Non-existent	General	
Nano-scale	Type I	$\tilde{\phi}=0^\circ$		$\frac{1}{\sqrt{3}}[1;1;1]_P$	Zig-zag	
(NM nano-twins)	Type II	$\tilde{\phi}\sim 70^\circ$		Non-existent	General	

A:B and C:B laminates (since $D\equiv B$ in this case) with $\mathbf{n}_{A:B}=(1/\sqrt{2})[1;1;0]_P$ and $\mathbf{n}_{C:B}=(1/\sqrt{2})[0;1;1]_P$ are formed with the volume fractions $\lambda_{A:B}=\lambda_{C:B}=3/5$. Following Kaufmann et al. (2010), we take the NM unit cell with the hypothetical c/a ratio equal to 1.16 for the calculations.

4.2. Application of the model over all length-scales

Now we can proceed to analyze the motion at all length-scales. At each scale, we check the conditions for the formation of the special microstructures and discuss the possible effect on the twinning stress. The results are summarized in Table 2 and can be interpreted as follows:

- At the *meso-scale*, the A:C and B:D compatible interfaces can exist (these are the microscopic Type I and Type II interfaces), and it can be easily shown that the macro-twin boundary can be obtained as their combination. For both the Type I and Type II interfaces the incompatibility indicators are identically equal to zero (the upper part of Table 2). Under the assumption that the volume fractions are the same in both the laminates forming the macro-twin, the crossing-twins morphology can form. However, there is a difference in the effect this morphology has on the twinning stress: the A:B- and C:D-laminates for the Type II interface are parallel to each other ($\mathbf{n}_{A:B}=\mathbf{n}_{C:D}$) and perpendicular to the mobile interface. For this reason, the Type II interface can move freely without pinning, since the connection between the A:B and C:D twinning planes is never broken and the general morphology never forms. For the Type I interface, in contrast, the $\mathbf{n}_{A:B}$ and $\mathbf{n}_{C:D}$ vectors are perpendicular to each other, and so the pinning can be expected. Thus, although the crossing-twins morphology forms at the meso-scale in both cases, it can have any impact on the twinning stress only for the Type I interface.
- At the *micro-scale*, the A:C and B:D interfaces are simple twinning planes between 10 M single variants. For the case of Type I boundary, the A:C and B:D Type I twins are both lying along the $(1/\sqrt{2})(1;0;-1)_P$ plane and can be, thus, obviously composed into the macro-twinning plane. Furthermore, the first indicator is exactly equal to zero (see the middle part of Fig. 2), so all the four twinning planes intersect in one line. The second indicator is small but non-zero ($\psi<0.5^\circ$). However, as shown by Balandraud and Zanzotto (2007) for Cu–Zn–Al, by Seiner et al. (2009) and by Stupkiewicz and Górzyńska-Lengiewicz (2012) for Cu–Al–Ni, and by Heczko et al. (2013b) for Ni–Mn–Ga at the meso-scale, such small misfit can be easily compensated by elastic strains. Thus, it can be expected that the crossing-twins morphology forms. Anyway, since obviously also $\tilde{\phi}=0$, the motion of the Type I interface is, at this scale, possibly hindered by pinning. On the contrary, both the incompatibility indicators are significantly large for the Type II interface. Also the simplified indicator $\tilde{\phi}$ is approximately 70°. This means that this interface, if exists, must form the general morphology and, consequently, moves freely without pinning.
- At the *nano-scale*, the situation becomes slightly more complicated. Only three variants are coming into play which makes the crossing-twins morphology impossible. However, the difference between the Type I and Type II interface is, again, obvious: while for the Type I we obtain $\tilde{\phi}=0$, so the zig-zag morphology can be expected, the Type II seems to be unable to form any special morphology. On the other hand, it must be taken into account that at the nano-scale the laminates are only few atomic spacings thick and have, therefore, only very limited ability to branch or to form tapering needles. Within the frame of our model, we can only say that the morphology of the Type I interface at the nano-scale must oscillate correspondingly during the motion of the interface with the period of ten atomic layers. Thus the energy of the macro-twin should oscillate as well, leading to a pinning mechanism for the Type I interface even at this scale. On the contrary, for the Type II interface, all positions of the macro-twin are fully equivalent; there is no reason for any periodic oscillation of the energy, and, consequently, for any pinning mechanism. Finally, let us point out that such arrangement at the nano-scale does not, in fact, require the concept of the adaptive phase of martensite. If the 10 M unit cell was not composed of NM lamina, but was, instead, a modulated cell with periodic (possibly incommensurate Li et al., 2012) oscillations of the atomic positions, our model would work in a similar manner. The Type I interface is a mirror plane between the 10 M unit cells, and so the shearing planes along which the modulation appears can meet perfectly at this

interface ($\tilde{\phi} = 0$ in some generalized sense) and the energy of the Type I twin may depend on whether the oscillations of the atomic positions meet 'in-phase' or 'out-of-phase'. In such point of view, we obtain again the periodic changes of the energy of the Type I twin with its position, which leads to pinning and increase of the twinning stress.

In summary, we have obtained a fundamental multi-scale picture of the motion, able to explain the difference in the twinning stresses of the Type I and Type II boundaries. While for the Type II there are no reasons for microstructural pinning at any of the considered scales, the motion of the Type I can be hindered by such pinning at all scales.

5. Comparison of the model and experimental observations

The calculations in the previous section predict that there can be different microstructures appearing in the vicinity of the macro-twin interfaces for different types of macro-twins and that these microstructures evolve differently during the motion. In principle, it is difficult to observe such evolution experimentally at any of the considered spatial scales. For the meso-scale, the static images of the crossing-twins morphology were published (Straka et al., 2011; Heczko et al., 2013b,c; Chulist et al., 2013), obtained by optical-microscopy or by EBSD. To illustrate these morphologies, Fig. 6 shows the optical micrographs demonstrating the intersection of the modulation laminates with Type I and Type II boundaries. It is apparent that these two twinning systems (or rather macro-twinning systems, keeping in mind the a–b lamination and the concept of adaptive martensite) can fully intersect each other without any branching and refinement of the lamina close to the interfaces. This observation just indicates that the crossing-twins morphology is energetically preferred and forms instead of the general one. The impact on the twinning stress is, however, hard to discern. The characteristic length-scales of the modulation laminates are in this case large, comparable with the dimensions of the samples used in the experiments. Moreover, the large difference between the mobilities of the Type I and Type II twins was observed also for the cases where the modulation twinning was fully absent (e.g. Faran and Shilo, 2013; Heczko et al., 2013c), so the pinning at this spatial scale can be excluded as the main source of this difference.

For this reason, a more detailed discussion must be focused on the micro-scale: at this spatial scale, even a static observation of the morphology is not easy to obtain. Classical optical microscopy with Nomarski contrast does not give sufficient information: the a–b lamina have characteristic thicknesses of 20 μm only or probably even less (Chulist et al., 2013), and angle of the 'roof' created on the surface by the a–b lamination is 0.1°, which is both at or beyond the resolution limit of this method. Moreover, the sample bends and rotates under the external loads, and the bending and rotation angles are much higher than the angle of this 'roof' created on the surface by the a–b lamination. Imaging methods able to measure the 3D morphology of the roof (AFM, SEM, white light interferometry) or those able to visualize the a–b laminate due to different orientations of the variants (EBSD, AFM with the modulus mapping option) give only a very local information and are, in principle, too slow to enable the analysis of the microstructure evolution with the motion of the interface. Thus, a direct experimental proof of the validity of the above described model at the micro-scale is hard to achieve. Nevertheless, there are at least two experimental observations documented in the literature that indirectly support the assumption that the a–b lamination may significantly affect the twinning stress:

1. As described by Straka et al. (2012), the room temperature twinning stress for the Type I interface increases strongly with increasing transition (A_S) temperature, while the twinning stress for Type II interface does not depend on it. Simultaneously, the difference between the a and b dimensions of the 10 M monoclinic unit cell is also increasing in a similar manner with increasing A_S temperature (Lanska et al., 2004). These similar trends in the dependences suggest that the twinning stress is indeed correlated with the a–b lamination. Moreover, when this lamination almost disappears due to $a \doteq b$ for A_S being near the room temperature, the difference in the twinning stress disappears as well. In other words, the material seems to follow the tendency outlined in Fig. 4, with the height of the barriers increasing with the increasing a–b misfit for Type I, but with the energy landscape independent of the a–b misfit for Type II. A detailed

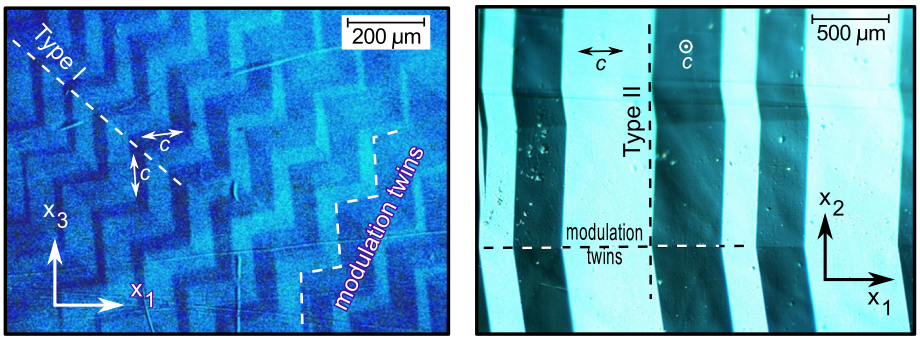

Fig. 6. Optical micrographs of compatible crossings of the modulation twins with lamina of the Type I (on the left) and Type II (on the right) systems. For each system, the orientation of the c-axis (changing at the Type I or Type II interfaces) is shown. (Optical microscopy with Nomarski (DIC) contrast enhancement.)

investigation is underway on determination of detailed temperature dependences of a and b lattice constants and their correlation with the twinning stress. Apart of this discussed dependency, very strong temperature dependence of twinning stress appears at low temperature far from transformation for Type I (Heczko and Straka, 2003; Heczko et al., 2013a; Straka et al., 2013) (but for Type II this effect is much weaker); this behaviour suggests that also the thermal activation must play some role in overcoming the energy barriers. Indeed, the motion of the Type I as described by our model requires repeated nucleation of new fine needles of martensite close to the interface, which is a thermally activated process, while no such nucleation is required for Type II.

2. Recently, the measurements by Faran and Shilo (2012, 2013) indicate that there are some energetic barriers affecting the mobility of the Type I twins with the characteristic length-scale of about 20 μm, while for the Type II interface this effect is much weaker (Faran, personal communication). This correlates very well with the dimensions of the a–b laminate obtained from the EBSD observation (Chulist et al., 2013). In addition, Benichou et al. (2013) estimated the height of this barriers to be $\Phi = 0.16\ \mathrm{J\,m^{-2}}$. According to Benichou and Givli (2013), the material with the Type I interface behaves as a material undergoing a sequence of discrete phase transitions, jumping discontinuously between minima separated by such barriers. If we take into account the fact that the energy Φ is comparable with the energy of the twinning plane (Shilo et al., 2007; Waitz et al., 2005), it is plausible that these barriers correspond to breaking the connections between the A:B and C:D twinning planes for the crossing-twins morphology.

At the nano-scale, the pinning mechanism results from the periodicity of the modulation. At this scale, our model is closely related to the finding of Faran and Shilo (2013) that the motion of the interface is provided by nucleation and growth of small steps and that the energy of the steps differs from Type I to Type II. According to our model, such steps can have arbitrary heights for the Type II interface but must be affected by the 10 M periodicity for the Type I interface; this can be the origin of the different energy, if, for example, the steps for the Type I interface tend to have a fixed height of ten (or five) atomic layers, but can be smaller for Type II. There are, however, other factors to be taken into account at the nano-scale. As discussed by Heczko et al. (2013b), the Type I interface at the meso-scale runs along a crystallographic plane of the 10 M lattice, while the Type II twin in this case is irrational. This definitely also plays some role for the twinning stress; nevertheless, as mentioned above, it is not even clear how does the real Type I interface look like at the nano-scale. The modulation induces periodic misplacements of the atoms from the $(1;0;-1)$ plane, so the resulting interface cannot be a flat lattice plane anymore. It opens new questions which are beyond the frame of continuum mechanics, and thus, beyond the applicability of our model. As seen from TEM observations by Matsuda et al. (2012), there is indeed a difference between nano-morphology of the Type I and Type II twins between two modulated martensites: while for the Type I interface the nano-twinning planes end at the mobile interface, forming indeed some kind of the zig-zag morphology, for the Type II interface these planes disappear relatively far away from the interface and the mobile interface itself is rather broad and blurry. Although the inner structure of the 10 M modulated unit cell can be properly discussed only at the atomistic level, our model can give some insight into the origin of the different twinning stress for the Type I and Type II interfaces even at the nano-scale.

6. Conclusions

The presented model demonstrates that macro-twins of different types can be differently affected in their twinning stress by microstructures forming in the vicinity of the macro-twinning planes. We showed that if particular conditions are satisfied, special morphologies can (at least locally) form in the interfacial region, which results in pinning.

We applied this model to 10 M modulated martensite of Ni–Mn–Ga, where the macro-twins with very different mobilities were observed experimentally. For this material, the predictions of the model are in agreement with the experiments; while the predicted pinning mechanism can appear for the Type I interface at all discussed length-scales, no such mechanism is possible for the Type II interface. Thus the twinning stress of Type I interface is predicted to be much higher in accordance with experiment.

The model, however, cannot predict which length-scale plays the most important role for the twinning stress. From the indirect experimental observations it looks like that the pinning both at the micro-scale and at the nano-scale play some role, while the role of pinning on meso-scale may be negligible. The available experiments further suggest that the most important is a pinning on the micro-scale, since the a–b lamination has the same characteristic dimension as the experimentally measured distance between energetic barriers. Moreover, the evolution of the twinning stress with the A_S temperature predicted by the model at the micro-scale agrees well with the experimental observations (Straka et al., 2012), which also indicates that the pinning on the a–b laminate could be important. The role of the other two scales (meso- and nano-) remains unresolved. Full analysis of this point requires further detailed experimental work and this model can serve as a guide.

We demonstrated the applicability of the model on the important case of Ni–Mn–Ga martensite, but the model presented in this paper is general, not restricted to any class of martensites or any specific material. It can help the understanding of the formation of macro-twins and their role for the effective response of modulated phases or other complex microstructures of any shape memory alloys.

Acknowledgments

The authors would like to acknowledge Dr. Miroslav Frost (IT ASCR, Prague) for his help with revision of this paper. This work has been supported by the Academy of Sciences of the Czech Republic (international collaboration Grant no. M100761203), by Czech Science Foundation (Project nos. 101/09/0702 and 107/11/0391) and by the Academy of Finland.

References

Balandraud, X., Zanzotto, G., 2007. Stressed microstructures in thermally induced M9R-M18R martensites. J. Mech. Phys. Solids 55, 194–224.
Ball, J.M., James, R.D., 1987. Fine phase mixtures as minimizers of energy. Arch. Ration. Mech. Anal. 100, 13–52.
Ball, J.M., James, R.D., 1992. Proposed experimental tests of theory of fine microstructure and the two-well problem. Philos. Trans.: Phys. Sci. Eng. 338, 389–450.
Ball, J.M., Koumatos, K., Seiner, H., 2009. An analysis of non-classical austenite–martensite interfaces in CuAlNi. In: Olson, G.B., Lieberman D.S., Saxena A. (Eds.), Proceedings of the International Conference on Martensitic Transformations (ICOMAT-08), Santa Fe, NM, June 29–July 5. The Minerals, Metals & Materials Society (TMS), Warrendale, pp. 383–390. ⟨http://arxiv.org/abs/1108.6220⟩).
Benichou, I., Givli, S., 2013. Structures undergoing discrete phase transformation. J. Mech. Phys. Solids 61, 94–113.
Benichou, I., Faran, E., Shilo, D., Givli, S., 2013. Application of a bi-stable chain model for the analysis of jerky twin boundary motion in NiMnGa. Appl. Phys. Letters 102, 011912-1–011912-3.
Bhattacharya, K., 2003. Microstructure of martensite. Oxford Series on Materials Modelling, Oxford University Press, New York.
Bhattacharya, K., Li, B., Luskin, M., 1999. The simply laminated microstructure in martensitic crystals that undergo a cubic to orthorhombic phase transformation. Arch. Ration. Mech. Anal. 149, 123–154.
Boullay, Ph., Schryvers, D., Kohn, R.V., 2001. Bending martensite needles in $Ni_{65}Al_{35}$ investigated by two-dimensional elasticity and high-resolution transmission electron microscopy. Phys. Rev. B 64, 144105-1–144105-8.
Chernenko, V.A., Cesari, E., Kokorin, V.V., Vitenko, I.N., 1995. The development of new ferromagnetic shape memory alloys in Ni–Mn–Ga system. Scr. Metall. Mater. 33. 1239-124.
Chu, C., 1993. Hysteresis and Microstructure: A Study of Biaxial Loading on Compound Twins of Copper–Aluminum–Nickel Single Crystals (Ph.D. thesis), University of Minnesota.
Chulist, R., Skrotzki, W., Oertel, C.-G., Böhm, A., Pötschke, M., 2010. Change in microstructure during training of a $Ni_{50}Mn_{29}Ga_{21}$ bicrystal. Scr. Mater. 63, 548–551.
Chulist, R., Straka, L., Lanska, N., Soroka, A., Sozinov, A., Skrotzki, W., 2013. Characterization of mobile type I and type II twin boundaries in 10 M modulated Ni–Mn–Ga martensite by electron backscatter diffraction. Acta Mater. 61, 1913–1920.
Faran, E., 2012. Personal communication.
Faran, E., Shilo, D., 2011. The kinetic relation for twin wall motion in NiMnGa. J. Mech. Phys. Solids 59, 975–987.
Faran, E., Shilo, D., 2012. Implications of twinning kinetics on the frequency response in NiMnGa actuators. Appl. Phys. Lett. 100, 151901-1–151901-4.
Faran, E., Shilo, D., 2013. The kinetic relation for twin wall motion in NiMnGa – Part 2. J. Mech. Phys. Solids 61, 726–741.
Ge, Y., Jiang, H., Sozinov, A., Söderberg, O., Lanska, N., Keränen, J., Kauppinen, E.I., Lindroos, V.K., Hannula, S.-P., 2006. Crystal structure and macrotwin interface of five-layered martensite in Ni–Mn–Ga magnetic shape memory alloy. Mater. Sci. Eng. A 438–440, 961–964.
Heczko, O., Sozinov, A., Ullakko, K., 2000. Giant field-induced reversible strain in magnetic shape memory NiMnGa alloy. IEEE Trans. Magn. 36 (5 I), 3266–3268.
Heczko, O., Straka, L., 2003. Temperature dependence and temperature limits of magnetic shape memory effect. J. Appl. Phys. 94, 7139–7143.
Heczko, O., Kopecky, V., Sozinov, A., Straka, L., 2013a. Magnetic shape memory effect at 1.7 K. Appl. Phys. Lett. 103, 072405-1–072405-4.
Heczko, O., Straka, L., Seiner, H., 2013b. Different microstructures of mobile twin boundaries in 10 M modulated Ni–Mn–Ga martensite. Acta Mater. 61, 622–631.
Heczko, O., Kopeček, J., Straka, L., Seiner, H., 2013c. Differently mobile twin boundaries and magnetic shape memory effect in10 M martensite of Ni–Mn–Ga. Mater. Res. Bull., 48, 5105–5109.
Kaufmann, S., Rößler, U.K., Heczko, O., Wuttig, M., Buschbeck, J., Schultz, L., Fähler, S., 2010. Adaptive modulations of martensites. Phys. Rev. Lett. 104 (14). 145702-1–145702-4.
Kaufmann, S., Niemann, R., Thersleff, T., Rößler, U.K., Heczko, O., Buschbeck, J., Holzapfel, B., Schultz, L., Fähler, S., 2011. Modulated martensite: why it forms and why it deforms easily. New J. Phys. 13, 053029-1–053029-24.
Khachaturyan, A.G., Shapiro, S.M., Semenovskaya, S., 1991a. Adaptive phase formation in martensitic transformation. Phys. Rev. B 43, 1083–10843.
Khachaturyan, A.G., Shapiro, S.M., Semenovskaya, S., 1991b. Adaptive phase in martensitic transformation. Mater. Trans. Jpn. Inst. Met. 33 (3), 278–281.
Kouznetsova, V.G., Geers, M.G.D., 2008. A multi-scale model of martensitic transformation plasticity. Mech. Mater. 40 (8), 641–657.
Lanska, N., Söderberg, O., Sozinov, A., Ge, Y., Ullakko, K., Lindroos, V.K., 2004. Composition and temperature dependence of the crystal structure of Ni–Mn–Ga alloys. J. Appl. Phys. 95, 8074–8078.
Li, Z., Zhang, Y., Esling, C., Zhao, X., Zuo, L., 2012. Evidence for a monoclinic incommensurate superstructure in modulated martensite. Acta Mater. 60. 6982–6990.
Matsuda, M., Yoshihiro, Y., Kimiaki, H., Hara, T., Nishida, M., 2012. Transmission electron microscopy of twins in 10 M martensite in Ni–Mn–Ga ferromagnetic shape memory alloy. Mater. Trans. 53, 902–906.
Niemann, R., Rößler, U.K., Gruner, M.E., Heczko, O., Schultz, L., Fähler, S., 2012. The role of adaptive martensite in magnetic shape memory alloys. Adv. Eng. Mater. 14, 562–581.
O'Handley, R.C., Murray, S.J., Marioni, M., Nembach, H., Allen, S.M., 2000. Phenomenology of giant magnetic-field-induced strain in ferromagnetic shape-memory materials (invited). J. Appl. Phys. 87, 4712–4717.
Pitteri, M., Zanzotto, G., 1998. Generic and non-generic cubic-to-monoclinic transitions and their twins. Acta Mater. 46, 225–237.
Ruddock, G., 1994. A microstructure of martensite which is not a minimiser of energy: the X-interface. Arch. Ration. Mech. Anal. 127, 1–39.
Righi, L., Albertini, F., Pareti, L., Paoluzi, A., Calestani, G., 2007. Commensurate and incommensurate “5 M” modulated crystal structures in Ni–Mn–Ga martensitic phases. Acta Mater. 55, 5237–5245.
Schryvers, D., Boullay, Ph., Potapov, L.P., Kohn, R.V., Ball, J.M., 2002. Microstructures and interfaces in Ni–Al martensite: comparing HRTEM observations withcontinuum theories. Int. J. Solid Struct. 39, 3543–3554.
Seiner, H., Landa, M., 2009. Non-classical austenite–martensite interfaces observed in single crystals of Cu–Al–Ni. Phase Trans. 82, 793–807.
Seiner, H., Glatz, O., Landa, M., 2009. Interfacial microstructures in martensitic transitions: from optical observations to mathematical modeling. Int. J. Multiscale Comp. Eng. 7, 445–456.
Shilo, D., Medelovich, A., Novák, V., 2007. Investigation of twin boundary thickness and energy in CuAlNi shape memory alloy. Appl. Phys. Lett. 90, 193113-1–193113-4.
Sozinov, A., Lanska, N., Soroka, A., Straka, L., 2011. Highly mobile type II twin boundary in Ni–Mn–Ga five-layered martensite. Appl. Phys. Lett. 99., pp. 124103-1–124103-1.
Straka, L., Heczko, O., Seiner, H., Lanska, N., Drahokoupil, J., Soroka, A., Fähler, S., Hänninen, H., Sozinov, A., 2011. Highly mobile twinned interface in 10 M modulated Ni–Mn–Ga martensite: analysis beyond the tetragonal approximation of lattice. Acta Mater. 59, 7450–7463.

Straka, L., Soroka, A., Seiner, H., Hänninen, H., Sozinov, A., 2012. Temperature dependence of twinning stress of Type I and Type II twins in 10 M modulated Ni–Mn–Ga martensite. Scr. Mater. 67, 25–28.
Straka, L., Sozinov, A., Drahokoupil, J., Kopecky, V., Hänninen, H., Heczko, O., 2013. Effect of intermartensite transformation on twinning stress in Ni–Mn–Ga 10 M martensite. J. Appl. Phys. 114, 063504-1–063504-7.
Stupkiewicz, S., Górzyñska-Lengiewicz, A., 2012. Almost compatible X-microstructures in CuAlNi shape memory alloy. Continuum Mech. Thermodyn. 24, 149–164.
Turteltaub, S., Suiker, A.S.J., 2006. A multiscale thermomechanical model for cubic to tetragonal martensitic phase transformations. Int. J. Solids Struct. 43 (14–15), 4509–4545.
Waitz, T., 2005. The self-accommodated morphology of martensite in nanocrystalline NiTi shape memory alloys. Acta Mater. 53, 2273–2283.
Waitz, T., Spišák, D., Hafner, J., Karnthaler, H.P., 2005. Size-dependent martensitic transformation path causing atomic-scale twinning of nanocrystalline NiTi shape memory alloys. Europhys. Lett. 71, 98–103.

3.4 Shrnutí získaných poznatků

Vysoce pohyblivá rozhraní ve slitině Ni-Mn-Ga jsou jednou z aktuálně nejřešenějších tématik v oblasti termoelastických martenzitů. V této kapitole bylo ukázáno, že pro pochopení mechanismů řídících vysokou pohyblivost je třeba popisovat mřížku 10 M modulovaného Ni-Mn-Ga nikoliv jako tetragonální, ale jako plně monoklinickou, zohledňující směr a orientaci modulace. Jak je ukázáno v podkapitole 3.1, takové rozšíření umožňuje identifikovat vysoce pohyblivá rozhraní jako makro-dvojčatová rozhraní Typu 1 a Typu 2, přičemž právě u Typu 2 jsou pozorována reorientační napětí až řádově 0.1 MPa.

Jak je dále diskutováno v podkapitole 3.2, díky monoklinicitě mřížky 10 M martenzitu může v tomto materiálu vznikat velmi široké spektrum pohyblivých mikrostruktur různých mikromorfologií, přičemž na základě mechaniky kontinua lze tyto morfologie teoreticky analyzovat a predikovat, které z nich budou energeticky výhodnější. Tato predikce se ukazuje být v dobré shodě s experimentem.

Na základě mikromechanického modelu navrženého v podkapitole 3.3 lze rovněž predikovat, které z makrodvojčatových rozhraní budou vysoce pohyblivá a pro která naopak pohyb vyžaduje tepelně aktivované překonávání energetických bariér a lze u nich proto očekávat výrazný pokles mobility s klesající teplotou. Zcela ve shodě s výsledky tohoto modelu je právě rozhraní Typu 2 vysoce pohyblivé, zatímco u rozhraní Typu 1 je pohyblivost výrazně závislá na teplotě a reorientační napětí jsou řádově vyšší.

Výsledky shrnuté v této kapitole budou prezentovány na vyzvané plenární přednášce [62] na sympoziu ESOMAT 2015 (15-19. září, Antverpy, Belgie).

Kapitola 4

Pohyblivé mikrostruktury ve vysokoteplotních fázích

Vysokoteplotní fáze termoelastických martenzitů vykazují vysoké třídy symetrie (většinou kubickou symetrii), proto v nich nemohou vznikat klasické martenzitické lamináty nebo podobné mikrostruktury. Přesto však se i v nich vyskytují mikrostruktury výrazně ovlivňující průběh termoelastické martenzitické transformace a ve výsledku i vlastnosti slitiny a její technologickou využitelnost. Jelikož transformace při podchlazení vysokoteplotní fáze probíhá smykovým mechanismem se vznikem spontánního transformačního strainu, hraje zde opět významnou roli schopnost těchto mikrostruktur reagovat adaptabilně na vnější mechanické namáhání a pohybovat se pomocí anelastických mechanismů. Chápání termínu *pohyblivost* u těchto mikrostruktur je tedy poněkud odlišné než jak je tomu v případě klasických martenzitických mikrostruktur.

Elasticita vysokoteplotních fází se obecně u termoelastických martenzitů vyznačuje především anomálním chování nejměkčího akustického smykového fononu (TA_2), plynoucího z nestability vysokoteplotní mřížky. Elastická konstanta spojená s tímto fononem odpovídá odporu kubické mřížky vůči smykům podél diagonálních rovin $\{110\}$ v diagonálních směrech a obvykle se označuje jako c'. Měknutí c' směrem k transformační teplotě při ochlazování je považováno za symptomatické pro austenitickou fázi a odpovídá představě zanikání austenitického minima v termodynamickém konceptu multikonvexní volné energie (viz Kapitola 1, obrázek **Obr.1.5**).

V následujících komentovaných publikacích je ukázáno, že vliv na průběh martenzitické transformace a na prekurzorové efekty ji předcházející mohou mít přinejmenším čtyři druhy mikrostruktur:

- **Magnetická mikrostruktura** - ve feromagnetických slitinách s tvarovou pamětí, tedy například ve slitině Ni-Mn-Ga, vykazují austenitické fáze díky své strukturní nestabilitě často velmi nízké hodnoty magnetokrystalické anizotropie a zároveň relativně vysoké hodnoty magnetostrikce. V důsledku toho mohou monokrystaly těchto fází část vnějšího mechanického napětí anelasticky relaxovat změnami mikrostruktury magnetických domén a s nimi spojenou magnetostrikcí. Toto efektivní anelastické měknutí (takz-

vaný $\Delta E-$efekt, se v těchto materiálech superponuje na výše zmíněné strukturní měknutí způsobené nestabilitou nejměkčí fononové větve a vzniká tak mřížka extrémně měkká vůči smykovému namáhání, přičemž výsledná efektivní hodnota parametru c' je značně závislá na teplotě a vnějším magnetickém poli. V komentovaných článcích v podkapitolách 4.1 a 4.2 je tento efekt experimentálně analyzován a teoreticky diskutován pro slitinu Ni-Mn-Ga, v podkapitole 4.4 potom pro slitinu Co-Ni-Al.

- **Mikrostruktura antifázových rozhraní** - ve vysokoteplotních fázích uspořádaných slitin (intermetalik) se nezbytně vyskytuje také mikrostruktura antifázových rozhraní, tedy hranic mezi oblastmi s různou fází intermetalického uspořádání. Tato rozhraní jsou dokonale koherentní a oddělují oblasti stejných a stejně orientovaných krystalových mřížek, z hlediska klasické mechaniky by tedy neměly nijak ovlivňovat elastické konstanty materiálu a tím pádem ani koeficient c'. V Heuslerových slitinách jsou nosičem feromagnetického uspořádání atomy jinak nemagnetických kovů, které získávají feromagnetickou interakci díky vzájemným vzdálenostem vnuceným jim intermetalickým uspořádáním (v Ni-Mn-Ga jsou to atomy manganu). Na antifázových rozhraních je však uspořádanost narušena a interakce mezi sousedícími atomy manganu je buď paramagnetická nebo antiferomagnetická; v důsledku toho jsou antifázová rozhraní lokálně energeticky výhodnými místy pro magnetické doménové stěny a dochází na nich k jejich silnému pinování. Struktura antifázových rozhraní tedy přímo indukuje mikrostrukturu magnetickou a ta ovlivňuje chování materiálu způsobem popsaný v předchozím odstavci. V podkapitole 4.2 je tento efekt prokázán porovnáním elastických koeficientů c' pro monokrystaly Ni-Mn-Ga s malou a vysokou hustotou antifázových rozhraní.

- **Jemná disperze koherentních částic netransformujících fází** - ve vícefázových slitinách může průběh transformace výrazně ovlivňovat přítomnost jemně dispergovaných koherentních precipitátů, které sice nenarušují kontinuitu mříže a tím pádem ani nijak neovlivňují podmínky na kinematickou kompatibilitu rozhraní vznikajících při transformaci, ale jsou vhodnými nukleačními centry pro nízkoteplotní fáze. Hustota a morfologie těchto částic tak může mít značný vliv na prekurzorové měknutí koeficientu c'. Tento efekt je v podkapitole 4.4 ukázán na příkladu feromagnetické slitiny s tvarovou pamětí Co-Ni-Al obsahující jemnou mikrostrukturu částic netransformující $\gamma-$fáze.

- **Premartenzitický tweed**[1] - je jemná prekurzorová struktura projevující se v transmisní elektronové mikroskopii specifickým periodickým kontrastem. Tweedová mikrostruktura je efektivně stále kubická, nedochází u ní k feroelastickému spontánnímu narušení symetrie a nevytváří klasické martenzitické lamináty, proto se počítá k vysokoteplotním

[1] I v česky psané literatuře se je zvykem používat anglického zápisu *tweed* namísto českého *tvíd*, název je však skutečně odvozen od tvídové látky, jejíž strukturu premartenzitický tweed svým uspořádáním připomíná.

fázím. Na atomární úrovni na ni však lze nahlížet na jako na jemnou dvojčatovou strukturu tetragonálního martenzitu. Tato struktura prochází značnými mokromorfologickými změnami s teplotou, neboť změnami teploty dochází ke změnám v tetragonální distorzi jednotlivých elementárních buněk a tím pádem i k jejich natáčení ve struktuře. Důsledkem je měknutí bazálních smyků (popsaných elastickou konstantou c_{44}) a tuhnutí těch diagonálních (popsaných c'), jak je ukázáno pro případ premartenzitu slitiny Ni-Mn-Ga v podkapitole 4.3.

4.1 Publikace *Vliv kombinace strukturního měknutí a magneto-elastické vazby na elastické konstanty austenitu Ni-Mn-Ga.*

Bibliografická citace: Seiner, H., Heczko, O., Sedlák, P., Bodnárová, L., Novotný, M., Kopeček, J., Landa, M. Combined effect of structural softening and magneto-elastic coupling on elastic coefficients of NiMnGa austenite (2013) Journal of Alloys and Compounds, 577 (SUPPL. 1), pp. S131-S135.

Stručná anotace: V této publikaci je ukázáno, že výrazné smykové měknutí austenitické fáze slitiny Ni-Mn-Ga je způsobeno superpozicí dvou nezávislých efektů - strukturního měknutí v důsledku nestability mřížky magnetoelastického měknutí způsobeného takzvaným $\Delta E-$efektem. Tento poznatek je prokázán měřením změn smykového koeficientu c' se změnami vnějšího magnetického pole. Jak je předpokládáno pro magneto-elastickou vazbu, vyvíjí se tento koeficient s kvadrátem magnetizace.

Příspěvek habilitanta: Podíl habilitanta spočíval především ve vyhodnocení průběhů rezonančních spekter měřených vzorků s teplotou a polem a diskuzi interpretace těchto průběhů ve vztahu k mikrostruktuře. Habilitant se rovně podílel na samotných měřeních metodou rezonanční ultrazvukové spektroskopie v nulovém poli.

Journal of Alloys and Compounds 577S (2013) S131–S135

Contents lists available at ScienceDirect

Journal of Alloys and Compounds

journal homepage: www.elsevier.com/locate/jallcom

Combined effect of structural softening and magneto-elastic coupling on elastic coefficients of Ni—Mn—Ga austenite

Hanuš Seiner[a], Oleg Heczko[b,*], Petr Sedlák[a], Lucie Bodnárová[a], Michal Novotný[a], Jaromír Kopeček[b], Michal Landa[a]

[a] Institute of Thermomechanics, Academy of Sciences of the Czech Republic, Dolejškova 5, 182 00 Prague 8, Czech Republic
[b] Institute of Physics, Academy of Sciences of the Czech Republic, Na Slovance 2, 182 21 Prague 8, Czech Republic

ARTICLE INFO

Article history:
Received 26 September 2011
Received in revised form
25 November 2011
Accepted 2 January 2012
Available online 11 January 2012

Keywords:
Ni_2MnGa
Elastic constants of Ni—Mn—Ga austenite
Magnetic shape memory effect
Martensitic transformation
Elastic softening

ABSTRACT

Using two complementary ultrasonic methods the complete set of elastic constants of the austenite phase of Ni—Mn—Ga ferromagnetic shape memory alloy was measured in magnetic field up to saturation and in temperature range 295–400 K. While the coefficients c_{11} and c_{44} were nearly independent of the field and the temperature, the shear coefficient c' increased strongly with increasing field and temperature. Experiment indicates that two independent mechanisms contribute to the anomalous shear softening of the c' coefficient in Ni—Mn—Ga austenite; the structural softening of the bcc lattice and the softening due to magneto-elastic coupling. Above the Curie point and in the saturation field only the structural softening took place with rate about 10 MPa/K. In the demagnetized state the combined softening was approximately 35 MPa/K. Similar dependencies on the temperature and the magnetic field were also observed for the ultrasound attenuation of the shear mode.

1. Introduction

Ni—Mn—Ga is a prototypical magnetic shape memory alloy exhibiting up to 10% of magnetic field induced deformation in the modulated 14M martensite phase [1–3]. In the past two decades the structural transitions in this alloy (martensitic, intermartensitic and premartensitic) have been subjects of numerous detailed experimental and theoretical studies [4–7]. The important parts of these studies are the experimental investigations and subsequent interpretations of the evolution of the elastic coefficients of individual phases with temperature [8–11]. In particular, when approaching the martensitic transition temperature from above, the high-temperature phase, cubic austenite is expected to exhibit an increasing shear instability as observed for many (non-magnetic) shape memory alloys [12–15]. This increase of the shear instability is a precursor phenomenon of the martensitic transformation, observable as an anomalous softening of particular elastic coefficients. In magnetic shape memory alloys (such as Ni—Mn—Ga), the structural softening of the lattice in the vicinity of the transition temperature can be strongly affected by magneto-elastic coupling. Neutron diffraction demonstrates that the ferromagnetic ordering affects significantly the softest (TA_2) phonon branch in the single crystal of Ni—Mn—Ga austenite [16].

Some results for the temperature dependencies of the elastic coefficients of Ni—Mn—Ga austenite can be found in the literature [8–11]. The findings are, nevertheless, quite diverse; the experimentally evaluated shear coefficient in [9,10] differs nearly fivefold. Similar differences can be found for the theoretical calculations [17–19]. Additionally Pérez-Landazábal et al. [20] observed a strong temperature dependence of the effective shear modulus in polycrystalline samples using resonant ultrasound spectroscopy.

The effect of magnetic field was studied by Gonzalez-Comas et al. [21,22], who analyzed the field dependencies of the elastic coefficients and the damping coefficient at room temperature by the ultrasonic pulse-echo method. The observed changes are relatively small and comparable for all measured elastic coefficients. On the contrary, Zhao et al. [11] observed a significant difference between the results in an external magnetic field and without a field using the ultrasonic continuous-wave method. These results demonstrate that the application of the external magnetic field leads to the increase of the shear stiffness of the lattice and the decrease of the damping coefficient. However, the published results are incomplete and rather ambiguous and there is a need for a systematic and thorough study of the combined effect of the magnetic field and temperature.

This paper brings the results of a detailed experimental analysis of the elastic properties of the Ni—Mn—Ga austenite in the

* Corresponding author. Tel.: +420 266 052 714.
E-mail address: heczko@fzu.cz (O. Heczko).

0925-8388/$ – see front matter © 2012 Elsevier B.V. All rights reserved.
doi:10.1016/j.jallcom.2012.01.007

temperature range between the room temperature and the Curie point (T_C) and for the external magnetic field up to saturation. The results of this analysis are related to the magnetic properties of the examined material, which enables us to distinguish between the shear softening induced by the instability of the lattice and the magneto-elastic effects.

2. Experiment

The studied material was air-quenched single crystal of nearly stoichiometric Ni_2MnGa prepared by the Bridgman method. Magnetization as a function of field and temperature was measured using the vibrating sample magnetometer. The magnetization curve exhibited very low hysteresis not discernible with the used method (<0.2 mT). The transformation temperatures were determined from magnetization measurements at low field (10 mT): the Curie temperature T_C = 383 K, the martensitic transformation temperature M_s = 219 K, the premartensitic transformation temperature [7] T_{pm} = 252 K. While the martensitic transformation exhibited about 9 K thermal hysteresis, the hysteresis of the premartensitic transformation was less than 2 K. Thus all measurements of elastic constant reported in this study were done well above the premartensitic transformation.

To determine the complete set of elastic coefficients of cubic austenite a combination of two ultrasound methods was used; the conventional pulse-echo and resonant ultrasound spectroscopy (RUS) [23–25]. For the pulse-echo method, a 4.4 mm thick tablet (cylindrical, 12 mm in diameter) oriented perpendicular to the [1 0 0] direction was prepared. The specimen for the RUS measurements was a 4.4 mm × 5.6 mm × 7.7 mm rectangular parallelepiped cut approximately along the principal {1 0 0} planes of the austenite lattice. The exact orientations of the individual faces of the specimen were determined by the X-ray Laue method.

The instrumentation of the ultrasonic experiments was as follows: the phase velocities in the [1 0 0] direction were evaluated by the echo-overlapping method using the 50 MHz pulse/receiver system DPR50+(JSR Ultrasonics Inc.) with the ultrasonic transducers VSP-50 (Ultran Group, nominal frequency 30 MHz) for the longitudinal waves (c_{11}) and V157-5/0.125″ (Panametrics, nominal frequency 20 MHz) for the shear waves (c_{44}); for the RUS method the vibrations were induced and recorded by two miniature piezoelectric transducers VP-1093. The excitation was performed by a chirp signal in frequency range from 20 kHz to 1 MHz, output signals were detected by the acquisition system in the time domain, averaged, and transformed into the final spectra by FFT in a frequency range 20–200 kHz (which covers approximately the first 25 resonant frequencies of the examined specimen). All ultrasound experiments were performed in a temperature-controlled chamber in a homogeneous magnetic field between the poles of a 6″ electromagnet. The maximum magnitude of the applied field was 2 T. The amplitudes of the strains in the pulse-echo and RUS measurements were similar of the order of 10^{-6}.

The elasticity of cubic material as Ni—Mn—Ga austenite is fully described by three independent elastic coefficients. In shorten (Voigt's) notation, these coefficients are c_{11}, c_{12} and c_{44}. The meaning of the individual coefficients is [26]: the c_{11} coefficient describes the elastic response of the lattice to uniaxial elongations along the ⟨1 0 0⟩ directions; the c_{44} coefficients determines the elastic stiffness of the lattice with respect to the shears in the ⟨1 0 0⟩ directions along the {1 0 0} planes; the elasticity of the shears in the ⟨1 $\bar{1}$ 0⟩ directions along the {1 1 0} planes is described by the coefficient c', which is equal to $(c_{11} - c_{12})/2$.

The combination of two different ultrasonic methods allows an unequivocal determination of all these elastic coefficients: the pulse echo method was used for the determination of the elastic constants c_{11} and c_{44}, whereas RUS was utilized for determination of the shear coefficient c'. In principle, the c' coefficient can be also determined by the pulse echo-method; either by the direct measurement of the phase velocity of the slowest shear mode of ultrasonic waves in the [1 1 0] direction [10], or by the indirect evaluation of this coefficients from the velocities of the longitudinal and faster shear waves in the [1 0 0] and [1 1 0] directions as adopted in [8,9]. These methods, however, do not provide satisfying accuracy for this coefficient mainly due to strong elastic anisotropy of this material. Above all, this strong anisotropy leads to suppression of the energy fluxes of both the longitudinal and the slowest shear waves in the [1 1 0] direction, since the curvatures of the corresponding slowness curves in these directions are maximal (see e.g. [27] for more details). Moreover, when the c' is calculated from c_{11}, c_{44} and from the velocity of the longitudinal waves in the [1 1 0] direction, the resulting error may get unacceptably high due to the disproportionality between the magnitudes of c' and the other coefficients (see [28] for a quantitative analysis). The error in determination of shear coefficient is comparable to the shear coefficient itself [29]. Additional complication in the determination of the c' coefficient by the pulse-echo method arises due to attenuation of the ultrasonic waves of the modes related to this shear coefficient, which is a consequence of the structural and magneto-elastic effects described below.

The RUS method, on the contrary, is sensitive to the softest shear coefficient of the examined material. From the sensitivity analysis described in [30] it follows that for cubic Ni—Mn—Ga austenite exhibiting strong elastic anisotropy (the elastic anisotropy factor higher than 10), the method is completely insensitive to c_{11} and c_{44}, but enables accurate determination of c'.

Table 1
Room temperature values of elastic coefficients and anisotropy coefficient $A = c_{44}/c'$ in zero field and in saturation. The experimental errors for the pulse-echo measurements were calculated for 5 μm uncertainty in the specimens thicknesses and 1 ns in the time-of-flight measurements. For the RUS measurements, the experimental errors were estimated via the sensitivity analysis described in [30].

	c_{11} (GPa)	c_{44} (GPa)	c' (GPa)	A (1)
Zero field	140 ± 3	104 ± 2	3.6 ± 0.2	27
Saturation (>0.4 T)	141 ± 3	104 ± 2	5.9 ± 0.2	18

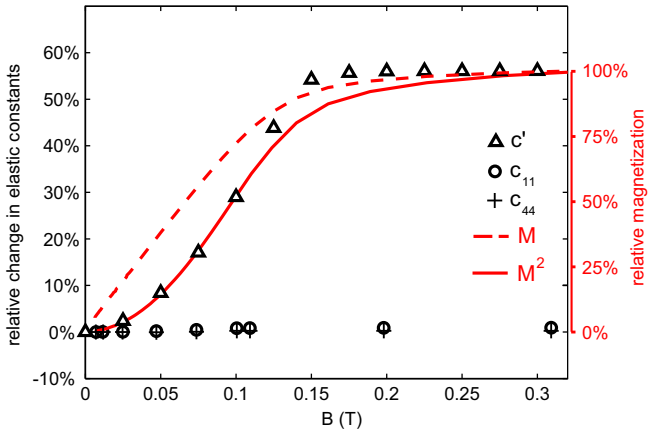

Fig. 1. Field dependencies of the coefficients c', c_{11} and c_{44} compared to the magnetization curve (M, dashed line) and the square of magnetization (M^2, solid line).

3. Results

The comparison of all elastic coefficients at room temperature with and without field is given in Table 1. The values without field are comparable with the recent calculation [19] and some previous measurement [10]. While there is a weak dependence of the 'hard' elastic coefficients c_{11} and c_{44}, the shear coefficient c' changes significantly with the magnetic field. This is clearly seen in Fig. 1, where the field dependencies of the c_{11}, c_{44} and c' coefficients are compared with the magnetization curve. It is apparent that the c' coefficient is approximately proportional to the square of the magnetization. Moreover, the difference of the coefficient in the zero field and in the saturation field is more than 50%. The changes of the c_{11} coefficient with the applied field are much smaller (less than 1%). For c_{44}, the changes are even smaller less than 0.5%.[1] The difference between field dependencies of c_{44} and c' result in a significant change of the elastic anisotropy coefficient (Table 1).

Similar behavior can be also observed for the temperature dependencies of the individual elastic coefficients [31]. While the coefficients c_{11} and c_{44} at the room temperature and at above the Curie point do not differ by more than 5%, the c' coefficient depends strongly on the temperature. Additionally, there is no discernible change of the dc_{ii}/dT slope observable at the Curie point for the c_{11} and c_{44} coefficients, while there is a significant jump of the dc'/dT slope, which is in agreement with [11]. Since the 'hard' coefficients c_{11} and c_{44} are nearly independent of the field and the temperature and the c' is the one most affected by the structural softening of

[1] This is in a sharp contrast with the results of Zhao et al. [11], who observed a strong dependence of c_{44} on the magnetic field. However, the magnitudes of c_{44} reported in [11] are about ten times smaller than our results and what can be found elsewhere in the literature [8–10]. Therefore the comparison is somehow questionable.

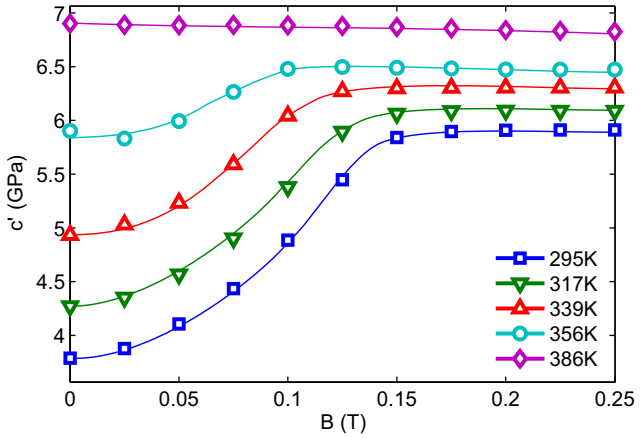

Fig. 2. Field dependencies of the c' coefficient at different temperatures. The solid lines are just guide for eye (data fitted by four-point Bézier curves).

the lattice in the vicinity of the transition temperature [12], we will further focus on this coefficient only.

The field dependencies of the c' coefficient are plotted in Fig. 2 for different temperatures ranging from RT to above the Curie point. The character of the field dependence, i.e. the proportionality to square of magnetization, does not change until the Curie temperature T_C is reached. The magnitudes of magnetic field at which the c' coefficients reach their saturated values decrease due to decreasing saturation magnetization close to T_C. Above T_C, the c' coefficient is independent of the field. With the increasing temperature, the values of c' increase both in the zero field and in saturation.

The resonant spectra from RUS measurements also enable to evaluate the evolution of the damping properties with the field and temperature. In this case, the attenuation is obtained as the quality factors (Q-factor) of the resonant spectra. The Q-factors are defined as $Q = f/\mathrm{d}f$, where f is the resonant frequency and $\mathrm{d}f$ is the full-width at the half maximum of the corresponding peak in the spectrum; i.e. the higher the quality factor, the lower damping in the material. The reciprocal value of Q describes the internal friction in the material, which is used in [32,11]. Details on the application of RUS to determine the damping coefficient are in [25].

The evolution of the Q-factor of Ni—Mn—Ga austenite with the external field for different temperatures is shown in Fig. 3. The Q-factors plotted in this figure are the mean values of the Q-factor

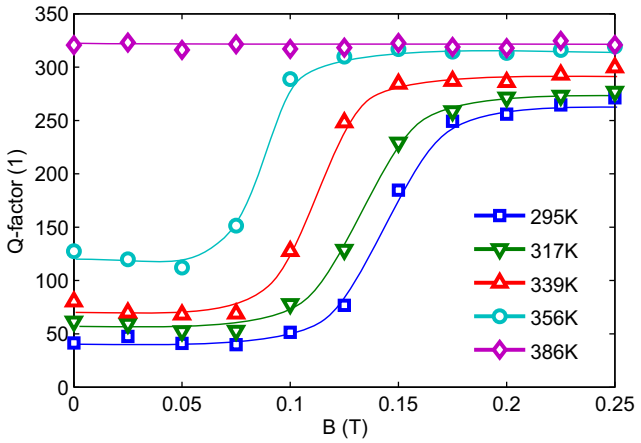

Fig. 3. Field dependencies of the quality factors of the RUS spectra at different temperatures. The solid lines are just guide for eye (data fitted by four-point Bézier curves).

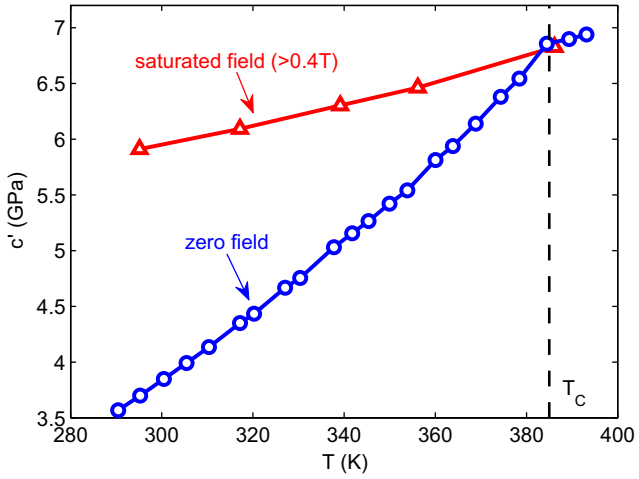

Fig. 4. Comparison of the $c'(T)$ curves in zero field and in the saturation field. T_C denotes the Curie point.

of the five highest peaks in each spectrum[2]. At the room temperature, the Q-factor increases from about 40 for the demagnetized sample (zero field) to above 250 in magnetically saturated sample. This increase is relatively high. For comparison, for a specimen of microcrystalline Ni with similar saturation magnetization and with similar dimensions as the analyzed specimen of Ni—Mn—Ga, the Q-factors obtained by the same experimental setup were about 220 in the demagnetized state and increased only to 230 in saturation. As it is also apparent from Fig. 3, the Q-factors do not follow the evolution of the c' coefficient. The field dependencies have, instead, the form of S-curves with steep increases, i.e. steep decreases of the damping, below the saturation close to the maxima of the slopes of the $c'(B)$ curves. Above the Curie point the damping is independent of the magnetic field. Below the Curie point, the damping increases with the decreasing temperature both in the zero field and in the saturated state. There is no comparable effect of the magnetic field and of the temperature on the damping observed during the pulse-echo measurements in the [1 0 0] direction. In other words, the behavior of the damping is similar to the behavior of the individual coefficients: the damping corresponding to the c' coefficient is much more dependent on the temperature and external field than the damping related to the c_{11} and c_{44} coefficients.

4. Discussion

The most important results are plotted in Fig. 4 showing temperature dependencies of the c' coefficient for zero and saturation magnetic field. Both dependencies decrease monotonously from high temperatures towards the room temperature but the softening of the zero-field coefficient is much larger. It decreases about 50% from 7 GPa at 400 K to 3.6 GPa at 290 K with a well pronounced change of the slope at the Curie point, i.e. at the onset of ferromagnetic ordering. Moreover, it is also apparent that the $\mathrm{d}c'/\mathrm{d}T$ slope for the saturation field in the whole temperature interval is approximately the same as the $\mathrm{d}c'/\mathrm{d}T$ slope for the zero field above the Curie point, where both curves coincide. This indicates that the additional softening of the c' coefficient in the demagnetized state below T_C is induced by the creation of ferromagnetic domains with different orientation of magnetization. In saturation the whole sample is in one, single domain state with homogeneous

[2] The qualities of the individual resonant peaks within any of the experimentally obtained spectra did not vary by more than 5%, which means that the resulting mean value of the Q-factor represents each individual spectrum quite accurately.

magnetization aligned along the external magnetic field and this additional softening disappears. Above the Curie point or in magnetic saturation, the dc'/dT slope is approximately 10 MPa/K, which is comparable with the effect of the shear instability of the bcc lattice observed in non-magnetic shape memory alloys [13–15]. In zero (or low) magnetic fields below the Curie point the lattice softening is fully overwhelmed by additional softening of magnitude about 25 MPa/K resulting in the total softening about 35 MPa/K.

The origin of this softening can lie in the unique magnetic properties of Ni—Mn—Ga austenite. Firstly the magnetocrystalline anisotropy K_{cr} of this material is extremely low $\sim 10^2$ J/m^3 [33,11,29]. Secondly the magnetoelastic coupling or magnetostriction is relatively high with the magnetostrictive strains $\sim 10^{-4}$ and it increases with the decreasing temperature [33,34]. Moreover, when the magnetization vector rotates between two, mutually perpendicular $\langle 1\,0\,0\rangle$ easy magnetization directions the shear induced anelastically by the magnetostriction is the same shear as the shear described by c' coefficient.

Thanks to very low magnetic anisotropy the small rotations of the magnetization vector from the easy axis are energetically inexpensive. Consequently, a significant part of any shear straining in the $\langle 1\,\bar{1},0\rangle$ direction along the $\{1\,1\,0\}$ plane can be relaxed by this magnetostrictive mechanism and does not contribute to the elastic stress response of the lattice. As a result, the ratio between the stress response of the material and strain magnitude of the lattice is lowered and the c' coefficient becomes effectively softened. Considering that the anisotropy energy induced by the ultrasonic vibrations K_σ is approximately equal to $\sigma(\mathbf{x}, t)\lambda$, where σ is the proper component of the stress tensor and λ is the magnetostriction, we can make a qualitative comparison of this energy to the energy of the magnetocrystalline anisotropy. The amplitude of σ is given by the amplitude of the corresponding shear strain ($\varepsilon \sim 10^{-6}$) multiplied by the c' coefficient of the lattice without the magneto-elastic coupling taken into account ($c' \sim 6 \times 10^9$ Pa). The stress induced anisotropy is then $K_\sigma \sim 6 \times 10^{-1}$ J/m^3. This is of the same order as the increase of the energy due to the rotation of the magnetization vector resulting in the same shear strains approximately equal to $(\varepsilon/\lambda)K_{cr}$. Thus the energy K_σ induced by the ultrasonic vibrations is relaxed by the rotation of the magnetization vector resulting in additional softening. Described magneto-elastic phenomenon is fully analogous to the so-called ΔE effect [35] observed during the tensile tests of ferromagnetic materials with low magnetic anisotropy and high magnetostriction.

The application of the external magnetic field introduces a preference of magnetization direction which results in a higher energetic penalty for vector rotation. This external constrain of magnetic field gradually suppresses the anelastic effect and results in the scaling the constant c' with the square of magnetization (Fig. 2), which is typical for magnetoelastic coupling. In the saturation the magnetization vector is fixed along the direction of the external field that prevents any anelastic shearing. Consequently only the structural softening of the lattice is observed, which continues undisturbed from above the Curie point.

Observed shear damping in the zero magnetic field and its decrease with increasing magnetic field (Fig. 3) can be attributed to the interaction of ultrasonic vibrations with the large amount of magnetic domain walls present in demagnetized specimen. According to TEM observation [36], air cooled single crystal of Ni—Mn—Ga austenite contains a dense net of anti-phase boundaries serving as pinning centers for the domain walls. Together with very low magnetic anisotropy this results in fine irregular magnetic microstructure. The application of small magnetic field leads only to the rotations of the magnetization vector (see [37] for illustrative TEM micrographs of this effect) and the number of the domain walls interacting with the ultrasonic vibrations remains approximately constant and thus the damping does not change. When the increasing magnetic field becomes strong enough to unpin the domain walls from the defects, the amount of domain walls is reduced by annihilation and the damping strongly decreases.

In our experimental study we observed a much more pronounced dependence of the c' coefficient both on the field and on the temperature in the given temperature interval than what was reported using the pulse-echo and transmission-through ultrasonic measurements [8–10,21,22]. First of all using specimens with slightly different stoichiometries may affect the magnitude of c' coefficient. Main discrepancy, however, may arise due to fact that the pulse-echo and transmission-through methods are as mentioned in experimental part, relatively rough tool for the determination of c' coefficient. Additionally due to the strong elastic anisotropy these methods are also very sensitive to the exact orientations of the specimens used in the measurements. As we have checked by a calculation, for c' equal to 3.6 GPa the pulse-echo measurements in direction declined by 5° from [1 1 0] may give the value of c' up to 5.3 GPa, which is the relative error of nearly 40%. Moreover, any deviation of the measurement direction from [1 1 0] leads to a weaker observed dependence of the measured velocity on the changes of real c' and thus to underestimating the effect. Simultaneously, the deviation from perfect orientation can affect the pulse-echo measurements of the other elastic constants (c_{11} and c_{44}), since the velocities of the ultrasonic waves in such declined directions are already influenced by the c' coefficients and therefore more sensitive to the external magnetic field.

On the other hand, the temperature dependence of the c' coefficient reported here is also significantly more pronounced than in Refs. [11,32] using the cantilever oscillation method (COM) and DMA[3] respectively. In this case, the possible reason is that the amplitude of stresses applied on the material during the DMA and COM measurements is incomparably larger than for the ultrasonic methods. Since the anelastic contribution to the shear strains is limited to the magnitude of the magnetostriction, the c' softening effect is amplitude-dependent and decrease with the increasing amplitude. This is again analogous to the amplitude-dependence of the ΔE effect. In particular, the maximum shear strains in the COM and DMA measurements are typically $\sim 10^{-3}$, which is about ten times higher than the value of magnetostriction. Therefore, the contribution of the ΔE effect is much smaller than in our ultrasonic measurements.

The experimental data presented in this paper show that the c' coefficient of the Ni—Mn—Ga austenite is anomalously softened due to a combination of structural softening, which is quantitatively comparable to the structural softening of non-magnetic shape memory alloys and the softening due to magneto-elastic coupling. The magneto-elastic part is the direct consequence of the extremely weak magnetocrystalline anisotropy of Ni—Mn—Ga austenite that enables the magnetostriction to contribute significantly to the shear strains corresponding to the c' coefficient. However, the range of strain amplitude in which this phenomenon can be observed is limited by the magnitude of the magnetostriction. Thus, the enormously strong dependence of the c' coefficient on the temperature and the external field is fully observable only by the ultrasonic methods. It might be also observed by inelastic neutron scattering, however, all reported inelastic scattering experiments were done without magnetic field.

Anomalous elastic softening and resulting very high elastic anisotropy of the ferromagnetic cubic phase of Ni—Mn—Ga is quite exceptional among known cubic materials. It might have a profound consequence for the martensitic transformation and thus for

[3] The Young's modulus in the [1 0 0] direction obtained by the DMA measurements is closely related to the c' coefficient, especially for strongly anisotropic cubic materials.

the magnetic shape memory effect. Similar detailed experimental studies for other ferromagnetic shape memory alloys would be of indubitable importance for further exploration of this phenomenon.

Acknowledgements

This work has been financially supported by the Czech Scientific Foundation under grants No. 107/10/0824, No. 101/09/0702 and No. 107/11/0391, by the institutional project of IT ASCR v.v.i. (CEZ:AV0Z20760514), and by the research center 1M06031 of the Ministry of Education of the Czech Republic.

References

[1] K. Ullakko, J.K. Huang, C. Kantner, R.C. O'Handley, V.V. Kokorin, Appl. Phys. Lett. 69 (1996) 1966–1968.
[2] O. Heczko, A. Sozinov, K. Ullakko, IEEE Trans. Magn. 36 (2000) 3266–3268.
[3] O. Soderberg, I. Aaltio, Y. Ge, O. Heczko, S.P. Hannula, Mater. Sci. Eng. A 481–482 (2008) 80–85.
[4] A.N. Vasilev, A.D. Bozhko, V.V. Khovailo, I.E. Dikshtein, V.G. Shavrov, V.D. Buchelnikov, M. Matsumoto, S. Suzuki, T. Takagi, J. Tani, Phys. Rev. B 59 (1999) 1113–1120.
[5] A. Ayuela, J. Enkovaara, R.M. Nieminen, J. Phys.: Condens. Matter 14 (2002) 5325–5336.
[6] V.V. Khovaylo, V.D. Buchelnikov, R. Kainuma, V.V. Koledov, M. Ohtsuka, V.G. Shavrov, T. Takagi, S.V. Taskaev, A.N. Vasiliev, Phys. Rev. B 72 (2005) 1–10.
[7] P. Entel, V.D. Buchelnikov, V.V. Khovailo, A.T. Zayak, W.A. Adeagbo, M.E. Gruner, H.C. Herper, E.F. Wassermann, J. Phys. D: Appl. Phys. 39 (2006) 865–889.
[8] M. Stipcich, L. Manosa, A. Planes, M. Morin, J. Zarestky, T. Lograsso, C. Stassis, Phys. Rev. B 70 (2004) 054115-1–054115-5.
[9] L. Manosa, A. Gonzalez-Comas, E. Obrado, A. Planes, V.A. Chernenko, V.V. Kokorin, E. Cesari, Phys. Rev. B 55 (1997) 11068–11071.
[10] J. Worgull, E. Petti, J. Trivisonno, Phys. Rev. B 54 (1996) 15695–15699.
[11] P. Zhao, L. Dai, J. Cullen, M. Wuttig, Metall. Mater. Trans. A 38A (2007) 745–751.
[12] A. Planes, L. Manosa, Solid State Phys. 55 (2001) 159–267.
[13] X. Ren, K. Taniwaki, K. Otsuka, T. Suzuki, K. Tanaka, Y.I. Chumlyakov, I. Yu, T. Ueki, Philos. Mag. A 79 (1999) 31–41.
[14] M. Landa, P. Sedlák, P. Šittner, H. Seiner, V. Novák, Mater. Sci. Eng. A 462 (2007) 320–324.
[15] G. Mazzolai, A. Biscarini, R. Campanella, B. Coluzzi, F.M. Mazzolai, J. Alloys Compd. 310 (2000) 318–323.
[16] U. Stuhr, P. Vorderwisch, V.V. Kokorin, P.-A. Lindgard, Phys. Rev. B 56 (1997) 14360–14365.
[17] Q.M. Hu, C.M. Li, R. Yang, S.E. Kulkova, D.I. Bazhanov, B. Johansson, L. Vitos, Phys. Rev. B 79 (2009), art. no. 144112.
[18] C. Bungaro, K.M. Rabe, A. Dal Corso, Phys. Rev. B 68 (2003) 1341041–1341049.
[19] S. Ozdemir Kart, T. Cagin, J. Alloys Compd. 508 (2010) 177–183.
[20] J.I. Pérez-Landazábal, V. Sanchéz-Alarcos, C. Góméz-Polo, V. Recarte, V.A. Chernenko, Phys. Rev. B 76 (2007) 092101-1–092101-3.
[21] A. Gonzalez-Comas, E. Obrado, L. Manosa, A. Planes, V.A. Chernenko, B.J. Hattink, A. Labarta, Phys. Rev. B 60 (1999) 7085–7090.
[22] A. Planes, E. Obrado, A. Gonzalez-Comas, L. Manosa, Phys. Rev. Lett. 79 (1997) 3926–3929.
[23] R.G. Leisure, F.A. Willis, J. Phys.: Condens. Matter 9 (1997) 6001–6029.
[24] J. Maynard, Phys. Today 46 (1996) 26–31.
[25] R.G. Leisure, K. Foster, J.E. Hightower, D.S. Agosta, Mater. Sci. Eng. A 370 (2004) 34–40.
[26] M.J.P. Musgrave, Crystal Acoustics, San Francisco, Holden-Day, 1998.
[27] J.P. Wolfe, Imaging Phonons (Acoustic Wave Propagation in Solids), Cambridge University Press, Cambridge, 1970.
[28] M. Landa, H. Seiner, P. Sedlák, L. Bicanová, J. Zídek, L. Heller, in: M. Everett, L. Pedroza (Eds.), Horizons in World Physics, vol. 268, Nova Publishers, New York, 2009, pp. 97–136.
[29] O. Heczko, J. Kopeček, D. Majtás, M. Landa, J. Phys. Conf. Ser. 303 (2011) 012081.
[30] M. Landa, P. Sedlák, H. Seiner, L. Heller, L. Bicanová, P. Šittner, V. Novák, Appl. Phys. A 96 (2009) 557–567.
[31] H. Seiner, L. Bicanová, P. Sedlák, M. Landa, L. Heller, I. Aaltio, Mater. Sci. Eng. A 521–522 (2009) 205–208.
[32] V. Chernenko, J. Pons, C. Segui, E. Cesari, Acta Mater. 50 (2002) 53–60.
[33] R. Tickle, R.D. James, J. Magn. Magn. Mater. 195 (1999) 627–638.
[34] O. Heczko, Mater. Sci. Forum 635 (2010) 125–130.
[35] S. Chikazumi, C. Graham, Physics of Magnetism, first ed., R.E. Krieger Pub, Huntington, NY, 1978.
[36] S. Venkateswaran, N. Nuhfer, M. De Graef, Acta Mater. 55 (2007) 2621–2636.
[37] Y. Murakamia, D. Shindo, K. Kobayashi, K. Oikawa, R. Kainumaa, K. Ishida, Mater. Sci. Eng. A 438–440 (2006) 1050–1053.

4.2 Publikace *Vliv antifázových rozhraní na elastické vlastnosti austenitu a premartenzitu Ni-Mn-Ga.*

Bibliografická citace: Seiner, H., Sedlák, P., Bodnárová, L., Drahokoupil, J., Kopecký, V., Kopeček, J., Landa, M., Heczko, O. The effect of antiphase boundaries on the elastic properties of Ni-Mn-Ga austenite and premartensite (2013) Journal of Physics Condensed Matter, 25 (42), art. no. 425402.

Stručná anotace: Tato publikace navazuje na publikaci uvedenou v podkapitole 4.2 tím, že jako zdroj jemné magnetické mikrostruktury indukující $\Delta E-$efekt identifikuje strukturu anti-fázových rozhraní. Je zde popsán jednak mechanismus pinningu (zachycení) doménových stěn na antifázových rozhraních, jednak mechanismus, kterým tento pinning přispívá k magnetoelastickému měknutí kubických struktur austenitu a premartenzitu a magnetoelastickému útlumu.

Příspěvek habilitanta: Habilitant kromě podílu na měření rezonanční ultrazvukovou spektroskopií a vyhodnocování dat z těchto měření (viz podíl na předchozí publikaci) přispěl zejména navržením koncepce pinningu a popisovaným strukturním modelem vlivu pinningu na elastické koeficienty.

J. Phys.: Condens. Matter **25** (2013) 425402 (10pp) doi:10.1088/0953-8984/25/42/425402

The effect of antiphase boundaries on the elastic properties of Ni–Mn–Ga austenite and premartensite

Hanuš Seiner[1], Petr Sedlák[1], Lucie Bodnárová[1], Jan Drahokoupil[2], Vít Kopecký[2], Jaromír Kopeček[2], Michal Landa[1] and Oleg Heczko[2]

[1] Institute of Thermomechanics, Academy of Sciences of the Czech Republic, Dolejškova 5, 182 00 Prague 8, Czech Republic
[2] Institute of Physics, Academy of Sciences of the Czech Republic, Na Slovance 2, 182 21 Prague 8, Czech Republic

E-mail: heczko@fzu.cz

Received 29 May 2013, in final form 14 July 2013
Published 25 September 2013
Online at stacks.iop.org/JPhysCM/25/425402

Abstract
The evolution of elastic properties with temperature and magnetic field was studied in two differently heat-treated single crystals of the Ni–Mn–Ga magnetic shape memory alloy using resonant ultrasound spectroscopy. Quenching and slow furnace cooling were used to obtain different densities of antiphase boundaries. We found that the crystals exhibited pronounced differences in the c' elastic coefficient and related shear damping in high-temperature ferromagnetic phases (austenite and premartensite). The difference can be ascribed to the formation of fine magnetic domain patterns and pinning of the magnetic domain walls on antiphase boundaries in the material with a high density of antiphase boundaries due to quenching. The fine domain pattern arising from mutual interactions between antiphase boundaries and ferromagnetic domain walls effectively reduces the magnetocrystalline anisotropy and amplifies the contribution of magnetostriction to the elastic response of the material. As a result, the anomalous elastic softening prior to martensite transformation is significantly enhanced in the quenched sample. Thus, for any comparison of experimental data and theoretical calculations the microstructural changes induced by specific heat treatment must be taken into account.

(Some figures may appear in colour only in the online journal)

1. Introduction

Martensitic transformation from cubic austenite to a low symmetry phase (martensite) is an essential condition for the existence of the magnetic shape memory (MSM) effect [1, 2]. This transformation affects the MSM materials across many spatial scales, often leading to the formation of modulated structures at the nano-scale [3–5] and of martensitic microstructures at the micro-scale [6–8]. This complexity of ferromagnetic martensites has been recently intensively studied in order to understand the origin of the MSM effect, and the mechanisms of formation of the observed hierarchical arrangements are relatively well understood [9, 10]. However, the martensitic transformation is often preceded by a so-called premartensitic phase the character of which is not clear yet and is the subject of wide discussions [11–16]. In this paper, we focus on the case of Ni–Mn–Ga, which has been the most thoroughly studied MSM alloy during the past decade, as the modulated martensite of this alloy exhibits giant magnetic field induced strain or an MSM effect [17–19]. Such unique properties of the modulated phase are motivations for a detailed analysis of the mechanisms of the martensitic transition itself, since understanding the formation of martensite from cubic austenite is a prerequisite for understanding these effects.

For the Ni–Mn–Ga alloys the premartensitic transformation appears for compositions close to stoichiometry Ni_2MnGa. The premartensite phase has a transversely modulated structure [12, 13]. As shown by Mañosa *et al* [20], the premartensitic transition is closely related to magnetoelastic coupling. Our recent ultrasound experiments [21, 22] have shown that the elasticity and ultrasound wave damping in the austenite phase prior to premartensite transformation are also strongly affected by magnetoelastic effects. Additionally, Venkateswaran *et al* and DeGraef *et al* [23, 24] recently showed that the austenite and premartensite phases of Ni–Mn–Ga contain fine magnetic domain patterns similar to the magnetic structures appearing in Ni–Mn–Ga–Al [25, 26] and other manganese-based Heusler alloys [27–29]. The origin of these fine domain structures is ascribed to mutual interaction between ferromagnetic domain walls (DWs) and antiphase boundaries (APBs). The coupling arises from the fact that the exchange interactions between the manganese atoms lying on the opposite sides of the APB can be significantly weaker than inside the ordered phase, or even turned from ferro- into antiferromagnetic [29]. Thus the APBs are energetically preferred sites for the DWs, which leads to a fine magnetic domain pattern and pinning of DWs.

According to TEM observations [23], there is a significant difference in the APB density between differently heat treated Ni–Mn–Ga alloys. In particular, according to [23] the APB density in the air-quenched material is very high with an average distance less than 50 nm, while for slowly cooled material the density of APBs is much lower. Also the recent quantitative x-ray studies [30] prove that annealing of quenched Ni–Mn–Ga leads to an increase of ordering without changing interatomic distances or bonding geometry, i.e. to a decrease of disorder defects such as APBs. This opens the question as to whether the premartensitic transition and the elastic anomalies close to this transition can be affected by different densities of the antiphase boundaries caused by different heat treatment.

In the available experimental studies of elasticity of the high-temperature phases (austenite and premartensite) of Ni–Mn–Ga [31–33], the authors always directly correlate the macroscopic elastic constants obtained by ultrasonic methods to the phonon branches, i.e. to elasticity at length-scales comparable to the unit cells. The differences between the values of the elastic constants obtained by different authors are usually ascribed solely to the differences in stoichiometry without considering the differences in the heat treatment. As shown in [23, 24] different heat treatment can lead to changes in the density of APBs and consequently to differences in the magnetic microstructure, which in turn can affect the elastic properties.

In this paper, we show that the presence of APBs affects significantly the macroscopic elasticity of austenite and premartensite of Ni–Mn–Ga. We focus on the shear elastic constant coefficient c' the softening of which is commonly understood as a precursor of the martensitic or premartensitic transformation in MSM materials. Although the elastic coefficients are commonly considered as intrinsic properties [31–33], we demonstrate that the c' coefficient is strongly affected by macroscopic properties such as the arrangement of domain walls and the presence of antiphase boundaries. Thus, we demonstrate that the results of the ultrasonic methods cannot be directly linked to the properties obtained for the given stoichiometry e.g. by *ab initio* calculations, unless additional information on the magnetic microstructure is taken into account.

2. Experiment

2.1. Materials

The material used for the experiments was a Ni–Mn–Ga single crystal grown by the Bridgman method, with stoichiometry very close to Ni_2MnGa. The material was subjected to the following heat treatment: (i) the crystal ingot was annealed at 1273 K (homogenization annealing) in an evacuated quartz ampule and then subjected to further annealing (two days at 1073 K in an argon-filled quartz ampule) followed by quenching of the whole ampule in ice water. This is an established procedure to obtain ordered Ni–Mn–Ga crystals [19]. As the ingot was in a quartz ampule, the rate of quenching was mild and comparable with the air quenching of samples used in [23]. From this quenched ingot a rectangular bar of approximately (100) orientation of faces was cut. This bar was further cut into two parts, one was left in the quenched state, and the second one was again annealed in a quartz ampule filled with argon at 1073 K for 12 h and slowly cooled in the furnace (about 24 h). These different heat treatments of otherwise identical samples were used to obtain samples with different densities of APBs [23, 24]. There should be no significant change in stoichiometry between these two materials since the annealing prior to the quenching was done under exactly the same conditions as prior to the furnace cooling and samples were cut from the same bar.

Rectangular parallelepiped-like samples for resonant ultrasound spectroscopy (RUS, [34, 35]) were prepared from these differently treated materials and characterized, prior to the RUS measurement, by x-ray and magnetization measurements. The x-ray measurements were used for the determination of the exact orientation of the samples' faces by means of the Laue method. It was verified that the samples were cut along the principal directions with a deviance smaller than 3°. The $L2_1$ ordering state of cubic austenite in the quenched and slowly cooled specimens was analyzed by x-ray diffraction using principal (400) and superstructure (111) and (200) lines. X-ray diffraction was performed using the powder diffractometer XPert Pro PANalytical equipped with a cobalt anode ($\lambda = 0.178\,901$ nm). An experimental setting with a parabolic Göeble mirror in the primary beam and a parallel plate collimator at 0.09° in the diffracted beam was chosen for better accuracy of measurements. Firstly, the crystals were oriented in the texture sample holder ATC-3 to find the strong diffractions of (400) or (220) or (111) lines. Then the 2θ scan was made. The lattice constants for the quenched and slowly cooled crystals were $a = 0.583\,04$ nm and $a = 0.583\,14$ nm, respectively determined from (h00) lines. The difference is at the edge of the measurement precision.

Table 1. Properties of the specimens used for RUS measurements (dimensions and transition temperatures).

	Dimensions (mm)			Transition temperatures (K)		
Heat treatment	d_1	d_2	d_3	T_C	T_{PM}	M_S
Quenched	4.33	4.42	5.57	385	258	220
Slowly cooled	4.06	3.30	2.09	385	256	209
Accuracy	±0.01	±0.01	±0.01	±2	±2	±2

Magnetization curves and the temperature dependence of magnetization and the initial magnetic susceptibility of these samples[3] were measured by a vibrating sample magnetometer and the AC magnetic susceptibility option in PPMS Quantum Design. The transition temperatures were determined for each material by an initial AC magnetic susceptibility measurement at a frequency of 180 Hz and an AC field of 5 Oe and were confirmed by measuring the temperature dependence of the DC magnetization at 100 Oe for the annealed sample. In table 1, the dimensions of the samples are listed together with the following transition temperatures: the Curie point T_C for the transition between paramagnetic and ferromagnetic states of the austenite phase; the T_{PM} temperature for the premartensitic transition between austenite and premartensite; and the martensite start (M_s) temperature, i.e. the temperature at which the martensitic transition starts.

2.2. RUS measurement

To determine the temperature dependence of the softest shear coefficient $c' = (c_{11} - c_{12})/2$ of both materials, two different RUS methods were used: (i) non-contact laser-based RUS with the vibrations both generated and detected by lasers (LRUS [39–41], for instrumentation details see [42]); (ii) the classical contact RUS method with the specimen clamped between two piezoelectric transducers. The non-contact modification has higher accuracy and enables better quantitative determination of the internal friction (damping) coefficients, since the quality of the obtained spectra is not affected by temperature-dependent damping of the transducers. This method was used for monitoring of the c' coefficient evolution with temperature during cooling in the temperature range between 400 K (i.e. above the Curie point) and in the vicinity of M_S for each material and in zero external magnetic field. On the other hand, the LRUS approach cannot be applied in the external magnetic field since the sample has to be fixed between the poles of the electromagnet. For this reason, the measurements in the external magnetic field (0.4 T, i.e. safely above the saturation limit) were performed by the classical contact RUS with the whole RUS apparatus placed between the poles of an electromagnet.

It was checked that at zero field the c'-s obtained by the classical RUS method did not differ by more than 0.2 GPa from the values determined by LRUS in the whole temperature range, which is less than the experimental accuracy of the contact RUS method. This proves that differences between the $c'(T)$ dependences with and without the external field reported in the next section cannot be attributed to the fact that these data were obtained by two different methods.

[3] As these samples were prepared for RUS, which demands parallelepipeds with sharp corners, the samples were not very suitable for magnetic measurements due to the large effect of the demagnetization field. In magnetically soft magnetic material, such as Ni–Mn–Ga austenite, the slope of the magnetization curve is mostly determined by the demagnetization factor. The same is valid for AC magnetic susceptibility and thus even large intrinsic changes of susceptibility cause only very small changes in the measured value.

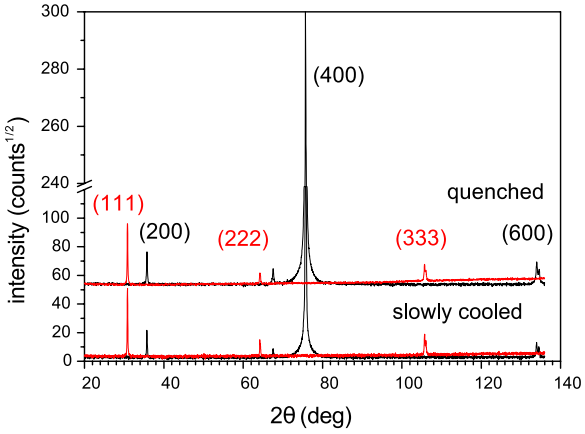

Figure 1. X-ray diffraction patterns of single-crystal Ni–Mn–Ga subjected to different heat treatment marked in the figure. The superstructure and fundamental lines are identified in the figure. The small unmarked peak close to the fundamental (400) is a residual β line. The (400) plane is approximately parallel to the surface. The different background of the x-ray pattern for the (111) line is due to the necessary tilt of the sample. The patterns of the quenched sample are shifted by 50 units to facilitate the comparison. To enhance the visibility of weak superstructure peaks, there is a break in the y-axis.

3. Results

The x-ray diffraction patterns shown in figure 1 demonstrate that there is no pronounced structural difference between the slowly cooled and quenched materials: the intensity of the superstructure peak corresponding to the $L2_1$ order (111) is high. Also another superstructure peak (200) corresponding to the B2 order is in both cases about 1–2% of the intensity of the principal peak (400). This confirms the high level of ordering for both cases. The high degree of $L2_1$ order can be expected as the B2-$L2_1$ transition can be considered as being nearly a second-order transition. The result is in good agreement with the conclusions of Chaboy *et al* [30] and shows that the annealing does not change the interatomic distances. What, however, differs is the number of APBs: as shown by Venkateswaran *et al* [23], the quenched material is supersaturated by APBs. Since there is no significant broadening of the lines of the quenched sample and the diffraction patterns are very similar for both cases, we can exclude the presence of a significant amount of internal stress in the quenched sample.

The transformation temperatures are listed in table 1. The magnetic Curie T_C temperature is unaffected by the

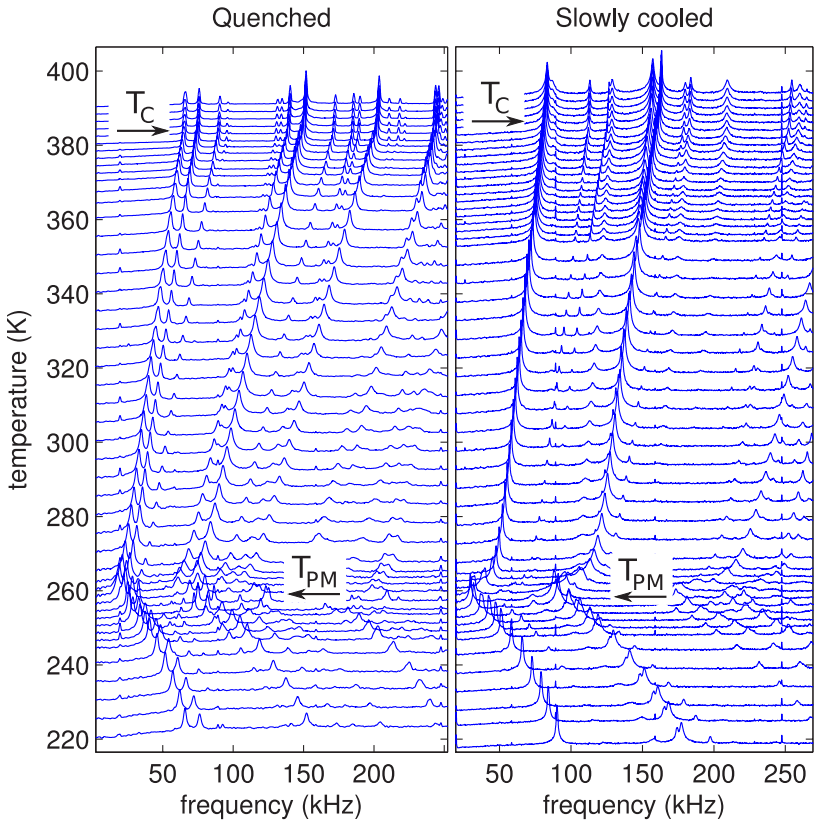

Figure 2. Evolution of LRUS resonant spectra with temperature for both materials. T_C indicates the Curie point and T_{PM} the temperature of the premartensitic transition.

heat treatment, but the martensitic start temperature M_S is shifted downwards for the slowly cooled material. A small temperature shift can be observed also for the premartensitic temperature T_{PM}, but this shift is comparable to the experimental error. The shift of the martensitic temperature can be caused by a minute change of composition due to additional annealing, nevertheless, it can be also argued that the quenched material (supersaturated by APBs) is in a less stable state with lower nucleation barriers for the transitions, and thus both the premartensitic and martensitic transitions can be initiated at higher temperatures than for the slowly cooled case. On the other hand, this observed small shift of the transition temperatures upward confirms that the degree of the $L2_1$ atomic order is not significantly decreased in the quenched sample, as already indicated by the x-ray measurements. However, according to [36], a decrease of the degree of order should lead to an decrease of the transformation temperature as it is also valid for the order–disorder transition temperature [37].

The magnetization curves of both materials indicated that the material is magnetically soft. There were no discernible differences between these magnetization curves. The saturation was reached in the field above 2000 Oe and was determined by demagnetization only, since the magnetic anisotropy of the austenite is relatively small, of the order of hundreds of J m^{-3} [38]. The magnetic hysteresis was very small, below the resolution of the magnetometer measurements, i.e. less than a few Oe for both the quenched and the slowly cooled materials. This indicates that the different density of APBs has only a negligible effect on the magnetization process.

Figure 2 shows the LRUS resonant spectra of the studied samples in the whole temperature range. These spectra were used for inverse determination of the elastic constants, i.e. for finding such elastic constants that the spectra calculated for them fit the experimentally obtained ones in some optimal way (the so-called inverse problem of RUS, see [34, 35]). The austenite phase is cubic, with three independent elastic coefficients (c_{11}, c_{12} and c_{44}). For strongly anisotropic cubic materials (anisotropy factor higher than 10, as in the case of Ni–Mn–Ga), however, the first few tens of resonant modes are sensitive only to $c' = (c_{11} - c_{12})/2$ [21]. For this reason, all spectra obtained above the T_{PM} temperature corresponded well to spectra calculated for a cubic material with rough estimates of the coefficients c_{11} and c_{44}, and finely optimized c', i.e. all these spectra enabled a relatively accurate determination of the c' coefficient.

Below T_{PM}, the situation is slightly different. The unit cell of premartensite exhibits, due to transversal modulation, a weak deviation from cubic symmetry, which should be reflected in the symmetry of the elastic properties. However, even in premartensite all the obtained spectra were acceptably well fitted under the assumption of the cubicity of the material. Indeed, it is apparent from figure 2 that the main character of the spectrum does not change significantly throughout the whole temperature interval. The reason for this is that

the sample does not transform into a single variant or large variants of premartensite, but forms, instead, some kind of self-accommodated fine microstructure (tweed), that can, for symmetry reasons, behave effectively as a cubic material, i.e. the overall cubic symmetry is retained in agreement with the observations of Kokorin *et al* [11]. Hence, we can use the cubic description throughout the whole analyzed temperature range, keeping in mind that the coefficient c' below T_{PM} represents some averaged softest shear modulus of the premartensitic microstructure.

The temperature dependences of elastic coefficient c' for quenched and slowly cooled samples in zero and saturation magnetic field are shown in figure 3. Above the Curie point (in the paramagnetic state) the value of coefficient c' is equal for all cases. This is another confirmation that there is no significant amount of internal stress in the quenched sample as this stress would affect the measured elastic coefficient. In the magnetically saturated state, the behavior of both materials (quenched and slowly cooled) is also nearly identical. The curves differ from each other within the range of the experimental error only, both exhibiting a steep decrease on cooling towards T_{PM} which is followed by a similarly steep increase in the premartensitic phase.

In the demagnetized state the $c'(T)$ curves have similar characteristics for both materials: there is a significant change of the slope at the T_C temperature, which is not observed in the magnetically saturated state, and then a continuous decrease towards the T_{PM} temperature, where both curves reach their minima. Below T_{PM}, both curves are nearly identical and steeply increase until the M_S temperature. This increase between T_{PM} and M_S is in a good agreement with the results obtained by RUS on polycrystalline Ni–Mn–Ga materials by Pérez-Landazábal *et al* [43] and by Kokorin *et al* [11] by DMA measurements. However, the behavior of $c'(T)$ differs significantly for the quenched and the slowly cooled samples in the $[T_{PM}; T_C]$ interval. For the quenched specimen, the slope of the $c'(T)$ curve is approximately constant (34 MPa K^{-1}). For the slowly cooled specimen, the slope below T_C is smaller (26 MPa K^{-1}), but increases sharply at temperature $T_0 \sim 264$ K. Then, both curves coincide close to the T_{PM}. As figure 3(b) shows in detail, the change of the slope of the $c'(T)$ curve for the slowly cooled material in saturation is at about the same temperature as the beginning of the steep decrease of c' for the slowly cooled material without field. This suggests that this material behaves identically with and without external field except for some additional softening between T_C and T_{PM}. Additionally, the curves shown in figures 3(a) and (b) demonstrate that the difference of $c'(T)$ appears only in the austenite phase but not in premartensite. This difference is of magnetoelastic origin particular to austenite, since the quenched and the slowly cooled samples behave identically above T_C in the paramagnetic state and in the magnetically saturated state. Moreover, the curves are also approximately identical in premartensite.

This is further supported by the measurement of c' as a function of magnetic field from zero to magnetic saturation. Such measurements were done in the whole temperature range, i.e. both for austenite and for premartensite, and for

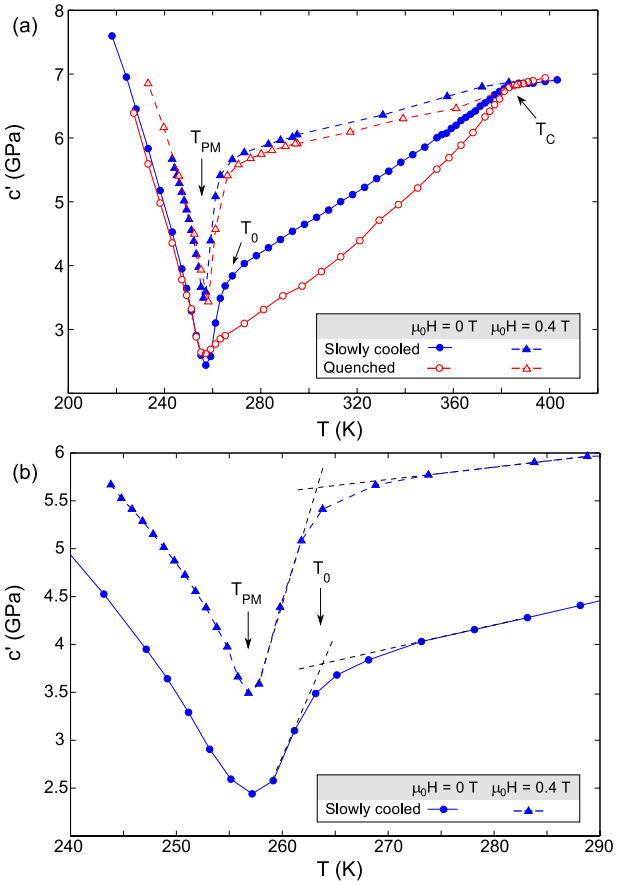

Figure 3. Temperature dependences of the c' coefficients obtained by RUS measurements without the external magnetic field (circles) and in a saturated magnetic field (triangles). Open symbols correspond to the quenched material, filled symbols to the slowly cooled one; dashed lines are used for the contact (classical) RUS measurements, solid lines for contact-less laser RUS: (a) comparison of the behaviors of the quenched and the slowly cooled materials; (b) an enlarged area of the upper subplot, showing the behavior of the slowly cooled material in the vicinity of the T_{PM} transition temperature.

both materials. The results fully confirm what was observed for the quenched material in austenite in [21, 22], i.e. that the c' coefficient increases with the square of magnetization until saturation is reached. This further confirms the magnetoelastic origin of the coupling. Additional details on the sensitivity of RUS spectra to the external magnetic fields can be found in [44].

The non-contact LRUS technique in zero magnetic field, i.e. in the demagnetized state, also enabled us to determine the damping or internal friction of the shear vibrations of both materials. The internal friction can be represented by the reciprocal of the Q-factor quantifying the quality of the RUS resonant spectra [45], i.e. by the parameter Q^{-1}. The temperature dependence of Q^{-1} for both materials is shown in figure 4: the slowly cooled material exhibits only a very weak increase of Q^{-1} below the Curie point, but there is a significant doubled attenuation peak surrounding the T_{PM} temperature for this sample.

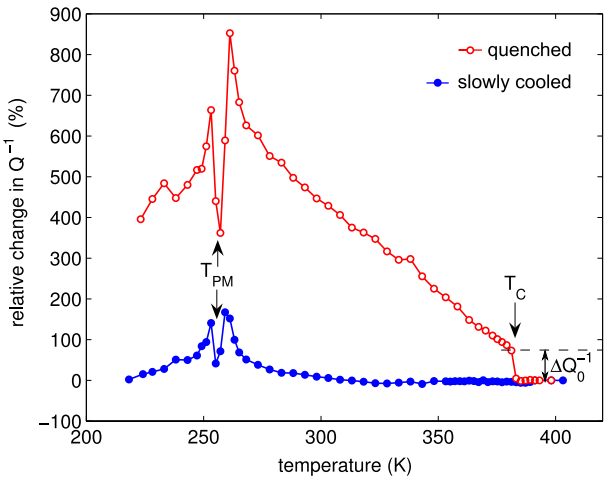

Figure 4. Temperature dependences of damping (reciprocal value of the spectrum quality Q) for both examined materials measured without magnetic field, i.e. in a demagnetized state.

For the quenched material, the situation is different. At the onset of ferromagnetic ordering (i.e. at T_C), the damping discontinuously increases by nearly 100% (denoted ΔQ_0^{-1} in figure 4). Upon further cooling, the damping increases about linearly until a pronounced doubled peak appears at around T_{PM}. Below this temperature, the damping decreases, but remains more than four times higher than for the slowly cooled material. In other words, whereas the $c'(T)$ curves for the quenched and the slowly cooled material are identical in this temperature interval, the damping is still markedly different.

4. Discussion

4.1. Additional c' softening due to fine magnetic microstructure

The microstructural origin of the observed phenomena is discussed below. The most straightforward is the interpretation of the difference between the $c'(T)$ curves between T_{PM} and T_C of quenched and slowly cooled material in zero field. We assume that the shear strains in the examined material can be decomposed as $\varepsilon = \varepsilon^\sigma + \varepsilon^{\mathbf{m}}$, where ε^σ is the elastic shearing of the lattice given by the external mechanical loads σ, and $\varepsilon^{\mathbf{m}}$ is the inelastic (magnetostrictive) deformation induced by the rotation of the magnetization vector $\mathbf{m}$. We also consider that there exists some equilibrium strain field $\varepsilon^\sigma + \varepsilon^{\mathbf{m}}$ which forms spontaneously in the demagnetized state and corresponds to some minimum of the entire free energy. Under the action of ultrasonic vibrations, this equilibrium strain field is slightly disturbed (by some $\delta\varepsilon^\sigma$ and $\delta\varepsilon^{\mathbf{m}}$), and the energy increases by some amount

$$\delta F = \tfrac{1}{2}\left[c'_{\mathrm{sat}}(\delta\varepsilon^\sigma)^2 + \gamma\,\delta\varepsilon^{\mathbf{m}}\delta\varepsilon^\sigma + R(\delta\varepsilon^{\mathbf{m}})^2\right], \qquad (1)$$

where c'_{sat} corresponds to the magnetically saturated state where no rotation of the magnetization vectors is allowed, γ is a coupling constant and R denotes the resistance of the lattice against the rotation of the magnetization vector. This resistance can be expressed as a derivative of the magnetocrystalline anisotropy energy with respect to infinitesimal rotations of the magnetization vector $\mathbf{m}$. Then, the effective c' coefficient measured by the ultrasound methods is

$$c' = 2\delta F/(\delta\varepsilon)^2 = 2\delta F/(\delta\varepsilon^\sigma + \delta\varepsilon^{\mathbf{m}})^2. \qquad (2)$$

The value of $\delta\varepsilon^{\mathbf{m}}$ is bounded from above by the magnitude of the magnetostriction ($\delta\varepsilon^{\mathbf{m}}_{\mathrm{max}}$). When the mechanical loads are small, $\delta\varepsilon^\sigma \lesssim \delta\varepsilon^{\mathbf{m}}_{\mathrm{max}}$, the material in the demagnetized state becomes effectively softened by the magnetostrictive contribution, $c' < c'_{\mathrm{sat}}$, which is the well-known ΔE-effect [46].

This ΔE-effect is additionally affected by the fine magnetic microstructure. Within the frame of a first-order linear approximation, we can assume that the coupling term can be neglected, i.e. that the elastic strains are never large enough to affect the shape of the magnetocrystalline anisotropy energy landscape and, vice versa, that the lattice still exhibits cubic symmetry of elasticity, regardless of the weak tetragonalization induced by magnetostriction. Then, since c'_{sat} is the same for both materials, it is obvious that the difference between the elasticity of the quenched and slowly cooled material must originate from the difference in the resistance against magnetization rotation R.

TEM micrographs in [23] (and similar micrographs for Ni–Mn–Ga–Al alloys in [25, 26]) clearly show that the magnetic microstructure consists not only of sharp 0°–180° DWs pinned on the APBs, but also of relatively wide 0°–90° domain walls, which are not directly pinned on APBs, but ensure the formation of the closed loops of the magnetization vectors inside the antiphase domains. The large width of the 0°–90° DWs is caused by the very low magnetocrystalline anisotropy of the material. This width is comparable to or even exceeds the distances between the individual APBs and thus the orientation of the vectors $\mathbf{m}$ varies nearly smoothly inside the antiphase domains and, consequently, only a minor part of these vectors lies in the easy {100} directions. Since the easy directions correspond to the minima of the magnetocrystalline anisotropy energy, i.e. to the directions in which the resistance of the lattice is maximal, the presence of 0°–90° DWs results in an additional decrease of the effective (averaged) value of R at the macro-scale as outlined in figure 5. Thus, the resistance against magnetization rotation $\varepsilon^{\mathbf{m}}$ decreases with the increasing density of wide 0°–90° DWs, and consequently it is significantly lower in the quenched material. This results in a strong magnetic field dependence of c' (see [21, 22]). This additional softening effect is totally wiped out in saturation, where external field keeps the magnetization vector along the field and no rotation can occur.

The measured slope $\mathrm{d}c'/\mathrm{d}T$ for the slowly cooled material (26 MPa K^{-1}) is in very good agreement with the value 27.98 ± 1.31 MPa K^{-1} obtained recently by Li *et al* [47, 48] by *ab initio* calculations. The slope for the quenched material (34 MPa K^{-1}) on the other hand cannot be directly compared to the results of [47, 48], since this slope comprises both

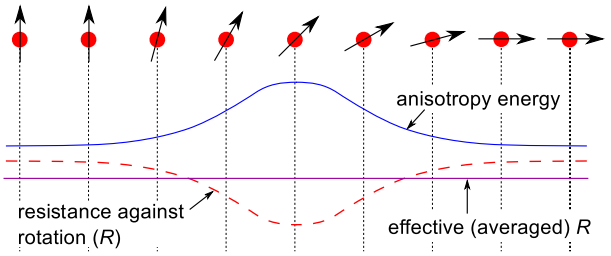

Figure 5. Decrease of the effective resistance R due to a 0°–90° DW.

the magnetoelastic softening at the atomistic length-scales (obtainable by *ab initio* calculations) and the additional softening effect due to specific magnetic microstructure.

Below T_0, the material becomes significantly elastically softened. The resistance of the lattice to ε^{σ} strongly decreases due to the vicinity of the T_{PM} transition temperature. The third term R is also affected by transition and may become less important as the austenite-to-premartensite transition at T_{PM} changes the character of the material. The premartensite phase exhibits modulated microstructure with a tweed pattern [14] which affects the magnetic domain structure [49, 24] due to strong magnetoelastic coupling, resulting in the so-called magnetoelastic tweed. The presence of such a tweed can result in an increase of local magnetic anisotropy and thus a decrease of magnetoelastic softening. The sudden drop of AC susceptibility at T_{PM} [20, 41] (as shown also in figure 6 and will be discussed later in detail) indicates a relatively large increase of magnetic anisotropy. Additionally the increase of magnetic anisotropy is indirectly indicated by a shift of transitional temperature in magnetic field [50]. Thus it is probable that although this tweed microstructure is still correlated with the APBs (see [24]), the original magnetic microstructure with wide 0°–90° DWs is completely overridden, and the difference of R for the quenched and the slowly cooled material fully disappears.

The effect of magnetic field is lowered in the premartensite phase and it is similar for both materials. The reason for this decrease can be inferred from the behavior of AC susceptibility in the vicinity of the premartensitic transition temperature (figure 6). On cooling, the susceptibility exhibits a sharp, localized dip at T_{PM}, and although it partially recovers in premartensite, the difference between its values above and below this drop is still significant[4]. Such a decrease of susceptibility indicates the significant increase of magnetocrystalline anisotropy in premartensite resulting in the thinning of the 0°–90° DWs

[4] Although the susceptibility changes seem to be small, it must be taken into account that the measured susceptibility is strongly affected by demagnetization, since the slope of the magnetization curve is predominantly determined by the demagnetization factor, which is a consequence of small magnetocrystalline anisotropy. Thus, the observed susceptibility evolution with temperature can be taken only as a qualitative indicator and cannot be taken quantitatively for an estimation of magnetic anisotropy changes. By a simple calculation using the demagnetization factor of a cube and estimated low magnetic anisotropy of austenite, it was checked that an increase of magnetocrystalline anisotropy by one order of magnitude results in a susceptibility change of only a few per cent.

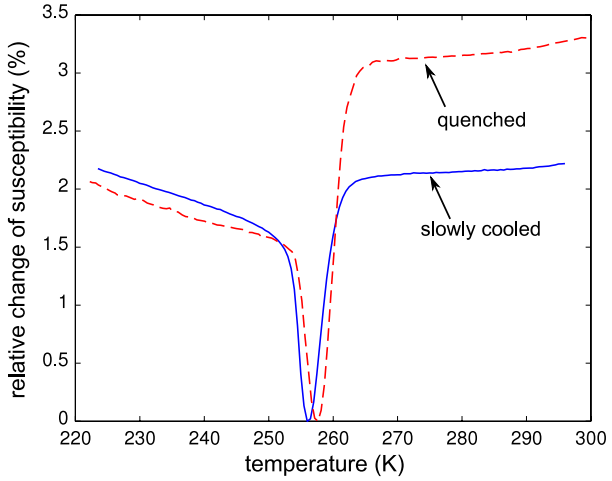

Figure 6. Temperature dependences of the AC initial magnetic susceptibility (at 4 Oe) for the quenched and the slowly cooled material, normalized with respect to the minimal value (i.e. to the value at T_{PM}).

and consequently the increase of R and the smaller effect of magnetic field on c' below T_{PM}.

The application of the external field led to elastic hardening of both materials in the whole temperature range except for the paramagnetic state above T_C (figure 3) where no effect occurred. In contrast to the experiment, Bar'yakhtar *et al* [51] have shown by a theoretical calculation that the external magnetic field can also induce softening in c'. This effect is expected for the external field aligned with the [110] direction and at ultrasonic frequencies above 100 MHz where the elastic waves start to couple with the spin waves. In the RUS measurements with all frequencies analyzed being below 1 MHz, the external magnetic field only prevents the rotation of the magnetization vector. And thus, the application of the external field should always lead to elastic hardening of c' due to suppression of $\varepsilon^{\mathbf{m}}$, regardless of the direction of the field.

4.2. Damping peaks in the vicinity of the premartensitic transition temperature

To discuss the damping $Q^{-1}(T)$ in zero magnetic field, three mechanisms contributing to the attenuation in the material can be considered: (i) multiple-scattering effects due to heterogeneity caused by the magnetic microstructure, i.e. scattering on magnetic domain walls; (ii) dissipation due to inelastic strains $\varepsilon^{\mathbf{m}}$; (iii) criticality close to the premartensitic transition. The quenched material exhibits a sudden increase of ΔQ_0^{-1} at the T_C temperature followed by a nearly linear increase. Since there is no discontinuous jump in c' at T_C, the effect of inelastic strains $\varepsilon^{\mathbf{m}}$ goes to zero close to the Curie point. This is a consequence of vanishing magnetoelastic coupling close to the Curie point. Hence, the observed jump ΔQ_0^{-1} is related to a different damping mechanism than the subsequent increase of Q^{-1} upon further cooling. The jump of the damping at the Curie point indicates the creation of the scattering centers due to the formation of a high density of DWs pinned on APBs.

Then, with the increasing magnetostriction [38], the inelastic strain $\varepsilon^{\mathbf{m}}$ increases, which leads to a continuous increase of the damping between T_C and T_{PM}.

In the vicinity of T_{PM}, the magnetoelastic damping superposes with the criticality damping common for both materials. The splitting of the criticality peak into two distinct peaks can be related to anomalous structural and magnetic changes close to the premartensitic transition. The most apparent change is in the behavior of magnetic susceptibility in this temperature region, as shown in figure 6. The curves for both materials exhibit a sharp dip at the transition temperature. The magnitude of this dip is only 3% or less of the absolute value but this small decrease represents relatively strong changes of intrinsic susceptibility of the material (see footnote 4). This indicates that there is a sharply localized increase of magnetocrystalline anisotropy close to T_{PM}. This prevents the magnetization vectors from rotating from the easy axis and results in a localized decrease of magnetoelastic damping. Similar splitting of the damping peak close to T_{PM} can also be seen in the results of the cantilever oscillation method (COM) by Zhao *et al* [33] (figure 3 in this reference[5]). Ludwig *et al* [52] reported a split peak in acoustic emission activity during premartensitic transition. In the RUS measurements of polycrystalline Ni–Mn–Ga by Peréz-Landazábal *et al* [43], however, only a single damping peak at T_{PM} was observed. This can be attributed to the fact that the internal stresses and intergranular geometric constraints result in slightly different T_{PM} temperatures in different grains (a high sensitivity of the T_{PM} temperature was reported by González-Comas *et al* [53]), which may lead to blurring of the doubled peak.

Furthermore, the observed dip in the susceptibility is not common. When a material transforms from one phase into another with different magnetic properties, the values of susceptibility within the transition region can be expected to fall between the respective values for these two phases, following the rule of mixtures. This is a normal situation, e.g. a sharp and monotonous drop of susceptibility is observed in the austenite–martensite transformation of Ni–Mn–Ga without premartensite [18]. Here, however, the transition (upon cooling) seems to be composed of two consecutive processes: the first leading to a decrease of susceptibility (stronger for the quenched material and weaker for the slowly cooled one) and the second leading to its partial recovery. This may indicate that the first process is the premartensitic transition itself, during which the magnetocrystalline anisotropy of a unit cell increases, but without changing the DWs pinned on APBs. However, due to higher anisotropy, the 0°–90° DWs inside the antiphase domains become narrowed and the difference between the quenched and the slowly cooled material disappears. Then, the second process, the reconfiguration of the DWs, probably still interacting with the APBs, takes place due to the formation of the magnetoelastic tweed. In such an interpretation, each of the two peaks observed on the Q^{-1} curve can be ascribed to one of these processes. This is in agreement with the fact that the maxima of the peaks approximately correspond to the maximal slopes of the susceptibility curves. In addition, while for the slowly cooled material these two peaks are of similar heights, for the quenched material the peak above T_{PM} is significantly higher. This again well corresponds to the susceptibility curves. The dip in the vicinity of T_{PM} is much more asymmetric for the quenched material with a stronger decrease above T_{PM}. Lastly, the assumption that the two damping peaks surrounding the T_{PM} temperature correspond to two different processes is also in agreement with the $c'(T)$ curves obtained in the saturation magnetic field (and also the one obtained for the slowly cooled material in zero field). The damping peak above T_{PM} corresponds well by its position and width to the $[T_{PM}; T_0]$ interval, where the $\mathrm{d}c'(T)/\mathrm{dT}$ slope steeply increases. In contrast, for the damping peak below T_{PM} no such well-defined temperature interval is apparent on the $c'(T)$ curve increasing monotonously towards M_S. This may indicate that the damping process above T_{PM} is related to phonon softening and changes of the unit cell, while the process below T_{PM} may reflect only some additional reconfiguration of the magnetic microstructure.

What remains open is the question of why the damping in premartensite, i.e. below T_{PM}, differs for the slowly cooled and the quenched material in contrast with the nearly identical behaviors of the c' coefficient. The most plausible explanation is that the APBs still affect the resulting microstructure of premartensite, e.g. by increasing the number of magnetic domain walls, which increases the scattering of the ultrasonic waves. With increasing stiffening of the c' coefficient, this mechanism becomes less efficient and the damping decreases. On the other hand, if, as discussed above, the second peak is due to the formation of the magnetoelastic tweed within the net of APBs, it is also possible that this formation is not fully completed in the vicinity of T_{PM}, but partially continues upon further cooling. Then, for the quenched material with high density of APBs, the corresponding damping peak could be spread in the whole temperature interval between T_{PM} and M_S.

5. Conclusion

We showed that high concentration of APBs has a significant impact on macroscopic shear elasticity in Ni–Mn–Ga austenite. When comparing the $c'(T)$ dependence for the quenched material and for the slowly cooled material with the same stoichiometry but lower density of APBs, the difference becomes clear: whereas both materials behave identically in saturated external magnetic field, the magnetoelastic softening in the demagnetized state is much more pronounced for the quenched material. The difference is the consequence of fine magnetic microstructure induced in the quenched material by the formation and pinning of domain walls on APBs.

[5] Unlike what has been reported in [33], we did not observe any damping peak close to the Curie point. One of the possible explanations is that the relaxation damping associated with the magnetic transition is dependent on frequency and/or amplitude; the used frequencies differ by two orders ($\leq$1 kHz for COM and $\geq$0.1 MHz for RUS) and the amplitudes by three orders (10^{-3} for COM and 10^{-6} for RUS). On the other hand, it can be concluded that the splitting of the damping peak is observable in a wide range of frequencies and amplitudes.

The main conclusion is that the macroscopically obtained elastic constants of Ni–Mn–Ga austenite and possibly also other ordered (Heusler) alloys with strong magnetoelastic coupling cannot be directly linked to *ab initio* predictions without considering thermal treatment, since the magnetoelastic softening depends on the resulting microstructure. The magnetoelastic softening is apparently enhanced by high density of APBs. In contrast, the possible presence of the internal stresses due to quenching would results in an increase of magnetocrystalline anisotropy and thus in a decrease of magnetoelastic softening. This conclusion is supported by the fact that only for the slowly cooled material the experimentally determined dc'/dT slope is in good agreement with the recent first-principles calculations [47, 48].

Surprisingly, this relatively strong contribution of the magnetic microstructure to the c'-softening of the quenched material fully disappears below the premartensitic transition temperature. In contrast, the damping behavior still exhibits strong differences below T_{PM}. To discuss the origin of this difference in more detail it would be necessary to analyze the relations between the magnetoelastic tweed microstructure of premartensite and the microstructure of APBs, which falls beyond the scope of this paper. Nevertheless, from changes of c' in magnetic field it is clear that in premartensite the magnetic microstructure also has some non-negligible impact on the macroscopic (effective) behavior of Ni–Mn–Ga single crystal.

Acknowledgments

We thank professor S Fähler (IFW Dresden) for critical reading of the manuscript and for his helpful advice about the text. This work has been financially supported by the Czech Science Foundation grants Nos P107/11/0391, 101/09/0702, and by the Grant Agency of the Academy of Sciences of the Czech Republic, project No. M100761203.

References

[1] Chernenko V A and Lvov V A 2008 *Mater. Sci. Forum* **583** 1
[2] Mañosa L and Planes A 2000 *Adv. Solid State Phys.* **40** 361–74
[3] Pons J *et al* 2000 *Acta Mater.* **48** 3027
[4] Khachaturyan A G, Shapiro S M and Semenovskaya S 1991 *Phys. Rev.* B **43** 10832
[5] Kaufmann S, Rößler U K, Heczko O, Wuttig M, Buschbeck J, Schultz L and Fähler S 2010 *Phys. Rev. Lett.* **104** 145702
[6] Straka L, Heczko O, Seiner H, Lanska N, Drahokoupil J, Soroka A, Fähler S, Hänninen H and Sozinov A 2011 *Acta Mater.* **59** 7450
[7] Heczko O, Straka L and Seiner H 2013 *Acta Mater.* **61** 622
[8] Heczko O, Kopeček J, Straka L and Seiner H 2013 *Mater. Res. Bull.* at press
[9] Diestel A, Backen A, Rößler U K, Schultz L and Fähler S 2011 *Appl. Phys. Lett.* **99** 092512
[10] Niemann R, Rößler U K, Gruner M E, Heczko O, Schultz L and Fähler S 2012 *Adv. Eng. Mater.* **14** 562
[11] Kokorin V V, Shapiro S M, Wochner P, Schwartz A, Wall M and Tanner L E 1996 *J. Phys.: Condens. Matter* **8** 6457
[12] Brown P J, Crangle J, Kanomata T, Matsumoto M, Neumann K-U, Ouladdiaf B and Ziebeck K R A 2002 *J. Phys.: Condens. Matter* **14** 10159
[13] Singh S *et al* 2013 *J. Phys.: Condens. Matter* **25** 212203
[14] Zheludev A, Shapiro S M, Wochner P, Schwartz A, Wall M and Tanner L E 1995 *Phys. Rev.* B **51** 11310
[15] Entel P V, Buchelnikov D, Khovailo V V, Zayak A T, Adeagbo W A, Gruner M E, Herper H C and Wassermann E F 2006 *J. Phys. D: Appl. Phys.* **39** 865
[16] Chernenko V A, Pons J, Seguí C and Cesari E 2002 *Acta Mater.* **50** 53
[17] Ullakko K, Huang J K, Kantner C, O'Handley R C and Kokorin V V 1996 *Appl. Phys. Lett.* **69** 1966
[18] Heczko O, Sozinov A and Ullakko K 2000 *IEEE Trans. Magn.* **36** 3266
[19] Soderberg O, Aaltio I, Ge Y, Heczko O and Hannula S P 2008 *Mater. Sci. Eng.* A **481/482** 80
[20] Mañosa L, Gonzàlez-Comas A, Obradó E, Planes A, Chernenko V A, Kokorin V V and Cesari E 1997 *Phys. Rev.* B **55** 11068
[21] Seiner H, Heczko O, Sedlák P, Bodnárová L, Novotný M, Kopeček J and Landa M 2013 *J. Alloys Compounds* at press
[22] Heczko O, Seiner H, Sedlák P, Kopeček J and Landa M 2012 *J. Appl. Phys.* **111** 07A929
[23] Venkateswaran S P, Nuhfer N T and De Graef M 2007 *Acta Mater.* **55** 2621
[24] De Graef M 2009 *ESOMAT 2009: 8th Eur. Symp. on Martensitic Transformations (Prague)* ed P Šittner *et al* (Paris: EDP Sciences) 01002
[25] Murakami Y, Shindo D, Kobayashi K, Oikawa K, Kainuma R and Ishida K 2006 *Mater. Sci. Eng.* A **438–440** 1050
[26] Umetsu R Y, Ishikawa H, Kobayashi K, Fujita A, Ishida K and Kainuma R 2011 *Scr. Mater.* **65** 41
[27] Jakubovics J P and Baker G S 1971 *J. Phys. (Paris)* **32** C1–259
[28] Lapworth A J and Jakubovics J P 1974 *Phil. Mag.* **29** 253
[29] Young A P and Jakubovics J P 1975 *J. Phys. F: Met. Phys.* **5** 1866
[30] Chaboy J, Lázpita P, Barandiarán J M, Gutiérrez J, Fernández-Gubieda M L and Kawamura N 2009 *J. Phys.: Condens. Matter* **21** 016002
[31] Worgull J, Petti E and Trivisonno J 1996 *Phys. Rev.* B **54** 15695
[32] Stipcich M, Mañosa L, Planes A, Morin M, Zarestky J, Lograsso T and Stassis C 2004 *Phys. Rev.* B **70** 054115
[33] Zhao P, Dai L, Cullen J and Wuttig M 2007 *Metall. Mater. Trans.* A **38A** 745
[34] Leisure R G and Willis F A 1997 *J. Phys.: Condens. Matter* **9** 6001
[35] Maynard J 1996 *Phys. Today* **49** 26
[36] Sánchez-Alarcos V, Pérez-Landazábal J I, Recarte V, Rodríguez-Velamazán J A and Chernenko V A 2010 *J. Phys.: Condens. Matter* **22** 166001
[37] Overholser R W, Wuttig M and Neumann D A 1999 *Scr. Mater.* **40** 1095
[38] Heczko O, Kopeček J, Majtás D and Landa M 2011 *J. Phys.: Conf. Ser.* **303** 012081
[39] Reese S J, Telschow K L, Lillo T M and Hurley D H 2008 *IEEE Trans. Ultrason. Ferroelectr. Freq. Control* **55** 770
[40] Hurley D H, Reese S J and Farzbod F 2012 *J. Appl. Phys.* **111** 053527
[41] Seiner H, Bicanová L, Sedlák P, Landa M, Heller L and Aaltio I 2009 *Mater. Sci. Eng.* A **521/522** 205
[42] Sedlák P, Landa M, Seiner H, Bicanová L and Heller L 2008 *Proc. 1st Int. Symp. on Laser Ultrasonics: Science, Technology and Applications (Montreal, 2008)* 34 (www.ndt.net)
[43] Pérez-Landazábal J I, Sanchéz-Alarcos V, Goméz-Polo C, Recarte V and Chernenko V A 2007 *Phys. Rev.* B **76** 092101
[44] Heczko O, Seiner H, Sedlak P, Kopeček J, Kopecký V and Landa M 2013 *Eur. Phys. J.* B **86** 62
[45] Leisure R G, Foster K, Hightower J E and Agosta D S 2004 *Mater. Sci. Eng.* A **370** 34

[46] Chikazumi S and Graham C 1978 *Physics of Magnetism* (Huntington, NY: Krieger)
[47] Li C M, Luo H B, Hu Q M, Yang R, Johansson B and Vitos L 2011 *Phys. Rev.* B **84** 174117
[48] Li C M, Hu Q M, Yang R, Johansson B and Vitos L 2011 *Appl. Phys. Lett.* **98** 261903
[49] Saxena A, Castan T, Planes A, Porta M, Kishi Y, Lograsso T A, Viehland D, Wuttig M and De Graef M 2004 *Phys. Rev. Lett.* **92** 197203
[50] Barandiaran J M, Chernenko V A, Lazpita P, Gutierrez J and Orue I 2009 *Appl. Phys. Lett.* **94** 051909
[51] Bar'yakhtar V G, Danilevich A G and L'vov V A 2011 *Phys. Rev.* B **84** 134304
[52] Ludwig B, Strothkaemper C, Klemradt U, Moya X, Mañosa L, Vives E and Planes A 2009 *Phys. Rev.* B **80** 144102
[53] Gonzàlez-Comas A, Obrado E, Mañosa Ll, Planes A, Chernenko V A, Hattink B J and Labarta A 1999 *Phys. Rev.* B **60** 7085

4.3 Publikace *Elasticita a magnetické vlastnosti premartenzitického tweedu v Ni-Mn-Ga.*

Bibliografická citace: Seiner, H., Kopecký, V., Landa, M., Heczko, O. Elasticity and magnetism of Ni2MnGa premartensitic tweed (2014) Physica Status Solidi (B) Basic Research, 251, pp. 2097-2103.

Stručná anotace: Publikace se zaměřuje na elasticitu a magnetické vlastnosti premartenzitické fáze slitiny Ni-Mn-Ga s tweedovou mikrostrukturou a pomocí dvojdimenzionálního mikrostrukturního modelu ukazuje, že experimentálně pozorované měknutí elastické konstanty c_{44} může být způsobeno spojitou změnou tetragonality mřížky a následnými změnami v geometrii tweedu. Zároveň je ukázáno, že tyto změny nemohou indukovat experimentálně pozorovaný nárůst elastického koeficientu c', což prokazuje, že anomální fononová větev TA_2 se v premartenzitické fázi stabilizuje a její měknutí tedy nemůže být prekurzorem transformace premartenzit $\rightarrow$ austenit.

Příspěvek habilitanta: Habilitant přispěl především návrhem a numerickou implementací dvojdimenzionálního modelu tweedové mikrostruktury a výpočtem souvisejících vývojů elastických konstant c_{44} a c' s tetragonalizací elementární buňky.

Phys. Status Solidi B **251**, No. 10, 2097–2103 (2014) / **DOI** 10.1002/pssb.201350415

Part of Special Issue on
Ferroic Glasses: Magnetic, Polar and Strain Glass

physica status solidi b
www.pss-b.com
basic solid state physics

Elasticity and magnetism of Ni_2MnGa premartensitic tweed

Hanuš Seiner[1], Vít Kopecký[2], Michal Landa[1], and Oleg Heczko[*,2]

[1] Institute of Thermomechanics, Academy of Sciences of the Czech Republic, Dolejškova 5, 182 00 Prague 8, Czech Republic
[2] Institute of Physics, Academy of Sciences of the Czech Republic, Na Slovance 2, 182 21 Prague 8, Czech Republic

Received 20 December 2013, revised 12 March 2014, accepted 17 March 2014
Published online 25 April 2014

Keywords magneto-elastic coupling, Ni–Mn–Ga, premartensite, tweed microstructure

[*] Corresponding author: e-mail heczko@fzu.cz, Phone: +420 266 052 714, Fax: +420 286 890 527

Magnetic, magneto-elastic and elastic measurements were used to characterize the thermal evolution of the premartensite phase of Ni_2MnGa. The premartensitic transition is shown to correspond to a sharp maximum of magnetostriction and a pronounced minimum of the (110) $\langle 1\bar{1}0\rangle$ shear stiffness (the c' elastic coefficient); no additional softening of the c' coefficient prior to the martensitic transformation was observed. In contrast, a significant softening of the (100) $\langle 010\rangle$ stiffness (the c_{44} elastic coefficient) was observed in the vicinity of the martensitic transition, while this coefficient is fully unaffected by the premartensitic transition. A simple two-dimensional model of the tweed is presented to explain this mutual independence between the c' and c_{44} shears and the effect of tweed formation on both of them.

1 Introduction Heusler alloys based on the Ni–Mn–Ga system are the main class of materials exhibiting the magnetic shape memory effect. The essential condition for this effect is a martensitic transformation from a cubic phase (austenite) to a low symmetry phase (martensite). The temperature of the martensitic transformation is very sensitive to the ratio of constitutive elements; for ordered compounds close to stoichiometry (Ni_2MnGa), this transition is preceded by a so-called premartensitic transition. The premartensitic transition is weakly first-order and originates from softening of the c' elastic coefficient [1, 2] corresponding to a minimum on the slowest transversal phonon branch [3–5]. At the transition the material exhibits some kind of anomaly in the elastic [2, 6], thermal [1], electric [7], and magnetic properties [8, 9].

Macroscopically the premartensite phase of Ni_2MnGa keeps an overall cubic symmetry [10, 11] of the parent L21 phase; however, high resolution electron microscopy showed that the premartensite contains a very fine mixture of variously oriented spontaneous strain states on the scale of nanometers [3]. This makes the character of Ni–Mn–Ga premartensite superficially similar to the strain-glass phases reported for the NiTi alloy [10, 12]. The strain glass is assumed to be formed due to high structural disorder [13]. However, in Ni–Mn–Ga the tweed is formed only close to stoichiometry, i.e., in the compound where the structural disorder is expected to be minimal. Moreover, unlike what is commonly understood for the glassy states, the spontaneous strains in premartensite are not fully randomly oriented. Instead, they form fine, locally regular patterns called tweeds. As all possible orientations of the spontaneous strains are equivalently distributed over the tweed, the premartensitic phase exhibits averaged cubic symmetry, which is reflected both in the structural and mechanical properties. The observed cubic structure suggests that the tweed domains are smaller than coherent length of the X-ray structural method. Despite of the overall cubic symmetry, high resolution synchrotron X-ray diffraction [11] shows that the premartensite phase/tweed exhibits the modulation or shuffling with approximate wave vector [1/3, 1/3, 0]. There is a discussion whether this modulation is commensurate [11] or incommensurate [14], but it does not change the overall picture that the premartensite can be considered as consisting of fine (approximate) 6 M modulated phase with all possible modulation directions randomly distributed, or, equivalently, as adaptive phase with $(2\bar{1})_2$ shuffling period [15, 16].

Recent X-ray diffraction experiments [11] prove that the tweed microstructure of premartensite can be at least partially reoriented by mechanical loading. However, further increase of the load results in transformation into 10 M martensite. This may indicate that either the internal interfaces in the premartensitic tweed are relatively rigid (and, thus, the martensitic transition is induced earlier than the

reorientation is finished), or that the premartensite consists of the same or similar basic building blocks as the martensite itself, as it is assumed in adaptive concept with $(2\bar{1})_2$ stacking.

Since the elasticity of the Ni–Mn–Ga austenite and premartensite is strongly coupled with magnetism, the term magneto-elastic tweed is often used to emphasize the fact that the fine, tweed-like pattern can be observed not only in the spontaneous strains, but also in the orientation of the magnetization vector [2, 17]. Due to this strong coupling it can be expected that the formation of the tweed during the premartensitic transition is reflected in the changes of magnetic microstructure. However, the magnetic properties of austenite and premartensite are quite similar and hard to distinguish. On the other hand the detailed investigation of the evolution of elastic constants in magnetic field and temperature in austenite and premartensite reveals that elastic coefficient c', instrumental for premartensite transformation, is strongly dependent on magnetic field particularly in austenite phase [6, 19–21]. The c' scales with square of magnetization revealing strong magnetoelastic coupling. Large c' softening in austenite is due to vanishing magnetic anisotropy and relatively large magnetostriction. Moreover, the field dependence of c' is also strongly affected by heat treatment, which was explained by the high concentration of antiphase boundaries [18].

The effect of magnetic field is weakened in the premartensite [20]. Additionally we observed that the effect of heat treatment in premartensite is nearly negligible [18]. In agreement with consideration that c' softening is *prime facie* evidence for premartensitic transformation, this coefficient exhibits a minimum at the premartensite transformation temperature. In premartensite the coefficient steeply increases with decreasing temperature [6, 18]. In the vicinity of the martensitic transformation temperature it reaches the value which is comparable to its value at one hundred degrees above the premartensitic transformation. This opens the question if there is any precursor phenomenon preceding the martensitic transformation itself, since it is not the c' which increases toward it. To answer this question is the main aim of this paper. We examine the magnetic and elastic properties of premartensite and their evolution with temperature toward the martensitic transition. As shown in this paper, the observed behaviors cannot be directly explained without taking the fine tweed-like microstructure of premartensite into account; on this purpose, we build a simplified two-dimensional model of the tweed enabling a deeper insight into micromechanics of such microstructure.

2 Experimental The sample used for the experiments was a $4.4\times4.3\times5.6\,\mathrm{mm}^3$ prismatic bar of nearly stoichiometric Ni_2MnGa cut along the principal $\{100\}$ planes of the parent austenite phase. Possible misalignment and the mosaicity of single crystal was checked by X-ray diffraction. The temperature dependence of AC magnetic susceptibility was used to determine the premartensitic transition temperature $T_{PM} = (258 \pm 2)$ K, the martensite start temperature $M_S = (220 \pm 2)$ K, and the Curie point $T_C = 383$ K. Upon cooling, the premartensite phase was stable between the T_{PM} and M_S temperatures, i.e., in a temperature interval of nearly 40 K. In attempt to understand the details of the structural and magnetic changes accompanying the premartensitic transition we measured AC magnetic susceptibility, magnetization curves up to 5 T and magnetostriction. In addition, we measured dilatation in zero field. Magnetic properties in this interval were measured by vibrating sample magnetometer Cryogenic and the linear expansion with temperature and striction in magnetic field up to 1 T by a custom-made dilatometer in PPMS.

For evaluation of elastic properties, the premartensitic microstructure formed from cubic austenite at T_{PM} was considered as macroscopically cubic, i.e., following the symmetry of the parent phase. This leaves only three independent elastic constants: (i) the longitudinal elastic constant c_{11}; (ii) the hard shear modulus c_{44} related to basal (100) $\langle 010\rangle$ shears; (iii) the soft modulus $c' = (c_{11} - c_{12})/2$ related to the diagonal (110) $\langle 1\bar{1}0\rangle$ shears, where the shearing directions are meant with respect to the cubic lattice of austenite. To obtain these elastic constants in reasonable precision two different ultrasonic methods were used in the investigated temperature range. The c_{11} and c_{44} constants were measured by a conventional pulse-echo method, i.e., from times-of-flight of ultrasonic longitudinal and shear waves, respectively, between the largest faces of the sample. As the pulse-echo method is less suitable for the determination of the c' coefficient particularly for material with large elastic anisotropy, this shear modulus was measured by resonant ultrasound spectroscopy (RUS), see [6, 18, 19, 22] for more details on these measurements. To determine the effect of the magnetic field, the soft (i.e., in demagnetized state) and hard c' elastic modulus (i.e., in magnetic saturation [23]) were measured at zero field and at field of 0.4 T, which is above magnetic saturation of the sample [6].

3 Results

3.1 Magnetic measurements The result of dilatation measurements in zero field is seen in Fig. 1(a); the dilatation is linear with temperature and it exhibits a localized dip at the premartensite transition. This anomaly suggests the volume changes of about 0.1% upon transition. The dilatation has visibly different slopes and linear expansion coefficient changes from about 17×10^{-6} in austenite to 13×10^{-6} in premartensite.

Similarly the magnetic susceptibility exhibits the minimum at T_{PM} and then close to M_S it increases to value even higher than at room temperature. This was also confirmed by measurement of magnetization loops which shows only tiny change upon the transformation. Far from T_{PM} the curves in premartensite and austenite are undistinguishable within the measurement error. In contrast with Barandian et al. [8] we did not observe significant differences between the magnetization curves. Previously observed changes might be ascribed to vicinity of martensitic transformation and possible structure reorientation. As shown and discussed by Seiner

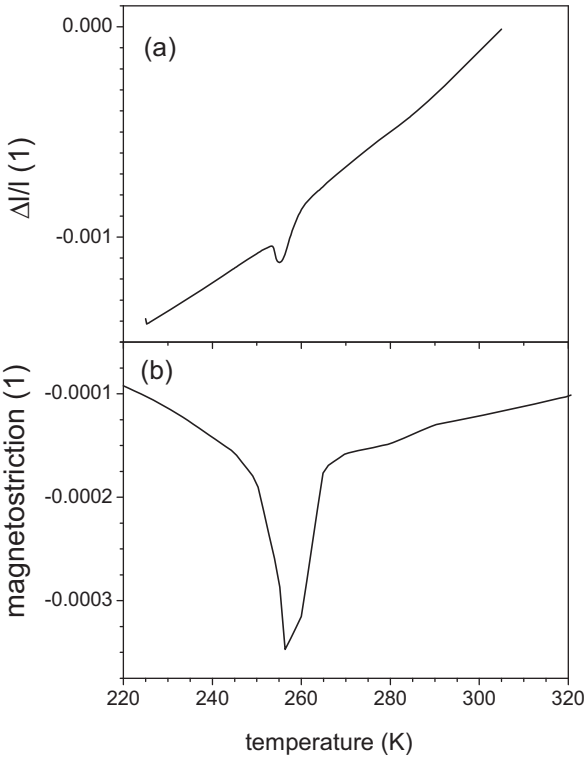

Figure 1 (a) Dilatation in austenite and premartensite measured during cooling. (b) Saturation magnetostriction λ_{100} measured in [100] direction along the field. The magnitude of magnetostriction is determined from field dependence of striction measured from 220 to 340 K.

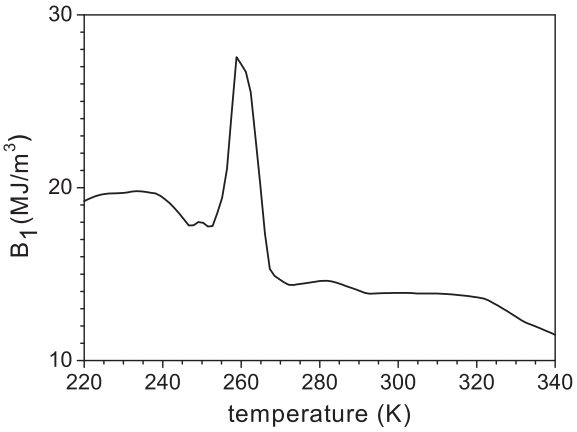

Figure 2 Magneto-elastic coupling constant B_1 obtained from measured magnetostriction and shear elastic constant c' measured at zero magnetic field.

et al. [18] the susceptibility dip (which is similar to dilation dip) can signify two different processes during transition, the premartensite transformation itself (i.e., phonon instability) and the formation of tetragonal unit cells in a nanotwinned $(2\bar{1})_2$ structure followed by the formation of the tweed. Moreover, the susceptibility peak does not depend on magnetic field frequency. This can be taken as a further indication that the formed phase is not a strain glass. In such a case, there should be local random fluctuations of strain which should, due to relatively strong magneto-elastic coupling, result in local fluctuation of magnetization directions and thus in the formation of spin glass-like state. In this state a dependence on frequency is expected.

Figure 1(b) shows the [100] magnetostriction λ_{100} along the field direction. The magnetostriction is negative, i.e., the sample shrinks in the direction of the field. The magnitude of magnetostriction increases linearly with decreasing temperature and exhibits sharp, more than threefold increase at the premartensitic transformation temperature compared to room temperature. Below premartensite transition temperature, however, the magnitude of magnetostriction sharply recovers. This behavior is similar to AC-susceptibility, and rightly so as the drop of magnetic susceptibility is caused by increased magnetic anisotropy. This increase can be ascribed to increasing magnetostriction, which induces magnetic anisotropy proportional to it. The minimum might be also related to the above mentioned anomalous volume change upon transition.

A possible explanation of this peak is that at the T_{PM} temperature the tweed is not fully formed, and thus some areas can be somehow reoriented by the external field assisted by the compressive stress from the dilatometer. So at least partly the large increase of magnetostriction can be explained by reorientation. Upon further cooling, however, the interfaces forming the tweed become inter-locked and thus more rigid, such reorientation becomes impossible and the apparent magnetostriction decreases again.

With knowledge of the λ_{100} magnetostriction and the temperature dependence of the c' coefficient (see Section 3.2) we can determine fundamental magneto-elastic coupling constant B_1 as

$$B_1 = -3\lambda_{100}c'. \tag{1}$$

The result is shown in Fig. 2. The coupling coefficient B_1 is about constant before premartensite transition and decreases with increasing temperature close to Curie temperature. It exhibits sharp maximum at premartensitic transformation and then decreases again and approximately levels off at higher value than in austenite.

However, if we assume that the measured magnetic striction at transformation is due to rearrangement as discussed above, the observed peak in B_1 may just reflect the structural reorientation instead of intrinsic changes in magnetoelastic coupling. No measurable changes in other magnetic properties suggest that the B_1 constant should change with temperature smoothly without any sharp changes. Using this assumption we can in reverse estimate what part of measured striction is due to reorientation. The calculated value of magnetostriction from Eq. (1) is about 200 ppm and thus about 150 ppm is due to reorientation. As the reorientation depends on tweed structure (which is basically a random process, similar to the observed reorientation during martensitic transition

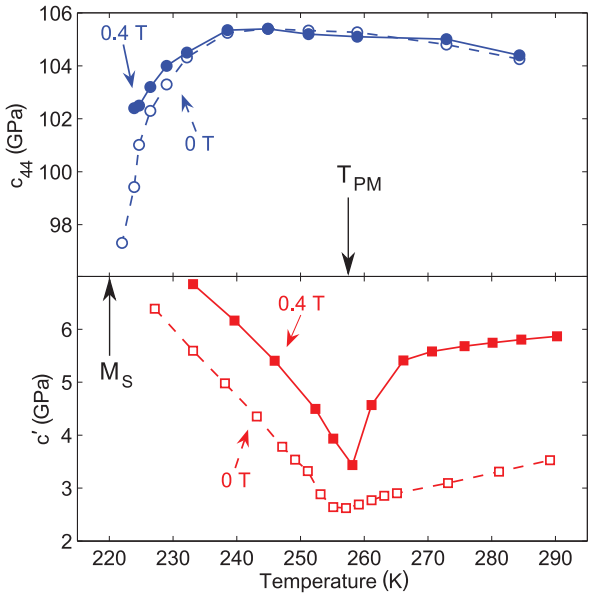

Figure 3 Evolution of elastic constants c_{44} and c' with temperature in the premartensitic interval. The open symbols correspond to zero external magnetic field, the filled symbols to saturation field.

[24]) the size of reorientation can differ in every transition cycle and for different samples and thus the peak value of magnetostriction can strongly differ from case to case.

3.2 Ultrasonic measurements The evolution of all three elastic coefficients was obtained between the room and M_S temperatures, i.e., covering the precursor softening of the austenite lattice prior to the premartensitic transition, the transition itself and the evolution of the elastic constants of premartensite toward the martensitic transition. The results are shown in Fig. 3. Let us discuss at first the behaviors of the elastic coefficients in zero magnetic field. It is clearly seen that the most pronounced effect of the premartensitic transition is on the c' coefficient, for which the $\mathrm{d}c/\mathrm{d}T$ slope abruptly changes in sign at the T_{PM} temperature and the coefficient itself exhibits stiffening from 2.5 to 6.5 GPa (160% increase) until the M_S temperature. For the c_{44} coefficient, the changes are less significant but still clearly detectable. Between room temperature and T_{PM}, this coefficient exhibits a weak, increasing, approximately linear trend; close to T_{PM}, the values of c_{44} start deviating from this trend, decreasing toward the martensitic transition. The decrease is the steepest close to the M_S temperature, where $c_{44} = 95$ GPa (a 10% decrease compared to $c_{44} = 105$ GPa at T_{PM}). Small decrease can be also observed for the c_{11} coefficient (not shown), which softens by approximately 2 GPa (1.5 %) close to the M_S temperature. However, this change is somehow comparable to the possible effect of the mosaicity of the examined crystal ($\pm 0.5^\circ$) and of the misorientation due to imprecise cutting of the sample ($\lesssim 2.5^\circ$). This imperfections results in some sensitivity of the longitudinal waves to c_{44} and c' in the direction perpendicular to the chosen face of the sample. Thus the measured changes of the c_{11} coefficient are most probably just an experimental error.

In the saturation field (0.4 T), again the c' coefficient is strongly affected by the premartensitic transition. The sudden decrease above the T_{PM} temperature is the result of vanishing ΔE-effect [18]; in the premartensitic phase, however, the value of c' appears to be just constantly shifted compared to the zero field data. There is again no direct measurable effect of the premartensitic transition on the c_{44} coefficient, except of that this temperature approximately corresponds the start of a smooth change of the $\mathrm{d}c_{44}/\mathrm{d}T$ slope. Similarly to the zero field case, this coefficient softens close to the M_S temperature, but this softening is weaker than in the demagnetized state.

4 Discussion The experimentally observed evolution of the elastic constants of the premartensitic tweed can be explained as a combination of two effects:

1. changes of elasticity due to formation of the tweed and due to evolution of the tweed geometry,
2. changes of elasticity of the individual constituents of the tweed, i.e., of the unit cell of premartensite.

In order to discuss these two effects separately, we construct a simple geometric model of the tweed; this model gives us semi-quantitative predictions for the macroscopic elasticity of the tweed like-pattern, which can be then subtracted from the experimental data to reveal the real softening of the premartensite unit cell.

4.1 A two-dimensional tweed model For the model, we consider a two-dimensional, simplified geometry of the tweed. Moreover, we assume that the premartensite phase exhibits perfectly commensurate three-layered 6 M modulations, and can be thus well approximated by a $(2\bar{1})_2$ stacking sequence of nano-twins of tetragonal building blocks (NM martensite), following the concept of adaptive martensite [15, 16]. The tetragonal building blocks result from a cubic-to-tetragonal transition of the unit cells of austenite, as sketched schematically in two dimensions in Fig. 4(a). In the stacking sequence, the NM building blocks compose into an effective monoclinic 6 M supercell (Fig. 4(b)), which is then understood as a unit cell of the modulated premartensitic phase. According to [15], the c/a ratio of the building blocks is equal to approximately 1.015 close to the T_{PM} temperature; nevertheless, upon further cooling these building blocks reorganize into 10 M stacking with $c/a = 1.16$ and further into 14 M stacking with $c/a = 1.22$, which indicates that the c/a ratio in premartensite may increase toward M_S. The tetragonal building blocks form nano-twins along the {110} planes; as seen in Fig. 4(b), the compatibility conditions induce slight rotations of the NM martensite symmetrically about the twinning planes. The rotation angle is given by the c/a ratio as

$$\vartheta = \arctan\frac{c}{a} - \frac{\pi}{4}. \qquad (2)$$

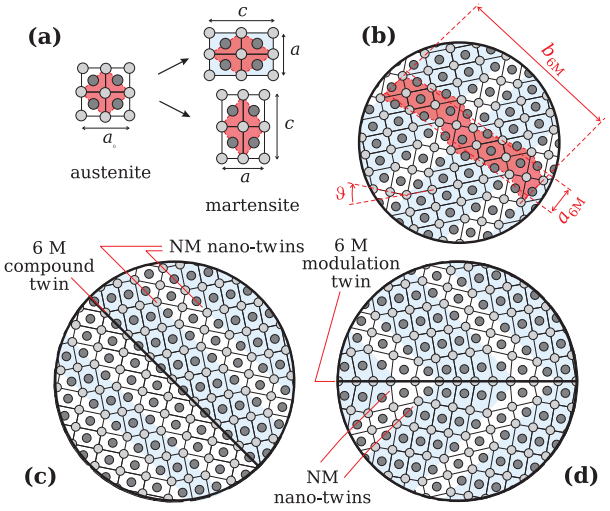

Figure 4 Construction of a two-dimensional model of the pre-martensitic tweed: (a) transition from austenite to an individual building block of NM martensite; (b) composition of NM building blocks into 6 M modulated structure; (c and d) two possible twinning systems of 6 M martensite enabling a construction of effectively cubic regular tweed.

Due to the extremely strong elastic anisotropy, such small misorientation can induce measurable changes in macroscopic elasticity of the tweed. As the tweed exhibits macroscopically a perfectly cubic behavior, it is necessary that all the possible misorientations with respect to the original cubic coordinate system of austenite must be involved in the tweed with the same volume fraction; similarly the c- and a-orientations and the directions of modulation must be equivalently included in the tweed microstructure. This means that besides the nano-twinning planes between the individual NM building block, the tweed must include also some additional twinning of the 6 M phase. In our two-dimensional setting, these twinning planes can be those sketched in Fig. 4(c) and (d), which are the compound twins and the modulation twins [25], respectively. The compound twinning plane runs along the {110} plane and separates regions with the same modulation direction but different stacking sequence (and, consequently, different orientation of the a- and b-dimensions of the 6 M unit cell); the modulation twinning plane runs along the {100} plane and separates regions with different modulation direction but the same orientation of the a- and b-dimension of the unit cell. As seen from the sketch, these two types of 6 M twins may differ significantly in energy. While the compound twin is equivalent to just a change of the stacking sequence (i.e., a phase shift in modulation), and its energy can be assumed as the same as of the nano-twins, the energy of the modulation twin includes also the energy of elastic strains required at the interface to enable local compatibility. These strains increase with increasing c/a ratio, and thus the tweed tends to reduce the number of this type of interfaces when this ratio increases.

Nevertheless, it is clear from the Fig. 4(c) and (d) that these two twinning types do not induce any additional rotations to the lattice. In other words, all rotations of the NM unit cell with respect to the effective cubic coordinate system are those following from the compatibility at the nano-twinning planes, regardless of what microstructure is formed by the compound and modulation twins. For this reason, if we take any fixed, artificially chosen micromorphology of the tweed such that all a- and b-orientations and modulation direction are involved with the same volume fraction, the effective elasticity calculated for this microstructure can be understood as a good approximation of any real general morphology of the tweed.

In this sense, we took a tweed as a regular herring-bone pattern [26] with equivalently altering orientations of the modulation and with periodic compound twinning. Let us point out that such a two-dimensional herring-bone pattern is essentially very similar to the chessboard microstructure resulting from pseudospinodal decomposition, which is another possible formation mechanism of the tweed [27], alternative to the adaptive nano-twinning. In the chessboard microstructure, the compatibility conditions again require mutual rotations of the individual constituents of the pattern by the same angle ϑ, so the material is finally composed of the same mixture of NM unit cells with slight c- and a-misorientations. In other words, although the proposed model of the tweed was constructed by sequence of lamination in the adaptive concept, its predictions are at least qualitatively valid also for the concept based on the pseudospinodal decomposition.

The elasticity of this microstructure was calculated by a homogenizing procedure for martensitic laminates described in [28]. This procedure is more precise than the Voigt or Reuss homogenization procedures, since it fully reflects the geometric arrangement of the interfaces and the mutual rotations of the material due to the compatibility conditions. For the calculation, the elasticity of the NM martensite was assumed as cubic, with c_{11} =142 and c_{44} = 105 GPa taken as fixed and for three different values of c' (denoted c'_{NM}) within the ranges of the experimental results. In particular, the values c'_{NM} of 2, 4, and 6 GPa were chosen, as this set covers well the observed evolution of the c' coefficient of the premartensite phase from the T_{PM} temperature toward M_{S} as seen in Fig. 3. Moreover, such values are also in a good agreement with the values of the softest shear coefficient of the pure NM martensite phase reported by Dai et al. [29]. The results are seen in Fig. 5, where the evolution of the c_{11}, c_{44}, and c' coefficients of the tweed with the c/a ratio of the NM building blocks is shown. It is clearly seen that the formation of the tweed has the most pronounced effect on the c_{44} coefficient. This coefficient softens significantly even for very small c/a ratios, especially if c' is very low, i.e., if the anisotropy factor of the material is high. Thus, the drop-down by nearly 10 GPa of c_{44} can be fully described by the geometric effect of the tweed and does not probably result from any softening of the TA_1(fast shear) phonon branch.

On the other hand, close to the T_{PM} temperature where the tetragonal distortion of the NM unit cells is small ($c/a \to 1$, [15]), the effect of the tweed formation on the c_{44} coefficient is

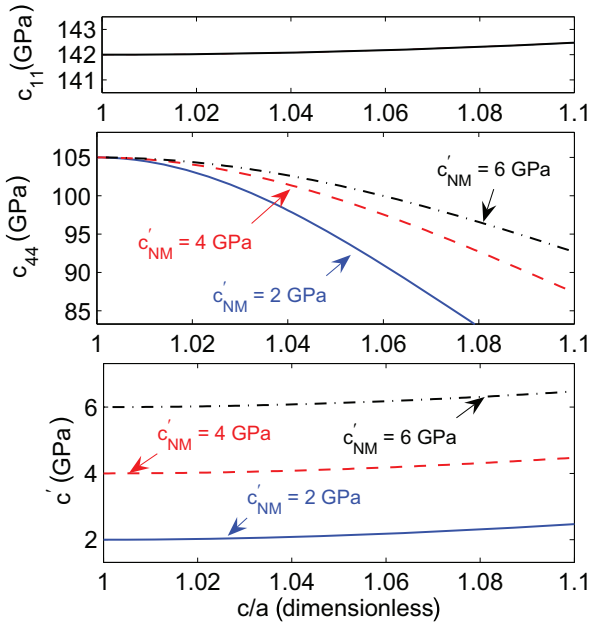

Figure 5 The effect of the tweed geometry (c/a ratio of the individual NM building blocks) on the macroscopic elastic constants of the tweed. For the c_{11} coefficient the curves for $c' = 2$ GPa, $c' = 4$ GPa, and $c' = 6$ GPa fully coincide.

negligible and also the derivative $\mathrm{d}c_{44}/\mathrm{d}(c/a)$ limits to zero. For this reason, no observable softening of this coefficient appears directly at T_{PM}, but c_{44} gradually decreases toward M_S where also an increase of the c/a ratio can be expected, as mentioned above.

The model also predicts well the difference between c_{44} evolution with and without external magnetic field. In the saturation, the c' coefficient of the tweed is higher (see Fig. 3), which indicates that c'_{NM} is increased by magneto-elastic coupling. As a result, the softening of the c_{44} coefficient with the same evolution of the c/a ratio is weaker in the saturation field.

4.2 Structural softening of the premartensitic unit cell In the above paragraph it was shown that the steep increase of the c' coefficient below T_{PM} cannot be explained by the geometric effect of the tweed. Instead, this increase must necessarily be a result of stiffening of c'_{NM}. It is well known that the E modulus of NM martensite phase sharply increases with decreasing temperature from the transformation [30], which indicates a similarly strong increase of c' of nonmodulated martensite, since E is proportional to c' for strongly anisotropic materials. A significant stiffening below the martensitic transition temperature was also observed for all shear coefficients of the NM phase [29]. In the above discussed premartensitic tweed, such stiffening at the level of the individual NM building blocks appears simultaneously with the observed c_{44} softening which, however, occurs only at the homogenized level and due to the tweed geometry. The martensitic transformation from premartensite to modulated martensite then occurs due to lattice instability caused by high elastic anisotropy and increasing c/a ratio of basic building blocks of the premartensitic phase. The transition to premartensite occurs only for materials close to stoichiometry and at a relatively constant temperature about 250 K, resulting from a freezing of soft phonons [31] With increasing deviation from stoichiometry the martensitic transformation temperature increases and overcomes the premartensitic temperature. Moreover the c/a ratio of transforming martensite phase becomes gradually large, and thus no premartensite i.e., 6 M modulation can occur, as this phase requires particular c/a ratios.

As it is apparent from Fig. 3, the coefficient c' of the premartensite is still quite affected by magnetic field. In contrast it was shown that the effect of magnetic field on the elastic response of Ni–Mn–Ga martensite is negligible [20]. As the tweed is assumed to consist of martensitic NM unit cells, the observed field dependence in premartensite is the property of the tweed due to magneto-elastic interaction.

In line with the proposition by Wang et al. [13] that the austenite can be considered as strain-disordered paraelastic state and martensite as long range ordered ferroelastic state we suggest another alternative view on the tweed. Ren et al. [31] consider the tweed as equivalent of unfrozen state of strain glass. However, the tweed exhibits long range ordering albeit on nanoscale and only these nanosized tweed block are randomly distributed. In the analogy with the superparamagnetism [32], in which the magnetic moment is ordered but only in small volumes while these blocks are randomly oriented, the tweed can be considered as superparaelastic state. The sequence in stoichiometric Ni_2MnGa can then be described by going from paraelastic to superparaelastic and finally to ferroelastic i.e., martensite state.

5 Conclusion Our measurements show that the magnetic states of the austenite and premartensite are very similar. This is connected with averaged cubic structure of the premartensite. On the other hand the elastic properties of austenite and premartensite are quite different and even evolve in opposite direction with temperature. To explain this anomalous behavior we suggested a model based on adaptive concept of premartensite explaining the softening of c_{44} and apparent c' stiffening prior to the martensitic transformation. The discussed case of premartensite is, however, an exception limited to Ni_2MnGa materials close to stoichiometry. In materials with temperature of martensitic transformation above the room temperature i.e., in material with few atomic % deviation from stoichiometry, we observed the usual softening of c' till the M_S temperature [33]. In other words, the observed evolution of the elastic constants c_{44} and c' in the premartensitic phase is specific for this phase and it is not a necessary prerequisite for the martensitic transition itself.

Acknowledgements This work was supported by the Czech Scientific Foundation Grant No. P107/11/0391, and by Czech Academy of Sciences (international collaboration project M100761203).

References

[1] V. V. Kokorin, V. A. Chernenko, E. Cesari, J. Pons, and C. Segui, J. Phys.: Condens. Matter **8**, 6457 (1996).
[2] L. Manosa, A. Gonzalez-Comas, E. Obrado, A. Planes, V. A. Chernenko, V. V. Kokorin, and E. Cesari, Phys. Rev. B **55**, 11068 (1997).
[3] A. Zheludev, S. M. Shapiro, P. Wochner, A. Schwartz, M. Wall, and L. E. Tanner, Phys. Rev. B **51**, 11310 (1995).
[4] U. Stuhr, P. Vorderwisch, V. V. Kokorin, and P.-A. Lindgard, Phys. Rev. B **56**, 14360 (1997).
[5] P. J. Brown, J. Crangle, T. Kanomata, M. Matsumoto, K.-U. Neumann, B. Ouladdiaf, and K. R. A. Ziebeck, J. Phys.: Condens. Matter **14**, 10159 (2002).
[6] O. Heczko, M. Landa, and H. Seiner, J. Appl. Phys. **111**, 07A929 (2012) .
[7] V. V. Khovailo, T. Takagi, A. D. Bozhko, M. Matsumoto, J. Tani, and V. G. Shavrov, J. Phys.: Condens. Matter **13**, 9655 (2001).
[8] J. M. Barandiaran, V. A. Chernenko, P. Lazpita, J. Gutierrez, I. Orue, J. Feuchtwanger, and S. Besseghini, Appl. Phys. Lett. **94**, 051909 (2009).
[9] V. A. Chernenko, S. Besseghini, T. Kanomata, H. Yoshida, and T. Kakeshita, Scr. Mater. **55**, 303 (2006).
[10] K. Otsuka and X. Ren, Prog. Mater. Sci. **50**, 511 (2005).
[11] Z. H. Nie, Y. Ren, Y. D. Wang, D. M. Liu, D. E. Brown, G. Wang, and L. Zuo, Appl. Phys. Lett. **97**, 171905 (2010).
[12] S. Sankar, X. Ren, and K. Otsuka, Phys. Rev. Lett. **95**, 205702 (2005).
[13] D. Wang, Y. Wang, Z. Zhang, and X. Ren, Phys. Rev. Lett. **105**, 205702 (2010).
[14] S. Singh, J. Nayak, A. Rai, P. Rajput, A. H. Hill, S. R. Barman, and D. Pandey, J. Phys.: Condens. Matter **25**, 212203 (2013).
[15] S. Kaufmann, U. K. Rößler, O. Heczko, M. Wuttig, J. Buschbeck, L. Schultz, and S. Fähler, Phys. Rev. Lett. **104**, 145702 (2010).
[16] R. Niemann, U. K. Rößler, M. E. Gruner, O. Heczko, L. Schultz, and S. Fähler, Adv. Eng. Mater. **14**, 562 (2012).
[17] S. P. Venkateswaran, N. T. Nuhfer, and M. De Graef, Acta Mater. **55**, 2621 (2007).
[18] H. Seiner, P. Sedlák, L. Bodnárová, J. Drahokoupil, V. Kopecký, J. Kopeček, M. Landa, and O. Heczko, J. Phys.: Condens. Matter **25**, 425402 (2013).
[19] H. Seiner, O. Heczko, P. Sedlák, L. Bodnárová , M. Novotný, J. Kopeček, and M. Landa, J. Alloys Compd. **557S**, S131–S135 (2013).
[20] O. Heczko, H. Seiner, P. Sedlák, J. Kopeček, V. Kopecký, and M. Landa, Eur. Phys. J. B **86**, 62 (2013).
[21] A. Gonzalez-Comas, E. Obrado, Ll. Manosa, A. Planes, V. A. Chernenko, B. J. Hattink, and A. Labarta, Phys. Rev. B **60**, 7085 (1999).
[22] H. Seiner, L. Bicanová, P. Sedlák, M. Landa, L. Heller, and I. Aaltio, Mater. Sci. Eng. A **521–522**, 205 (2009).
[23] G. Petculescu, R. Wu, and R. McQueeney, Magnetoelasticity of bcc Fe–Ga alloys, in: Handbook of Magnetic Materials, Vol. 20, edited by K. H. J. Buschow (Elsevier, North-Holland, 2012), pp. 123–226.
[24] L. Straka, O. Heczko, V. Novák, and N. Lanska, J. Phys. IV (France) **112**, 911 (2003).
[25] L. Straka, O. Heczko, H. Seiner, N. Lanska, J. Drahokoupil, A. Soroka, S. Fähler, H. Hänninen, and A. Sozinov, Acta Mater. **59**, 7450 (2011).
[26] T. Waitz, Acta Mater. **53**, 2273 (2005).
[27] Y. Ni and A. G. Khachaturyan, Nature Mater. **8**, 410 (2009).
[28] M. Landa, P. Sedlák, H. Seiner, L. Heller, L. Bicanová, P. Šittner, and V. Novák, Appl. Phys. A **96**, 557 (2009).
[29] L. Dai, J. Cullen, and M. Wuttig, J. Appl. Phys. **95**, 6957 (2004).
[30] V. A. Chernenko, J. Pons, C. Segui, and E. Cesari, Acta Mater. **50**, 53 (2002).
[31] X. Ren, Y. Wang, Y. Zhou, Z. Zhang, D. Wang, et al., Philos. Mag. **90**, 141 (2010).
[32] J. M. D. Coey, Magnetism and Magnetic Materials (Cambridge Univ. Press, Cambridge, 2010), p. 296.
[33] O. Heczko, H. Seiner, M. Landa, and P. Sedlák, in preparation.

4.4 Publikace *Mikrostruktura, martenzitická transformace a anomálie v $c'-$měknutí ve feromagnetické slitině s tvarovou pamětí Co-Ni-Al.*

Bibliografická citace: Seiner, H., Kopeček, J., Sedlák, P., Bodnárová, L., Landa, M., Sedmák, P., Heczko, O. Microstructure, martensitic transformation and anomalies in c′-softening in Co-Ni-Al ferromagnetic shape memory alloys (2013) Acta Materialia, 61 (15), pp. 5869-5876.

Stručná anotace: Publikace se zabývá prekurzorovými efekty ve vysokoteplotní fázi slitiny Co-Ni-Al a jejich souvislostí s mikrostrukturou částic netransformujících $\gamma-$fází. Porovnáním mechanických vlastností, mikrostruktury a strukturního měknutí elastického koeficientu c' monokrystalů s různým tepelným zpracováním je ukázána přímá souvislost mezi nukleací martenzitu a mikrostrukturou $\gamma-$částic. Zároveň je ukázáno, že ve slitině nedochází ke vzniku žádné intermediální (premartenzitické) fáze, protože anomálie v měknutí koeficientu c' je způsobena magnetoelastickou interakcí.

Příspěvek habilitanta: Příspěvek habilitanta spočíval ve vyhodnocení měření rezonanční ultrazvukové spektroskopie a především v jejich interpretaci ve vztahu k magnetoelastickému měknutí, prekurzorovým efektům a nukleaci martenzitické fáze. Habilitant rovněž provedl a analyzoval mesoskopická optická pozorování nukleace martenzitu na hranách vzorku a na částicích $\gamma-$fáze.

Available online at www.sciencedirect.com

SciVerse ScienceDirect

Acta Materialia 61 (2013) 5869–5876

Acta MATERIALIA

www.elsevier.com/locate/actamat

Microstructure, martensitic transformation and anomalies in c'-softening in Co–Ni–Al ferromagnetic shape memory alloys

Hanuš Seiner [a], Jaromír Kopeček [b], Petr Sedlák [a], Lucie Bodnárová [a], Michal Landa [a], Pavel Sedmák [c], Oleg Heczko [b,*]

[a] Institute of Thermomechanics, Academy of Sciences of the Czech Republic, Dolejškova 5, 18200 Prague, Czech Republic
[b] Institute of Physics, Academy of Sciences of the Czech Republic, Na Slovance 2, 18221 Prague, Czech Republic
[c] Faculty of Nuclear Sciences and Physical Engineering, Czech Technical University in Prague, Trojanova 13, 12000 Prague, Czech Republic

Received 4 April 2013; received in revised form 12 June 2013; accepted 17 June 2013
Available online 12 July 2013

Abstract

The morphology, microstructure and elastic softening in single crystals of Co–Ni–Al ferromagnetic shape memory alloy were studied to clarify the conditions for martenstic transformation in this alloy. We used two-phase (β matrix + γ particles) samples with different heat treatments, as-cast and annealed at temperatures from 1523 to 1623 K, and a sample of pure β (B2) phase. A complete set of elastic coefficients at room temperature and the temperature dependence of the softest shear coefficient (c') of the $Co_{38}Ni_{33}Al_{29}$ austenite was measured by a combination of pulse echo and resonant ultrasound spectroscopy in the range 208–398 K. All examined materials exhibit anomalous c'-softening for the whole temperature range except the interval 258– 328 K, in which a change in the slope appears. However, only annealed samples transformed to martensite. The change in the slope is ascribed to (i) magnetoelastic softening with the absence of a sharp Curie point; (ii) structural stiffening that prevents the martensitic transition in both the as-cast and single-phase alloys. No signature of the premartensite phenomenon was found.

Keywords: Ferromagnetic shape memory alloys; Resonant ultrasound spectroscopy; Premartensitic phenomena

1. Introduction

Ferromagnetic shape memory alloys (FSMAs) have been intensively studied since the discovery of the magnetically induced reorientation (MIR) effect by Ullakko et al. [1,2]. The ability of these alloys to deform reversibly under the action of the external magnetic field with strain amplitudes up to 10% [3,4] makes them highly interesting from the perspective of possible smart applications, including magnetically driven actuators, micromanipulators, pumps, etc. [5,6]. These materials are important not only from a practical point of view but also from the theoretical perspective as the coupling between two ferroic orderings (ferroelasticity and ferromagnetism) in FSMAs opens new challenges for mathematical modeling at different spatial scales [7–10]. As well as the Ni–Mn–Ga [1,3,11] and Fe–Pd [12,13] systems, which exhibit MIR, attention should be paid to the other ferromagnetic Heusler alloys undergoing martensitic transformation [14] as this transformation is a basic precondition for MIR.

One important class of FSMAs is Co–Ni–Al, since the thermomechanical properties of this material can be sensitively tuned by heat treatment [15–17] and moreover the alloying elements for this system are cheap. These alloys undergo martensitic transformation from the cubic (B2) to tetragonal ($L1_0$) structure [18,19], which is similar to the high-temperature non-modulated martensite in Ni–Mn–Ga [20]. In the tetragonal structure there are only three different variants of martensite, which limits the type of possible martensite microstructure in comparison with the rich structures of modulated martensites in

* Corresponding author. Tel.: +420 266052714; fax: +420 286890527.
E-mail address: heczko@fzu.cz (O. Heczko).

1359-6454/$36.00 © 2013 Acta Materialia Inc. Published by Elsevier Ltd. All rights reserved.
http://dx.doi.org/10.1016/j.actamat.2013.06.035

Ni–Mn–Ga [21,22]. However, contrary to previous belief, the tetragonal structure does not preclude MIR as recently shown by Sozinov [23]. Despite the simple martensite microstructure in Co–Ni–Al alloys the processes accompanying both the forward and reverse martensitic transformation can be rather complex due to the presence of fine γ-phase (A1) precipitates in transforming B2 matrix (e.g. [18]).

Murakami et al. [17] observed that the martensitic transformation in Co–Ni–Al alloy was preceded by a tweed-like modulation of austenite lattice. This precursor phenomenon, called the premartensitic transition, is a well-known phenomenon in Ni–Mn–Ga alloys [24]. In Ni–Mn–Ga the premartensitic modulation is magnetoelastic in origin [25] and its formation results in pronounced, anomalous changes of elastic constants of the austenite phase [26,27]. On the other hand, Brown et al. [28] used neutron powder diffraction to follow the structure evolution of $Co_{38}Ni_{33}Al_{29}$ during the transformation. They concluded that the presence of premartensitic phase should be indicated by a weak additional diffraction peak appearing in the vicinity of the transition temperature, but in contrast to Murakami et al. they found that the martensitic transition in this material proceeded without any significant intermediate step.

Since the transition in Co–Ni–Al belongs to the cubic-to-tetragonal class, the changes of elasticity preceding the transition are related to the transverse accoustic TA_2 phonon branch, i.e. to shearing along the $\{1\,1\,0\}$ planes with $\langle 1\,\bar{1}\,0\rangle$ polarization [33]. The resistance of the lattice to such shearing is described by the coefficient c', defined as $\frac{1}{2}(c_{11}-c_{12})$ using three independent elastic constants of the cubic material (c_{11}, c_{12} and c_{44}). Similarly to other shape memory alloys, this shear elastic coefficient is significantly lower than the coefficient c_{44} representing shears along the principal $\{1\,0\,0\}$ planes. The anisotropy factor $A = c_{44}/c'$ is usually larger than 10. The coefficient c' softens further with decreasing temperature towards the transformation. For this reason, we refer to so-called anomalous c'-softening. As discussed in Ref. [27,29], the most appropriate method for accurate determination of the c' coefficient of such highly anisotropic cubic materials is resonant ultrasound spectroscopy (RUS) [30,31]. RUS is an experimental technique based on measurements of resonant frequencies of free elastic vibrations of a small sample. The lowest resonant frequencies correspond to the shearing vibration related to the softest shear coefficient and thus detecting a limited number of the first few resonances is sufficient for accurate determination of c'. Moreover, when RUS is applied to a fully non-contact regime using lasers for both generation and detection of the vibration modes, it enables very sensitive tracing of the c' coefficient with temperature. As shown in this paper, even very weak changes in the dc'/dT slope or other anomalies can be detected. On the other hand, the experimental requirements of RUS, in particular the need for the sample to have a perfect parallelepiped shape, limits to some extent the applicability of this method to material in the early stages of martensitic transition, as also shown in the experimental part of this paper.

The main aim of this paper is to probe elastic softening and expected premartensitic phenomena by measurements of the (magneto) elastic properties of Co–Ni–Al single crystals in the vicinity of the martensite starting temperature M_s and to relate these to the microstructure and structural changes during transformation. A comparison with the prototypical magnetic shape memory compound Ni–Mn–Ga is discussed. The results of contactless RUS measurement indicate that additional anomalous softening is very weak and there is no sign of premartenstic phenomena. The observed small anomalies can be ascribed to the presence of martensite nuclei stress-induced in the vicinity of γ-phase precipitates.

2. Materials and methods

Five different samples were used in the experiments, referred to as "single-phase", "as-cast" and "annealed at X temperature", where $X = 1523$, 1548 and 1573 K. The samples were cut from single-crystal ingots grown by the Bridgman method in argon atmosphere using two different growth rates, 17 and 104 mm h^{-1}. The nominal composition of the initial alloy was $Co_{38}Ni_{33}Al_{29}$. All samples were cuboids with approximate dimensions 3.2 mm × 2.8 mm × 2.3 mm and the orientation of sides was $(0\,1\,-1) \times (1\,0\,0) \times (0\,1\,1)$.

The microstructure of the single-crystalline ingot grown at 17 mm h^{-1} splits into two different regions: two phases ($\beta + \gamma$) exterior and one phase (β) interior [34]. No significant redistribution of elements was observed. The "one phase" sample was cut from the interior of this crystal [35]. The crystal was in the as-cast state. Other samples were cut from the single-crystal ingot grown at 104 mm h^{-1}. This crystal has a two-phase microstructure with interdendritic γ particles distributed homogeneously within the β (B2) matrix [34]. The composition of matrix is approx. $Co_{38}Ni_{32}Al_{30}$ and the composition of particles is about $Co_{53}Ni_{30}Al_{17}$ [35]. The composition of particles and matrix remains the same for the higher growth rates and the redistribution of elements occurs only through the number of particles in the matrix. The sample marked "as-cast" is in state immediately after Bridgman growth without any heat treatment. To evaluate the effect of heat treatment, three samples were annealed at temperatures from 1523 to 1573 K for 1 h and quenched into cold water. The phase identification and orientation were determined by electron backscatter diffraction (EBDS) and their compositions were checked by energy-dispersive spectroscopy (EDS).

As the Co–Ni–Al alloys are ferromagnetic, the martensite transformation temperatures can be detected by magnetic measurement. The martensite temperatures and ferromagnetic Curie point were determined by measuring the temperature dependence of DC magnetization at 100 Oe for each material in the temperature range 10–360 K

using a vibration sample magnetometer. Additionally, the AC magnetic initial susceptibility was used to confirm the transformation temperatures. In both cases PPMS instruments from Quantum Design were used. Stress-induced martensite transformation in the samples was probed by compression tests up to 350 MPa. The curves were corrected for the deformation of the grips.

The contactless or non-contact resonant ultrasound spectroscopy (n-RUS) method was applied to determine the temperature evolution of the softest shear coefficient from above the Curie point (398 K) towards the vicinity of the M_S temperature. Prior to these temperature-resolved measurements, a complete determination of the elastic coefficients (constants) at room temperature was done for each sample by using a combination of pulse-echo and RUS measurements as follows: (i) velocities of (quasi-) longitudinal ultrasonic waves in the directions perpendicular to the faces of the sample were determined by the pulse-echo method; (ii) a detailed RUS spectrum was determined with the modal shapes of individual eigenmodes recorded by laser-Doppler interferometry. For this contactless RUS was employed in which the vibrations of the sample are both generated and detected by lasers (for instrumentation and other details see Ref. [32,37]). The modal shapes were used for the identification of the individual resonant peaks in the vibration spectrum [38]. Consequently the results of both methods, i.e. the velocities $v^{\text{exp.}}_{1,\dots,3}$ and resonant frequencies $f^{\text{exp.}}_{1,\dots,n}$ (the superscript exp. in both cases denotes the experimental values), were simultaneously inverted by minimizing the objective function [39]

$$F(c_{11},c_{44},c') = \sum_{p=1}^{n}\left(f_p^{\text{exp.}} - f_p^{\text{calc.}}(c_{11},c_{44},c')\right)^2 + w^2\sum_{q=1}^{3}\left(v_q^{\text{exp.}} - v_q^{\text{calc.}}(c_{11},c_{44},c')\right)^2, \quad (1)$$

where w is a weighting factor taken in this case as $w = V^{-1/3}$ with V being the volume of the sample. The calculated values of the resonant frequencies $\left(f_p^{\text{calc.}}\right)$ and of the velocities $\left(v_q^{\text{calc.}}\right)$ were obtained by the Ritz–Rayleigh method and from Christoffel's equation, respectively. For all examined samples the value of n was between 10 and 20, which is sufficient for the determination of c'. Such joint inversion resulted in a complete set of elastic constants for each sample, as given in Table 1.[1]

Table 1
The complete set of elastic coefficients for all samples at room temperature, A stands for the anisotropy factor $A = c_{44}/c'$. The coefficients obtained from pulse echo measurement c_{11}, c_{44} are determined with error ± 2 GPa, while coefficient c' from n-RUS is determined with error ±0.05 GPa. The error of elastic anisotropy is about ±0.5.

	c_{11} [GPa]	c_{44} [GPa]	c' [GPa]	A [1]
As cast	175	114	7.32	18.9
Annealed at 1523 K	173	120	5.15	23.3
Annealed at 1548 K	172	122	5.00	24.4
Annealed at 1573 K	172	123	4.81	25.6
One phase	177	101	6.04	16.7

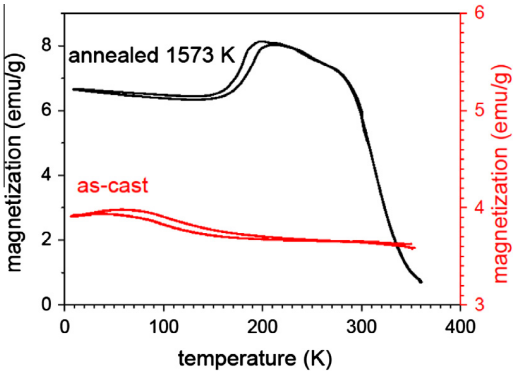

Fig. 1. Low field magnetization (measured at 100 Oe) as a function of temperature for as-cast and annealed (1523 K) samples. The decrease in the magnetization at low temperature indicates the onset of martensite transformation. The gradual decrease at high temperature marks the smeared ferromagnetic transition.

The temperature evolution of the RUS spectra was measured upon cooling from 400 K downwards. For each temperature, the c' coefficient was determined by minimizing the error function (1) with fixed values of c_{11} and c_{44}. At each temperature it was checked that such minimum corresponded to a good fit between the $f_p^{\text{exp.}}$ and $f_p^{\text{calc.}}$ velocities, in particular that the maximal misfit was lower than 1%. This approach was successfully applied for determination of the $c'(T)$ curve down to 208 K, which is the limit of the temperature chamber and sufficiently close to the onset of martensite transformation.

3. Results and discussion

3.1. Martensitic transformation and microstructure

Fig. 1 shows the DC magnetization as a function of temperature for samples annealed at 1573 K and as-cast. The drop in magnetization indicates the onset of martensitic transformation due to higher magnetic anisotropy of the martensite. While for the as-cast and the one-phase material no apparent transition occurred until 10 K, all annealed materials exhibited a reversible martensite transition with a martensite start temperature between 190 and 195 K which slightly increased with increasing annealing temperature [40]. The hysteresis of bulk martensite transformation was about 10 K for all alloys. Similar temperatures were observed on powder samples investigated in situ by neutron diffraction [41].

Magnetization measurements were also used to detect the magnetic transition temperature, i.e. the Curie point. In agreement with Murakami et al. [17] and Liu et al.

[1] The significantly lower experimental error for the c' coefficient follows from the fact that this coefficient was mainly determined by RUS, while the others came from the pulse-echo results. On the other hand, the relative errors for all coefficients are approximately the same.

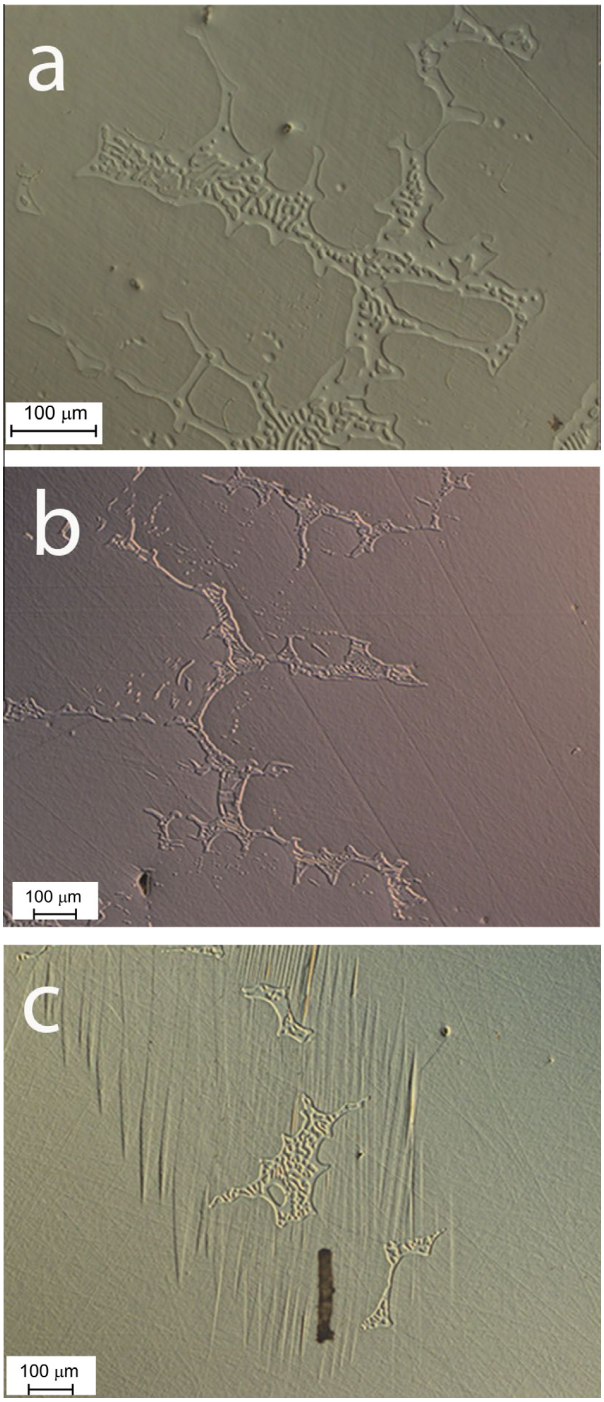

Fig. 2. Microstructure of the Co–Ni–Al alloy in (a) as-cast state; (b) after annealing at 1423 K and quenching; and (c) after annealing at 1523 K and quenching.

[19], the low field magnetization of the annealed sample exhibited no sharp drop close to Curie point as is usual in Ni–Mn–Ga. The continuous decrease in the magnetization over the temperature interval 300–350 K suggests that the magnetic transition is smeared over broader interval in contrast with Ni–Mn–Ga, in which the Curie point is sharply defined [11]. This smearing can be caused by random distribution of the ferromagnetic elements in the alloys

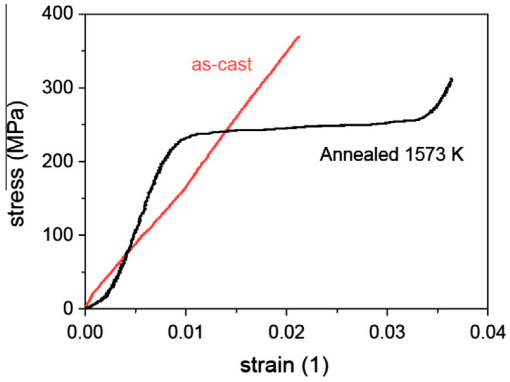

Fig. 3. Stress–strain curves of as-cast and annealed (1523 K) samples. Curves are measured in compression.

with B2 ordering (in contrast with $L2_1$ ordering in Ni–Mn–Ga), which may cause fluctuation of the exchange coupling. The residual magnetization even above 360 K can be ascribed to the two-phase structure and higher Curie point for the interdendritic γ-phase with higher content of Co. There is no significant drop of magnetization for the as-cast sample, indicating that the magnetic transition in this material is smeared over a broader region and the ferromagnetic ordering persists above 360 K.

Fig. 2 shows the microstructures of differently annealed two-phase single-crystal samples. Optical microscopy showed that the interdentritic γ particles are largest in the as-cast state (Fig. 2a) and increasing the annealing temperature causes these particles to dissolve slowly while preserving their network [36]. This network of particles seems to follow the cubic symmetry of the B2 matrix as demonstrated in Fig. 4, which shows the whole sample. Additionally, the detailed image in Fig. 2c reveals that in the vicinity of the interdentritic γ particles there are traces of martensite in the form of the needles pinned on the particles. This martensite is stress-induced mostly in the places of dissolved particles. There is no stress-induced martensite in the as-cast sample. In the annealed samples the amount of stress-induced martensite increases with increasing annealing temperature. This increase, however, does not affect significantly the transformation of the bulk matrix as determined from magnetic measurements.

The stress–strain curves measured in compression for two-phase as-cast and annealed samples are shown in Fig. 3. The curves were measured in the [1 0 0] direction, which is the softest direction for elastic deformation. The as-cast sample does not transform to martensite up to 350 MPa and its deformation is approximately linear throughout the whole range, whereas the annealed sample transformed to martensite at about 250 MPa as indicated by the plateau in the stress–strain curve. Similar behaviour was observed for other annealed samples but not for the single-phase sample, which behaved similarly to the as-cast two-phase material. We can conclude that only the annealed samples transform to martensite. A full analysis of the stress-induced martensite transformation measured

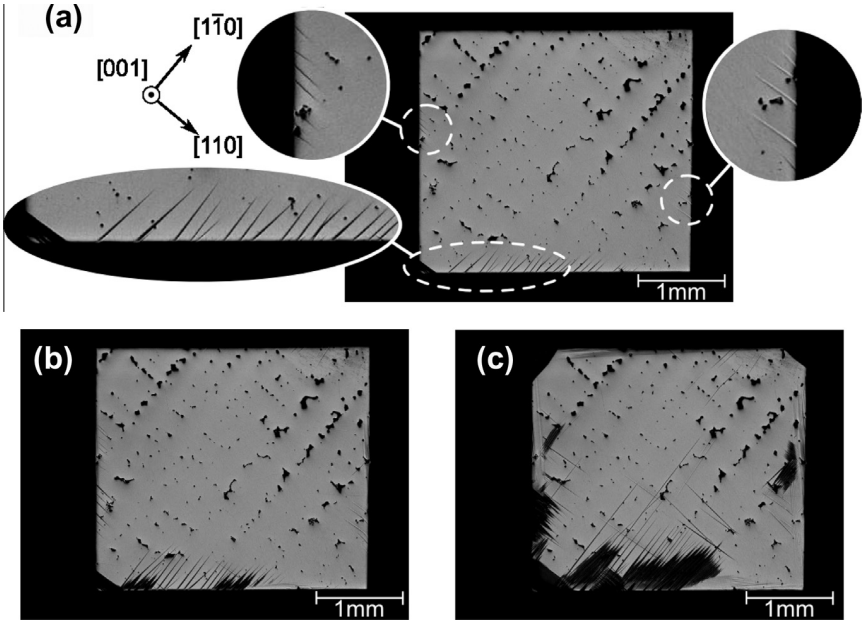

Fig. 4. Evolution of microstructure with cooling of the sample annealed at 1573 K: (a) at 258 K with the zoomed area showing the newly nucleated martensitic needles at the edges and the corners of the sample; (b) at 238 K; (c) at 208 K. The black islands are areas with a high concentration of γ-phase particles highlighted by chemical polishing of the surface. It can be seen that the spatial arrangement of these particles follows the cubic symmetry of the B2 matrix.

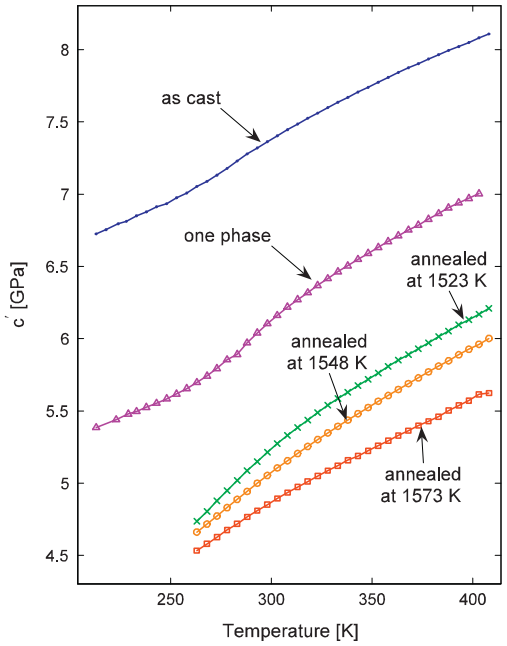

Fig. 5. Softening of the c' coefficient measured by RUS for all samples as marked in figure.

in different directions will be published elsewhere. The moduli determined from the initial slopes of the curves correspond to the measurement of elastic constants by n-RUS for both cases. However, the annealed sample exhibits some stiffening during loading resulting in a gradual increase in the modulus for larger deformation. This stiffening is not reflected in RUS measurements which rely on small deformations.

The temperature evolution of the microstructure above martensitic transformation is shown in Fig. 4. When cooling from room temperature, large mezoscopic martensitic needles overgrow from the initial stress-induced martensite nuclei in the vicinity of the γ particles. The martensitic needles appear close to the edge of the sample due to the relaxed constraint of surrounding material at the surface [42]. Optical microscopy shows relatively large areas affected above 200 K, which is higher than the measured transformation temperature. However, the magnetization measurements, which detect the bulk properties, are not significantly affected. This proves that the observed martensite is mostly a surface phenomenon.

3.2. Elastic constants at room temperature

The complete set of elastic constants obtained by joint inversion (Eq. (1)) is given in Table 1 for each sample. While the c_{11} coefficient is approximately the same for all samples, the shear coefficients c_{44} and c' depend on the heat treatment and the microstructure. The shearing along the principal planes, i.e. c_{44} coefficient, seems to be closely related to the microstructure and presence of the γ-phase particles: the absence of these particles leads to significant softening of this shear, i.e. in the one-phase sample, and two-phase samples exhibit higher coefficients. The finer dispersion of the particles by annealing and quenching leads to further stiffening of c_{44}, which very slightly increases

with increasing annealing temperature. The observed stiffening might also be related to the increased presence of martensitic needles.

On the other hand more pronounced changes can be observed for the c' coefficient. Although the absence of the γ-phase leads again to some softening of the corresponding shearing compared to the as-cast two-phase ($\beta + \gamma$) sample, the annealing further reduces the c' coefficient and this decrease can be correlated with the increase in the annealing temperature. This softening is apparently related to the decreasing volume of γ-phase particles and the increasing amount of stress-induced martensite attached to these particles. Due to the significant drop in the c' coefficient, the anisotropy factor increases up to $A > 25$, which represents an extremely large elastic anisotropy. This anisotropy is higher than the elastic anisotropy of Ni–Mn–Ga in the vicinity of martensitic transformation [27,29]. The instability of the cubic lattice is the largest for the annealed samples, in good agreement with the fact that the thermally induced martensite transformation occurred only in these samples.

3.3. Evolution of c′-softening with temperature

Temperature evolution of the RUS spectra was measured upon cooling from 400 K for all samples (Fig. 5). For the as-cast and the single-phase material the temperature dependence of $c'(T)$ could be determined down to 208 K. These materials, according to the magnetization measurement, do not transform to martensite at low temperatures and there is no stress-induced transformation either.

For all annealed samples, however, the value of the objective function (1) increased abruptly already at 258 K, which makes the determination of c' from the spectra at lower temperatures impossible. The reason for such abrupt decrease in the goodness-of-fit is apparent from Fig. 4a for the sample annealed at 1573 K. At 258 K visual observation indicates that the martensitic transformation has already started; there are martensitic needles appearing at the edges of the sample and in the corners. Although such a small volume fraction of the transformed phase does not affect the bulk properties in any way, the RUS spectra are very sensitive to small changes in the microstructure and thus the inverse calculation of c' was no longer possible. As seen in Fig. 4b,c, obtained at 238 and 208 K, respectively, the transition proceeds very slowly through the sample. Even at 208 K only a small volume fraction is transformed. This agrees well with the magnetic measurements which indicate that the M_S temperature for the bulk of this sample is even lower at 194 K. Clearly, the bulk of the material transformed more than 60 K below the first appearance of martensite needles. A detailed inspection of the thermomagnetic curve (Fig. 1) gives some indication of the early onset of martensitic transformation as the increase in susceptibility deviates from nearly linear dependence below 240 K.

On the other hand the fit of the RUS spectra above 258 K was acceptably good despite the presence of a small amount of martensitic nuclei pinned on the γ-phase particles, as shown in Fig. 2c. This means that the sample with such nuclei still behaves as a perfect parallelepiped of homogeneous cubic material. The reason may be that the γ-phase particles are fully ordered with the defined orientation to the B2 matrix. Then the stress-induced martensitic nuclei, and thus also the resulting microstructure, still maintain the cubic symmetry of the matrix regardless of whether the nuclei are slightly growing or shrinking with temperature.

The $c'(T)$ curves are summarized for all examined samples in Fig. 5. Some general conclusions can be directly drawn from this figure:

1. All materials exhibit a monotonous softening throughout the whole temperature range for which c' was measurable. This indicates that the B2 structure becomes more unstable upon cooling, even for the as-cast and single-phase materials for which no transition occurs with further cooling. The dc'/dT slopes are approximately the same for annealed samples, especially in the high-temperature region close to 400 K. The slope is lowest for the as-cast sample. There is no sharp change in slope indicating the Curie point for any of the materials, in contrast to Ni–Mn–Ga [27].
2. For all samples there is a smooth, weak but discernible increase in the slope upon cooling below approximately 350 K. While for the annealed samples this increase continues below 258 K, where the thermally induced transition starts, for the as-cast samples (one or two phases) this increase is interrupted by an inflection point below which the slope stabilizes and the softening continues linearly to low temperatures.
3. The differences between the c' coefficients of the annealed samples nearly disappear close to the M_S temperature. In this region, all the values are between 4.5 and 4.7 GPa, which corresponds to an anisotropy factor as high as $A \cong 27$ assuming that the c_{44} coefficient does not change significantly.

Considering the temperature $M_S \cong 258$ K as the real martensite start temperature, at which the first spontaneous nucleation of the thermally induced martensite occurs, we can assume that the all expected premartensitic phenomena should appear above this temperature, i.e. in the temperature interval covered by our RUS measurement.

3.4. Anomalies in c′-softening

For the annealed materials, the appearance of the first visually observable (mezoscopic) martensitic needles is preceded by a continuous change in the slope dc'/dT. The question is whether this anomaly can be related to some premartensitic phenomenon, i.e. to any precursor of the

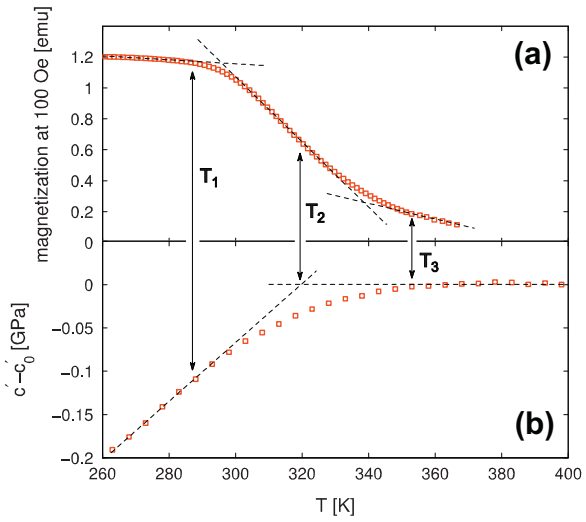

Fig. 6. Comparison of the temperature dependence of the low field magnetization and the c'-softening curve after subtracting the high-temperature linear trend c'_0. See the text for the definitions of temperatures $T_{1,\ldots,3}$.

transition as it is in Ni–Mn–Ga. Apart from the softening of the c' coefficients, there are no other signatures of such phenomena, and thus the answer is probably no. Moreover, the temperature region in which the change of the slope appears corresponds exactly to the wide interval of magnetic susceptibility change during the magnetic transition.

This is demonstrated in detail in Fig. 6 for the case of the material annealed at 1573 K. When a high-temperature linear trend $c'_0(T) = aT + b$ is subtracted from the $c'(T)$ curve, it is apparent that the change in the slope begins at temperature T_3, which is the same as the temperature where the magnetization starts increasing. Further, the point of maximal change of the slope of $c'(T)$ corresponds well to the point of maximal slope of the magnetization (T_2), and the anomaly terminates simultaneously with the levelling of the magnetization at some temperature T_1. Equivalent behaviour is observed for the two other annealed (transforming) samples. Hence, it is plausible that similarly as for the Ni–Mn–Ga alloy [29], the onset of the ferromagnetic ordering at the Curie point triggers the contribution of the magnetostriction to the overall elastic response of the material, which leads to the so-called ΔE-effect [43]. This contribution superposes with the structural softening due to the instability of the B2 lattice, and the dc'/dT slope increases. Similar softening occurs for the as-cast sample, though the anomaly in c'softening starts at a higher temperature and is wider, in agreement with the magnetic measurement (Fig. 1).

On the other hand, in sharp contrast with Ni–Mn–Ga, this magnetoelastic contribution to the overall softening is very weak as indicated in Fig. 6. At room temperature, for example, the c' coefficient decreased only by 0.1 GPa with respect to the linear part $c'_0(T)$. This very weak dependence agrees well with our recent observation of the evolution of RUS spectra of Co–Ni–Al samples in a magnetic field [44]. The RUS spectra do not change significantly with increasing magnetic field. The observed shift of the first resonant peaks was nearly negligible (about 0.3%) and consequently the change in elastic coefficient c' is very small (approximately 0.1 GPa in saturation). The elastic damping stays constant up to magnetic saturation [44]. This confirms very weak magnetoelastic coupling in Co–Ni–Al. For comparison, the change in the c' coefficient under the action of a saturated magnetic field for the Ni–Mn–Ga austenite at room temperature is very large, about 80% or 2.5 GPa, i.e. 25 times larger than in Co–Ni–Al, and the damping in Ni–Mn–Ga sharply decreases with increasing magnetic field [27,29].

In the annealed samples, the magnetoelastic softening apparently continues until the bulk sample transforms. For the as-cast and single-phase alloys, however, the situation is different. At about 290 K, the weak additional softening stops and the dc'/dT slope becomes again constant (Fig. 5). A detailed look at the temperature dependence of $c'(T)$ of non-transforming alloys reveals some additional details. In the as-cast sample the slopes of the low- and high-temperature parts are about the same, whereas in the single-phase sample the low-temperature slope is lower than the high-temperature one. This suggests that there is some stiffening mechanism working against the structural softening of the B2 lattice. In particular, this stiffening can prevent the martensitic transition and suppress the nucleation of martensite. In the annealed alloys, where the martensite nuclei are already present at the vicinity of γ-phase particles, the nucleation barrier does not need to be overcome, and the transition can proceed smoothly by moving the existing interfaces.

4. Summary

RUS measurements of the elastic coefficients (constants) indicate that there are pronounced differences between the elastic properties of Co–Ni–Al samples with the same stoichiometry but with different heat treatments and/or phase composition, resulting in different transformation behaviour. While the c_{11} coefficient is approximately constant in all investigated samples, the shear elastic coefficients differ significantly at room temperature. The difference can be related to the presence of the γ-phase particles and stress-induced martensite nuclei in the vicinity of these precipitates. In single-phase sample (which is also as-cast) the c_{44} coefficient is the smallest, and the coefficient increases for a two-phase system and with annealing. On the other hand, the presence of the γ-phase in the form of a dense net of particles stiffens the shears related to the c' coefficient. If such particles are absent or are partly dissolved by annealing, the c' coefficient significantly decreases, and thus the elastic anisotropy at room temperature increases with increasing annealing temperature. The observed c'-softening with decreasing temperature indicates that the B2 structure is

unstable against shear. However, only annealed material transforms to martensite. In the as-cast samples there is some additional stiffening mechanism, which works against this softening and results in the inflection-like anomaly. As a result, despite continuing c'-softening, the materials without martensite nuclei do not transform into martensite.

None of the reported measurements indicated the existence of any real premartensitic phase; the continuous anomalous change of the dc'/dT slope observable for all samples can be fully attributed to the magnetic transition and presence of martensitic nuclei induced in the vicinity of γ-precipitates well above bulk martensite transformation.

Acknowledgments

This work has been financially supported by the Czech Science Foundation Grant Nos. P107/11/0391 and 101/09/0702, and by the Academy of Sciences of the Czech Republic, bilateral international collaboration project No. M100761203.

References

[1] Ullakko K, Huang JK, Kantner C, O'Handley RC, Kokorin VV. Appl Phys Lett 1996;69:1966–8.
[2] Ullakko K, Huang JK, Kokorin VV, O'Handley RC. Scripta Mater 1997;36:1133–8.
[3] Heczko O, Sozinov A, Ullakko K. IEEE Trans Mag 2000;36:3266–8.
[4] Sozinov A, Likhachev AA, Lanska N, Söderberg O, Ullakko K, Lindroos VK. Mater Sci Eng A 2004;378:399–402.
[5] Kohl M, Reddy YS, Khelfaoui F, Krevet B, Backen A, Fähler S, et al. Mater Sci Forum 2010;635:145–54.
[6] Ullakko K, Wendell L, Smith A, Müllner P, Hampikian G. Smart Mater Struct 2012;21:115020.
[7] Kiefer B, Lagoudas DC. Philos Mag 2005;85:4289–329.
[8] Entel P, Buchelnikov VD, Khovailo VV, Zayak AT, Adeagbo WA, Gruner ME, et al. J Phys D: Appl Phys 2006;39:865–89.
[9] Gauthier J-Y, Hubert A, Abadie J, Chaillet N, Lexcellent C. Sens Actuat A 2008;141:536–47.
[10] Jiles DC. Acta Mater 2003;51:5907–39.
[11] Heczko O, Scheerbaum N, Gutfleisch O. Magnetic shape memory phenomena. Berlin: Springer; 2009. p. 399.
[12] Cui J, Shield TW, James RD. Acta Mater 2004;52:35–47.
[13] Furuya Y, Hagood NW, Kimura H, Watanabe T. Mater Trans JIM 1998;39:1248–54.
[14] Graf T, Felser C, Parkin S. Prog Solid State Chem 2011;39:1–50.
[15] Oikawa K, Ota T, Gejima F, Ohmori T, Kainuma R, Ishida K. Mater Trans 2011;42:2472–5.
[16] Oikawa K, Omori T, Sutou Y, Kainuma R, Ishida K. J Phys IV 2003;112 II:1017–20.
[17] Murakami Y, Shindo D, Oikawa K, Kainuma R, Ishida K. Acta Mater 2002;50:2173–84.
[18] Tanaka Y, Ohmori T, Oikawa K, Kainuma R, Ishida K. Mater Trans 2004;45:427–30.
[19] Liu ZH, Dai XF, Zhu ZY, Hu HN, Chen JL, Liu GD, et al. J Phys D: Appl Phys 2004;37:2643–7.
[20] Soederberg O, Straka L, Novak V, Heczko O, Hannula S-P, Lindroos VK. Mater Sci Eng A 2004;386:27.
[21] Straka L, Heczko O, Seiner H, Lanska N, Drahokoupil J, Soroka A, et al. Acta Mater 2011;59:7450–63.
[22] Heczko O, Straka L, Seiner H. Acta Mater 2013;61:622–31.
[23] Sozinov A, Lanska N, Soroka A, Zou W. Appl Phys Lett 2013;102:021902.
[24] Zheludev A, Shapiro SM, Wochner P, Tanner LE. Phys Rev B 1996;54:15045.
[25] Manosa L, Gonzalez-Comas A, Obrado E, Planes A, Chernenko VA, Kokorin VV, et al. Phys Rev B 1997;55:11068.
[26] Perez-Landazebal JI, Sanchez-Alarcos V, Gomez-Polo C, Recarte V, Chernenko VA. Phys Rev B 2007;76. 092101-1-3.
[27] Heczko O, Seiner H, Sedlak P, Kopecek J, Landa M. J Appl Phys 2012;111:07A929.
[28] Brown J, Ishida K, Kainuma R, Kanomata T, Neumann K-U, Oikawa K, et al. J Phys: Condens Matter 2005;17:1301–10.
[29] Seiner H, Heczko O, Sedlak P, Bodnarova L, Novotny M, Kopecek J, et al. J. Alloys Compd, in press. http://dx.doi.org/10.1016/j.jallcom.2012.01.007.
[30] Leisure RG, Willis FA. J Phys: Condens Matter 1997;9:6001–29.
[31] Maynard J. Phys Today 1996;46:26–31.
[32] Seiner H, Bodnarova L, Sedlak P, Janecek M, Srba O, Kral R, et al. Acta Mater 2010;58:235–47.
[33] Bhattacharya K. Microstructure of martensite. New York: Oxford University Press; 2003.
[34] Kopeček J, Jurek K, Jarošová M, Drahokoupil J, Sedláková-Ignácová S, Šittner P, et al. IOP Conf Ser: Mater Sci Eng 2010;7. 012013-1-8.
[35] Kopeček J, Sedláková-Ignácová S, Jurek K, Jarošová M, Drahokoupil J, Šittner P, et al. ESOMAT 2009; 2009. article no. 02013. http://dx.doi.org/10.1051/esomat/200902013.
[36] Kopeček J, Jarošová M, Jurek K, Heczko O. 24th National conference on heat treatment with international participations ECOSOND s.r.o., Čerčany; 2012. p. 372–80. ISBN 978-80-904462-5-0.
[37] Sedlak P, Landa M, Seiner H, Bicanová L, Heller L. NDT database J. In: International symposium on laser ultrasonics: science, technology and applications 1, August 16–18, 2008, Montreal, Canada; 2008. p. 1–6, article no 34. <http://www.NDT.net>.
[38] Ogi H, Sato K, Asada T, Hirao M. J Acoust Soc Am 2002;112:2553–7.
[39] Janovska M, Sedlak P, Seiner H, Landa M, Marton P, Ondrejkovic P, et al. J Phys Cond Matter 2012;24:385404.
[40] Kopecek J, Kopecky V, Landa M, Heczko O. Mater Sci Forum 2013;738–739:416–20.
[41] Kopeček J, Yokaichiya F, Laufek F, Jarošová M, Jurek K, Drahokoupil J, et al. Acta Phys Pol A 2012;122:475–7.
[42] Ball JM, Koumatos K, Seiner H. J Alloys Compd, in press. http://dx.doi.org/10.1016/j.jallcom.2011.11.070.
[43] Chikazumi S, Graham C. Physics of magnetism. first ed. Huntington, NY: R.E. Krieger Pub.; 1978.
[44] Heczko O, Seiner H, Sedlak P, Kopecek J, Kopecky V, Landa M. Eur Phys J B 2013;86:62-1-5.

4.5 Shrnutí získaných poznatků

Společným jmenovatelem efektů popisovaných v této kapitole je vliv mikrostruktur na elastické koeficienty vysokoteplotních fází, zejména na smykové koeficienty c' a c_{44}. Tyto smykové koeficienty jsou důležitými parametry vysokoteplotních fází, neboť v sobě nesou informaci o anomálně měkkých větvích akustických fononů, které umožňují samotnou termoelastickou martenzitickou transformaci.

Jak bylo ukázáno v podkapitolách 4.1 a 4.2, velmi výrazný vliv na tyto smykové koeficienty má v slitině NiMnGa magnetoelastická interakce. Doménové stěny jsou zachycené na antifázových rozhraních a vytvářejí velmi jemnou magnetickou mikrostrukturu, která se může snadno pod vnějším napětím reorientovat a přispívat tak prostřednictvím magnetostrikce k deformaci materiálu. Výsledkem je další smykové změknutí konstanty c' odpovídající diagonálním smykům a její výrazná závislost na vnějším magnetickém poli.

Smyková konstanta c_{44}, odpovídající smykům bazálním, je naopak tímto efektem zcela neovlivněna. U ní však dochází ke změknutí jiným mechanizmem: v oblasti těsně nad martenzitickým přechodem, kde se mřížka vysokoteplotní fáze nachází ve stavu takzvaného premartenzitického tweedu, způsobují vzájemné rotace elementárních buněk tweedu efektivní změknutí bazálních smyků, jak je experimentálně zdokumentováno a teoretickým modelem vysvětleno v podkapitole 4.3.

Podobné efekty jako ve slitině NiMnGa lze pozorovat, ovšem v podstatně menší míře, také ve vysokoteplotních fázích slitiny CoNiAl (podkapitola 4.4). Magnetoelastická interakce je zde slabší a magnetický přechod probíhá v širokém teplotním intervalu, proto se tyto efekty projeví jenom jako konkávní odchylka závislosti c' na teplotě od lineárního trendu. Při nižších teplotách pak opět dochází k drobnému zpevnění této konstanty, což může být efekt opět vyplývající z tweedového charakteru. Kritickým faktorem se naopak jeví být přítomnost martenzitických zárodků na jemně dispergovaných částicích netransformující fáze - ta zřejmě ovlivňuje jak elastické konstanty vysokoteplotní fáze, tak transformační teplotu.

Závěr

V této habilitační práci bylo ukázáno, jak zásadní vliv může mít morfologie mikrostruktury a mechanismy její nukleace, růstu a pohybu materiálem na makroskopické vlastnosti monokrystalů termoelastických martenzitů. Tématicky práce pokrývá všechny tři možné druhy mikrostruktur v těchto materiálech: mikrostruktury formující se přímo při transformaci za účelem zajištění kinematické kompatibility mezi vysokoteplotními a nízkoteplotními fázemi (rozhraňové mikrostruktury, Kapitola 2), mikrostruktury v nízkoteplotních fázích (martenzitické dvojčatové struktry, Kapitola 3) a mikrostruktury ve vysokoteplotních fázích (doménové struktury v austenitu a premartenzitický tweed, Kapitola 4).

Experimentální a teoretický výzkum mikrostruktur v termoelastických martenzitech na úrovni monokrystalů je základem pro hlubší pochopení termomechanického chování těchto pokročilých materiálů. Výstupy tohoto výzkumu lze pak, s jistým zjednodušením, aplikovat i na predikci a interpretaci chování polykrystalů [64, 65], nebo naopak pro formulování obecnějších relací mezi krystalovou strukturou a vlastnostmi mikrostruktur v materiálech s bezdifúzními fázovými transformacemi [66].

Publikace uvedené a komentované v této práci přispěly relativně podstatnou měrou k tomuto výzkumu, přinejmenším pro slitinu s tvarovou pamětí Cu-Al-Ni a feromagnetickou slitinu Ni-Mn-Ga. Celkově byly k datu odevzdání práce tyto publikace více jak 80-krát citovány (přičemž nejstarší z nich byly publikovány v roce 2009 a nejnovější v roce 2014). Řada z nich inicializovala další a podrobnější teoretické studie kinematické kompatibility mikrostruktur (např. [63,67,68] pro slitinu Cu-Al-Ni) nebo další experimentální výzkum pohyblivosti (např. [69–71]).

Výzkum v oblasti termoelastických martenzitů patří v současnosti mezi nejaktuálnější témata na pomezí fyziky pevných látek, materiálového inženýrství a fyzikální metalurgie. Jsou vyvíjeny jak zcela nové slitiny s unikátními vlastnostmi (např. materiály s nadkritickým transformačním chováním [72, 73]), tak publikovány podrobné experimentální a teoretické studie vlastností slitin stávajících, často s využitím moderních prostředků počítačového ab-initio modelování, nebo in-situ elektronové mikroskopie, která umožňuje studovat detailně mechanismy pohybu a morfologických změn jednotlivých mikrostruktur [74].

Použitá literatura

[1] Salzbrenner, R.J., Cohen, M. On the thermodynamics of thermoelastic martensitic transformations (1979) Acta Metallurgica, 27 (5), pp. 739-748.

[2] Ortin, J., Planes, A. Thermodynamic analysis of thermal measurements in thermoelastic martensitic transformations (1988) Acta Metallurgica, 36 (8), pp. 1873-1889.

[3] Olson, G.B., Cohen, M. Thermoelastic behavior in martensitic transformations (1975) Scripta Metallurgica, 9 (11), pp. 1247-1254.

[4] Otsuka, K., Wayman, C.M. (Eds.)Shape memory materials. Cambridge: Cambridge University Press, 1998.

[5] Bhattacharya, K. Microstructure of Martensite. Oxford: Oxford University Press, 2003.

[6] Otsuka, K., Wayman, C.M., Nakai, K., Sakamoto, H., Shimizu, K. Superelasticity effects and stress-induced martensitic transformations in CuAlNi alloys (1976) Acta Metallurgica, 24 (3), pp. 207-226.

[7] Tobushi, H., Shimeno, Y., Hachisuka, T., Tanaka, K. Influence of strain rate on superelastic properties of TiNi shape memory alloy (1998) Mechanics of Materials, 30 (2), pp. 141-150.

[8] Auricchio, F., Taylor, R.L., Lubliner, J. Shape-memory alloys: Macromodelling and numerical simulations of the superelastic behavior (1997) Computer Methods in Applied Mechanics and Engineering, 146 (3-4), pp. 281-312

[9] Ren, X., Otsuka, K. Origin of rubber-like behaviour in metal alloys (1997) Nature, 389 (6651), pp. 579-582.

[10] Murray, S.J., Marioni, M., Allen, S.M., O'Handley, R.C., Lograsso, T.A. 6% magnetic-field-induced strain by twin-boundary motion in ferromagnetic Ni-Mn-Ga (2000) Applied Physics Letters, 77 (6), pp. 886-888.

[11] Likhachev, A.A., Ullakko, K. Magnetic-field-controlled twin boundaries motion and giant magneto-mechanical effects in Ni-Mn-Ga shape memory alloy (2000) Physics Letters, Section A: General, Atomic and Solid State Physics, 275 (1-2), pp. 142-151.

[12] Masud, A., Xia, K. A variational multiscale method for inelasticity: Application to superelasticity in shape memory alloys (2006) Computer Methods in Applied Mechanics and Engineering, 195 (33-36), pp. 4512-4531

[13] Turteltaub, S., Suiker, A.S.J. A multiscale thermomechanical model for cubic to tetragonal martensitic phase transformations (2006) International Journal of Solids and Structures, 43 (14-15), pp. 4509-4545.

[14] Salje, E.K.H., Ishibashi, Y. Mesoscopic structures in ferroelastic crystals: Needle twins and right-angled domains (1996) Journal of Physics Condensed Matter, 8 (44), pp. 8477-8495.

[15] Salje, E.K.H., Hayward, S.A., Lee, W.T. Ferroelastic phase transitions: Structure and microstructure (2005) Acta Crystallographica Section A: Foundations of Crystallography, 61 (1), pp. 3-18.

[16] Bhattacharya, K., Li, B., Luskin, M. The simply laminated micro structure in martensitic crystals that undergo a cubic-to-orthorhombic phase transformation (1999) Archive for Rational Mechanics and Analysis, 149 (2), pp. 123-154.

[17] Ball, J.M., Carstensen, C. Compatibility conditions for microstructures and the austenite-martensite transition (1999) Materials Science and Engineering A, 273-275, pp. 231-236.

[18] Seiner, H., Heczko, O., Sedlák, P., Bodnárová, L., Novotný, M., Kopeček, J., Landa, M. Combined effect of structural softening and magneto-elastic coupling on elastic coefficients of NiMnGa austenite (2013) Journal of Alloys and Compounds, 577 (SUPPL. 1), pp. S131-S135.

[19] Seiner, H., Sedlák, P., Bodnárová, L., Drahokoupil, J., Kopecký, V., Kopeček, J., Landa, M., Heczko, O. The effect of antiphase boundaries on the elastic properties of Ni-Mn-Ga austenite and premartensite (2013) Journal of Physics Condensed Matter, 25 (42), art. no. 425402.

[20] Microstructure, martensitic transformation and anomalies in c?-softening in Co-Ni-Al ferromagnetic shape memory alloys (2013) Acta Materialia, 61 (15), pp. 5869-5876.

[21] Basinski, Z.S., Christian, J.W. Experiments on the martensitic trasformation in single crystals of Indium-Thallium alloys (1954) Acta Metallurgica 2, pp.148-166.

[22] Basinski, Z.S., Christian, J.W. Crystallography of deformation by twin boundary movements in Indium-Thallium alloys (1954) Acta Metallurgica 2, pp.102-116.

[23] Seiner, H., Sedlak, P., Landa, M. Shape recovery mechanism observed in single crystals of Cu-Al-Ni shape memory alloy (2008) Phase Transitions, 81 (6), pp. 537-551.

[24] Seiner, H., Glatz, O., Landa, M. Interfacial microstructures in martensitic transitions: From optical observations to mathematical modeling (2009) International Journal for Multiscale Computational Engineering, 7 (5), pp. 445-456.

[25] Chu, C-H.Hysteresis and microstructures: A study of biaxial loading on compound twinns of Copper-Aluminium-Nickel single crystals. PhD thesis, University of Minnesota, 1998.

[26] Sedlák, P., Seiner, H., Landa, M., Novák, V., Šittner, P., Manosa, Ll. Elastic constants of bcc austenite and 2H orthorhombic martensite in CuAlNi shape memory alloy (2005) Acta Materialia, 53 (13), pp. 3643-3661.

[27] Chernenko, V.A., Cesari, E., Kokorin, V.V., Vitenko, I.N. The development of new ferromagnetic shape memory alloys in Ni-Mn-Ga system (1995) Scripta Metallurgica et Materiala, 33 (8), pp. 1239-1244.

[28] Pons, J., Chernenko, V.A., Santamarta, R., Cesari, E. Crystal structure of martensitic phases in Ni-Mn-Ga shape memory alloys (2000) Acta Materialia, 48 (12), pp. 3027-3038.

[29] Oikawa, K., Ota, T., Gejima, F., Ohmori, T., Kainuma, R., Ishida, K. Phase equilibria and phase transformations in new B2-type ferromagnetic shape memory alloys of Co-Ni-Ga and Co-Ni-Al systems (2001) Materials Transactions, 42 (11), pp. 2472-2475.

[30] Murakami, Y., Shindo, D., Oikawa, K., Kainuma, R., Ishida, K. Magnetic domain structures in Co-Ni-Al shape memory alloys studied by Lorentz microscopy and electron holography (2002) Acta Materialia, 50 (8), pp. 2173-2184.

[31] Otsuka, K., Ren, X. Physical metallurgy of Ti-Ni-based shape memory alloys (2005) Progress in Materials Science, 50 (5), pp. 511-678.

[32] Delville, R., Malard, B., Pilch, J., Sittner, P., Schryvers, D. Transmission electron microscopy investigation of dislocation slip during superelastic cycling of Ni-Ti wires (2011) International Journal of Plasticity, 27 (2), pp. 282-297

[33] Kajiwara, S. Characteristic features of shape memory effect and related transformation behavior in Fe-based alloys (1999) Materials Science and Engineering A, 273-275, pp. 67-88.

[34] Ogawa, K., Kajiwara, S. HREM study of stress-induced transformation structures in an Fe-Mn-Si-Cr-Ni shape memory alloy (1993) Materials Transactions, JIM, 34 (12), pp. 1169-1176.

[35] Dolzmann, G. Variational Methods for Crystalline Microstructure - Analysis and Computation. Berlin–Heidelberg: Springer–Verlag 2003

[36] Ball, J.M., James, R.D. Fine phase mixtures as minimizers of energy (1987) Archive for Rational Mechanics and Analysis, 100 (1), pp. 13-52.

[37] Ball, J.M. Mathematical models of martensitic microstructure (2004) Materials Science and Engineering A, 378, pp.61-69.

[38] Ball, J.M., James, R.D. Local minimizers and phase transformations (1996) ZAMM Zeitschrift fur Angewandte Mathematik und Mechanik, 76 (SUPPL. 2), pp. 389-392.

[39] Seiner, H. Dynamic and transient phenomena in single crystals of shape memory alloys, Ph.D. Thesis, Prague: Czech Technical University 2008.

[40] Hane, K.F. Microstructures in thermoelastic martensites. PhD thesis, University of Minnesota, 1998

[41] Forclaz, A. Variational Methods in Materials Science. PhD Thesis, Oxford 2002.

[42] Kružík, M., Mielke, A., Roubíček, T. Modelling of microstructure and its evolution in shape-memory-alloy single-crystals, in particular in CuAlNi (2005) Meccanica, 40 (4-6 SPEC. ISS.), pp. 389-418.

[43] Ball, J.M., Carstensen, C. Nonclassical austenite-martensite interfaces (1998) Journal De Physique. IV : JP, 7 (5), pp. C5-35-C5-40.

[44] Balandraud, X., Zanzotto, G. Stressed microstructures in thermally induced M9R-M18R martensites (2007) Journal of the Mechanics and Physics of Solids, 55 (1), pp. 194-224.

[45] Shield, T.W. Orientation dependence of the pseudoelastic behavior of single crystals of CuAlNi in tension (1995) Journal of the Mechanics and Physics of Solids, 43 (6), pp. 869-895.

[46] Sun, Q.-P., Li, Z.-Q. Phase transformation in superelastic NiTi polycrystalline micro-tubes under tension and torsion - From localization to homogeneous deformation (2002) International Journal of Solids and Structures, 39 (13-14), pp. 3797-3809.

[47] Feng, P., Sun, Q.P. Experimental investigation on macroscopic domain formation and evolution in polycrystalline NiTi microtubing under mechanical force (2006) Journal of the Mechanics and Physics of Solids, 54 (8), pp. 1568-1603.

[48] Li, Z.Q., Sun, Q.P. The initiation and growth of macroscopic martensite band in nanograined NiTi microtube under tension (2002) International Journal of Plasticity, 18 (11), pp. 1481-1498.

[49] Ng, K.L., Sun, Q.P. Stress-induced phase transformation and detwinning in NiTi polycrystalline shape memory alloy tubes (2006) Mechanics of Materials, 38 (1-2), pp. 41-56.

[50] Vedantam, S., Abeyaratne, R. A Helmholtz free-energy function for a Cu-Al-Ni shape memory alloy (2005) International Journal of Non-Linear Mechanics, 40 (2-3), pp. 177-193.

[51] Kerr, W.C., Killough, M.G., Saxena, A., Swart, P.J., Bishop, A.R. Role of elastic compatibility in martensitic texture evolution (1999) Phase Transitions, 69 (3), pp. 247-270.

[52] Abeyaratne, R., Knowles, J.K., Evolution of phase transitions - a continuum theory. Cambridge: Cambridge University Press, 2006.

[53] Abeyaratne, R., Knowles, J.K. On the kinetics of an austenite $\rightarrow$ martensite phase transformation induced by impact in a Cu-Al-Ni shape-memory alloy (1997) Acta Materialia, 45 (4), pp. 1671-1683.

[54] Abeyaratne, R., Knowles, J.K. A continuum model of a thermoelastic solid capable of undergoing phase transitions (1993) Journal of the Mechanics and Physics of Solids, 41 (3), pp. 541-571.

[55] Truskinovsky, L., Vainchtein, A. Kinetics of martensitic phase transitions: Lattice model (2006) SIAM Journal on Applied Mathematics, 66 (2), pp. 533-553.

[56] Truskinovsky, L., Vainchtein, A. Quasicontinuum models of dynamic phase transitions (2006) Continuum Mechanics and Thermodynamics, 18 (1-2), pp. 1-21.

[57] Maugin, G.A. Nonlinear Waves in Elastic Crystals. Oxford: Oxford University Press, 2000.

[58] Seiner, H., Mobile Interfacial Microstructures in Single Crystals of Cu-Al-Ni Shape Memory Alloy (2015) Shape Memory and Superelasticity, 1 (1), accepted, doi:10.1007/s40830-015-0009-0.

[59] Straka, L., Heczko, O., Seiner, H., Lanska, N., Drahokoupil, J., Soroka, A., Fähler, S., Hänninen, H., Sozinov, A. Highly mobile twinned interface in 10 M modulated Ni-Mn-Ga martensite: Analysis beyond the tetragonal approximation of lattice (2011) Acta Materialia, 59 (20), pp. 7450-7463.

[60] Straka, L., Lanska, N., Ullakko, K., Sozinov, A. Twin microstructure dependent mechanical response in Ni-Mn-Ga single crystals (2010) Applied Physics Letters, 96 (13), art. no. 131903

[61] Straka, L., Soroka, A., Seiner, H., Hänninen, H., Sozinov, A. Temperature dependence of twinning stress of Type i and Type II twins in 10M modulated Ni-Mn-Ga martensite (2012) Scripta Materialia, 67 (1), pp. 25-28.

[62] Seiner, H. Highly mobile interfaces in shape memory alloys (2015), plenary lecture, ESOMAT 2015, Antwerp, Belgium.

[63] Stupkiewicz, S., Górzyńska-Lengiewicz, A. Almost compatible X-microstructures in CuAlNi shape memory alloy (2012) Continuum Mechanics and Thermodynamics, 24 (2), pp. 149-164.

[64] Sedlák, P., Frost, M., Benešová, B., Ben Zineb, T., Šittner, P. Thermomechanical model for NiTi-based shape memory alloys including R-phase and material anisotropy under multi-axial loadings (2012) International Journal of Plasticity, 39, pp. 132-151.

[65] Frost, M., Benešová, B., Sedlák, P. A microscopically motivated constitutive model for shape memory alloys: Formulation, analysis and computations (2015) Mathematics and Mechanics of Solids, in press, doi: 10.1177/1081286514522474.

[66] Chen, X., Srivastava, V., Dabade, V., James, R.D. Study of the cofactor conditions: Conditions of supercompatibility between phases (2013) Journal of the Mechanics and Physics of Solids, 61 (12), pp. 2566-2587. .

[67] Stupkiewicz, S., MacIejewski, G., Petryk, H. Elastic micro-strain energy of austenite-martensite interface in NiTi (2012) Modelling and Simulation in Materials Science and Engineering, 20 (3), art. no. 035001

[68] Ball, J.M., Koumatos, K. An investigation of non-planar austenite-martensite interfaces (2014) Mathematical Models and Methods in Applied Sciences, 24 (10), pp. 1937-1956.

[69] Faran, E., Shilo, D. Dynamics of twin boundaries in ferromagnetic shape memory alloys (2014) Materials Science and Technology (United Kingdom), 30 (13), pp. 1545-1558.

[70] Faran, E., Shilo, D. The kinetic relation for twin wall motion in NiMnGa - Part 2 (2013) Journal of the Mechanics and Physics of Solids, 61 (3), pp. 726-741.

[71] Faran, E., Shilo, D. Implications of twinning kinetics on the frequency response in NiMnGa actuators (2012) Applied Physics Letters, 100 (15), art. no. 151901

[72] Xiao, F., Fukuda, T., Kakeshita, T. Elastic limit of Fe-Pd alloys exhibiting lattice softening (2014) ISIJ International, 54 (6), pp. 1374-1378.

[73] Fukuda, T., Kakeshita, T. More than 6% elastic strain realized in a bulk single crystal of an Fe_3Pt alloy (2013) Scripta Materialia, 69 (1), pp. 89-91.

[74] Liu, Y., Karaman, I., Wang, H., Zhang, X. Two types of martensitic phase transformations in magnetic shape memory alloys by in-situ nanoindentation studies (2014) Advanced Materials, 26 (23), pp. 3893-3898.

Příloha A

Souhrn publikační činnosti autora

A.1 Publikace v impaktovaných časopisech

Uvedené impaktfaktory se vztahují k datům vydání jednotlivých publikací.

1. Thomasová, M., Sedlák, P., Seiner, H., Janovská, M., Kabla, M., Shilo, D., Landa, M. Young's moduli of sputter-deposited NiTi films determined by resonant ultrasound spectroscopy: Austenite, R-phase, and martensite (2015) Scripta Materialia, 101, pp.24-27. **(IF=2.968)**

2. Ben-David, E., Landa, M., Janovská, M., Seiner, H., Gutman, O., Tepper-Faran. T., Shilo, D., The effect of grain and pore sizes on the mechanical behavior of thin Al films deposited under different conditions (2015) Acta Materialia, 87, pp. 321-331. **(IF=3.940)**

3. Kruisová, A., Seiner, H., Sedlák, P., Landa, M., Román-Manso, B., Miranzo, P. Belmonte, M. Acoustic metamaterial behavior of three-dimensional periodic architectures assembled by robocasting (2014) Applied Physics Letters 105, art, no. 211904. **(IF=3.515)**

4. Stoklasová, P., Sedlák, P., Seiner, H., Landa, M. Forward and inverse problems for surface acoustic waves in anisotropic media: A Ritz-Rayleigh method based approach (2015) Ultrasonics, 56, pp.381-389. **(IF=1.805)**

5. Koller, M., Sedlák, P. Seiner, H. Ševčík, M., Landa, M., Stráská, J., Janeček, M. An ultrasonic internal friction study of ultrafine-grained AZ31 magnesium alloy (2015) Journal of Materials Science 50, pp. 808-818. **(IF=2.305)**

6. Nejezchlebová, J., Seiner, H., Ševčík, M., Landa, M., Karlík, M. Ultrasonic detection of ductile-to-brittle transitions in free-cutting aluminum alloys (2015) NDT&E International, 69, pp. 40-47. **(IF=1.717)**

7. Kabla, M., Seiner, H., Musilova, M., Landa, M., Shilo, D. The relationships between sputter deposition conditions, grain size, and phase transformation temperatures in NiTi thin films (2014) Acta Materialia, 70, pp. 79-91. **(IF=3.940)**

8. Seiner, H., Kopecký, V., Landa, M., Heczko, O. Elasticity and magnetism of Ni2MnGa premartensitic tweed (2014) Physica Status Solidi (B) Basic Research, 251, pp. 2097-2103. **(IF=1.605)**

9. Seiner, H., Straka, L., Heczko, O. A microstructural model of motion of macro-twin interfaces in Ni-Mn-Ga 10 M martensite (2014) Journal of the Mechanics and Physics of Solids, 64 (1), pp. 198-211. **(IF=4.289)**

10. Sedlák, P., Seiner, H., Zídek, J., Janovská, M., Landa, M. Determination of All 21 Independent Elastic Coefficients of Generally Anisotropic Solids by Resonant Ultrasound Spectroscopy: Benchmark Examples (2014) Experimental Mechanics, 54 (6), pp. 1073-1085. **(IF=1.567)**

11. Ball, J.M., Koumatos, K., Seiner, H. Nucleation of austenite in mechanically stabilized martensite by localized heating (2013) Journal of Alloys and Compounds, 577 (SUPPL. 1), pp. S37-S42. **(IF=2.726)**

12. Seiner, H., Heczko, O., Sedlák, P., Bodnárová, L., Novotný, M., Kopeček, J., Landa, M. Combined effect of structural softening and magneto-elastic coupling on elastic coefficients of NiMnGa austenite (2013) Journal of Alloys and Compounds, 577 (SUPPL. 1), pp. S131-S135. **(IF=2.726)**

13. Seiner, H., Sedlák, P., Bodnárová, L., Drahokoupil, J., Kopecký, V., Kopeček, J., Landa, M., Heczko, O. The effect of antiphase boundaries on the elastic properties of Ni-Mn-Ga austenite and premartensite (2013) Journal of Physics Condensed Matter, 25 (42), art. no. 425402. **(IF=2.223)**

14. Sedmák, P., Seiner, H., Sedlák, P., Landa, M., Mušálek, R., Matějíček, J. Application of resonant ultrasound spectroscopy to determine elastic constants of plasma-sprayed coatings with high internal friction (2013) Surface and Coatings Technology, 232, pp. 747-757. **(IF=2.199)**

15. Seiner, H., Kopeček, J., Sedlák, P., Bodnárová, L., Landa, M., Sedmák, P., Heczko, O. Microstructure, martensitic transformation and anomalies in c'-softening in Co-Ni-Al ferromagnetic shape memory alloys (2013) Acta Materialia, 61 (15), pp. 5869-5876. **(IF=3.940)**

16. Ctibor, P., Seiner, H., Sedlacek, J., Pala, Z., Vanek, P. Phase stabilization in plasma sprayed BaTiO3 (2013) Ceramics International, 39 (5), pp. 5039-5048. **(IF=2.086)**

17. Heczko, O., Seiner, H., Sedlák, P., Kopeček, J., Kopecký, V., Landa, M. Resonant ultrasound spectroscopy - A tool to probe magneto-elastic properties of ferromagnetic shape

memory alloys (2013) European Physical Journal B, 86 (2), art. no. 62. **(IF=1.463)**

18. Heczko, O., Kopeček, J., Straka, L., Seiner, H. Differently mobile twin boundaries and magnetic shape memory effect in 10 M martensite of Ni-Mn-Ga (2013) Materials Research Bulletin, 48 (12), pp. 5105-5109. **(IF=1.968)**

19. Seiner, H., Sedlák, P., Koller, M., Landa, M., Ramírez, C., Osendi, M.I., Belmonte, M. Anisotropic elastic moduli and internal friction of graphene nanoplatelets/silicon nitride composites (2013) Composites Science and Technology, 75, pp. 93-97. **(IF=3.633)**

20. Heczko, O., Straka, L., Seiner, H. Different microstructures of mobile twin boundaries in 10 M modulated Ni-Mn-Ga martensite (2013) Acta Materialia, 61 (2), pp. 622-631. **(IF=3.940)**

21. Janovská, M., Sedlák, P., Seiner, H., Landa, M., Marton, P., Ondrejkovič, P., Hlinka, J. Anisotropic elasticity of DyScO3 substrates (2012) Journal of Physics Condensed Matter, 24 (38), art. no. 385404. **(IF=2.355)**

22. Straka, L., Soroka, A., Seiner, H., Hänninen, H., Sozinov, A. Temperature dependence of twinning stress of Type i and Type II twins in 10M modulated Ni-Mn-Ga martensite (2012) Scripta Materialia, 67 (1), pp. 25-28. **(IF=2.821)**

23. Seiner, H., Sedlák, P., Bodnárová, L., Kruisová, A., Landa, M., De Pablos, A., Belmonte, M. Sensitivity of the resonant ultrasound spectroscopy to weak gradients of elastic properties (2012) Journal of the Acoustical Society of America, 131 (5), pp. 3775-3785. **(IF=1.646)**

24. Heczko, O., Seiner, H., Sedlák, P., Kopeček, J., Landa, M. Anomalous lattice softening of Ni 2MnGa austenite due to magnetoelastic coupling (2012) Journal of Applied Physics, 111 (7), art. no. 07A929. **(IF=2.210)**

25. Straka, L., Heczko, O., Seiner, H., Lanska, N., Drahokoupil, J., Soroka, A., Fähler, S., Hänninen, H., Sozinov, A. Highly mobile twinned interface in 10 M modulated Ni-Mn-Ga martensite: Analysis beyond the tetragonal approximation of lattice (2011) Acta Materialia, 59 (20), pp. 7450-7463. **(IF=3.755)**

26. Seiner, H., Glatz, O., Landa, M. A finite element analysis of the morphology of the twinned-to-detwinned interface observed in microstructure of the Cu-Al-Ni shape memory alloy (2011) International Journal of Solids and Structures, 48 (13), pp. 2005-2014. **(IF=1.875)**

27. Růžek, M., Sedlák, P., Seiner, H., Kruisová, A., Landa, M. Linearized forward and inverse problems of the resonant ultrasound spectroscopy for the evaluation of thin surface layers (2010) Journal of the Acoustical Society of America, 128 (6), pp. 3426-3437. **(IF=1.644)**

28. Seiner, H., Bodnárová, L., Sedlák, P., Janeček, M., Srba, O., Král, R., Landa, M. Application of ultrasonic methods to determine elastic anisotropy of polycrystalline copper processed by equal-channel angular pressing (2010) Acta Materialia, 58 (1), pp. 235-247. **(IF=3.781)**

29. Seiner, H., Landa, M. Non-classical austenite-martensite interfaces observed in single crystals of Cu-Al-Ni (2009) Phase Transitions, 82 (11), pp. 793-807. **(IF=0.935)**

30. Seiner, H., Glatz, O., Landa, M. Interfacial microstructures in martensitic transitions: From optical observations to mathematical modeling (2009) International Journal for Multiscale Computational Engineering, 7 (5), pp. 445-456. **(IF=0.734)**

31. Seiner, H., Bicanová, L., Sedlák, P., Landa, M., Heller, L., Aaltio, I. Magneto-elastic attenuation in austenitic phase of Ni-Mn-Ga alloy investigated by ultrasonic methods (2009) Materials Science and Engineering A, 521-522, pp. 205-208. **(IF=1.901)**

32. Landa, M., Sedlák, P., Seiner, H., Heller, L., Bicanová, L., Šittner, P., Novák, V. Modal resonant ultrasound spectroscopy for ferroelastics (2009) Applied Physics A: Materials Science and Processing, 96 (3), pp. 557-567. **(IF=1.595)**

33. Seiner, H., Sedlak, P., Landa, M. Shape recovery mechanism observed in single crystals of Cu-Al-Ni shape memory alloy (2008) Phase Transitions, 81 (6), pp. 537-551. **(IF=1.201)**

34. Landa, M., Sedlák, P., Šittner, P., Seiner, H., Heller, L. On the evaluation of temperature dependence of elastic constants of martensitic phases in shape memory alloys from resonant ultrasound spectroscopy studies (2008) Materials Science and Engineering A, 481-482 (1-2 C), pp. 567-573. **(IF=1.806)**

35. Landa, M., Sedlák, P., Šittner, P., Seiner, H., Novák, V. Temperature dependence of elastic properties of cubic and orthorhombic phases in Cu-Al-Ni shape memory alloy near their stability limits (2007) Materials Science and Engineering A, 462 (1-2), pp. 320-324. **(IF=1.475)**

36. Seiner, H., Landa, M. Differential geometry of ray surfaces in anisotropic solids and its contribution to NDE: Modelling and experiment (2006) Ultrasonics, 44 (SUPPL.), pp. e801-e806. **(IF=1.322)**

37. Sedlák, P., Seiner, H., Landa, M., Novák, V., Šittner, P., Mañosa, Ll. Elastic constants of bcc austenite and 2H orthorhombic martensite in CuAlNi shape memory alloy (2005) Acta Materialia, 53 (13), pp. 3643-3661. **(IF=3.430)**

38. Seiner, H., Landa, M. Sensitivity analysis of an inverse procedure for determination of elastic coefficients for strong anisotropy (2005) Ultrasonics, 43 (4), pp. 253-263. **(IF=1.175)**

A.2 Publikace v recenzovaných časopisech a sbornících

Uvedeny jsou pouze časopisy a sborníky indexované v databázích Web of Science a/nebo Scopus.

39. Seiner, H., Sedlák, P., Bodnárová, L., Landa, M., Stráská, J.V., Janeček, M. In-situ detection of surface micro-cracking in ultrafine-grained AZ31 magnesium alloy by resonant ultrasound spectroscopy (2014) Key Engineering Materials, 606, pp. 87-90.

40. Nejezchlebová, J., Seiner, H., Karlík, M. Detection of phase transition in free-cutting Al-Mg-Si alloys by resonant ultrasound spectroscopy (2014) Materials Science Forum, 794-796, pp. 21-26.

41. Růžek, M., Sedlák, P., Seiner, H., Landa, M. Determination of elastic properties of surface layers and coatings by resonant ultrasound spectroscopy (2011) Journal of Physics: Conference Series, 278 (1), art. no. 012004.

42. Landa, M., Verstraeten, B., Sermeus, J., Salenbien, R., Sedlák, P., Seiner, H., Glorieux, C. Thermomechanical properties of single crystals evaluated by impulsive stimulated thermal scattering technique (2011) Journal of Physics: Conference Series, 278 (1), art. no. 012023.

43. Seiner, H., Růžek, M., Sedlák, P., Bicanová, L., Landa, M. Resonant ultrasound spectroscopy for investigation of thin surface coatings (2009) WIT Transactions on Engineering Sciences, 64, pp. 237-248.

44. Ball, J.M., Koumatos, K., Seiner, H. An analysis of non-classical austenite-martensite interfaces in CuAlNi (2009) Proceedings of the International Conference on Martensitic Transformations, ICOMAT-08, pp. 383-390.

45. Šittner, P., Pilch, J., Lukas, P., Landa, M., Seiner, H., Sedlak, P., Malard, B., Heller, L. In-situ experimental methods for characterization of deformation processes in SMAs (2008) CIMTEC 2008 - Proceedings of the 3rd International Conference on Smart Materials, Structures and Systems - State-of-the-art Research and Application of SMAs Technologies, 59, pp. 47-56.

46. Seiner, H., Landa, M., Sedlák, P. Propagation of an austenite-martensite interface in a thermal gradient (2007) Proceedings of the Estonian Academy of Sciences: Physics, Mathematics, 56 (2), pp. 218-225.

47. Goldmann, T., Seiner, H., Landa, M. Determination of elastic coefficients of bone and composite materials by acoustic immersion technique (2006) Technology and Health Care, 14 (4-5), pp. 219-232.

48. Seiner, H., Sedlák, P., Landa, M. Improvement of the inversion procedure in resonant ultrasound spectroscopy for generally oriented, high anisotropic crystals (2006) Proceedings - IEEE Ultrasonics Symposium, 1, art. no. 4152463, pp. 2433-2436.

49. Seiner, H., Landa, M. Evaluation of all elastic moduli of anisotropic solids from ultrasonic wave inversion (2002) Acta Technica CSAV, 47 (4), pp. 401-418.

50. Landa, M., Růžek, M., Sedlák, P., Seiner, H., Bodnárová, L., Zídek, J., Novel approach to material evaluation of thin surface layers by resonant ultrasound spectroscopy (2010) Journal of Physics Conference Series, 214, art no. 012045.

51. Glatz, O. Seiner, H. Landa, M., FEM Modelling of Elastically Strained Interfacial Microstructures in Cu-Al-Ni Single Crystals (2009) 8th European Symposium on Martensitic Transformations (ESOMAT 2009), art. no. 03006.

52. Landa, M. Seiner, H., Sedlak, P., Bicanova, L., Zidek, J., Heller, L., Resonant Ultrasound Spectroscopy Close To Its Applicability Limits (2009) Horizons in World Physics Series 268, pp.97-136.

53. Goldmann, T.,Seiner, H., Landa, M., Application of Simplified Ray Method for the Determination of the Cortical Bone Elastic Coefficients by the Ultrasonic Wave Inversion (2007) 11th Mediterranean Conference on Medical and Biological Engineering and Computing (MEDICON 2007), IFMBE Proceedings 16 (1-2), pp. 1-2

A.3 Citovanost a *h*–index

K datu odevzdání habilitační práce byly publikace habilitanta celkem 332-krát citovány (podle citační databáze Scopus). Následuje výpis z této databáze shrnutím nejcitovanějších článků a vyznačnou hodnotou $h-$indexu ($h = 9$).

1	Elastic constants of bcc austenite and 2H orthorhombic martensite in CuAlNi shape memory alloy	Sedlák, P., Seiner, H., Landa, M., (...), Šittner, P., Mañosa, Ll.	2005	Acta Materialia	54
2	Highly mobile twinned interface in 10 M modulated Ni-Mn-Ga martensite: Analysis beyond the tetragonal approximation of lattice	Straka, L., Heczko, O., Seiner, H., (...), Hänninen, H., Sozinov, A.	2011	Acta Materialia	48
3	Modal resonant ultrasound spectroscopy for ferroelastics	Landa, M., Sedlák, P., Seiner, H., (...), Šittner, P., Novák, V.	2009	Applied Physics A: Materials Science and Processing	25
4	Different microstructures of mobile twin boundaries in 10 M modulated Ni-Mn-Ga martensite	Heczko, O., Straka, L., Seiner, H.	2013	Acta Materialia	21
5	Temperature dependence of twinning stress of Type i and Type II twins in 10M modulated Ni-Mn-Ga martensite	Straka, L., Soroka, A., Seiner, H., Hänninen, H., Sozinov, A.	2012	Scripta Materialia	20
6	Application of ultrasonic methods to determine elastic anisotropy of polycrystalline copper processed by equal-channel angular pressing	Seiner, H., Bodnárová, L., Sedlák, P., (...), Král, R., Landa, M.	2010	Acta Materialia	17
7	Anomalous lattice softening of Ni 2MnGa austenite due to magnetoelastic coupling	Heczko, O., Seiner, H., Sedlák, P., Kopeček, J., Landa, M.	2012	Journal of Applied Physics	12
8	Temperature dependence of elastic properties of cubic and orthorhombic phases in Cu-Al-Ni shape memory alloy near their stability limits	Landa, M., Sedlák, P., Šittner, P., Seiner, H., Novák, V.	2007	Materials Science and Engineering A	12
9	Anisotropic elastic moduli and internal friction of graphene nanoplatelets/silicon nitride composites	Seiner, H., Sedlák, P., Koller, M., (...), Osendi, M.I., Belmonte, M.	2013	Composites Science and Technology	9
10	Non-classical austenite-martensite interfaces observed in single crystals of Cu-Al-Ni	Seiner, H., Landa, M.	2009	Phase Transitions	9
11	Magneto-elastic attenuation in austenitic phase of Ni-Mn-Ga alloy investigated by ultrasonic methods	Seiner, H., Bicanová, L., Sedlák, P., (...), Heller, L., Aaltio, I.	2009	Materials Science and Engineering A	9
12	A microstructural model of motion of macro-twin interfaces in Ni-Mn-Ga 10 M martensite	Seiner, H., Straka, L., Heczko, O.	2014	Journal of the Mechanics and Physics of Solids	7
13	Linearized forward and inverse problems of the resonant ultrasound spectroscopy for the evaluation of thin surface layers	Růžek, M., Sedlák, P., Seiner, H., Kruisová, A., Landa, M.	2010	Journal of the Acoustical Society of America	7
14	Interfacial microstructures in martensitic transitions: From optical observations to mathematical modeling	Seiner, H., Glatz, O., Landa, M.	2009	International Journal for Multiscale Computational Engineering	7
16	Propagation of an austenite-martensite interface in a thermal gradient	Seiner, H., Landa, M., Sedlák, P.	2007	Proceedings of the Estonian Academy of Sciences: Physics, Mathematics	7
17	Determination of All 21 Independent Elastic Coefficients of Generally Anisotropic Solids by Resonant Ultrasound Spectroscopy: Benchmark Examples	Sedlák, P., Seiner, H., Zídek, J., Janovská, M., Landa, M.	2014	Experimental Mechanics	6